

**Adsorption of Hydrogen, Methane and Carbon Dioxide Gases in Metal-Organic
Frameworks using the Sticking Efficiency Concept;**

(A New Approach)

BY

ESOSA MARK IRIOWEN

A DISSERTATION

**Submitted as a partial fulfillment of the requirements
for the degree of Doctor of Philosophy in the
Applied Chemistry Graduate Program of
Delaware State University**

DOVER, DELAWARE

December 2015

DEDICATION

This doctoral research work is specially dedicated;

To: God Almighty.

To: My wife (*Dr.*) Rosemary Iriowen.

And my lovely son, Osawerene Iriowen (*my big little me*).

To: my father; (*Pastor*) Samuel Imuetinyan Iriowen (*April 7, 1933 – April 21, 2011*).

and

my mother, (*Deaconess*) Mary Iriowen.

To: brother (*Mr.*) Peter Iriowen (*Deceased*) and sister (*Ms.*) Itohan Iriowen (*Deceased*)

ACKNOWLEDGEMENTS

The writing of this dissertation has been one of the most significant academic challenges I have ever had to face. Without the support, patience and guidance of the following people, this study would not have been completed. It is to them that I owe my deepest gratitude.

- Dr. Andrew Goudy, (Director and Supervisor-Center for Hydrogen Storage Research (*CHSR*) at DESU) who undertook to act as my advisor despite his many other academic and professional commitments. His wisdom, knowledge and commitment to the highest standards inspired and motivated me.
- U.S. Department of Energy (DOE) and the U.S. Department of Transportation (DOT) for financially supporting this research.
- Dr. Cherese Winstead, (*Chairperson* of Chemistry Department of Delaware State University) for making my learning and knowledge acquisition in the Department of Chemistry-DESU a success.
- A big thank you to my Committee Members for their reviews of this masterpiece.
- All faculty, staff and students of the Chemistry Department at DESU-USA.
- Dr. Michael Casson *Jr.*, Director of the University Center for Economic Development and International Trade for love and peace you provided during my academic goal pursuit.
- My friends and colleagues,; (Drs.) Olanrewaju Sanusi, Orefuwa Samuel, Temitope Sabitu, Tolulope Durojaiye, Adeola Ibikunle, Kimberly Melligan, Jalaal Hayes and

Pushpika Katukampola, who inspired my final effort despite the enormous work pressures we were facing together. Also (Mrs.) Leida Sanchez, and others too many to list here due to space factor.

- Rosemary Iriowen (*MD*), my wife, without whom this effort would have been worth nothing. Your love, support and constant patience have taught me so much about sacrifice and discipline. You are my number one fan.
- (*Pastor*) Samuel and (*Deaconess*) Mary Iriowen, my parents, who have always supported, encouraged, prayed and believed in me through all my endeavors and who so lovingly and unselfishly cared for me.
- Osawerene Iriowen, my son, who was born before this dissertation was completed and who spent many days with his mother and grandmother at home to allow me to focus. I am deeply sorry for the time we spent apart and I deeply cherish and love every moment we are together playing and speaking gibberish over the phone.
- My siblings, (*Elder*) Victor Iriowen, (*Mrs*) Irene Obadiaru, (*Engr.*) Osaro Iriowen, (*Ms.*) Osatohanmwun Iriowen and my mother-in-law, (*Mrs.*) Bridget Oviasojie for all your encouragement and profound understanding.
- To the Almighty Father (GOD) in the Upper House (*Heaven*), thank you for “*Ephesians 3:20*” over me and my household.

**Adsorption of Hydrogen, Methane and Carbon Dioxide Gases in Metal-Organic Frameworks using the Sticking Efficiency Concept;
(A New Approach)**

Esosa Iriowen

Advisor: Dr. Andrew Goudy

ABSTRACT

In this research, the adsorptions of three different gases namely Hydrogen (H_2); Carbon Dioxide (CO_2) and Methane (CH_4) on a variety of Metal-Organic Frameworks (*MOFs*) such as zinc Benzene-1,4-dicarboxylate (Zn-BDC), Zinc 2,6- Naphthalenedicarboxylate (Zn-NDC), Copper 1,3,5-Benzenetricarboxylate (Cu-BTC), Zinc Methyl-Imidazolate (Zn-Mim) and Iron and 1,3,5-Benzenetricarboxylate (Fe-BTC) were studied and compared at low and high pressures under different temperatures. It was expected that *MOFs* with large surface areas would adsorb more gas(es) than those with smaller surface areas. However this is not always true because there are other factors such as the nature of the surface sites of these materials that also affect gas adsorption. Therefore, a new parameter denoted sticking efficiency (θ) was devised and tested to determine how well it would correlate with gas adsorption capacity. It was found that at low pressures, sticking efficiency correlated better with gas sorption capacity than did surface area. Since the sticking efficiency also correlated well with adsorption enthalpy, results show that the strength of interactions between the *MOF* surface and the adsorbed gas may be a

more important factor when it comes to adsorption capacity. However, at high pressures, surface area correlated better with the gas sorption capacity than did sticking capacity. The most likely reason for this is that saturation generally occurs at high pressures and, when the surfaces are fully covered, the MOF with the greatest surface area will adsorb the most.

TABLE OF CONTENTS

DEDICATION	ii
ACKNOWLEDGEMENTS	iii
ABSTRACT	v
TABLE OF CONTENTS	vii
LIST OF TABLES	xii
LIST OF FIGURES	xiv
CHAPTER ONE INTRODUCTION	1
1.0 Literature Review and Motivation	1
1.1 Hydrogen Gas, Properties and Storage.....	1
1.2 Methods of Hydrogen Storage from Department of Energy Perspective	2
1.3 Different Ways of Hydrogen Storage.....	3
1.3.1 Cryogenic Storage for Hydrogen	3
1.3.2 Compressed Storage for Hydrogen	4
1.3.3 Solid State method for Storing Hydrogen	5
1.3.4 Hydrogen Atoms in Metal (Chemisorption)	5
1.3.5 Hydrogen in Porous Materials (Physisorption).....	5
1.3.6 Compounds of Hydrogen with Ionic Character (Complex and Metallic Hydrides)	6
1.4 Carbon Dioxide Gas, Properties, and Storage	6

1.5 Carbon Dioxide Storage and Department of Energy (DOE) Goals	7
1.6 Methane Gas, Properties and Storage	8
1.7 Methane Storage and Department of Energy Target.....	8
1.7.1 Compressed Natural Gas (CNG).....	9
1.7.2 Liquefied Natural Gas (LNG)	9
1.7.3 Solid State Storage for Adsorbed Natural Gas (ANG)	10
1.8 Adsorption History, Importance, Principles and Applications	10
1.8.1 Adsorption by Powders	13
1.8.2 Adsorptions by Porous Materials	16
1.8.3 Classifications and Types of Adsorption Isotherms.....	16
1.8.4 Physisorption and Chemisorption Principles	18
1.9 Metal Organic Frameworks (MOFs); and IUPAC Understanding	19
1.9.1 Types, Applications and Limitations of Metal-Organic Frameworks.....	23
1.9.2 Overviews of All Selected MOFs-Materials for This Research.....	25
1.9.3 Zinc Benzene-1,4-dicarboxylate (Zn-BDC) or Isorecticular Metal-Organic Frameworks – 1 (IRMOF-1/MOF-5)	27
1.9.4 Zinc 2,6- Naphthalenedicarboxylate (Zn-NDC) or Isorecticular Metal-Organic Frameworks-8 (IRMOF-8 / MOF-8).....	28
1.9.5 Copper 1,3,5-Benzenetricarboxylate, (Cu-BTC) or Hong Kong University of Science and Technology (HKUST-1)	29
1.9.6 Zinc Methyl-Imidazolite (Zn-Mim) or Zeolitic Imidazolite Framework (ZIF-8)	29

1.9.7 Iron and 1,3,5-Benzenetricarboxylate (Fe-BTC) Framework (Basolite F300) ...	30
1.10 Problem Description.....	30
1.11 Objectives, Goals of This Research	31
CHAPTER TWO EXPERIMENTAL PROTOCOL.....	32
2.0 Experimental Protocol.....	32
2.1 Research Approach	32
2.2 Materials.....	32
2.3 Experimental Method.....	34
2.4 Sample Handling and MOF Synthesis	34
2.5 Zn-NDC Synthesis	35
2.6 Zn-BDC Synthesis.....	35
2.7 Cu-BTC Synthesis.....	36
2.8 Zn-Mim and Fe-BTC Synthesis	38
2.9 Material Characterizations, Measurements and Sample Handling	39
2.10 Glove Box	39
2.11 Using the X-RAY Diffraction (XRD) for Analysis	40
2.12 Thermogravimetric Analyzer (TGA)	41
2.13 Laser Diffraction Particle Size Analyzer (LDPSA).....	43
2.14 Fourier Infrared Spectroscopy Analyzer	45
2.15 Surface Area and Porosity Analyzer	47
2.16 High Pressure Volumetric Analyzer (HPVA).....	51
2.17 Scanning Electron Microscope (SEM).....	54

2.18 Summary	57
CHAPTER THREE MATERIAL CHARACTERIZATIONS.....	59
3.0 Characterizing the Selected Metal-Organic Frameworks (MOFs).....	59
3.1 Obtaining the Optimum Surface Area for Zn-BDC	59
3.2 Obtaining the Thermal Stabilities (TGA) of Synthesized MOFs.....	61
3.3 XRD Spectra of Synthesized MOFs.....	63
3.4 Laser Diffraction Particle Size Analysis (LDPSA) of Studied MOFs	65
3.5 Scanning Electron Microscope (SEM).....	66
3.6 Fourier Transformed Infrared Spectroscopy (FTIR) for Studied MOFs.....	69
3.7 Surface Areas and Pore Volume for Studied MOFs	70
3.8 Surface Area and Gas(es) Adsorption Isotherms	72
3.9 Summary	74
CHAPTER FOUR HYDROGEN GAS ADSORPTIONS.....	76
4.0 Sticking Efficiency (θ) the Concept	76
4.1 Relationship Between Surface Area (S_{SA}) and Sticking Efficiency ($S(\theta)$)	77
4.2 Hydrogen Adsorptions and Isotherms.....	78
4.3 Enthalpy of Adsorptions.....	96
4.4 Summary	100
CHAPTER FIVE METHANE GAS ADSORPTIONS.....	101
5.0 Methane Gas Adsorption Isotherms	101
5.1 Methane Adsorption and Sticking Efficiency (Θ).....	104
5.2 Enthalpy of Adsorptions.....	112

5.3 Summary	117
CHAPTER SIX CARBON DIOXIDE GAS ADSORPTIONS	118
6.0 Carbon Dioxide Gas Adsorption Isotherms	118
6.1 Carbon Dioxide Gas Adsorption	119
6.2 Enthalpy of Adsorptions.....	135
6.3 Summary	138
CHAPTER SEVEN CONCLUSION.....	139
7.0 Research Conclusion	139
7.1 Future Works Recommendation.....	140
References	141
Curriculum Vitae	151
Publications From This Research	158

LIST OF TABLES

Table 1.1 Quick Scan: Porous Solids.....	12
Table 1.2 Quick Scan: Powders	15
Table 1.3 Quick Scan: Adsorption.....	15
Table 3.1 Getting the synthesis temperature for Zn-BDC, using the rapid solvothermal method.....	60
Table 3.2 Particle sizes for the synthesized and purchased MOFs used for this work	65
Table 3.3 Showing both synthesized and purchased MOFs surface area and pore volume at 50 cm ³ /g	71
Table 4.1 Low Pressure (LP) and High Pressure (HP) values for hydrogen gas adsorptions on selected MOFs along with their BET surface area and corresponding sticking efficiencies	77
Table 4.2 Hydrogen adsorption analysis data at 77 K under low pressure.....	84
Table 4.3 High Pressure Hydrogen adsorption analysis data at 77 K.....	85
Table 5.1 Methane low and high pressure weight percent data.....	102
Table 5.2 High pressure data for CH ₄ adsorption @ 298 K	105
Table 5.3 Low pressure data for CH ₄ adsorption @ 298 K	114
Table 5.4 Low Pressure (LP) and High Pressure (HP) calculated values for methane gas adsorptions on selected MOFs	117

Table 6.1 Low Pressure (LP) and High Pressure (HP) calculated values for carbon dioxide gas adsorptions on selected MOFs.....	119
Table 6.2 Carbon Dioxide Adsorption Sticking Efficiency (Θ) at Low and High Pressures Studies.....	124

LIST OF FIGURES

Fig. 1.0. Probe accessibility over surface of material	14
Fig. 1.1 The figure indicates the classification of adsorption isotherms defined by IUPAC	17
Fig.1.2. Building block (red balls) held together with organic linker (green cylindrical shape)	21
Fig. 1.3.Pictorial structure of MOFs members formation sharing same topology and length. The expansions of their links increases their internal void space and allows for catenation formations.....	22
Fig. 1.4. Rational modification, otherwise known as MOFs functionalization	22
Fig. 1.5. Some structures of organic linkers for MOFs synthesis.....	26
Fig. 2.1 Ball-milling machine, courtesy of Center for Hydrogen Storage and Research (CHSR) laboratory at Delaware State University, Dover. U.S.A.	38
Fig. 2.2. The Glove Box. Courtesy of Delaware State University, Dover. Center for Hydrogen Storage and Research (CHSR).....	39
Fig. 2.3. A PANalytical X'pert X-Ray Diffractometer Instrument. Courtesy of Delaware State University, Dover. Center for Hydrogen Storage and Research (CHSR).....	41
Fig. 2.4. The Perkin-Elmer Diamond TG/DTA Analyzer. Courtesy of Delaware State University, Dover. Center for Hydrogen Storage and Research (CHSR).....	42

Fig. 2.5 Laser diffraction particle size analyzer (Model: SALD-2201) from Shimadzu. Courtesy of Delaware State University, Dover. Center for Hydrogen Storage and Research (CHSR).....	44
Fig.2.6. (a) IRPrestige-21 Spectrometer from Shimadzu.(b) Sample studs, potassium bromide (KBr) (from Sigma-Aldrich and sample holder. Courtesy of Delaware State University, Dover. Center for Hydrogen Storage and Research (CHSR).....	46
Fig.2.7. (a) Front-view of the Micromeritics ASAP 2020 surface area and porosity analyzer.(b) Back-view of the instrument showing the filters, vacuum pumps, beads column and all the different gas tanks connected. Courtesy of Delaware State University, Dover. Center for Hydrogen Storage and Research (CHSR)	48
Fig. 2.8. Sample glass-tube, filler rod and seal frit used for BET and gas adsorption analysis. Courtesy of Delaware State University, Dover. Center for Hydrogen Storage and Research (CHSR).....	49
Fig.2.9. (a) Front-view of the Micromeritics HPVA 100 (VTI) volumetric analyzer.(b) Rare-view of the instrument showing all the different gas tanks connected. The insert photo shows the sample holder (2cc) with the gasket supplied by Swagelok. Courtesy of Delaware State University, Dover. Center for Hydrogen Storage and Research (CHSR.	53
Fig. 2.10. (a) Coating instrument (Denton Vacuum Desk IV) (b) Sample studs with samples on top. Courtesy of University of Delaware, U.S.A. Center for Material Sciences, Department of Chemistry.....	54

Fig. 2.11. JOEL JSM 7400F scanning electron microscope instrument, with insert snapshot of its resting base. Courtesy of University of Delaware, U.S.A. Center for Material Sciences, Department of Chemistry	55
Fig. 2.12. Snapshots of Zn-BDC (MOF-5), Zn-NDC (MOF-8) and Cu-BTC (HKUST-1) after synthesis from CHSR-DSU Laboratory, U.S.A.	58
Fig. 3.1 Chart of MOF-5 synthesis for this work, showing various temperature range of synthesis and corresponding error bar	60
Fig. 3.2 Thermogravimetric (TGA) plots for synthesized and purchased MOFs used in this work.....	62
Fig. 3.3 XRD patterns for Cu-BTC, Fe-BTC, Zn-Mim, Zn-BDC and Zn-NDC for this work showing their peak intensities versus 2Θ -angle.....	64
Fig. 3.4. Particle distributions for the three synthesized MOFs and the two commercial MOFs used in this study	66
Fig. 3.5. SEM capture photo for Zn-Mim MOF for this work.....	67
Fig. 3.6. SEM capture photo for Zn-NDC MOF for this work.....	67
Fig. 3.7. SEM capture photo for Zn-BDC MOF for this work	68
Fig. 3.8 SEM capture photo for Fe-BTC MOF for this work.....	68
Fig. 3.9. SEM capture photo for Cu-BTC MOF for this work	69
Fig. 3.10. IR-band spectra for synthesized and purchased MOFs used in this work.....	70
Fig. 3.11a. Graph of surface area for synthesized and purchased MOFs	71
Fig. 3.11b. Graph of surface area and pore volume for synthesized and purchased MOFs	72

Fig. 3.12. BET- Isotherms for synthesized and purchased MOFs for this studies	73
Fig 4.1. Chart showing relationship between BET surface area and sticking efficiencies for hydrogen (H ₂) at liquid nitrogen temperature (77 K) under high pressure	77
Fig. 4.2 Hydrogen adsorptions Isotherms at low pressure (77 K) for MOFs used in this work	80
Fig. 4.3. Hydrogen adsorptions Isotherms at low pressure (196 K) for MOFs used in this work	81
Fig. 4.4. Hydrogen adsorptions Isotherms at low pressure (273 K) for MOFs used in this work	82
Fig. 4.5. Hydrogen adsorptions Isotherms at low pressure (298 K) for MOFs used in this work	82
Fig. 4.6. Hydrogen adsorptions Isotherms for high pressure (77 K) MOFs used in this work	86
Fig. 4.7. Hydrogen adsorptions Isotherms for high pressure (196 K) MOFs used in this work	86
Fig. 4.8. Hydrogen adsorptions Isotherms for high pressure (273 K) MOFs used in this work	87
Fig. 4.9. Hydrogen adsorptions Isotherms for high pressure (298 K) MOFs used in this work	87
Fig. 4.10 (Ai) Sticking efficiency vs Weight per cent for hydrogen gas adsorbed at 77 K for this work under low pressure (LP)	90

Fig. 4.10 (Aii) Surface area vs Weight per cent for hydrogen gas adsorbed at 77 K for this work under low pressure (LP).....	90
Fig. 4.10 (Bi) Sticking efficiency vs Weight per cent for hydrogen gas adsorbed at 77 K for this work with other studies including this study under low pressure (LP)	91
Fig. 4.10 (Bii) Surface area vs Weight per cent for hydrogen gas adsorbed at 77 K for this work other studies including this study under low pressure (LP).....	91
Fig 4.11 (Ai) High Pressure(HP) plots for hydrogen adsorption at 77 K Sticking efficiency vs Weight per cent for hydrogen gas adsorbed at 77 K for this work	92
Fig 4.11 (Aii) High Pressure(HP) plots for hydrogen adsorption at 77 K Surface area vs Weight per cent for hydrogen gas adsorbed at 77 K for this work	93
Fig 4.11 (Bi) Surface area vs Weight per cent for hydrogen gas adsorbed at 77 K for this work Other studies including this study under high pressure (HP)	93
Fig 4.11 (Bii) Other studies including this study sticking efficiency vs hydrogen gas adsorbed at 77 K under high pressure (HP)	94
Fig 4.12 (Ai) Low Pressure (LP) plots for hydrogen adsorption at 77 K of MOF with same organic linker for sticking efficiency vs hydrogen adsorbed.....	94
Fig 4.12 (Aii) Low Pressure(LP) plots for hydrogen adsorption at 77 K of MOF with same organic linker for surface area vs hydrogen adsorbed	95
Fig 4.13 (Ai) Low Pressure(LP) plots for hydrogen adsorption at 77 K of MOF with same metal for sticking efficiency vs hydrogen adsorbed	95
Fig 4.13 (Aii) Low Pressure(LP) plots for hydrogen adsorption at 77 K of MOF with same metal for surface area vs hydrogen adsorbed	96

Fig 4.14 (Ai) Sticking efficiency vs enthalpy heat of adsorption for this work	98
Fig 4.14 (Aii) Surface area vs enthalpy heat of adsorption for this work.....	98
Fig. 4.14 (Bi) Other studies including this study sticking efficiency vs enthalpy heat of adsorption.....	99
Fig. 4.14 (Bii) Other studies including this study surface area vs enthalpy heat of adsorption.....	99
Fig. 5.1 Methane adsorption Isotherms for low pressure (273 K)MOFs used in this work	102
Fig. 5.2. Methane adsorptions Isotherms for low pressure (298 K)MOFs used in this work	103
Fig.5.3. Methane adsorption Isotherms for high pressure (273 K)MOFs used in this work	103
Fig.5.4. Methane adsorption Isotherms for high pressure (298 K)MOFs used in this work	104
Fig.5.5 (Ai) Sticking efficiency vs Weight per cent for methane gas adsorbed at 298 K under high pressure (HP) for this work.....	106
Fig.5.5 (Aii) Surface area vs Weight per cent for methane gas adsorbed at 298 K under high pressure (HP) for this work.....	106
Fig. 5.5(Bi) Other studies including this study for sticking efficiency vs methane adsorbed at 298 K under high pressure (HP)	107
Fig. 5.5(Bii) Other studies including this study for methane adsorbed at 298 K under high pressure (HP)	107

Fig 5.6 (Ai) Low Pressure(LP) plots of surface area vs methane adsorbed for methane adsorption at 273 K.....	108
Fig 5.6. (Aii) Low Pressure(LP) plots for sticking efficiency vs methane adsorption at 273 K for this work.....	109
Fig 5.7. (Ai) Low Pressure(LP) plots for surface area vs methane adsorption at 298 K for this work.....	110
Fig 5.7. (Aii) Low Pressure(LP) plots for sticking efficiency vs methane adsorption at 298 K for this work.....	110
Fig 5.8. (Ai) High Pressure(HP) plots for surface area vs methane adsorption at 273 K for this study	111
Fig 5.8. (Aii) High Pressure (HP) plots for sticking efficiency vs methane adsorption at 273 K for this study.....	112
Fig 5.9. (Ai) Sticking efficiency vs enthalpy heat of adsorption for this study	113
Fig. 5.9. (Aii) Surface area vs enthalpy heat of Adsorption for this study	113
Fig. 5.9 (Bi) Surface area vs enthalpy heat of adsorption at 298 K with other studies .	115
Fig. 5.9. (Bii) Sticking efficiency vs enthalpy heat of adsorption including other studies	115
Fig. 5.9. (Ci) Sticking efficiency vs enthalpy heat of adsorption for this study	116
Fig. 5.9. (Cii) Surface area vs anthalpy heat of adsorption at 298 K low pressure for this study.....	116
Fig.6.1. Carbon dioxide adsorption Isotherms for low pressure (273 K)MOFs used in this work	120

Fig.6.2. Carbon dioxide adsorption Isotherms for low pressure (298 K)MOFs used in this work	121
Fig.6.3. Carbon dioxide adsorption Isotherms for high pressure (273 K)MOFs used in this work	123
Fig.6.4. Carbon dioxide adsorption Isotherms for high pressure (298 K)MOFs used in this work	123
Fig.6.5. (Ai) Sticking efficiency vs carbon dioxide gas adsorbed at 273 K under low pressure (LP) for this work	126
Fig.6.5. (Aii) Surface area vs carbon dioxide gas adsorbed @ 273 K under low pressure (LP) for this work.....	127
Fig.6.5. (Bi) Sticking efficiency vs carbon dioxide gas adsorbed including other studies	127
Fig.6.5. (Bii) Surface area vs carbon dioxide gas adsorbed including this stuiesy.....	128
Fig.6.6(Ai). Low pressure (LP) plots for carbon dioxide adsorption at 298 K for sticking efficiency for this work.....	129
Fig 6.6 (Aii) Low Pressure plots for carbon dioxide adsorption at 298 K with surface area for this work	129
Fig.6.6 (Bi). Other studies (Sticking Efficiency) including this study	130
Fig.6.6 (Bii). Other studies (Surface Area) including this study	130
Fig.6.7.(Ai). Sticking efficiency vs weight per cent for carbondioxide at 273 K under high pressure (HP) for this work.....	131
Fig.6.7 (Aii). Surface area vs weight per cent for this work.....	132

Fig.6.7 (Bi). Other studies for sticking efficiency vs carbon dioxide at 273 K under high pressure(HP)	132
Fig. 6.7 (Bii). Other studies with surface area included this study.....	133
Fig.6.8 (Ai). High Pressure plots for sticking efficiency vs carbon dioxide adsorption at 298K.....	134
Fig.6.8 (Aii). High Pressure plots for surface area vs carbon dioxide adsorption at 298K	134
Fig.6.8 (Bi). Other studies for sticking efficiency included in this study	135
Fig.6.8 (Bii). Other studies for surface area included in this study	135
Fig.6.9 (Ai). This study sticking efficiency vs enthalpy heat of adsorption.....	136
Fig.6.9 (Aii). This study surface area vs enthalpy heat of adsorption	137
Fig.6.9 (Bi). Other studies for sticking efficiency included in this study.....	137
Fig.6.9 (Bii). Other studies surface area included in this study.....	138

CHAPTER ONE

INTRODUCTION

1.0 Literature Review and Motivation

This part of the research thesis will introduce a new awareness into all that is needed in reaching and achieving desirable results toward the aim and objectives of this project. Energy spent on transportation accounts for a significant part of total energy consumption. It is estimated that in industrialized countries, one-third of all the energy generated annually is consumed in transportation.^{1, 2} A modern vehicle with a driving range of approximately 250 miles per tank of fuel needs about 8 kg of hydrogen for a combustion engine-driven automobile and 4 kg for a fuel-cell-driven one.³

1.1 Hydrogen Gas, Properties and Storage

Hydrogen is an attractive energy carrier because it is carbon-free, abundantly available from water, and has an exceptional mass energy density.⁴ Under ambient temperature or conditions, hydrogen unfortunately is an extremely volatile gas and it is very difficult to compress for on-board storage. For storage to be helpful or useful, two conditions are very important. First, it is required that it hold enough H₂ at the appropriate temperatures and secondly, it must be capable of releasing H₂ easily while not requiring more energy to release it than store it. A very important challenge for the use of hydrogen as an energy carrier is that, it should be compact and very safe for its storage.^{1, 4-9} Hydrogen is the cleanest fuel and it has a heating value that triples that of petroleum.

However, it is a man-made fuel and therefore bears a manufacturer cost, which makes it cost more in comparison to petroleum products.

1.2 Methods of Hydrogen Storage from Department of Energy Perspective

Studies have reported that the greatest challenge today is the manner and ways of storing gases (for example, hydrogen, methane, carbon dioxide, and so on).¹⁰ There are different methods for storing hydrogen, but it depends on what it is being used for. Hydrogen storage materials can also be of use as a method of gas purification, sensor, catalysis, and separation of gases in addition to storage use. These all depend on the nature of materials being used. For gas purification, materials used for achieving this can be beneficial in the removal of parts per million (ppm) traces of sulfur components from various gases including hydrogen. In the case of gas separation processes, the gas mixtures usually consist of components having concentrations in the same order of magnitude, this processes is in contrast to the gas purification processes.¹⁰ The fast consumption of petroleum deposits and the increasing air pollution problems resulting from burning fossil fuels have driven the global research community to look for cleaner and renewable energy resources. Hydrogen is an ideal energy carrier. It almost triples the gravimetric heat of combustion of gasoline (120 MJ/kg vs. 44.5 MJ/kg).^{1, 11} More importantly, the energy produced from hydrogen oxidation produces water as the only by-product.

In order to facilitate the research and application for hydrogen as an energy carrier, the Department of Energy in the United States has set targets for on-board hydrogen storage at 6.0 wt.% and 45 g/L by the year 2010 and 9.9 wt% and 81 g/L by 2015.¹

1.3 Different Ways of Hydrogen Storage

There are different ways used for storing hydrogen. There are basically five methods that have attracted common interest, namely; compression, liquefaction, physisorption, metallic hydrides, and complex hydrides.¹² Different types of hydrogen tanks have been used to store hydrogen. These tanks operate at very high pressures. Compressed hydrogen gas and cryogenically stored liquid hydrogen are known to be the most technologically advanced of these methods. These have proven to meet the technical aspect of the DOE 2010 visions, however, they are unlikely to agree with future ones which are more stringent.¹³ There is another method of storing this gas using tanks. Previous and current studies have shown that under room temperature (298.15 K), hydrogen storage is more difficult to achieve. This is basically because its enthalpy of adsorption is too weak (usually, 4-10 kJ mol⁻¹) to allow hydrogen adsorption as demonstrated by Bhatia et. al.¹⁴ The energy of adsorption of 15 kJ mol⁻¹ is required under room temperature. Studies are underway to increase this enthalpy of adsorption by way of reducing their (MOF materials) pore width. Presently hydrogen storage is achieved at liquid nitrogen temperature (LN₂ (77 K)).¹⁵⁻¹⁸

1.3.1 Cryogenic Storage for Hydrogen

There is a need to make hydrogen competitive with fossil-fuel energy technology which is becoming interestingly more challenging. Hydrogen can only liquefy at -251.9 °C and this tends to limit its use. Liquid hydrogen storage is known to have either met or even exceed some of the many gravimetric and volumetric density targets but the marked cost and energy required for its liquefaction is on the high side. Liquid hydrogen storage

requires dealing with the hazard of handling cryogenic hydrogen at 20 degrees above the absolute zero.^{9, 17, 19-21} The use of cryogenic tanks for hydrogen storage has a significant drawback due to the large amount of energy input needed for condensation. This method faces two challenges; these are the efficiency of the liquefaction process and the boil-off of the liquid. The theoretical work necessary to liquefy hydrogen gas at room temperature is 3.23 kW h/kg, but the technical work is about 15.2 kW h/kg, which is almost half of the lower heating value of hydrogen.¹²

Hence, liquid hydrogen can only be stored in an open system since the pressure in a closed system can be as high as 1000 MPa at room temperature. The boil-off point of this liquid is referred to as the emission of H₂ into the atmosphere. The relatively large amount of energy necessary for liquefaction and the continuous boil-off of liquid presents a huge limit to the storage system of this gas.

1.3.2 Compressed Storage for Hydrogen

This seems to be the simplest way of storing hydrogen in a pressurized cylinder up to 20 MPa, but the energy density is very low, which makes it difficult to satisfy the fuel demand for driving purpose. About 70 MPa (four times higher than pressure) is needed to meet automobile driving purpose. However, such industrial cylinders have not been commercially available. One of the major disadvantages of this method is the ability to hold little hydrogen for their weight as compared to their gas cylinders. The hydrogen density as such is much lower than the cryo-adsorption method and the high cost of compression and the cylinder might hinder the commercial acceptability of this method.

1.3.3 Solid State method for Storing Hydrogen

So far, finding materials that are capable of trapping larger amount of hydrogen at room temperature and atmospheric pressure is important for alternative energy storage. It must have the characteristic of being reversible. In solid state hydrogen storage, the binding of hydrogen molecules or atoms unto the sorbate materials is much stronger by way of ionic, ionic-covalent or a quasi-molecular bond rather than the van der Waals forces of attraction. These strong or weak interactions are what give birth to another phenomenon of hydrogen storage known as chemisorption or physisorption depending on the process taking place. This stronger bonding allows for optimizing the volumetric drawback obtained with the use of compressed tanks.^{1, 5, 7, 17, 19}

Thus, in solid-state storage, a hydrogen atom or molecule either forms a strong chemical bond to a solid support, a process called chemisorption, or interacts weakly with a sorbent a process known as physisorption.¹

1.3.4 Hydrogen Atoms in Metal (Chemisorption)

In this process, dihydrogen molecules split into hydrogen atoms when in contact with the solid support. The higher reactive hydrogen atoms will now form chemical bonds with the solid, thereby forming metal hydrides or chemical hydrides. This also depends on the nature of the solid support. Due to the short bonds between hydrogen and the solid, some hydride compounds can attain a relatively high hydrogen storage capacity.^{1, 5, 6, 19, 22, 23}

1.3.5 Hydrogen in Porous Materials (Physisorption)

The storage of hydrogen can also rely on physisorption because the adsorbed gas can be released reversibly. Physisorption of hydrogen in porous materials uses the same

principles of adsorptions. The fundamental base materials having porous characteristics are carbon-based. Examples of these are nanotubes, zeolite, fullerenes, graphenes, certain clathrates, ordered mesoporous carbon, and metal-organic frameworks. These materials have the potential to reversibly bind and release hydrogen at low temperatures via their weak attractive forces. However, their kinetics are fast with their enthalpy values usually between 4-7 kJ/mol. The amount of heat released is small during on-board refueling, which is a major advantage over other chemical hydrides.^{4, 5, 9, 17, 19-41}

Physisorption of hydrogen on nanotubes or nanofibers seems hopeless for enhancing the hydrogen density due to the surface area. However, finding a better technique of hydrogen storage remains a challenge.^{12, 42}

1.3.6 Compounds of Hydrogen with Ionic Character (Complex and Metallic Hydrides)

Some metals and alloys absorb hydrogen to form hydrides. There are two classes of hydrides: metallic hydrides and complex hydrides. The main difference between them is the transition of metals to ionic or covalent compounds upon absorbing hydrogen.²⁰ Some metal hydrides absorb and desorb hydrogen at ambient temperature and near the atmospheric pressure. The volumetric density of the hydrogen atoms present in the host lattice is extremely high. However, all the reversible hydrides working around ambient temperature and atmospheric pressure consist of transition metal; and, the gravimetric hydrogen density is limited to less than 3 wt%.

1.4 Carbon Dioxide Gas, Properties, and Storage

There is a major difference between carbon dioxide capture and storage. Many people misrepresent these two processes. Capture has to do with extractions or separations from

its other components, while storage is the process of preservation for future uses. There is one common similarity between them. They both use the same principles of sorption (adsorption or absorption). Our planet accommodates a lot of resources serving as fossil fuels. These are the by-products of both biological and geological ecology. The increase in atmospheric CO₂ influences the balance of incoming and outgoing energy in the earth's atmosphere, with CO₂ being the most significant anthropogenic greenhouse gas (GHG).⁴³⁻⁴⁷

CO₂ isotherms are usually studied at 273 K, but at this ice temperature, saturation pressure is ca. 3.5 MPa⁴⁸. Do and Do (2003),^{49, 50} outlined some characteristic features of derived pore size distribution that are regarded as effective. They mentioned that the pores in the carbons are irregular in shape and interconnected. Polar groups are attached to edge sites and molecular interactions do not conform to the simple model as in the case of nitrogen (N₂) adsorptions at 77 K.⁴⁹⁻⁵¹

1.5 Carbon Dioxide Storage and Department of Energy (DOE) Goals

DOE's Carbon Sequestration Program (CSP), which is currently being managed by the National Energy Technology Laboratory (NETL), is pursuing five technological avenues aimed at reducing Green House Gases-GHG's emissions. These include CO₂ separation and capture; carbon storage (sequestration); monitoring, mitigation, and verification of stored CO₂; control of non-CO₂ GHG's; and breakthrough concepts related to CCS. DOE's goal is to have the necessary technology ready for large scale field testing, should it become necessary to impose mandatory limits on CO₂ emissions. The specific goal was to have technologies developed by 2012 that have advanced beyond the pilot scale and

are ready for large scale field tests; that can achieve 90 % CO₂ capture with minimal increase in the cost of electricity of less than 20% for post-combustion and oxy-combustion and less than 10 % for pre-combustion capture. Capture and separation costs are a significant portion of the cost to sequester CO₂⁵². The current DOE target for carbon dioxide is set at 56 wt.%.⁵³

1.6 Methane Gas, Properties and Storage

Methane is the main constituent of natural gas. It is well known that natural gas contains a mixture of ethane and other hydrocarbon components such as carbon dioxide and nitrogen. Methane constitutes about 95 % of this mixture. There is no quadrupole moment, it polarizes with a spherical conformation. Methane's gravimetric heat of combustion can be compared to that of gasoline which has been determined to be 55.0 MJ/kg and 44.5 MJ/kg respectively. Due to its higher hydrogen-to-carbon ratio (H₂ : C) which results in lower carbon emission, it provides more energy as compared to petroleum oil. However, the lack of safe and effective storage methods for its mobile applications has posed a major hurdle in past and recent years. Presently, storage methods for methane are the compressed natural gas (CNG), solid state storage for adsorbed natural gas (ANG) and liquefied natural gas (LNG).⁵⁴⁻⁵⁷

1.7 Methane Storage and Department of Energy Target

Depletion of fossil oil deposits and the increasing threat of global warming have put clean energy research, which also includes searches for other carriers of clean energy like hydrogen and methane as well as the reduction of carbon dioxide emissions, on the urgent agenda. A significant technical challenge has been developed of a viable method

to trap hydrogen more efficiently, and also for methane and carbon dioxide gas molecules to be confined for various applications. Possible solutions to this problem employ highly porous materials as storage media. Porous metal–organic frameworks (MOFs), which have high surface areas as well as chemically-tunable structures, are playing an unusual role.⁵⁸⁻⁶² The first reported measurement of methane uptake by a porous MOF could date back to as early as 1997 reported by Kitagawa and coworkers but with very limited methane uptake.⁶³ However, the field of methane storage on MOFs has not developed as quickly as the hydrogen-storage field and studies on methane storage in porous MOFs are far less numerous than hydrogen.⁶⁴ Methane storage, which is an essential part of natural gas, is probably most advanced application of MOFs industrially.⁶⁵ The DOE target for methane storage is set at 18 wt.%.⁵³

1.7.1 Compressed Natural Gas (CNG)

Compressed natural gas tanks used for automobile application normally hold up to 3000 psi (200 bar) of methane and offer about 26 % of the volumetric density of gasoline. At this high pressure, safety becomes a major concern. Also cars having double CNG and gasoline as fuel will require two separate tanks which will add more weight and reduce cargo space in the vehicle.^{4, 25}

1.7.2 Liquefied Natural Gas (LNG)

Liquefied Natural Gas (LNG) design of storage for methane can provide about 72 % of the volumetric energy density of gasoline. This is only achievable at cryogenic temperatures similar to hydrogen, but at 112 K (-161.15 °C). Safety and energy inputs are also major drawbacks towards this technology.^{55, 56}

1.7.3 Solid State Storage for Adsorbed Natural Gas (ANG)

Solid state storage is another method for fuel storage. Liquefaction is impractical and compression requires high pressure (20 MPa) and an expensive multi-stage compression facility. At relatively low pressure (3–4 MPa) which is achievable by single-stage compression; adsorbed natural gas (ANG) has nearly the capacity of compressed natural gas (CNG). Monte Carlo calculations have been used to simulate the adsorption of natural gas on activated carbon. The model demonstrates pure methane intercalating between parallel planes of graphite at a slit of width 11.4 Å, optimized for ANG storage.⁵⁷ Solid state storage (adsorbed natural gas-ANG) is the storage of methane on a porous adsorbent. Volumetric energy storage for methane at 500 psi in porous materials has been investigated to be about 80 % that of CNG at 3000 psi. However, unlike hydrogen storage in porous materials, the heat of adsorption of methane is approximately 20 kJ/mol and this is within the Department of Energy (DOE) target goal set at 180 v/v or 18 wt% at ambient temperature and pressure of no more than 35 bar.^{53-55, 66} Hydrogen fuel cells are now emerging as a major alternative energy source in transportation and many other applications. Central to the development of hydrogen storage techniques is good, efficient and of viable storage.⁶⁷

1.8 Adsorption History, Importance, Principles and Applications

Adsorption occurs whenever a solid surface is exposed to a gas or liquid. Adsorption is defined as the enrichment of material or increase in the density of the fluid in the vicinity of an interface.^{51, 68, 69} Gas adsorptions are one of the most efficient and reliable ways for determining surface area and pore size distributions on powder and porous materials.

It has long been known that certain forms of charcoal are able to take up large volumes of gases, with the earliest recorded studies made by Scheele in 1773 and independently by Priestly in 1775 and the Abbe Fontana in 1777.⁷⁰⁻⁷² Decoloration of charcoal was first investigated by Lowitz in 1785, a Russian chemist. Similarly, the exothermal nature of gas adsorption was noted in 1814 by Saussure. In 1843, Mitscherlich gave an assumption that, the amount of gas adsorbed in a porous carbon was such that it was present in the liquid state.^{51, 72-74} Over the centuries, adsorption on solid materials has undergone lots of changes and developments.

The year 1916 brought a radical transformation in the understanding of surface sciences. Langmuir's first papers appeared during this time. He proposed that adsorption on both liquid and solid surfaces normally involved the formation of a monomolecular layer. Brunauer-Emmett-Teller (BET) were the first to use low temperature adsorption of nitrogen to determine the surface area using an iron synthetic ammonia catalyst in the year 1934.^{51, 75} The following equation was used:

$$\frac{x}{V(1-x)} = \frac{1}{V_m C} + \frac{(C-1)x}{V_m C} \quad 1.0$$

Where V is the volume of gas adsorbed, x is the relative pressure, V_m is the volume of gas required to form a monolayer and C is a constant. The equation was applied to their experimental data and published formally in 1938 by Brunauer, Emmett and Teller as the BET method for measuring surface areas of finely divided or porous solids. The method proved to be popular and is still used today throughout the world in surface work.^{51, 76} Prior to the scientific discovery of surface adsorptions, Langmuir stated in his paper in 1916 that with highly porous adsorbents such as charcoal, "*it is impossible to know*

definitely the area on which the adsorption takes place” and that *“there are some spaces in which a molecule would be closely surrounded by carbon atoms on nearly all sides”*.

He concluded that plane surfaces were not applicable to adsorption by charcoal.⁷⁷⁻⁷⁹

Another researcher Dubinin and his colleagues supported Langmuir’s work by putting forward further evidence. Dubinin and his group studied a wide range of activated carbons which he later classed into three groups of pores having different width: micropores, mesopores (previously termed transitional pores) and macropores (see Table 1.1).⁸⁰ Since this time, classification has undergone different refining, but the principles are still the same.

Table 1.1 Quick Scan: Porous Solids

Term	Quick Review
Porous solid	Solid having cavities or channels which are deeper than wide
Open pore	Cavity or channel with access to the surface
Interconnected pore	Pore which communicate with other pores
Blind pore	Pore with single connection to the surface
Closed pore	Cavity not connected to the surface
Void	Space between particles
Micropore	Pore of internal width >2 nm
Mesopore	Pore of internal with between 2 and 50 nm
Macropore	Pore of internal width <50 nm
Nanopore	Pore of internal width less than ~100 nm
Pore size	Diameter of cylindrical pore or distance between opposite walls of a slit
Pore volume	Volume of pores determined by stated method
Porosity	Ratio of total pore volume to apparent volume of particle or powder
Total porosity	Ratio of volume of voids and pores to volume occupied by solid
Open porosity	Ration of volume of voids and open pores to volume occupied by solid
Internal surface area	1] Area of all pore walls 2] Area of micropore walls

External surface area	1] Area of surface outside all pores 2] Area outside micropores
True density	Density of solid, excluding pores and voids
Apparent density	Density including closed and inaccessible pores, as determined by stated method

Source: Ref. No.⁵¹

1.8.1 Adsorption by Powders

Adsorption is the interaction of one or more components between two bulk phases, which is the interfacial layer or the adsorption space. One of these phases is a solid and the other is either a gas or liquid. In certain systems some metals are exposed to oxygen, hydrogen or water. In this case the adsorption is followed by desorption, which is the processes whereby the fluid penetrates into the solid phase.^{51, 81-85} Adsorption and desorption indicate the direction from which the equilibrium can be approached. When there is a difference in the amount of adsorption and desorption levels, then hysteresis is said to have occurred. A powder can be defined as a mass of small dry particles. In the science arena, it applies to materials exhibiting an appreciable surface area.

Surface area has been commonly determined where adsorption of gases or liquids on powder is taking place. But in principle, it can identify an experimentally accessible and r-distant surface areas (see Fig 1.0). Experimentally accessible surface area assesses the specific surface areas of adsorbents, catalyst, pigments and so many other finely divided and porous materials giving rise to true BET theory where nitrogen is still generally used as the adsorptive gas at liquid nitrogen (LN₂) temperature (-195.6 °C or 77 K).^{27, 48, 86, 87} Hence the BET equation can be set to cover a monolayer capacity (n_m) which is expressed in the linear form;

$$\frac{(p/p^0)}{n(1-p/p^0)} = \frac{1}{n_m C} + \left[\frac{C-1}{n_m C} \right] \times \left(\frac{p}{p^0} \right) \quad (1.3)$$

Where “ $n(n^a/m^s)$ ” is the amount adsorbed at relative pressure p/p^o and $nm (= n^a_m/m^s)$ is the monolayer capacity. The parameter “C” is exponentially related to the first-layer adsorption energy. The “r-distant” surface area is commonly referred to as the Connolly specific surface area which deals more with Monte Carlos simulations and this is

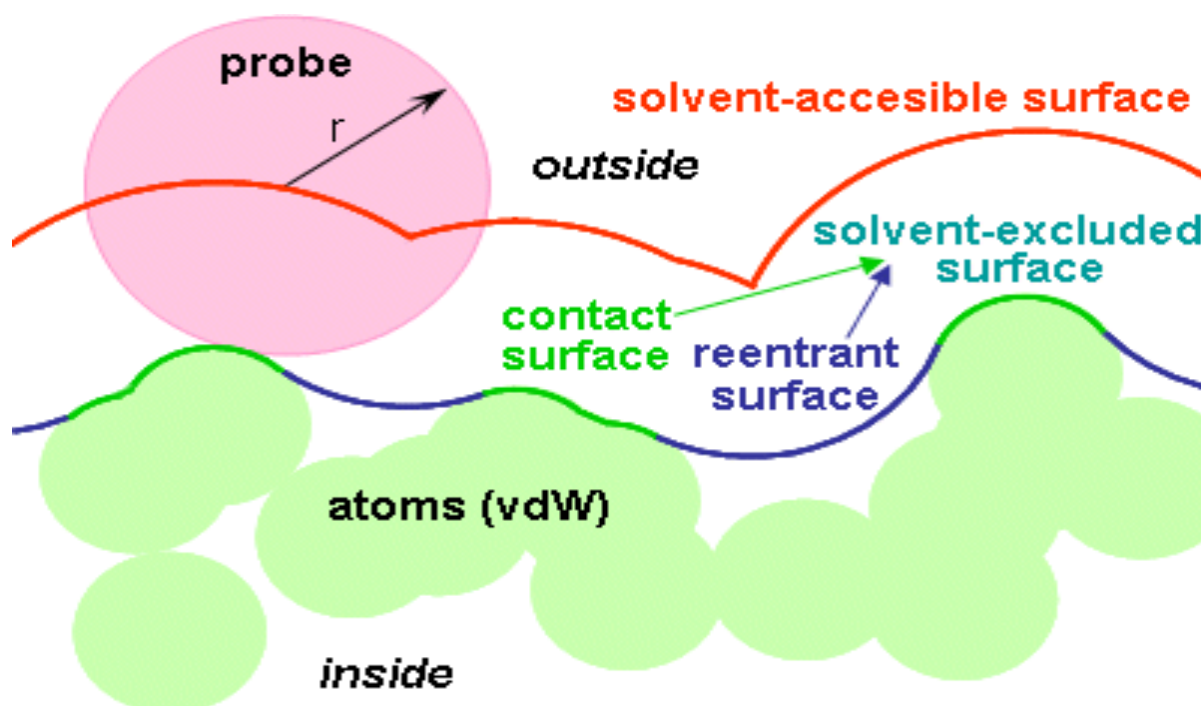


Fig. 1.0. Probe accessibility over surface of material (Source: Ref. No.⁵¹)

calculated from the bottom instead of the center of mass of the probe.⁸⁸ Adsorptions by powders and porous materials are best simply understood by having the basic definition terminologies of its application principles (See Table 1.2 and 1.3).

Table 1.2 Quick Scan: Powders

Term	Quick Review
Powder	Dry material composing of discrete particles less than ~ 1 mm
Fine Powder	Powder with particle size less than $\sim 1 \mu\text{m}$
Aggregate	Loose, Unconsolidated assemblage of particles
Agglomerate	Rigid, consolidated assemblage of particles
Compact	Agglomerate formed by compaction of powder
Acicular	This is a needle-shaped
Surface Area	The extent of the assessed surface by experimental or theoretical under any stated conditions
Specific Surface Area	Surface area of unit mass of the powder, as assessed under stated conditions
External Surface Area	1] Area outside any micropores 2] Area of external surface of particles without the porosity
Roughness Factor	Ratio of external surface area to area of smoothed envelope around particles
Divided Solid	Solid made up of more or less independent particles which maybe in the form of a powder, aggregate or agglomerate

Source: Ref. No.⁵¹

Table 1.3 Quick Scan: Adsorption

Term	Quick Review
Adsorption	When the vicinity of an interface is enriched with one or more components
Adsorbate	Substance in the adsorbed state
Adsorptive	Properties of substance in its fluid state to have absorbable ability
Adsorbent	The solid materials on which adsorption happens
Chemisorption	Adsorption with chemical bonding
Physisorption	Adsorption without chemical bonding
Monolayer Capacity	Chemisorbed amount needed to occupy all surface sites or physisorbed amount needed to cover all surface. Either one or the other
Surface Coverage	This is the ratio of adsorbed substance to monolayer capacity

Source: Ref. No.⁵¹

1.8.2 Adsorptions by Porous Materials

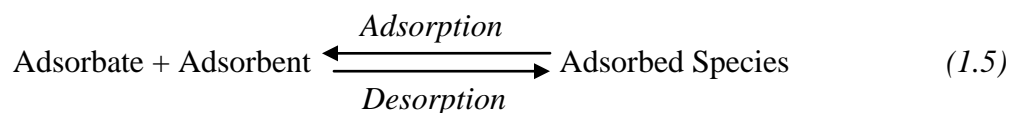
Solids with cavities are commonly termed as a porous materials. Fine powders are generally classified as materials having dimensions $\leq 1 \mu\text{m}$. The classification of pores from particle size definition gives rise to the term *micro*-porous and *macro*-porous. Hence the International Union of Pure and Applied Chemistry (IUPAC) termed porosity as the ratio of the volume of pores and voids to the volume occupied (see Table 1.2).⁸⁹ Although, nowadays nanopore is being used to replace the terms micro- or macro-porous, IUPAC does not recommend it (nanoporous) for pores wider than $\sim 100 \text{ nm}$.^{51, 85}

1.8.3 Classifications and Types of Adsorption Isotherms

Gas physisorption isotherms can be classified by the amount of gas adsorbed, (n^a); by the mass, (m^s), of the solid which is dependent on the equilibrium pressure (p); the temperature, (T); and the nature of the gas to solid system. This is represented with the equation below;

$$n^a / m^s = f(p)T \quad (1.4)$$

In the adsorption processes, the adsorbate gets adsorbed on the adsorbent.



Using Le-Chatelier's principle, equilibrium will shift towards the direction where the stress can be relieved. In cases of excess pressure the equilibrium will shift based on the direction where the number of molecules decreases. The resultant effect will give rise to different types of isotherm adsorptions as shown below.^{51, 90} Fig. 1.1 indicates the

adsorption isotherms classification as defined by IUPAC. The type of isotherm is defined by the pore size and surface character of the material.

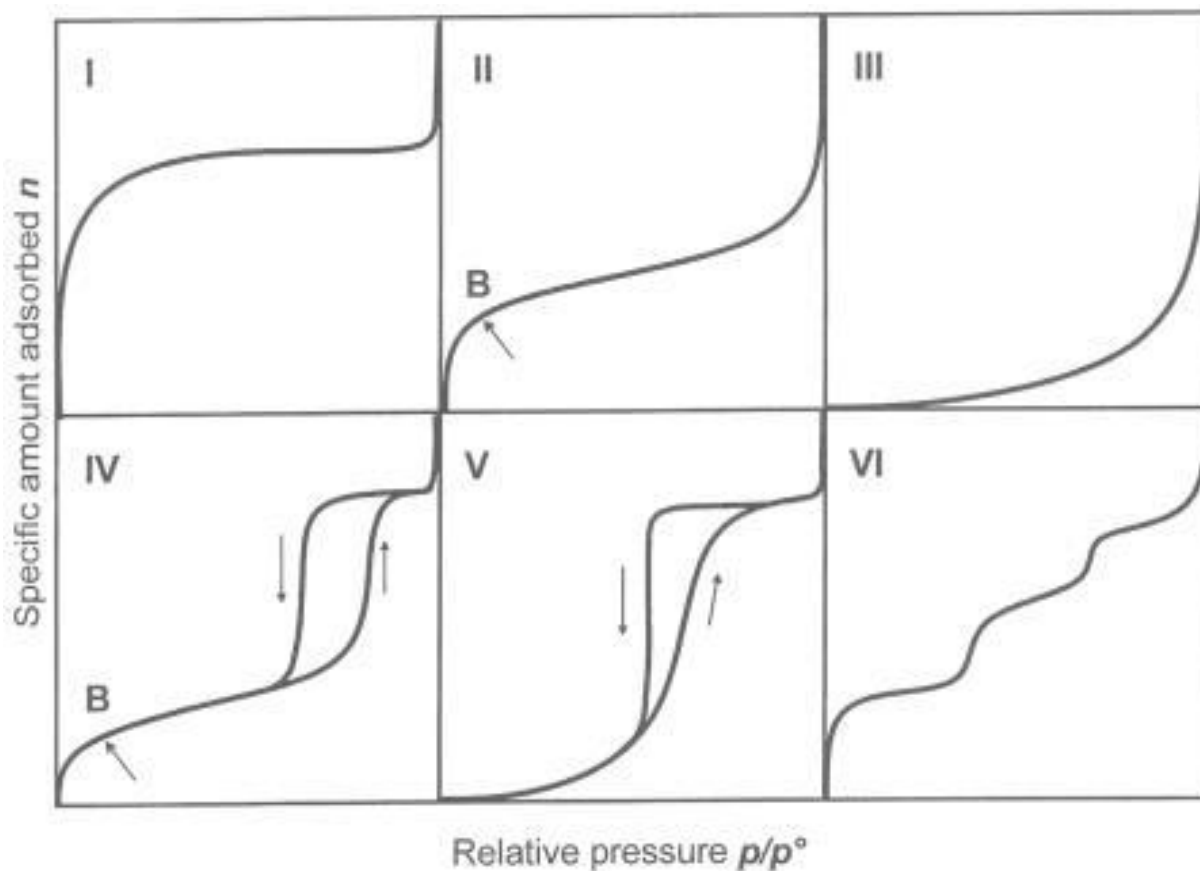


Fig. 1.1 The figure indicates the classification of adsorption isotherms defined by IUPAC.^{51, 90, 91}

Type (I) :represent Microporous materials (classes: Zeolite and Activated carbon), Type (II) : Non-porous materials (classes: Nonporous Alumina and Silica), Type (III) : Non-porous materials and materials which have the weak interaction between the adsorbate and adsorbent (classes: Graphite and water), Type (IV) : Mesoporous materials (classes: Mesoporous Alumina and Silica), Type (V) : Porous materials and materials that have the weak interaction between the adsorbate and adsorbent (classes Activated carbon and

water), Type (VI) : Homogeneous surface materials (classes. Graphite and Kr). Porous materials arise from the material pore structures. These pore structures are further classified into three different groups. Intra-crystalline which are generally of molecular dimension and they are arranged in a regular network pattern (e.g. zeolites, certain clays and MOFs). Another class is the assemblage (e.g. xerogel), which is mainly dependent on the size and packaging density composed of assembling of small particles. The last class consists of removing parts of the original structure so as to create new pores called the subtractive (e.g. carbonate).^{51, 92-94}

1.8.4 Physisorption and Chemisorption Principles

Since adsorptions occur by interactions between solids and molecules in the fluid state, science studies have been used to determine the types of forces involved in this process. The forces that are responsible for deviations from ideal gas characteristics, due to their condensation of vapors, are termed physisorption, while those forces primarily responsible for the formation of chemical compounds are called chemisorptions interactions.^{51, 85} Unlike chemisorbed processes, physisorption has a low degree of specificity and a molecule is able to keep its identity, and on desorption returns to the fluid phase in its originality. Physisorption is always exothermic but energy involved is generally not much larger than that of condensation of the adsorbate.⁵¹

In physisorption studies, the gravimetric (*wt. %*) and volumetric (*vol*) capacities of adsorbed gas is estimated with the equations.

$$wt\% = \frac{m_{H_2}}{m_{H_2} + m_s} * 100 \quad (1.6)$$

$$Vol = \frac{m_{H_2}}{V_s} = \frac{m_{H_2}}{m_s} \cdot \rho_s \quad (1.7)$$

Where m_{H_2} , represent the mass of hydrogen adsorbed, m_s is the mass of the solid adsorbent and ρ_s is the packing density. For mobile applications, the packing density is considered when calculating the volumetric uptake. However, the bulk density (obtained more easily from X-ray diffraction analysis or mercury pycnometry) is considered.^{17, 95}

1.9 Metal Organic Frameworks (MOFs); and IUPAC Understanding

The terminology of Metal-Organic Frameworks, (MOF) is still in IUPAC provisional nomenclature recommendation as at the year 2012. It was proposed as MOF or alternatively porous Coordination Network (PCNs), having an open framework that contains potential voids.^{51, 96, 97} Since IUPAC strongly discourages the use of identifying these materials with ‘hybrid organic-inorganic material’, they agree that their (materials) can be prefixed with place of origin followed by a number (e.g. HKUST-1 (Hong Kong University of Science and Technology)) rather than Cu-BTC, (btc,-Benzene tricarboxylate) by which this materials is also known.⁹⁸ In some other cases, where several metals have been used to make the same structure, the metal is represented in parenthesis. For example, ‘Materials of the Institut Lavoisier, chromium (Cr) based metal

can be represented as MIL-100(Cr),⁹⁹ coordination polymer nickel(Ni) based, CPO-27(Ni).¹⁰⁰

Metal-organic frameworks have attracted much attention in recent years as very suitable materials for gas sorption, sensors, gas separations, catalysis and most recently drug delivery. They consist of metal-oxygen vertices commonly known as secondary building units-SBU, held together with organic linkers to create pores and channels (Fig. 1.2). They are also highly crystalline and porous in composition and can be made inexpensively in large quantities.^{1, 4-6, 8, 9, 22, 24, 39, 40, 52, 95, 101-110} As illustrated in Fig.1.3 and Fig.1.4, MOFs are constructed of metals and metal cluster nodes which are joined through linkers which are organic moieties. Metals that can be used that are *di-*, *tri-*, or *tera-*valent, (Cu, Zn, Al, Cr, Ga, V, Zr etc), with almost every metal present in the periodic table having been used for MOF synthesis. Similarly, vast numbers of organic linkers have also been tested or introduced (e.g. phosphate, carboxylate, imidazolate, etc), and their (organic linker) length and degree of fictionalization have been varied enormously.^{51, 85}

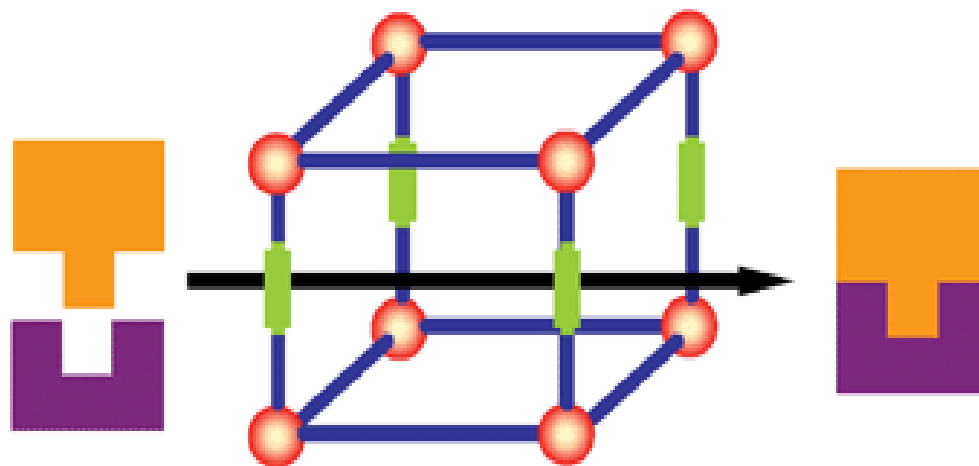


Fig.1.2. Building block (red balls) held together with organic linker (green cylindrical shape)

MOFs have been found to be highly crystalline and porous. They are also less expensive in large quantities. They are light and fairly stable over a wide range of temperatures and pressures. They can also be easily modified by changing their metal and organic ligands.^{1, 5, 23, 55} With MOFs synthesis, their pore sizes can be easily adjusted (angstroms to nanometers) by controlling their linker length to give new MOFs with almost the same topology but having a higher surface area.^{39, 56, 111}

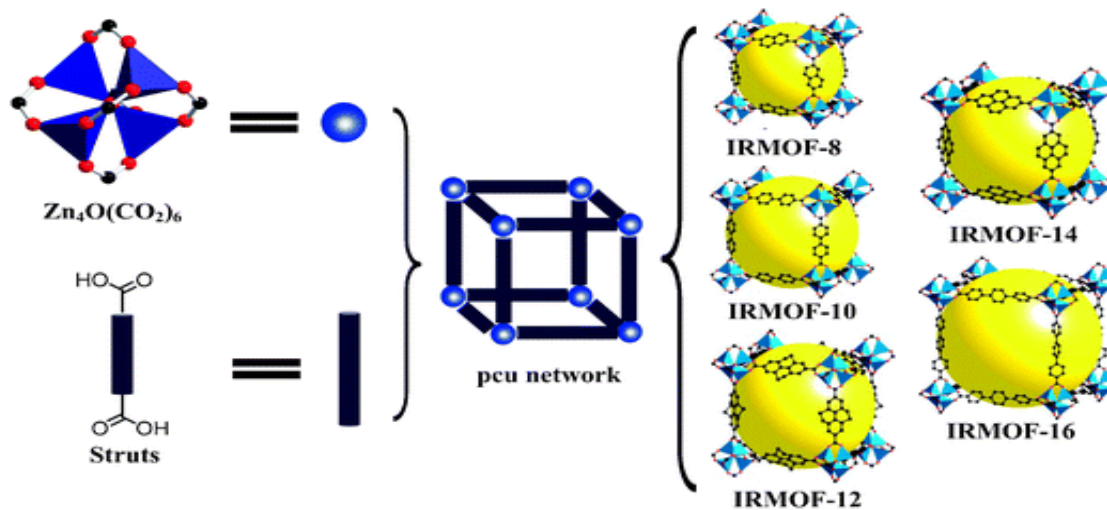


Fig. 1.3. Pictorial structure of MOFs members formation sharing same topology and length. The expansions of their links increases their internal void space and allows for catenation formations.¹¹²

While the linker can be modified, the metal can be partially unsaturated to give specific adsorption sites^{107, 113}. Since MOFs are cage-like structures which are composed of metallic nodes that are connected by a network of organic linkers, there is room for rational modification. Researchers have discovered that with a little twig or modification the functional groups placed along the organic linkers can alter a MOFs desired properties. This is good for carbon storage.



Fig. 1.4. Rational modification, otherwise known as MOFs functionalization

The uniqueness of MOFs apart from their flexibility with temperature change,¹¹⁴ mechanical pressure,^{115, 116} and probe molecule uptake, is their ability to possess a well-

defined structure. An example of this is MIL-88d¹¹⁷, based upon 200 % uptake of some fluids. In more of these, the organic linkers can also show some rotational movement with respect to uptake of specific molecules.^{118, 119} These processes have given birth to the ability to functionalize metal nodes and organic linkers with moiety, that can attract targeted species. Also, nanoparticles have been occluded in the pores to enhance a given species like hydrogen.^{36, 120, 121}

1.9.1 Types, Applications and Limitations of Metal-Organic Frameworks

The metal-organic frameworks (MOFs) and porous coordination polymers (PCPs) family,^{33, 39, 111, 122-124} cover a wide circle of materials with subsets that can be identified as zeolite imidazole frames (ZIFs),¹²⁵ Covalent Organic Frameworks (COFs),¹²⁶ Microporous Organic Polymers (MOPs) and so on.^{92, 127}

MOFs tend to have lower thermal stability compared to zeolite analogues. The reason for this is that the linker helps the metal binding energies, but many MOFs have high thermal stabilities, homogeneous pore sizes, exceptional surface areas and pore volumes and decompositions at temperatures such as 573 K.^{1, 13, 22, 39, 52, 54, 55}

MOFs also have some limitations like every other material. Some of their shortcomings are cost of synthesis is high compared with zeolites or activated carbon; thermal degradation resistance is limited to some degree; they are unstable in the presence of moisture; and they possess low density due to their open structure. However, many of these MOFs have good robustness under thermal conditions as they tend to withstand temperatures up to 450 °C (723 K).^{51, 85}

Gas separations or purification is another area where MOFs play an important role due to their good adsorption capacity and selectivity. They are able to undergo rotations or shifts in position about its axes.¹²⁸⁻¹³⁰ Previous studies have demonstrated that, with a MOF like PCN-17, the rotation was achieved positively and separation was by simple size-exclusion.¹³¹ There are other materials with promising values. Their turning properties are obtained by simply varying the temperature. An example of these are the “Mesh-Adjustable Molecular Sieves (MAMS)”. Similarly, their selectivity is based on possibilities of interaction between the different adsorbate - adsorbent (like HKUST-1 with known characteristics of having unsaturated metal coordination sites). Presently, MOFs appears to strike a great compromise between activated carbon and zeolites.^{132, 133}

In area of catalysis, MOFs should have good a future due to the wide adaptive nature of their pore structure and active transition metal. For example, during the synthesis of IRMOF-8 (Zn_4O (naphthalenedicarboxylate)₃), Nguyen and his colleagues, in 2011 were able to achieve this in their studies using the Friedel-Crafts acylation reactions.¹³⁴

In terms of drug delivery, MOFs due to their large capacity and high porosity combined with a controlled and slow release, show they can be relied on in field of medicine. MIL-101, whose pore size lies between 0.29-0.34 nm and having a window of 1.2-pentagonal and 1.6 nm-hexagonal was able to release very slowly over a 3 day time frame. MIL-53, from the studies by Horeajada et al., (2008, and 2010), and Loiseau, et al., (2004) shows that the drug ibuprofen had a 20% uptake in weight, due to its framework flexibility.¹³⁵⁻

MOFs have also found their way into sensors usage. Luminescent MOFs are being synthesized and have been shown to have great potential on the amount of species adsorbed.^{138, 139} Comparing MOFs with other adsorbents has been a tasking effort as many parameters have to be in place such as their bulk density and amounts adsorbed per unit volume. In the studies of Wiersum et al. (2013) and by Rege and Yang, in (2001), published in R.T. Yang book (2003), the working capacity, the selectivity and mainly the enthalpy of adsorption were addressed.^{132, 140} The cost of these adsorbents does not look good for MOFs compared to others. Some of them can be made via cheap organic linkers, for example Trimesic and Terephthalic acid, as demonstrated for Basolite A520 synthesis, and also currently MOF-5 synthesis from this work (this would be proven in details in later chapter in this dissertation). Plenty of different structures are continuously appearing either by theory or experimental synthesis.

1.9.2 Overviews of All Selected MOFs-Materials for This Research

Due to thousands of MOFs currently present, some of them were chosen in the course of this research work, among those briefly summarized below. Some fundamental basis for selections will be discussed in detail in later chapters. Also, the organic linkers needed for their synthesis (Fig. 1.5) are also given consideration during the course of this work. MOFs are made of organic linkers, and there are many organic linkers designed for specific MOFs, as some tend to be un-reactive when in contact with metals therefore producing “*no-product (MOF)*” formation” during and after synthesis.

Hence the quest to synthesize that specific organic linker for a specific MOF continues.

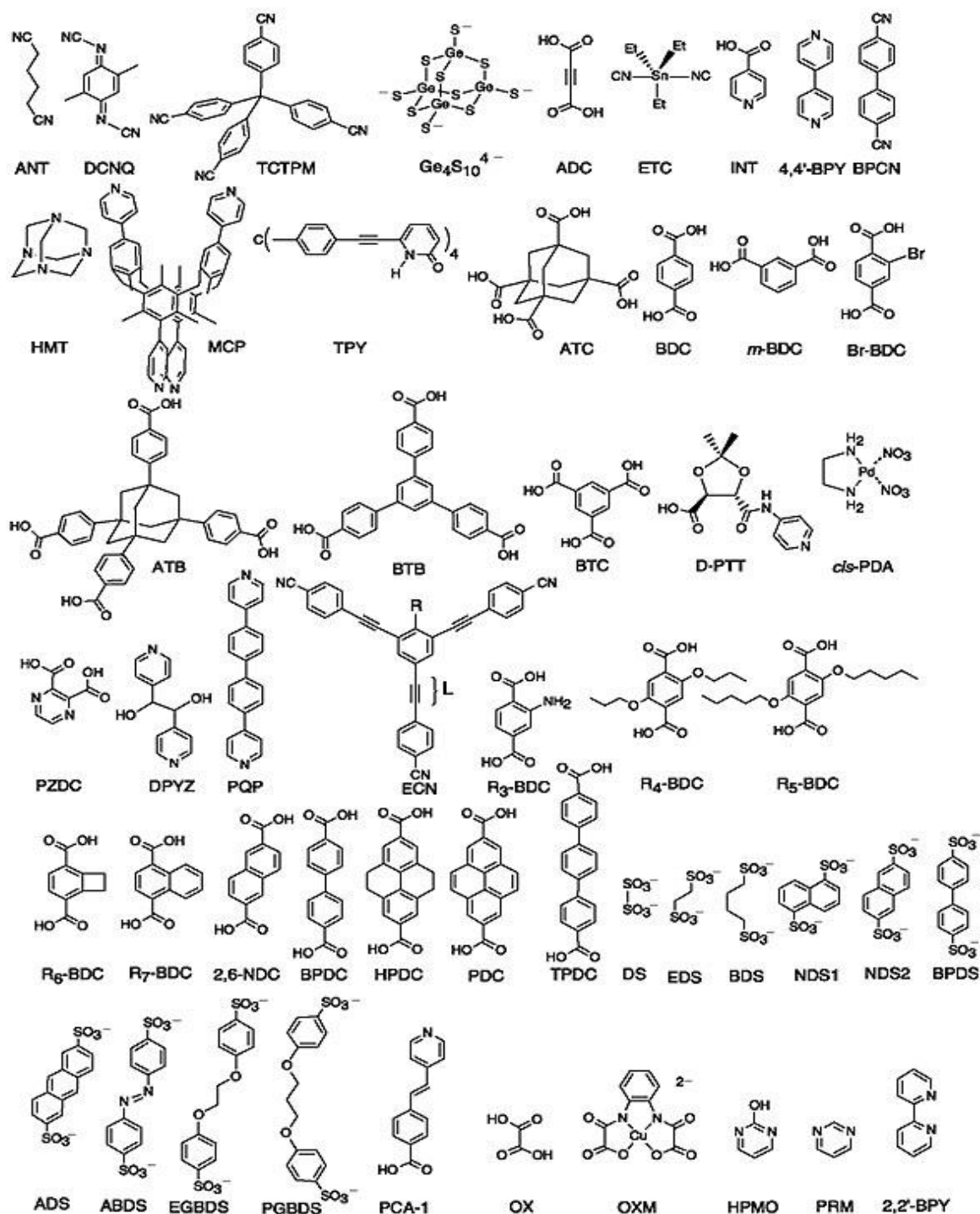


Fig. 1.5. Some structures of organic linkers for MOFs synthesis.¹¹³

1.9.3 Zinc Benzene-1,4-dicarboxylate (Zn-BDC) or Isostructural Metal-Organic Frameworks – 1 (IRMOF-1/MOF-5)

Reticular is basically defined as having the form of a net. Isostructural is based on the same net having the same topology. Hence from our literature reviews so far, MOF-*n*: Metal-Organic Framework where “*n*” is an integer assigned. Therefore, IRMOF-*n*: Isostructural MOF. Interpenetration, is a term used to describe the inter-growth of two or more networks in a structure where the networks are physically but not chemically linked. The term secondary building unit has been used to describe conceptual fragments of zeolites; in the context of reticular chemistry it refers to the geometry of the units defined by the points of extension (such as the carboxylate C atoms in most carboxylate MOFs).¹¹³ In line with this research, Zn-BDC will be used to as the acronyms for IRMOF-1 / MOF-5.

Isostructural metal-organic frameworks have since been a major challenge for designing and constructing new crystalline solid-state materials from molecular building blocks, and now recent research studies are showing promising success. This is an approach that requires the use of secondary building units to control the assembly of ordered pattern frameworks; this we can define as reticular synthesis. This chemistry has produced materials known to have predetermined structures, compositions and properties. Particularly, highly porous frameworks which are held together by strong metal–oxygen–carbon bonds and having exceptionally large surface areas and good capacity for gas storage. They have also been known by their pore metrics and are able to undergo variations and functionalization.¹¹³ Zn-BDC has been the most studied of all MOFs. It has pore openings of either 12.8Å or 9.2Å depending on the orientation of the aromatic

rings.¹⁴¹ Another characteristic of Zn-BDC is the inability to breathe due to its configuration which prohibits the positions of some of the ligands and symmetry rotations of the organic-linker.^{142, 143} Its BET surface area ranges variably from 896 m²/g to 3800 m²/g and the Langmuir surface area ranges from 1014 m²/g to 4400 m²/g. Studies of this MOF have shown that under high pressure (>1 bar) the hydrogen adsorptions are 4.95 wt.%, to 1.15 wt.% at LN₂ temperatures.^{39, 144-146}

1.9.4 Zinc 2,6- Naphthalenedicarboxylate (Zn-NDC) or Isorecticular Metal-Organic Frameworks-8 (IRMOF-8 / MOF-8)

Zinc 2,6- Naphthalenedicarboxylic (Zn-NDC), has carboxylate frameworks due to high acidity (pKa = 4) which allows in situ deprotonation.^{147, 148} Zn-NDC, at low temperatures of 77 K and low pressure (1 atm), has surface areas range 890 – 1601 m²/g depending on the synthesis method. The hydrogen capacity is within the ranges of 1.38 and 1.80 weight percent. Zn-BDC, MOF-177, and MOF-18 also have high surface areas of 3362, 4526, and 1501 m²/g respectively and hydrogen weight percentages of 1.32, 1.25, and 0.89 respectively at 77 K. Wang et al.¹⁴⁹ in their studies found hydrogen capacity at 298 K increased by almost 90 % when the zinc (Zn) metal in MOF-8 underwent platinum (Pt) doping. The surface area and the pore volume were conserved during the process¹⁴⁹. Other characteristics of Zn-NDC, is that its longer linker length leads to rigid conformations and its pore size plays a major role in adsorptions at low pressure.^{21, 28, 31}

When gases like carbon dioxide (CO₂) and methane (CH₄) are used for its storage, Zn-NDC appears to bind more strongly than others possibly due to its smaller pores and from interpenetrating products from synthesis. This was clearly noted by the work of Yao et al., in (2012).^{66, 150} Material studies of Zn-NDC show surface areas of 890 m²/g and 1466

m^2/g according to Krawiec et al.(2006) and Rowsell et al., (2004). They both obtained a close value for hydrogen adsorptions under high pressure at 77 K to be 1.45 and 1.48 wt.% respectively.^{13, 151}

1.9.5 Copper 1,3,5-Benzenetricarboxylate, (Cu-BTC) or Hong Kong University of Science and Technology (HKUST-1)

Highly porous MOFs with large pore volumes and high surface areas have been found to favor high gas storage capacities; however, weak interactions between gas molecules set limitations to their high gas storage capacities at low temperature (for example, 77 K for H_2) or high pressure of up to 100 bar to fully utilize the pore space. Furthermore, the low framework densities of some extremely porous MOFs have also been found to limit their volumetric gas storage capacities for example, Cu-BTC ($\text{Cu}_2(\text{BTC})_3$, BTC=1,3,5-benzenetricarboxylate) and MOF-505 ($[\text{Cu}_2(\text{BPTC})]$, BPTC=3,3',5,5'biphenyltetracarboxylate). The high density of open copper sites and small pores is found to favor high hydrogen storage of 2.9 wt% at 77 K and 1 bar but the moderate surface area causes limitations to hydrogen uptake (4.1 wt% at 77 K and 15 bar).¹⁵² Some studies on this MOF have shown surface areas of $1507 \text{ m}^2/\text{g}$ under low pressure and hydrogen adsorptions of 2.48 wt.% at 77 K.¹⁵³

1.9.6 Zinc Methyl-imidazolate (Zn-Mim) or Zeolitic Imidazolate Framework (ZIF-8)

Zn-Mim under CH_4 adsorptions at 298 K was found to adsorb 6.5 wt.% and under corresponding conditions with CO_2 gas, it was found to adsorb 35 wt.%. In general MOFs have higher capacities for CO_2 storage when compared to most zeolites and carbon nanotubes.⁴⁰ Studies of Zn-Mim have also shown this MOF containing Zn-metal to have

a surface area that was comparable to other MOFs in same ZIFs series. Park et al. (2006), in his work reported a BET surface area of $1630 \text{ m}^2/\text{g}$ for this particular MOF and a Langmuir surface area of $1810 \text{ m}^2/\text{g}$ and a pore volume of 0.64 cm^3 . Studies of this MOF under low pressure ($<1 \text{ bar}$) show 1.2 to 1.3 H_2 wt. % in excess and a heat of adsorption of 4.5 kJ mol^{-1} . At high pressure ZIFs studies have shown hydrogen adsorption as high as 3.01 wt.% at LN_2 temperature (77 K) and 0.13 wt.% at room temperature (298 K).¹⁵⁴⁻¹⁵⁶

1.9.7 Iron and 1,3,5-Benzenetricarboxylate (Fe-BTC) Framework (Basolite F300)

Few studies have been carried out on this MOF. Its sorption properties with gases like H_2 , CO_2 and CH_4 have not yielded favorable results probably due to the morphological structure it possesses.

1.10 Problem Description

For a very long time, scientists have believed that, the surface area of a material is directly proportional to the amount of gas the material can adsorb. They specifically base their concepts on the surface area and weight percent of gas adsorptions and a tag-along story of pore volumes, to explain the reason why some MOFs can have better gas adsorptions over others, but there is not always a good correlation between surface area and the weight percent of gas adsorbed by these MOFs. Studies have shown the interactions of gases such as hydrogen with surfaces (binding energy) may also affect adsorptions based on some reasons like the nature of the organic linkers, the metal sites of the material, and so on.^{51, 157-159} Since surface area may or may not have a good relationship with gas sorption of gas molecules in MOFs having different linkers and/or

metal sites, there is a need to determine if other parameters might correlate well with enthalpy and/or weight percent.

1.11 Objectives, Goals of This Research

- 1 To apply a shorter, faster and simpler method of synthesis to some of these MOFs (cost and time consuming).
- 2 To investigate the adsorptions of hydrogen (H_2), carbon dioxide (CO_2), and methane (CH_4) gases, using metal-organic frameworks (MOFs) as the adsorbents for their storage.
- 3 To compare the hydrogen, carbon dioxide and methane adsorption enthalpies on some selected MOFs
- 4 To characterize selected MOFs using the scanning electron microscope, thermogravimetric analysis, X-ray diffraction, particle size analysis, high pressure volumetric analysis, surface areas, and porosity analysis at low pressure as well as high pressure under different temperatures for hydrogen, carbon dioxide, and methane gas adsorptions.
- 5 To determine if other parameters may correlate better with the quantity of gas adsorbed than surface area.

CHAPTER TWO

EXPERIMENTAL PROTOCOL

2.0 Experimental Protocol

This section gives detailed methodology and approach as well as the materials used in this research. The procedures were carefully selected, reviewed and in some cases the protocols were modified from previous or existing protocols of past studies. In a rare case, a new protocol was also formulated and it achieved a much better and comparable surface area and gas (H₂, CO₂ or CH₄) storage capacity.

2.1 Research Approach

An approach was developed to primarily determine the activities of gas molecules on materials (MOFs) surfaces during gas adsorptions. This was in relation to their surface area, isosteric heat of adsorptions (enthalpy) and weight percent (wt.%) of the different gases (hydrogen, carbon dioxide and methane) adsorbed. A secondary interest was to take a look at their surface morphologies, their behavior under low and high pressures as well as temperatures under different conditions. This will be studied using the molar mass of the gases.

2.2 Materials

Some of the samples used in this research were obtained commercially. Supplies were obtained from Sigma-Aldrich U.S.A., Chemical Industry Company Limited of America (TCI America), and Fisher Scientific; U.S.A. Materials purchased from these companies

were used without further purification. Materials and consumables obtained from Sigma-Aldrich are, potassium bromide (KBr) FT-IR grade (99+ %) which was used for infrared analysis, zinc nitrate hexahydrate, $\text{Zn}(\text{NO}_3)_2 \cdot 6\text{H}_2\text{O}$ (≥ 99.0 % pure) which was used as the metal source for Zn-NDC and Zn-BDC. Organic linker (2,6- Naphthalenedicarboxylic acid, also referred to as 2,6- H_2NDC (99.0 % pure) was used for Zn-NDC for synthesis while anhydrous N,N-dimethylformamide (DMF, 99.8 % pure) was the solvent. Zn-NDC was purchased from the Sigma-Aldrich company-America. High purity gases were used as adsorbates; Nitrogen-(N_2) compressed gas (Grade 5.0), Compressed Air (Grade 2.0), Helium-He (Grade 5.0), Argon-Ar, and Carbon dioxide- CO_2 , were supplied by Keen compressed gas of Wilmington, Delaware. U.S.A. Methane- CH_4 (Grade: Research Purity), and Hydrogen- H_2 compressed (Grade 4.5) were purchased from Matheson Tri-Gas Incorporated, New Jersey. U.S.A. Hydrogen- H_2 (Grade 5.0) was supplied by BOC Gases of New Jersey, U.S.A.

Required materials for Zn-BDC were the same, except for the organic linker (terephthalic acid)- Benzene-1,4-dicarboxylic acid (98% purity H_2BDC) obtained from Sigma-Aldrich U.S.A. The solvent, N,N-Diethylformamide (DEF) was obtained from TCI-America. Acetone ($(\text{CH}_3)_2\text{CO}$)- 99.5+% was purchased from ACROS Organics-US.A., 2-Popanol (Histological Grade) and Chloroform (anhydrous, contains amylenes as stabilizer, $\geq 99\%$) were both obtained from Sigma-Aldrich, U.S.A. The materials for Cu-BTC synthesis, was supplied by Sigma-Aldrich.

2.3 Experimental Method

In most cases, the MOFs were synthesized by solvothermal or hydrothermal methods, in which the reactions were carried out in an organic solvent or in water at high-temperature in closed vessels. However, these methods typically require long reaction times, from several hours up to several days or months, depending upon the MOF of interest. The reaction solvent, temperature, reagent concentrations, and other parameters can also play a certain role. Hence, to achieve this project objective, it was necessary to design suitable methods for synthesizing, characterizing, and testing the materials. These synthesis methods included mechanical alloying using ball milling, applying a rapid solvothermal method to synthesize some of the MOFs and using other methods from other literature studies. Material thermal stabilities were determined using thermal gravimetric analysis X-ray diffraction was used to determine phase purity and crystal structure, the material particle sizes were determined using an infrared laser beam machine. Surface analysis was done on the sample using a porous size analyzer. A scanning electron microscope was used for some of the materials morphologies. FTIR was used to understand the adsorptive nature of these MOFs with gas.

2.4 Sample Handling and MOF Synthesis

All sample handling, weighing, storages and preliminary evacuations were performed in a glove box to prevent contamination from air and moisture as most of the MOFs in this work are air-sensitive. The glove box antechamber was evacuated and regularly cleaned several times using argon gas to remove air or moisture to keep its level below 10 ppm.

2.5 Zn-NDC Synthesis

Rapid solvothermal synthesis of Zn-NDC was performed using $\text{Zn}(\text{NO}_3)_2 \cdot 6\text{H}_2\text{O}$ (1.19 g) and 2,6- H_2NDC (0.43 g). These amount were placed into three(3), 50 ml pyrex conical flasks were dissolved in 40 mL of DMF. A magnetic stirrer was placed inside each flask sealed with glass stoppers and placed into a Fisher Scientific ultrasonic cleaner, FS60H. The sonication was carried-out at room temperature for 60 mins to obtain a clear solution. The flasks were then transferred to a Fisher Scientific isotemp/stirrer with aluminum foil wrapped around the upper part of the flask to reduce exposure to air and to hold a thermometer in place leaving just enough room for the stirrer. The stirrer was set at 350 rpm to prevent hot spot generation inside the inner wall and the bottom of the flask to also allow even distribution of heat. At temperatures of 155 °C, the solution turned yellow within 50 to 70 mins. Crystal formation was recorded within 30 to 60 mins of heating. Then the reaction was allowed to proceed for 1 hour at 155 °C. At the end of the process, the solution was allowed to cool to 40 -50 °C while still stirring. The yellow supernatant was decanted and the crystals were purified three times with 5 ml DMF. This was filtered and put under vacuum to dry. The need for the development of a rapid solvothermal method, by involving other steps such as sonication, stirring and sealing of the vessel was obtained from the literature.^{28, 34, 38, 160-165}

2.6 Zn-BDC Synthesis

The Zn-BDC was synthesized using the same method (Rapid Solvothermal Method) as with Zn-NDC, with a further adjustment of some parameters as developed by Orefuwa et al.^{34, 38} 1.89 g of zinc nitrate hexahydrate ($\text{Zn}(\text{NO}_3)_2 \cdot 6\text{H}_2\text{O}$) was put into a 50 ml Pyrex

flask mixed to react with 0.33 g of terephthalic acid (H_2BDC) then mixed into solution with 40 ml of anhydrous N,N-Dimethylformamide, 99.8% purchased from Sigma-Aldrich, U.S.A. A Magnetic stirrer was introduced into the sample bottle and transferred to a sonicator. All procedural activities at this stage were carried out inside an argon filled glove-box. Heat from the sonicator was applied during the sonication period. The resulting mixtures were heated over a hot-plate (supplied by Fisher-Scientific, U.S.A.) at 170 °C for about 120 mins. Other temperature ranges were also determined such as 120, 130, 150, 155, 165, 170, 175 and 180 °C and the surface area of the materials were also noted. This was used to obtain the optimum temperature for this synthesis, The flasks containing the mixtures were allowed to cool down to room temperature and the product was filtered and subjected to purification. Crystals were formed by washing three (3) times at 5 mins intervals with 5 ml of anhydrous chloroform containing amylenes as stabilizer $\geq 99\%$ purchased from Sigma-Aldrich. Filtration was further carried out on the sample and kept under vacuum overnight.¹⁶⁶

2.7 Cu-BTC Synthesis

Chui et al.,⁹⁸ was the first to report the synthesis of Cu-BTC by using a convectional solvothermal synthesis at 180 °C. Synthesis at high temperature seemed to have better effect on crystallinity but the significant amount of Cu_2O formed as a by-product was a major set-back. Other set-backs from solvothermal synthesis include usage of large amounts of organic solvent and longer time of reactions. Li et al.,¹⁶⁷ using ultrasonic irradiation for their synthesis at ambient temperature under optimized processing time of

60 min, were able to obtain Cu-BTC with 85.1 % purity and a BET surface area of 1100 m²/g.

Goudy et.al.,³⁶ has been able to develop a more efficient method for this MOF and same methodology has been used for this work. All the chemicals used in this synthesis were purchased from Sigma-Aldrich, U.S.A., and no additional purifications were needed. Two types of synthesis have been carried out in this group, (1) Solvent-free synthesis and (2) Solvent-assisted synthesis. The group was able to demonstrate that solvent-assisted synthesis resulted in higher surface areas compared to solvent-free synthesis under same mechano-chemical method of synthesis.

Cu-BTC was synthesized by mixing 1.090 g of anhydrous copper (II) acetate, Cu(OAc)₂ (98 %) salt, and 0.840 g of H₃BTC and loading into a 25 ml stainless steel milling vial (see Fig. 2.1) with a ball to powder ratio of 10:1 by weight and the grinding time was set to 10 mins using the SPEX 80000 Mixer/Mill.



Fig. 2.1 Ball-milling machine, courtesy of Center for Hydrogen Storage and Research (CHSR) laboratory at Delaware State University, Dover. U.S.A.

Prior to grinding ,400 μl of Ethanol ($\geq 99.5\%$) and deionized water were added in a volume ratio of 1:1 (v/v) using pipette.

2.8 Zn-Mim and Fe-BTC Synthesis

Zn-Mim, Fe-BTC were all purchased from Sigma-Aldrich, U.S.A. as Basolite Z1200, and Basolite F300 respectively.

Basolite Z1200 is an organophilic ZIF which can be reactivated at 100 $^{\circ}\text{C}$ with a surface area between 1300 – 1800 m^2/g .

2.9 Material Characterizations, Measurements and Sample Handling

This section deals with instrumentation used for and how the samples were handled and stored after synthesis for analysis.

2.10 Glove Box

All sample weighing or measurement, solution filtration, infiltration (composite formation) and post-synthetic handling were done using the Vacuum Atmosphere glove box (VAC, Model HE-493), which is fitted to a vacuum pump. The glove box antechamber was vacuum cleaned by evacuating it and refilling with argon gas from the gas tank attached to the glove box about 4-5 times to remove air and moisture trapped in it. Vessels, sample holders and other materials that might have had contact with the atmosphere were put back into the glove box (see Fig. 2.2).

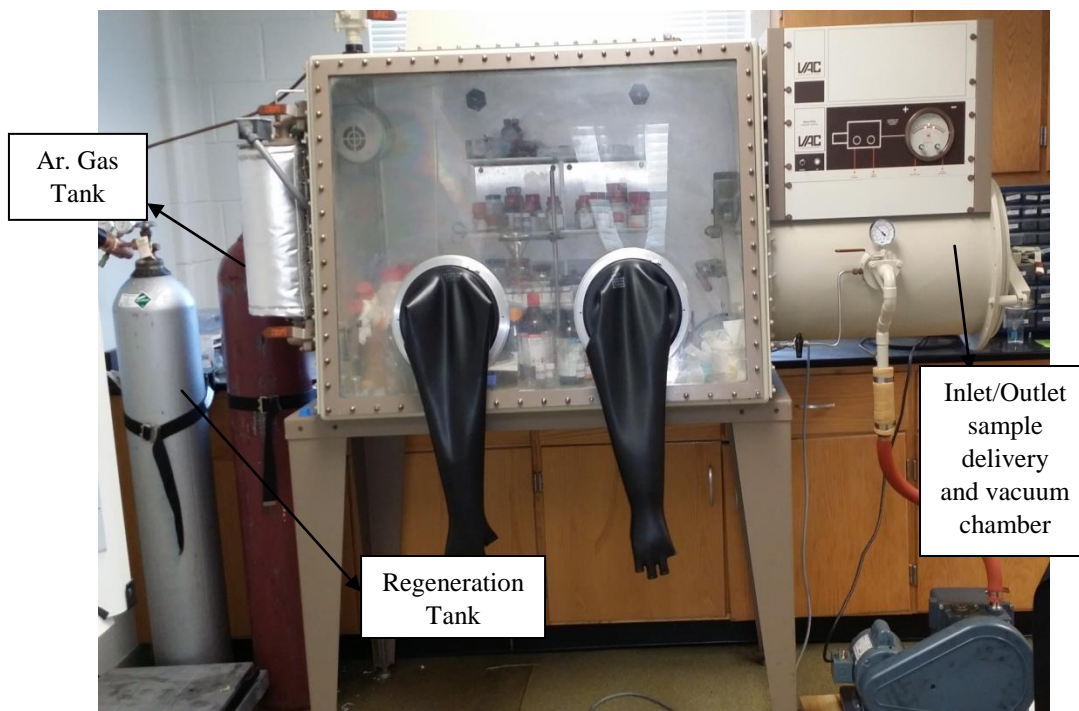


Fig. 2.2. The Glove Box. Courtesy of Delaware State University, Dover. Center for Hydrogen Storage and Research (CHSR)

This glove-box also served to store samples and help maintain a “No-Air” contact between the surrounding atmosphere and the synthesized materials.

2.11 Using the X-RAY Diffraction (XRD) for Analysis

The X-ray diffraction instrument was used for the synthesized samples materials to confirm their crystal purity or the formation of a new phase(s) upon reaction. The instrument used (see Fig. 2.3) was an X’pert Pro PANalytical X-ray Diffractometer with the model label *PW3040 Pro*. This instrument uses copper(Cu) radiation at a step size of 0.0167° in 2θ (2 Theta). The resulting peak signals were collected on an X’Celerator RTMS detector. The voltage and current applied were 40 kV and 20 mA respectively (This was programmed into the instrument). The sample loadings for all synthesized materials for this work were done in the glove box. Samples were transferred into the sample holder(s) and a razor or an object having a sharp edge was used to level the sample in order to ensure a smooth and even surface. A thin transparent Kapton polymer film was used to cover the sample to prevent exposure to air and moisture when it was out of the glove box and the lid was tightened to hold the film tightly to prevent sample being blown-off by air, and onto the x-ray sample holder.

The sample holder was then further taken away from the glove box through the chamber in-let /out-let compartment and transferred to the PANalytical X’pert Pro X-ray Diffractometer. The program for running the x-ray diffraction analysis was started by clicking X’pert data collector on the desktop which prompted the instrument’s connection. The total run time for each analysis was set to fifteen (15) minutes.

The X'pert data viewer software on the desktop was used for the after-analysis of each sample. Also the crystal structure and cell volumes of the samples under investigation could be determined.

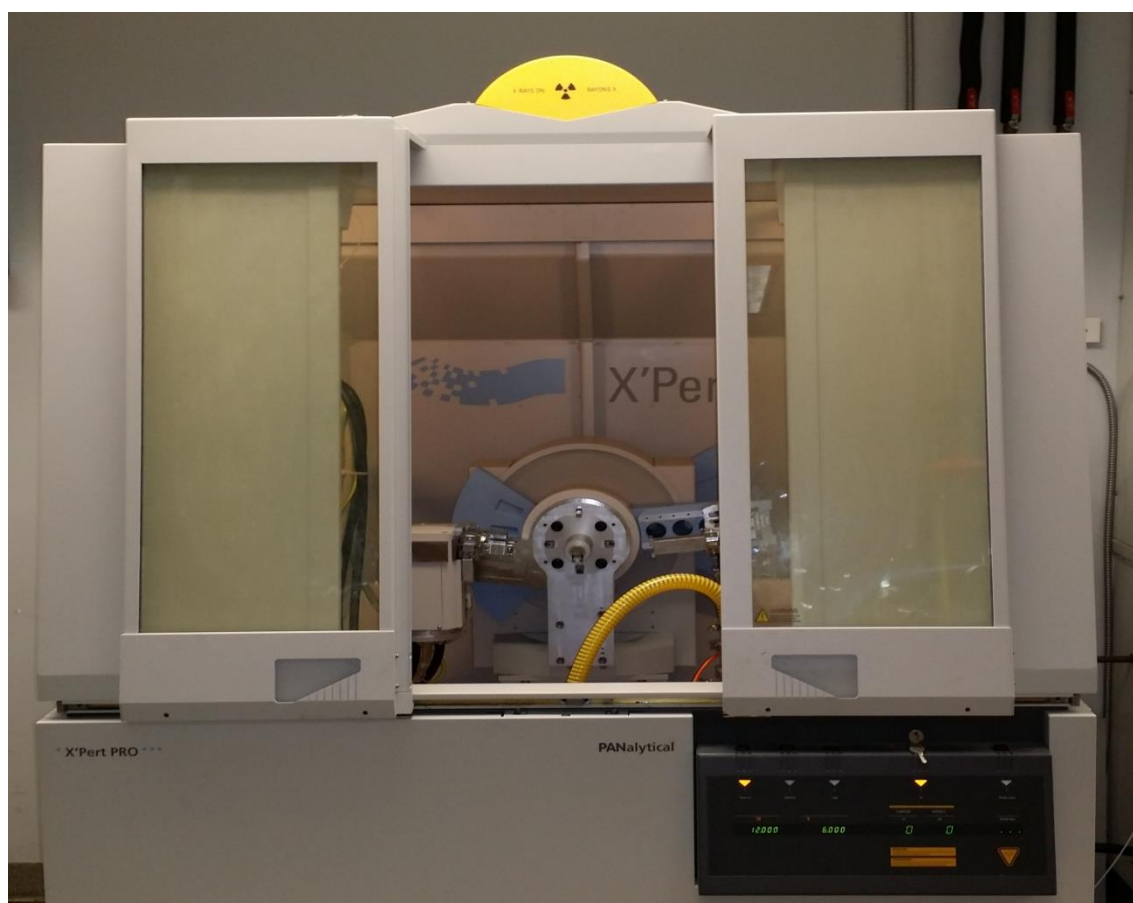


Fig. 2.3. A PANalytical X'pert X-Ray Diffractometer Instrument. Courtesy of Delaware State University, Dover. Center for Hydrogen Storage and Research (CHSR)

2.12 Thermogravimetric Analyzer (TGA)

The Perkin-Elmer Diamond TG/DTA (Model: Pyris Diamond High Temp 115) – see Fig. 2.4 was used to determine the stability of the synthesized samples thermally. This instrument was also equipped with air cooling control unit. The samples scanning rate was carried out at 5 °C per minute and up to a temperature of 600 °C under argon gas

flow. There is an argon gas tank attached to the instrument and a computer monitor to read the output.



Fig. 2.4. The Perkin-Elmer Diamond TG/DTA Analyzer. Courtesy of Delaware State University, Dover. Center for Hydrogen Storage and Research (CHSR)

The TGA instrument was turned on by switching the green power button and allowing the instrument to initialize. This took a few minutes until the word “*linkwait*” appeared on the LCD monitor attached to the instrument. The program software was then launched and the sample and program information were inputted into the dialogue box. The sample stage could be opened and closed by pushing the open button (blue in color) in front of the TGA machine. This is beside the furnace vent and will open and close the sample stage. Two identical high temperature ceramic pans located on two beams covered by the

stage served as reference pan and the sample pan. The weights of the two pans were both zeroed with ceramic pans empty. This (the zeroing) was repeated for about 4-5 times to ensure that the weight of the pans are in equilibrium. The sample stage was then opened by pushing the open button and the sample pan was carefully removed with forceps. A small amount (not more than 5 mg) of the sample to be analyzed was put into the pan and carefully placed on the beam. The stage was closed and the weight of the sample was measured by clicking on the weight icon on the program file. This was repeated 4-5 times to ensure equilibration. The program was then started by clicking the start button icon found on the program and allowed to run. The results from the TGA/DTA analysis are valuable in setting up a program for degassing the sample before the surface area and porosity analysis.

The file was copied into excel after exporting with ASCII file and converting this file into an excel spread-sheet. The graph was obtained by plotting the “sample temperature” versus “calibration”. The calibration values and results were obtained from the instrument onto excel spread sheets.

2.13 Laser Diffraction Particle Size Analyzer (LDPSA)

The particle size distributions of all samples (Zn-BDC, Zn-NDC, Cu-BTC, Zn-Mim, and Fe-BTC) were recorded using a laser diffraction particle size analyzer (Model: SALD-2201) from Shimadzu (see Fig. 2.5). The instrument was first turned “ON” before clicking the WIND-SALD icon on the PC, which is attached to the instrument and synched with the software. Once communication is established, the initialization was carried out to check for the adjustment of the rays. 60 mg of the sample was weighed

using the Denver instrument weighing device and dispersed in 20 ml of water in a beaker. With a Pasteur pipette, distilled water was put into the glass sample holder (to $\frac{3}{4}$ level mark of the transparent glass-holder) and loaded onto the sample compartment of the instrument. The stirring knob of the instrument was set to the desired speed. A blank measurement was carried out which was subtracted from the sample analysis.

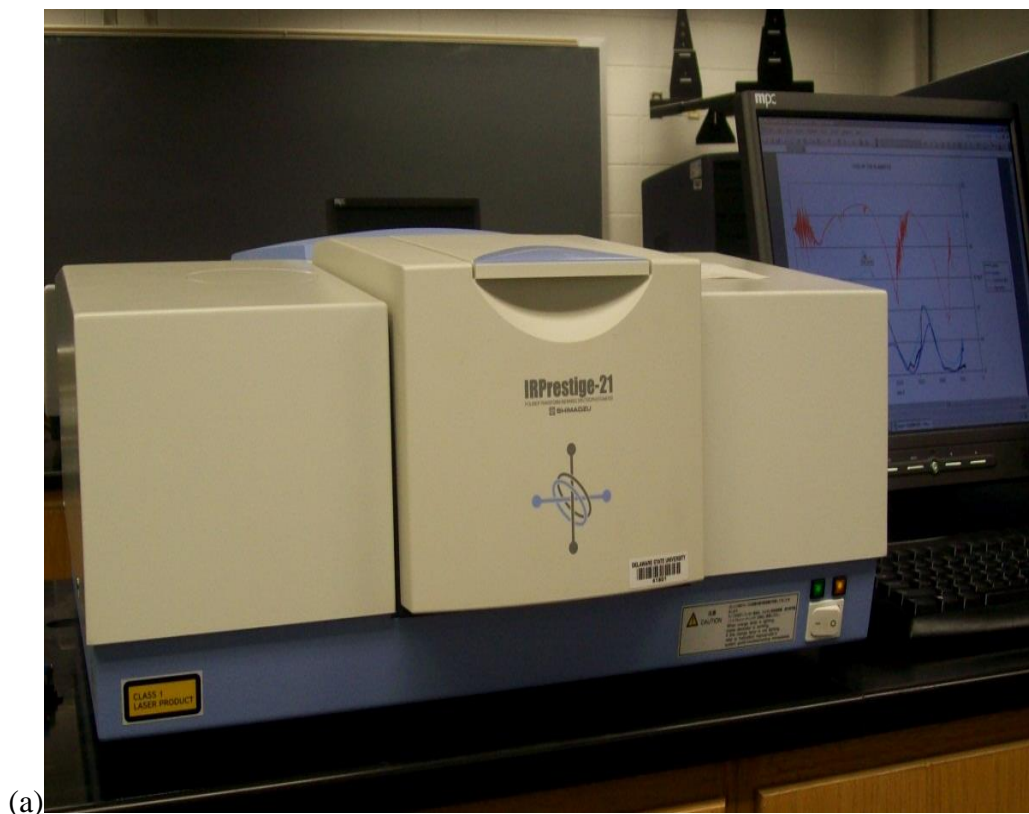


Fig. 2.5 Laser diffraction particle size analyzer (Model: SALD-2201) from Shimadzu. Courtesy of Delaware State University, Dover. Center for Hydrogen Storage and Research (CHSR)

To analyze the sample, a portion of the dispersed sample suspension was introduced into the sample holder. Using the same sonicator speed (to keep the particles in constant motion and in the direction of the light rays) the particle size was determined.

2.14 Fourier Infrared Spectroscopy Analyzer

Mamatha et al.,¹⁶⁸ procedures was used to carry out the solid-state infrared spectroscopy. The instrument used was purchased from Shimadzu Corporation (see Fig. 2.6). The FTIR instrument analysis reveals the functional groups present in the synthesized molecule and also the functional group(s) responsible for bond formation if any. All samples were mixed together inside a ceramic mortar and pestle with potassium bromide (KBr) purchased from Sigma-Aldrich in the sample to KBr ratio 1:10 respectively. The solid state infrared spectra were recorded in the range of 400 – 4000 cm^{-1} at ambient conditions using the IR Prestige-21 Fourier Transform Infrared Spectrophotometer (8400S from the Shimadzu Corporation). In an air tight container, the sample was taken out of the glove box and after pelletizing, it was loaded into a hollow little studs further pressed into a very thin pellet using the hydraulic press to create a thin homogeneous film.



(a)



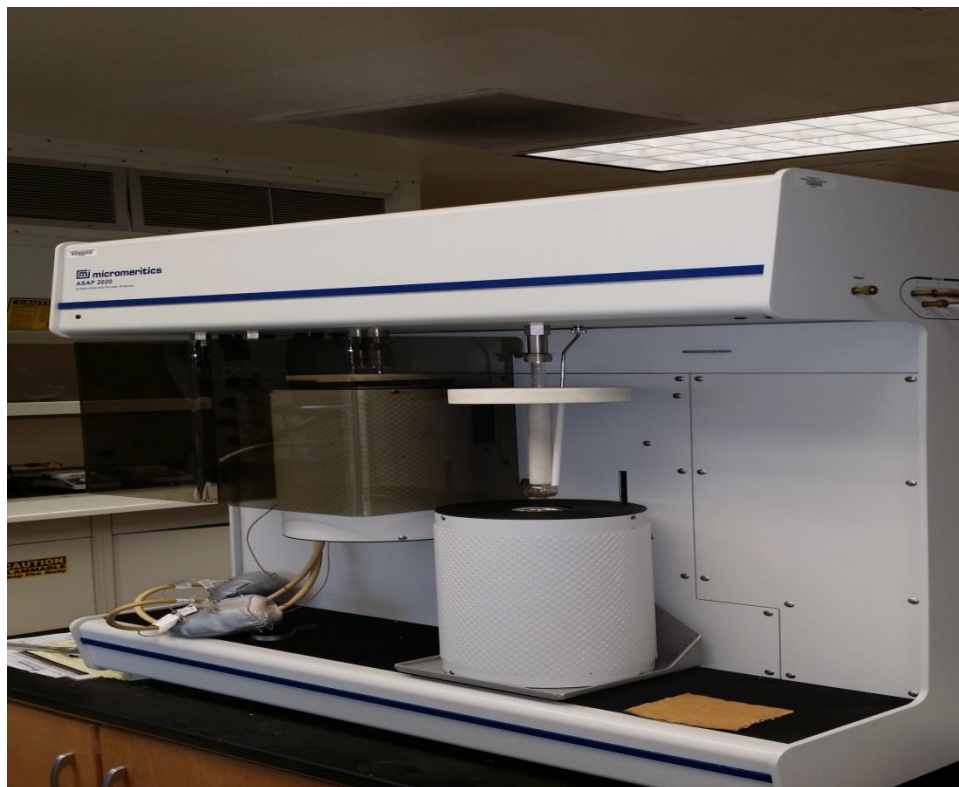
(b)

Fig.2.6. (a) IRPrestige-21 Spectrometer from Shimadzu.(b) Sample studs, potassium bromide (KBr) (from Sigma-Aldrich and sample holder. Courtesy of Delaware State University, Dover. Center for Hydrogen Storage and Research (CHSR)

The FTIR instrument was turned on and the IR solution icon on the computer was clicked. The measure button on the displayed page was clicked; the data and content of the sample to measure were entered. Initialization was done by clicking on the measurement button found on the top region icons on the PC - LED screen immediately after the appearance of the green lights. When initialization was completed, a background scan was done with, a total of 16 scans at a resolution of 2. The sample was then placed in the hollow studs (sample holder) and transferred into the sample compartment for data recording.

2.15 Surface Area and Porosity Analyzer

The surface area, pore volume and pore size of the synthesized samples were obtained using on a Micromeritics ASAP 2020 surface area and porosity analyzer (Norcross, GA. U.S.A), see Fig. 2.7 below. This instrument is fitted with two separate and independent vacuum systems (see Fig. 2.7b) of which one of the vacuum pumps allowed simultaneous degassing of two samples at same time as the analysis of another. The two-station degassing systems are fully automated with precise controlled heating scheme. Before degassing or analysis of the sample, the computer was turned on before turning the instrument “ON” to allow for communication between the instrument and the computer.



(a)



(b)

Fig.2.7. (a) Front-view of the Micromeritics ASAP 2020 surface area and porosity analyzer.(b) Back-view of the instrument showing the filters, vacuum pumps, beads column and all the different gas tanks connected. Courtesy of Delaware State University, Dover. Center for Hydrogen Storage and Research (CHSR)

The cold trap was filled with liquid nitrogen to the required volume mark, this is to allow good pressure to pull down the vacuum pumps during degassing as well as during the sample analysis. The standard ASAP 2020 comes equipped with six analysis gas inlets and a 1000 mmHg transducer, but the instrument used for this work came with “one” analysis port and “two” degassing ports.

Approximately 200-300 mg of all the synthesized and commercialized samples (Zn-BDC, Zn-NDC, Cu-BTC, Fe-BTC, and Zn-Mim), were measured inside the glove box into a standard ASAP 2020 sample tube having 1/2- inch stem size. A filler rod was inserted into the sample holder through the open channel. This is to reduce gas usage during measurement and a seal frit was used to cover the holder (see Fig.2.8).



Fig. 2.8. Sample glass-tube, filler rod and seal frit used for BET and gas adsorption analysis. Courtesy of Delaware State University, Dover. Center for Hydrogen Storage and Research (CHSR)

The Frit has a soft upper head which the needle on the porosity analyzer pierces, and has a rubber tight “O-ring” at the middle base to prevent escape of gasses. It also has a grating-like braces at the posterior end dipping into the tube channel. This helps in making the trapped solvent or gas to be withdrawn by the instrument and also prevent sample escape in time of excessive suction during analysis.

All samples (both synthesized and commercial) were weighed and evacuated based on the thermal stability of the sample from the TGA analysis until the outgas rate was $<10 \mu\text{mHg}$. For Zn-BDC, the sample was degassed under vacuum and at room temperature for 60 mins at 250°C for 600 mins (10 hrs). While Zn-NDC was degassed under the same initial conditions as Zn-BDC but at 200°C for 1200 mins (20 Hrs). Cu-BTC degassing was done at 200°C for 720 mins (12 Hrs).³⁶ The commercial sample Fe-BTC, was degassed at 200°C for 300 mins (5 hrs) while Zn-Mim was degassed for 100°C for 300 mins (5 hrs), with all samples initially degassed at room temperature for 60 mins (1 hr). All sample tubes, containing each sample, were re-weighed after degassing to obtain a consistent mass for the degassed sample. After degassing and cooling, the sample tube was covered with an isothermal jacket and the tube containing the sample was transferred to the analysis port.

At 77 K, N_2 -adsorption isotherms were measured volumetrically. Multipoint BET and Langmuir measurements were taken at relative pressures in the linear range of $P/P_0 = 0.01-0.05$ for BET plots and $0.05-0.3$ for Langmuir plots. The pore volume was calculated from N_2 adsorption measurements at liquid nitrogen temperature (77 K) and $P/P_0 = 0.50$. Nitrogen is commonly used because it is readily available in high purity; the

most appropriate coolant (liquid nitrogen) is readily available and cheap. Thirdly, the interactions of nitrogen with most solid surfaces are relatively strong and there is a wide acceptance of its cross-sectional area. Hydrogen, carbon dioxide and methane (99.999% pure H₂, CO₂ and CH₄) adsorption and desorption isotherms were measured by the Micromeritics ASAP 2020 running on version 3.0 of the software package.

Their free space was measured using helium (99.9999% purity). The gases were purchased from Keen gas and Matheson Gas Companies and used as received. Dry CO₂ was purchased from Safeway Store in Dover, Delaware, U.S.A. All isotherms were measured using samples that were activated, that is other than the initial evacuation of the sample in the sample cell for sorption measurements. No further treatments of the samples were performed. This was done to ensure that the nature of the materials used in the surface area measurements were the same as that being used in the gas sorption experiments.

2.16 High Pressure Volumetric Analyzer (HPVA)

Equilibrium gas adsorption and desorption isotherms were measured using the static volumetric method in an HPVA-100 (High Pressure Volumetric Analyzer VTI) instrument purchased and supplied from the Micromeritics Corporation (Norcross, GA, USA). The system was equipped with two electronic Bourdon gauge-type transducers (Mensor) that covered a range 0 - 1500 psi (accuracy 0.010% full scale). One was used to measure the pressure in the dosing manifold, while the other monitored the pressure in the sample cell (see Fig.2.9). The working temperature of the manifold was kept at 40 °C by heating the manifold compartment. The sample cell was a two- piece assembly that

consisted of a sample chamber (~ 2 ml) and a high pressure bellows valve. Both were connected via ¼" VCR fittings and the materials of construction were all stainless steel. Connection to the system was achieved by a ¼" VCO fitting. Two ports were available: one for out-gassing or degassing the sample and the other was the analysis port, which was outfitted to hold either a re-circulating bath or a small cryogenic Dewar bath. Ultra-high purity He (99.999%), H₂ (99.999 %), CH₄ (99.999 %) and CO₂ (99.999 %) were purchased from Keen and Matheson Gas Co. and used as received. In a typical experiment ~500 mg of sample was activated (at same temperatures used in the ASAP 2020) then transferred to the analysis port and evacuated at room temperature to 10⁻⁶ mbar prior to sorption experiments. After degassing, an isothermal jacket was placed around the sample holder, attached to the analysis port and the free space of the sample was first measured at room temperature.





Fig.2.9. (a) Front-view of the Micromeritics HPVA 100 (VTI) volumetric analyzer.(b) Rare-view of the instrument showing all the different gas tanks connected. The insert photo shows the sample holder (2cc) with the gasket supplied by Swagelok. Courtesy of Delaware State University, Dover. Center for Hydrogen Storage and Research (CHSR)

The value was then subtracted from the volume of the empty tube. The volume (V_{sp}) obtained and the mass (m_{sp}) of the sample after analysis was used to determine the skeletal density (ρ_{sk} in g/cm^3)¹⁷.

$$\rho_{sk} = \frac{m_{sp}}{V_{sp}} \quad (2.0)$$

The equation 2.0, can also be used to obtain the bulk or packing density of the metal-organic framework. Equation 2.1 can be used to calculate the pore volume.

$$V_{pore} = \frac{1}{\rho_{bulk}} - \frac{1}{\rho_{sk}} \quad (2.1)$$

Where V_{pore} is the pore volume in cm^3/g , ρ_{bulk} is the crystallographic density of the sample. In real time analysis, at temperatures other than ambient, the free space of the sample was measured first before logging in the information for the particular gas. At room temperature the sample free space and real time analysis were run at the same time.

2.17 Scanning Electron Microscope (SEM)

The scanning electron microscope was used to determine the surface morphologies of both the synthesized samples (Zn-BDC, Zn-NDC and Cu-BTC) and the purchased samples, Fe-BTC and Zn-Mim). The sample coating instrument (see Fig. 2.10), used to prepare the samples by coating them with the elements gold (Au) and palladium (Pd) in the ratio 60:40 (%) respectively this is to makes the sample conductive for imaging.

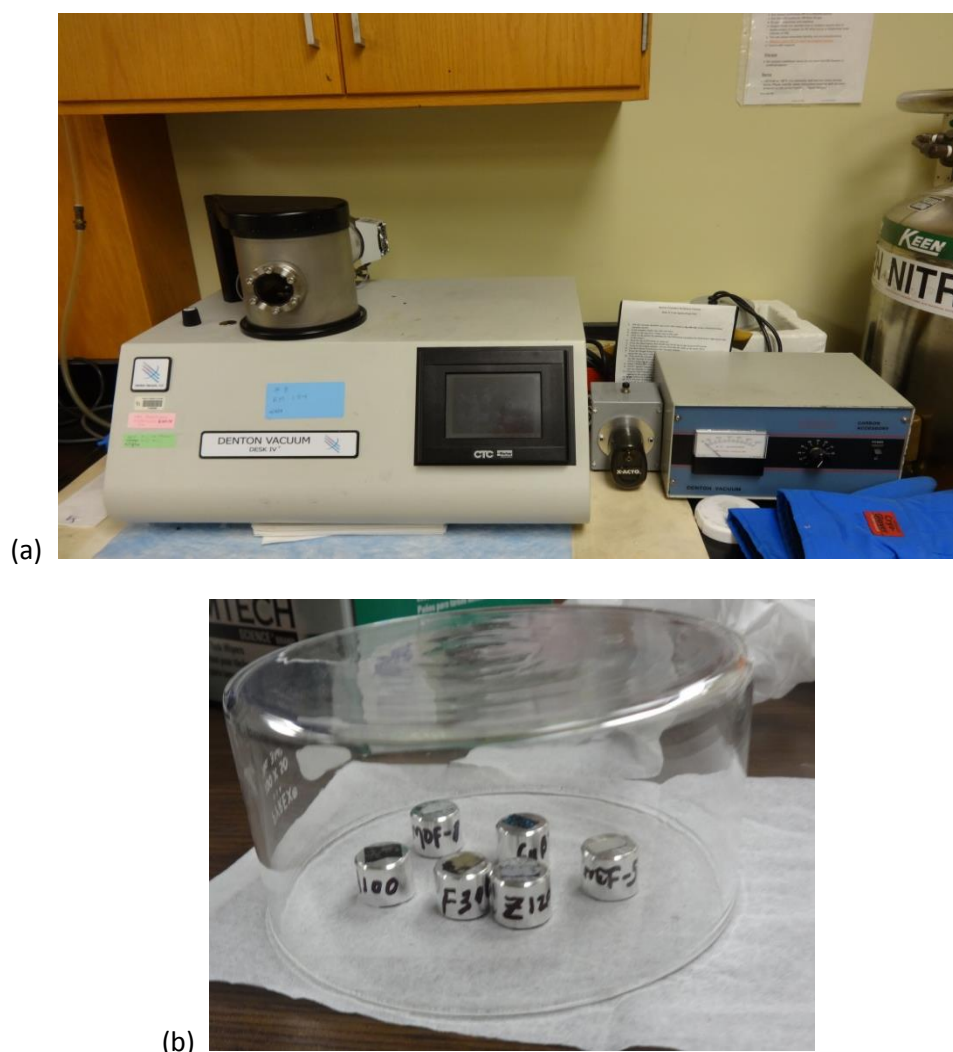


Fig. 2.10. (a) Coating instrument (Denton Vacuum Desk IV) (b) Sample studs with samples on top. Courtesy of University of Delaware, U.S.A. Center for Material Sciences, Department of Chemistry

This equipment also has a nitrogen tank attached to it that was supplied by Keen, U.S.A. The samples were held in place on top of the studs by a double-sided carbon tape. The air-duster was used to clean the surface of any excess spilled sample. It also helps to spread the sample uniformly across the studs/stones surface. The samples were loaded into the coating instrument and the sample surface was coated at approximately 15 – 20 Å. When coating was completed, the samples were immediately transferred into the scanning electron microscope -*JEOL JSM 7400F* instrument (see Fig. 2.11).



Fig. 2.11. JOEL JSM 7400F scanning electron microscope instrument, with insert snapshot of its resting base. Courtesy of University of Delaware, U.S.A. Center for Material Sciences, Department of Chemistry

The monitor attached to instrument was switched on with the PC-SEM software already pre-loaded onto it running as default. The Penning Vacuum Gauge (PVG) icon was clicked to check the vacuum which was expected to be reading a pressure of $9.63 \times 100^{0.05}$ Pa. The Anti-contamination device (ACD) was checked to ensure that it was filled with liquid nitrogen (LN₂), and the stage specimen holder exchange (SSHE) icon was clicked to open the specimen stage and also set the stage to exchange positions. The specimen holder having six (6) holding ports was chosen for this work and the lights on the side of the exchange chamber and in front of the microscope (EXCH POSN) remained "ON". The clip on the side of the chamber was loosened with the vent button flashing; the chamber vented swing door was open; and the sample holder containing the samples were mounted by following the direction of the arrow inscription displayed on the monitor screen; and the rod was pulled down and pushed in completely. The sample imaging was done by following the University of Delaware laboratory instructional manual. The detector used was the secondary electrode detector (SEI) and the current was allowed to reach 10 μ A, This enabled the detector to be noticed and the gun valve to be open. (The cuwas always rest anytime this falls below 8 Ma). The low magnification (LOW MAG) button was pressed to reduce the magnification to the minimum required for this work ($\times 25$). Brightness and contrast were adjusted to desirable levels and the area of interest on the samples were located using the "joystick" and mouse attached to the PC with signal controlled with the SEM instrument. The focusing was carried out using the knob on the console and the LOW MAG turned off.

The reduced view (RDC IMAGE) button was hit to get a better response at higher magnification, while the “Z” in stage control button was used to obtain the desired working distance. The gun was aligned by lowering the magnification (500-1000x) and the probe current increased to maximum (15). The align button was pressed and the “X” and “Y” were used to adjust the brightness to maximum brightness. The STIG button was hit to turn off alignment. Aligning the aperture was done by pressing the WOBB button on the console and the STIG button was hit when done and focused. Stigmatism (STIG), was done to obtain a higher magnification when needed and the picture taking was done by pressing the button Auto Contrast and Brightness (ACB) on the console and pressing the “PHOTO” button which took about 1 minute to scan.

During scanning, the frame was frozen and an adjustment to gray level and gamma was done after this process, with the images taken saved onto a storage device (Thumb-drive).

The instrument was shut down after scanning analysis was done.

2.18 Summary

As shown (see Fig. 2.12) below, synthesis of the Zn-BDC, Zn-NDC and Cu-BTC were successfully synthesized with all instructional details.



Fig. 2.12. *Snapshots of Zn-BDC (MOF-5), Zn-NDC (MOF-8) and Cu-BTC (HKUST-1) after synthesis from CHSR-DSU Laboratory, U.S.A.*

Initially, the procedure of Yaghi, et al was used for the synthesis of Zn-BDC, but however, this was time consuming as it take several days and weeks to synthesize, hence a new method (Rapid solvothermal) was developed. This was successful with comparable surface areas to those attained in other studies using different approaches.

CHAPTER THREE

MATERIAL CHARACTERIZATIONS

3.0 Characterizing the Selected Metal-Organic Frameworks (MOFs)

The results of synthesis and characterizations of material samples used in this work are discussed in this chapter as well as the correlations of the gases (Hydrogen-H₂, Carbon Dioxide-CO₂ and Methane-CH₄) for adsorptions on the synthesized materials, purchased materials and data materials from other studies.

3.1 Obtaining the Optimum Surface Area for Zn-BDC

Knowing the optimum temperature for synthesis and determining surface area is important. Experiments were first carried out under different conditions using different solvents for synthesis and purifications under wide range of temperatures, (see Table 3.1 and Fig.3.1 below). The optimum BET surface area for Zn-BDC and Zn-NDC were found to be 2163 m²/g and 1599 m²/g with corresponding Langmuir surface areas of 2442 m²/g and 1801 m²/g.^{38, 169}

Table 3.1 Getting the synthesis temperature for Zn-BDC, using the rapid solvothermal method

Temperature (°C)	Surface. Area (m ² /g)	Langmuir (m ² /g)
140	41	50
145	910	1030
150	946	1089
155	794	902
160	1004	1137
165	1027	1160
170	2163	2442
175	1005	1137
180	932	1050
185	910	1030
190	378	942

From the various sample analysis it was also possible to determine porosities or pore sizes and pore volumes. These parameters were determined using nitrogen gas adsorptions at 77 K.

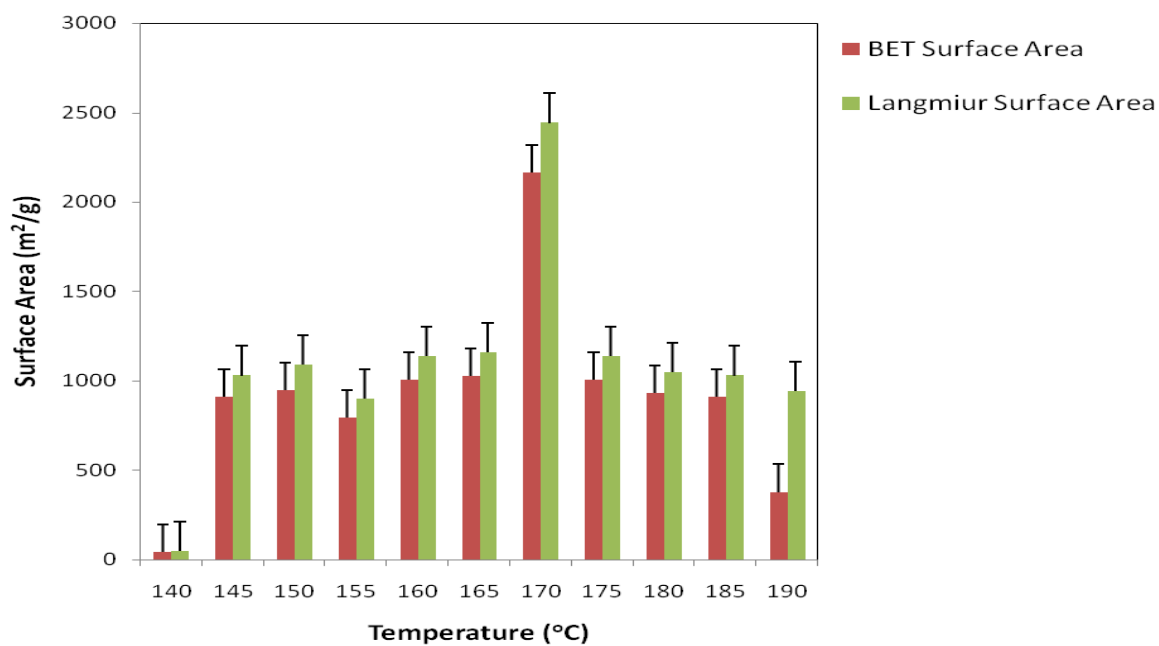


Fig. 3.1 Chart of MOF-5 synthesis for this work, showing various temperature range of synthesis and corresponding error bar

After determining the synthesis temperature which is optimum, it was also important to ensure that the amount of solvent used and time necessary for synthesis was achieved.

Past and recent studies have demonstrated that, MOFs can be made by different methods. Yaghi et al., (2002),¹⁰⁷ published a BET surface area for Zn-BDC of 2296 m²/g and a Langmuir surface area of 3840 m²/g.¹⁰⁷ Also in 2006, Panella et al.,¹⁴⁴ reported a high surface area for Zn-BDC to be same as that of Yaghi et al., (2002). But in the previous year (2005) he found that same material (Zn-BDC) had a BET surface area of 572 m²/g and a Langmuir surface area of 1014 m²/g using a different approach.^{144, 170} More work has been done with Zn-BDC than with any other metal-organic frameworks. In this thesis work, Zn-BDC has been easily and successfully synthesized and classified by using a shorter methods of synthesis such as the Rapid Solvothermal Method. This is more shorter than some other methods like microwave synthesis, solvothermal synthesis and so on, which possibly take from days to weeks.

3.2 Obtaining the Thermal Stabilities (TGA) of Synthesized MOFs

Obtaining their stabilities under thermal stress was performed for all the MOFs (both synthesized and the commercial). Their ability to withstand heat up to a given temperature was determined using TGA as shown in Fig. 3.2. During this process, there was a weight loss as the result of the elimination of guest molecules including water, which were used during the synthesis.

For the Zn-BDC, Zn-NDC and Cu-BTC, the initial slight drop of about 15 wt.% was probably due to the evaporation of guest molecules which were used during synthesis,

Zn-BDC was found to be stable up to 320 °C, while Zn-NDC was found to be stable up to 200 °C, and Cu-BTC was stable up to 270 °C.

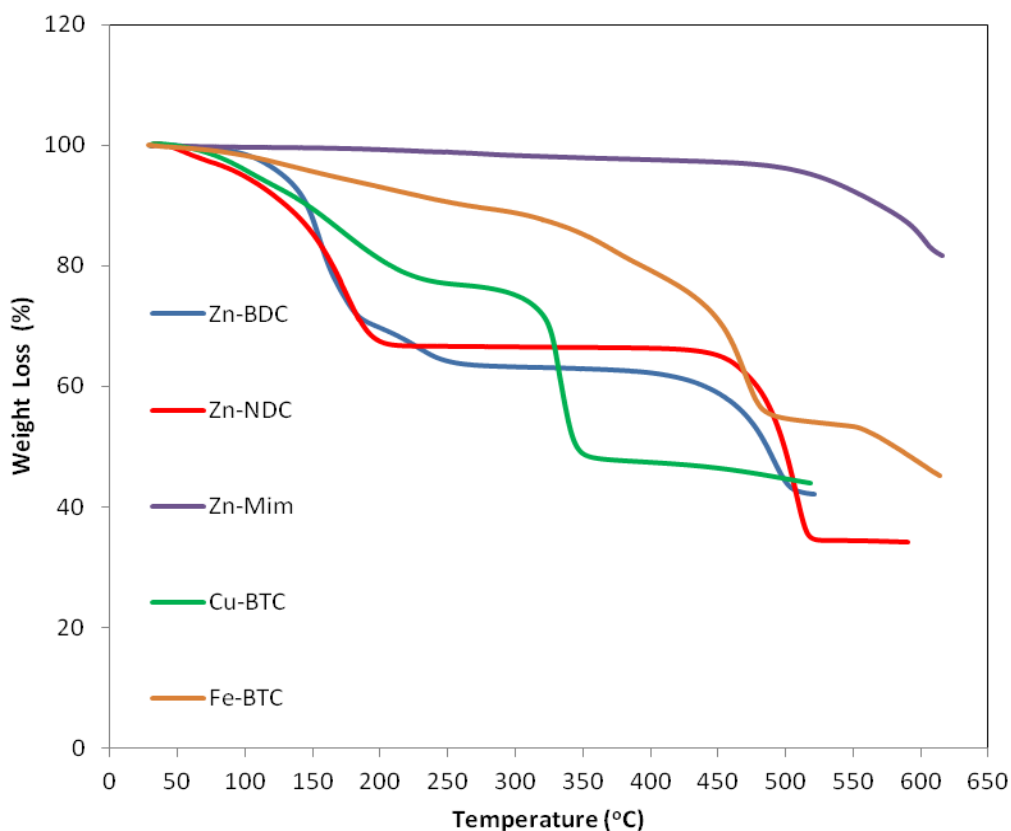


Fig. 3.2 Thermogravimetric (TGA) plots for synthesized and purchased MOFs used in this work

Most of the synthesized MOFs followed almost same pattern towards their final degradation under thermal stresses. Zn-BDC, Zn-NDC and Cu-BTC from Fig. 3.2., show a two steps trends. The first step shows loss due to crystallization, while the second step is attributed to the distortions or disappearance of the framework structure. These, according to Fig. 3.2, occurred at temperatures: $T > 320 > 270 > 200$ (°C) for Zn-BDC, Cu-BTC and Zn-NDC respectively.

The commercial MOFs materials Fe-BTC and Zn-Mim had a single-step pattern. However, their stabilities were found to be in the upper 90th percentile when compared with the manufacturers' charts. More also, Lin et al.,³¹ used these concepts to demonstrate that, materials having higher thermal stability will be useful for various applications such as hydrogen gas storage. This is because metal-organic frameworks are much lighter weight materials than hydrides.¹⁷¹

3.3 XRD Spectra of Synthesized MOFs

The powder XRD patterns of Cu-BTC, Zn-BDC and Zn-NDC, synthesized for this work using the ball-milling method for Cu-BTC and the rapid-solvothermal method for Zn-BDC and Zn-NDC, revealed the formation of the desired product in temperature range between 150 °C and 175 °C for Zn-BDC and Zn-NDC. Other published studies like Hafizovic et. al., Yaghi et. al, Wu et. al, have demonstrated that, Zn-BDC, despite its inconsistencies, normally has its product formation peak between 9.1 and 10.8 degrees 2-theta (2θ) angle¹⁷²⁻¹⁷⁴. The results from this work for Zn-BDC, using the rapid-solvothermal method, (See Fig 3.3) were in complete agreement with those obtained for this particular metal-organic framework no matter how it was synthesized. Also apart from their peak values (2θ), their aspect ratios (R_1 , R_2 and R_3), peak intensities, as well as their d -spacing, obtained from form other literatures, confirm that Zn-BDC was fully synthesized in this work using a new method of synthesis (Rapid Solvothermal).³⁴

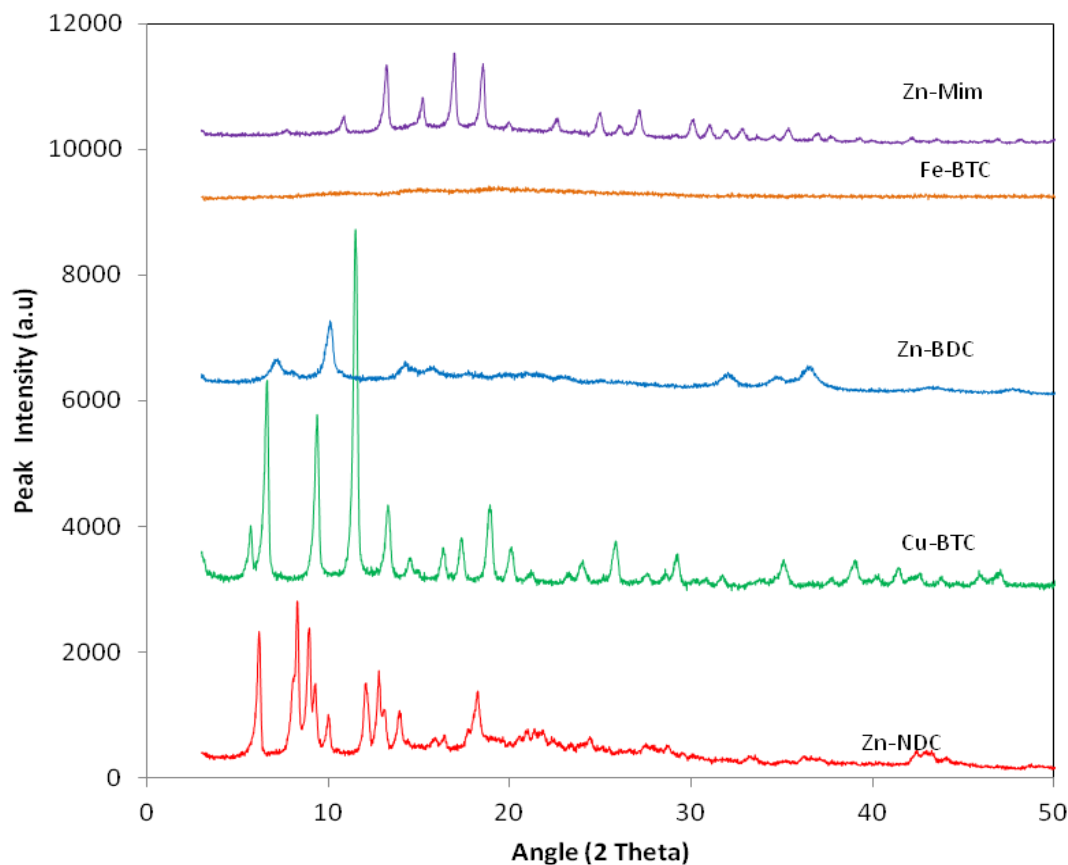


Fig. 3.3 XRD patterns for Cu-BTC, Fe-BTC, Zn-Mim, Zn-BDC and Zn-NDC for this work showing their peak intensities versus 2θ -angle.

The peaks for Zn-BDC, typically occur between 6.30 and 8.44 degrees as reported in the published work by Yaghi et al., and Yao et al.,^{107, 150} These were in agreement with this work. Another resemblance of this work to other literature reports is that Zn-NDC has diffraction pattern characteristics of six peaks which include the typical peaks earlier stated and reported by Yaghi et al.

The iron metal based MOF (Fe-BTC), tends to have an amorphous-like XRD diffraction pattern. As a result, there are no peaks for this material in the XRD pattern in Fig. 3.3. Other literature data reported similar findings due to homogeneous phase crystals that may show different diffraction patterns under different preparing conditions¹⁷⁵.

3.4 Laser Diffraction Particle Size Analysis (LDPSA) of Studied MOFs

To better understand how the synthesized MOFs particle sizes differ in terms of their particle distributions, the particle size were measured using a laser diffraction particle sizes analyzer (SALD-2201). Zn-NDC samples had particle diameters in the range of 9.49–114 μm (average of $43.27 \pm 0.42 \mu\text{m}$), Zn-BDC lies in the range of 19.97-116- μm (average of $32.31 \pm 0.29 \mu\text{m}$), see Table 3.2. Temperature or pressure differences during synthesis are conditions that might have effects on MOFs. For some synthesis of MOFs, like the solvothermal, and Fig. 3.4 shows particle size of MOFs in this study.

Table 3.2 Particle sizes for the synthesized and purchased MOFs used for this work

<i>Sample</i>	<i>Other Name(s)</i>	<i>D(50) μm</i>	<i>Std.Dev.</i>
Zn-BDC	IRMOF-1 [MOF-5]	32.31	± 0.29
Zn-NDC	IRMOF-8 [MOF-8]	43.27	± 0.42
Cu-BTC	MOF-199 [HKUST-1]	36.36	± 0.38
Zn-Mim	ZIF-8 (Z1200)	14.93	± 0.36
Fe-BTC	F300	11.61	± 0.28

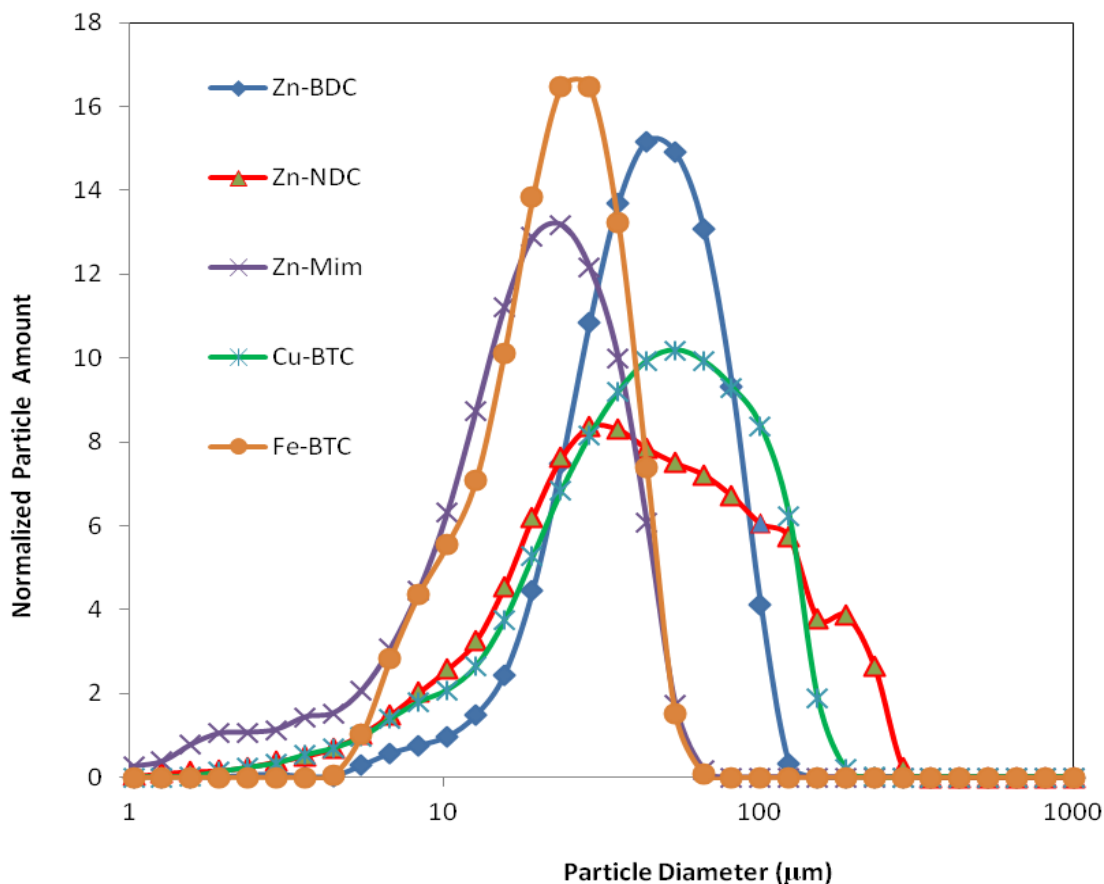


Fig. 3.4. Particle distributions for the three synthesized MOFs and the two commercial MOFs used in this study

3.5 Scanning Electron Microscope (SEM)

The surface morphologies of all the MOFs were viewed using the JEOL JSM 7400F. These MOFs were shown under different detectors, working distance and magnification to conform to other literature studies. Zn-BDC and Zn-NDC sample surface morphologies seems to have a spongy out-look. This is a possible reason for their high surface areas. The copper containing MOFs and the iron containing MOFs both have the same organic linker and they seems to have a common characteristics between them.

They both have smooth surface and edges in terms of their morphologies see Fig 3.5 - 3.9 for the MOFs used in this work.

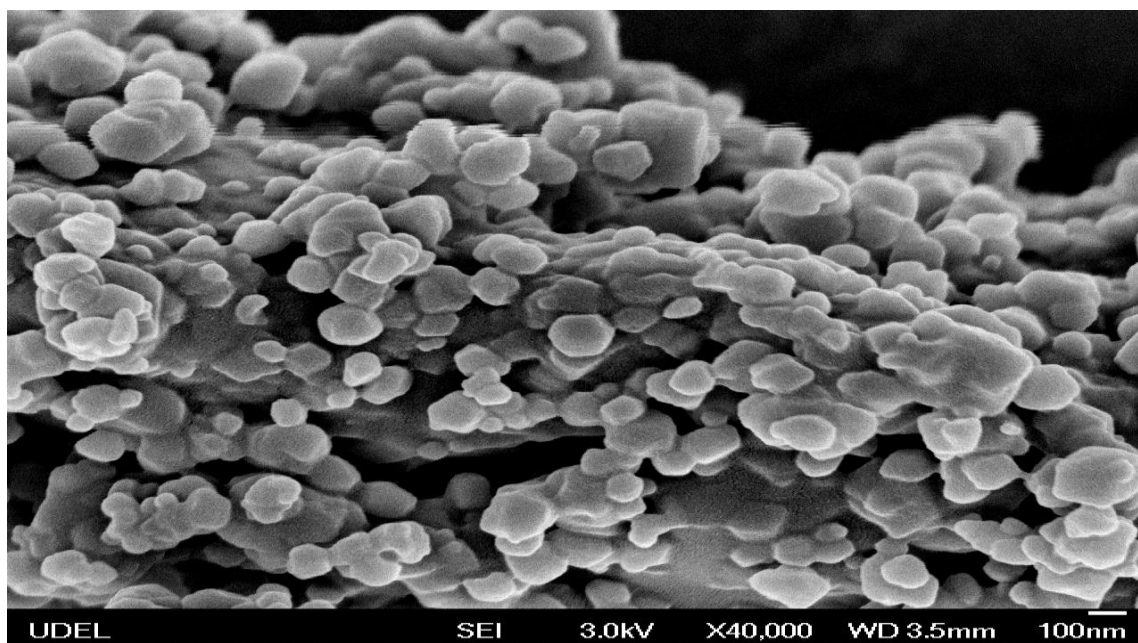


Fig. 3.5. SEM capture photo for Zn-Mim MOF for this work

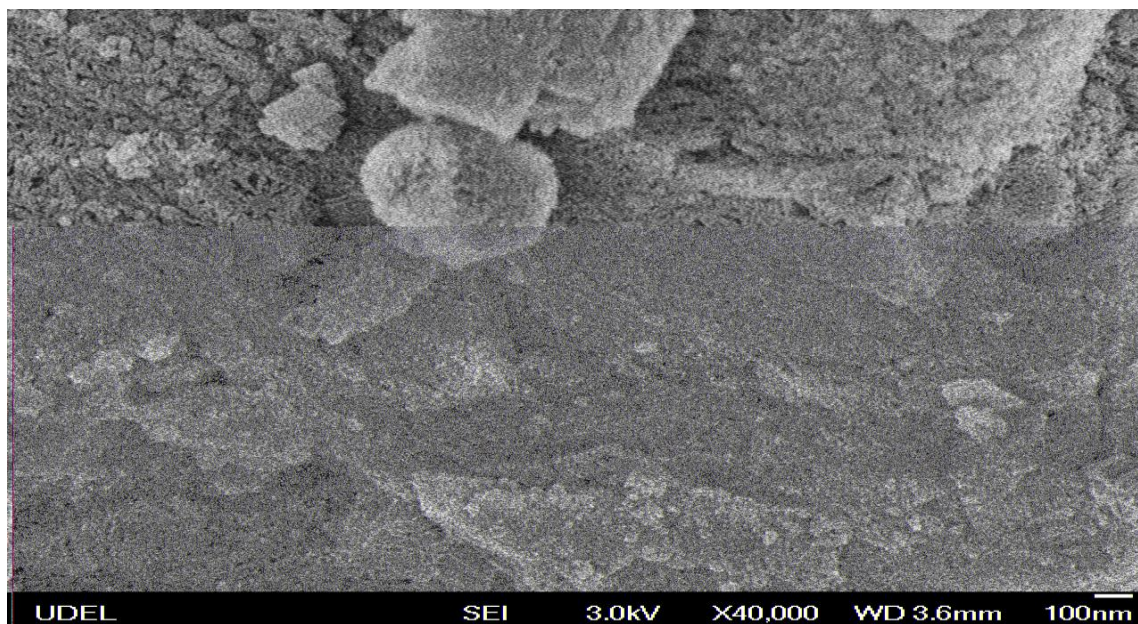


Fig. 3.6. SEM capture photo for Zn-NDC MOF for this work

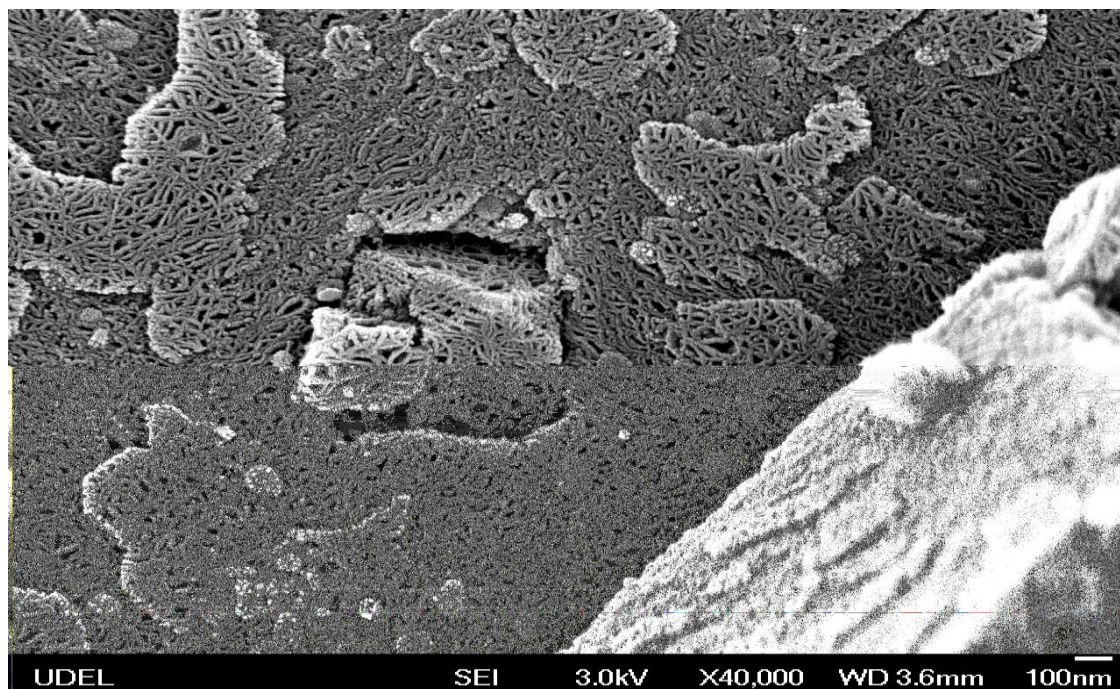


Fig. 3.7. SEM capture photo for Zn-BDC MOF for this work

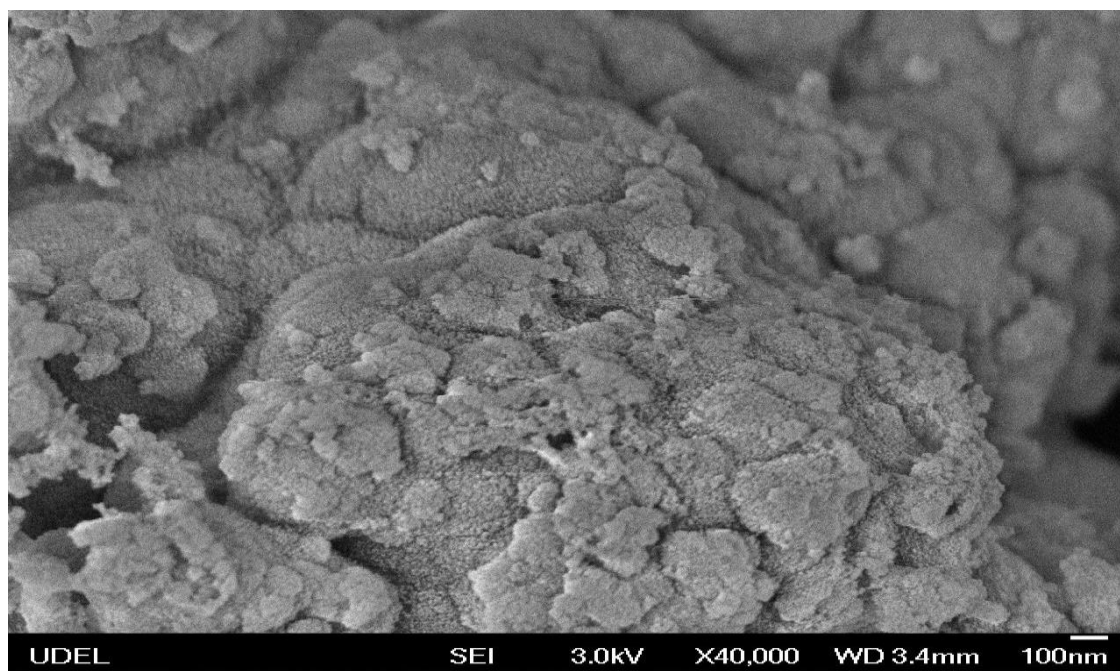


Fig. 3.8 SEM capture photo for Fe-BTC MOF for this work

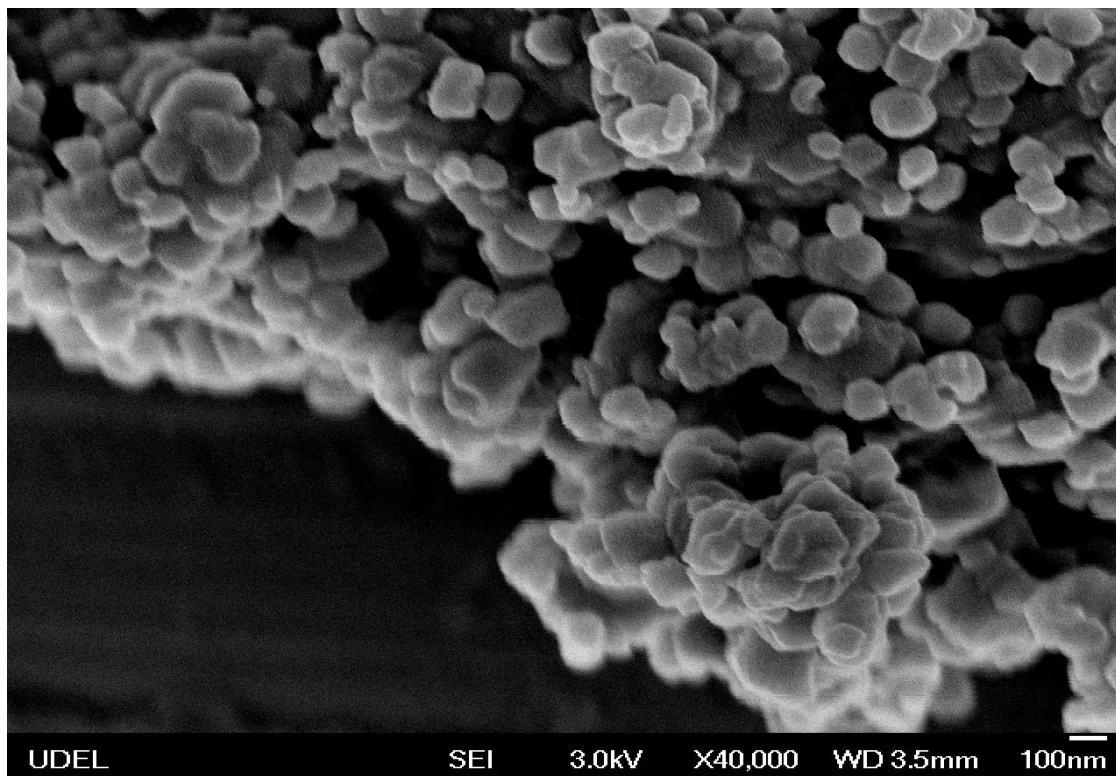


Fig. 3.9. SEM capture photo for Cu-BTC MOF for this work

3.6 Fourier Transformed Infrared Spectroscopy (FTIR) for Studied MOFs

Solid- state infrared spectroscopy was carried out at ambient conditions. Fig.3.10 contains the bands for the synthesized and purchased MOFs. Near 1700 cm^{-1} There are IR bands of the carbonyl functional group of the ligands. The IR bands of the synthesized and purchased MOFs were identical to what was expected although these were not shown in the figure. The absence of carbonyl (C=O) stretching vibration IR bands between 1650 and 1730 cm^{-1} in Fig. 3.10 shows that, the H_2NDC was fully coordinated. Hence the IR bands recorded at 1660 cm^{-1} , 1617 cm^{-1} , 1589 cm^{-1} , 1410 cm^{-1} , 1360 cm^{-1} , 1200 cm^{-1} , 1106 cm^{-1} , 788 cm^{-1} are in agreement with the literature spectral from other studies.^{48, 102,}

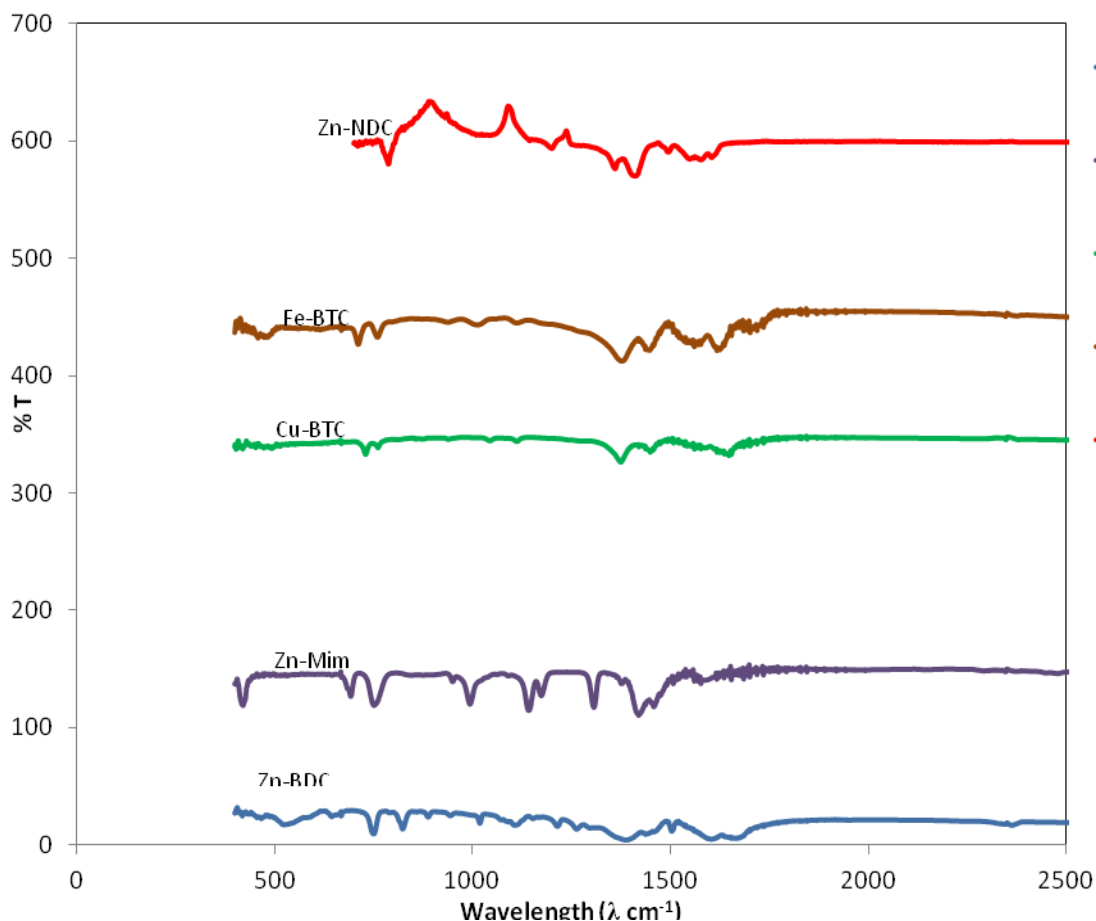


Fig. 3.10. IR-band spectra for synthesized and purchased MOFs used in this work

3.7 Surface Areas and Pore Volume for Studied MOFs

Surface areas and pore volumes were determined volumetrically from N₂ adsorption–desorption isotherms at 77 K, for the six MOFs that were prepared or purchased for this work (see Table 3.3, Fig 3.11a and Fig. 3.11b) shows the obtained BET surface area and the graphical relationship between surface area of the MOFs and their corresponding pore volumes.

Fig. 3.11a contains BET isotherms that were obtained using the porosity analyzer (ASAP 2020). Table 3.3 shows relational trends between the pore volume at 0.5 cm³/g of the

synthesized metal-organic frameworks materials and their corresponding surface area of these materials. Pore volumes are known to play a role in addition to surface area, during gas adsorptions by metal-organic frameworks.

Table 3.3 Showing both synthesized and purchased MOFs surface area and pore volume at 50 cm³/g

MOFs	Surf. Area (m ² /g)		PS@0.50 (nm)	PV@0.50 (cm ³ /g)
	BET	LANG		
Zn-BDC	2163	2442	1.61	0.87
Zn-NDC	1599	1801	1.60	0.63
Cu-BTC	1398	1622	1.66	0.58
Zn-Mim	1581	1767	1.62	0.64
Fe-BTC	1031	1248	1.70	0.43

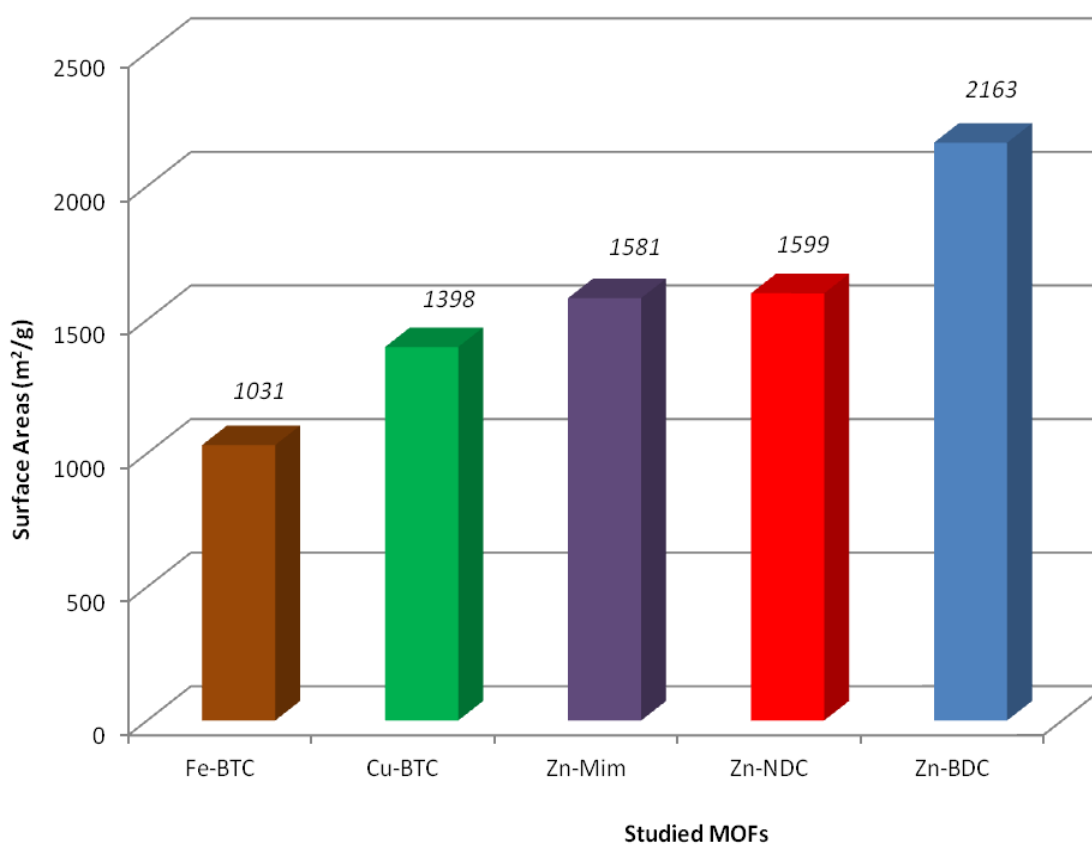


Fig. 3.11a. Graph of surface area for synthesized and purchased MOFs

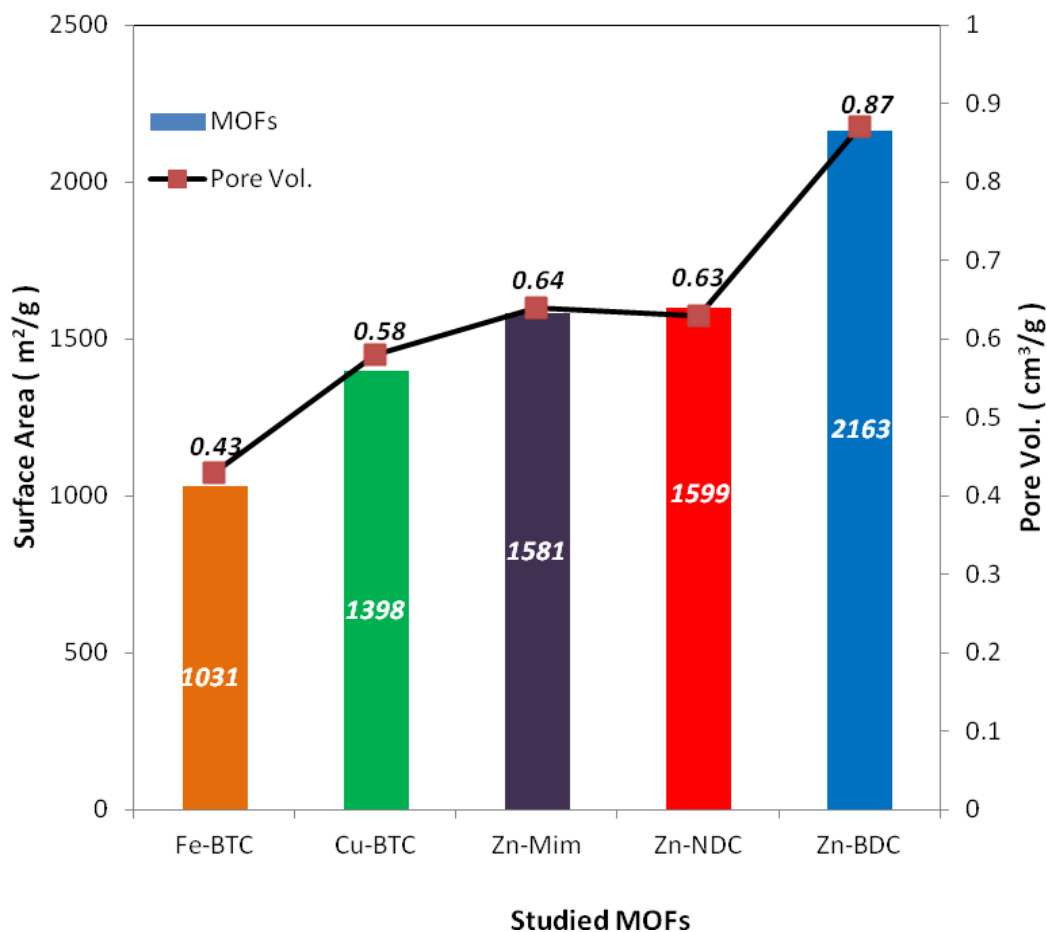


Fig. 3.11b. Graph of surface area and pore volume for synthesized and purchased MOFs

3.8 Surface Area and Gas(es) Adsorption Isotherms

The BET surface area, Langmuir surface area, pore volume and pore sizes were determined for different MOFs, under low pressure (mmHg/atm.) using nitrogen gas (see Fig. 3.12). Both low and high pressures at different temperatures of 77 K, 195 K, 273 K and 298 K were used to determine the adsorption capacities of three gases - hydrogen (H₂), carbon dioxide (CO₂) and methane (CH₄) on Zn-BDC, Zn-NDC, Cu-BTC, Zn-Mim, and Fe-BTC. The results and isotherms for these gases are displayed in subsequent

chapters (i.e chapter 4, 5, and 6) of this research dissertation. Krawiec et al., (2006)¹⁵¹ reported that, Cu-BTC has a surface area and pore volume of 1239 m²/g and 0.62 cm³ respectively.¹⁵¹

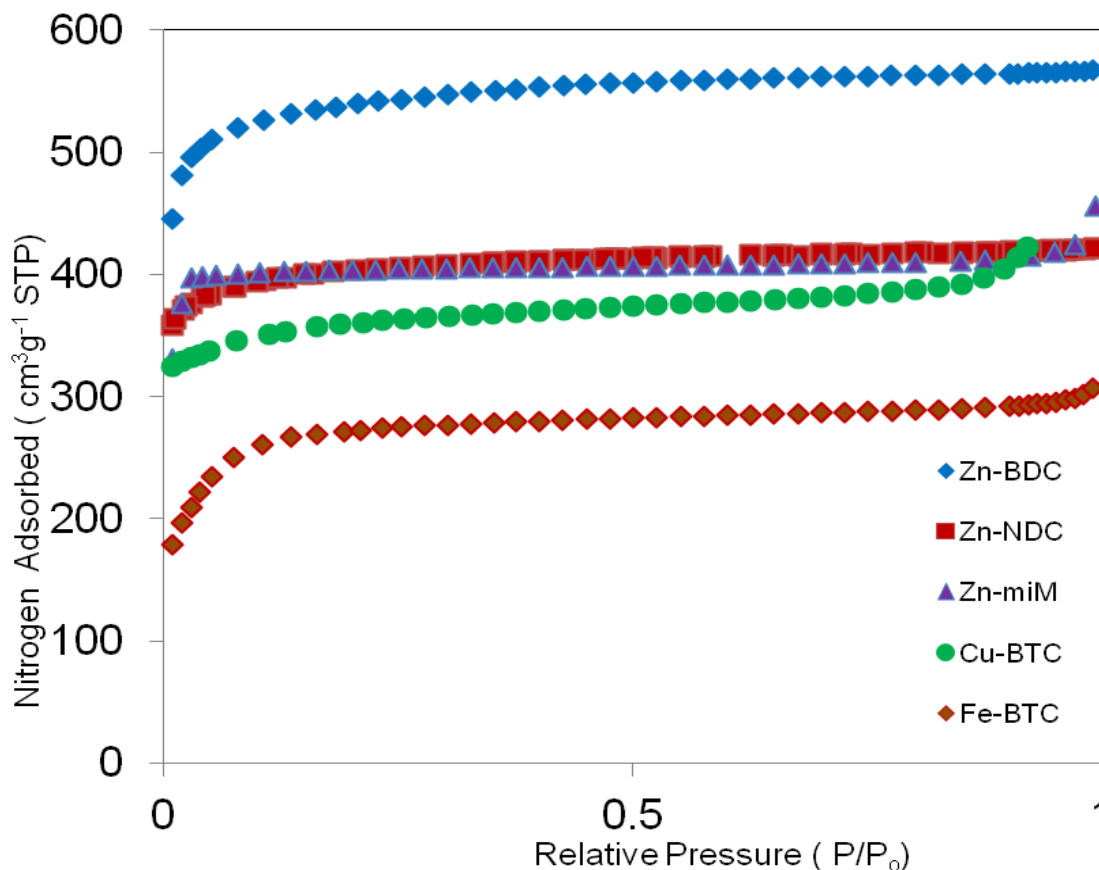


Fig. 3.12. BET- Isotherms for synthesized and purchased MOFs for this studies

Also Cu-BTC has shown a BET surface area, of 1507 m²/g with a Langmiur surface area of 2175 m²/g and a 0.75 cm³ pore volume.¹⁴⁴ A high surface area for this MOF was reported in 2006 by the Yaghi's group to be 1944 m²/g and 2260 m²/g for its BET and Langmiur surface area respectively.¹⁷⁶ A ball-milling method with the assistance of solvents during synthesis (a method called “mechanochemical assist synthesis)³⁶ was

used to obtain a BET value of 1398 m²/g and Langmuir of 1622 m²/g. Its pore size and pore volume were 1.66 nm and 0.88 cm³/g respectively.

For Zn-NDC, previous studies show that this material has a BET surface area of 890 m²/g, and pore volume of 0.45 cm³/g a result published by Krawiec et al.¹⁵¹

While Rowsell et al.,(2004), found that this same MOF to have a BET surface area of 1466 m²/g using a solvothermal reaction and purification with chloroform as the solvent.¹³ The results on Zn-NDC from this work show a higher surface area as well as shorter time for synthesis.^{38,48}

Zn-BDC is the oldest and most extensively studied MOFs. Many studies have been carried out on this MOF and there are on-going studies on it. Some of these results indicate that Zn-BDC has a BET surface area of 3800 m²/g and a Langmuir surface area of 4400 m²/g (Yaghi et al 2007).¹⁴⁶ In 2004, Dybtsev et al., found this MOF to have a BET surface area of 1450 m²/g, while Lee et al., (2007) reported a BET surface area of 1794 m²/g.^{177, 178} The result for this work showed a BET surface area of 2163 m²/g by using the rapid solvothermal method. However the solvent used for the synthesis and purification were different so also were other adjustments in procedures made during its synthesis. The commercial MOFs obtained from Sigma-Aldrich were shown to corresponding to same expected results obtained from the vendor's charts in terms of their characterizations.

3.9 Summary

The synthesized MOFs materials- Zn-BDC, Zn-NDC, and Cu-BTC and also the purchased MOFs materials- Fe-BTC and Zn-Mim were all successfully characterized

using different instruments. Parameters such as thermal stabilities, surface areas, dispersion in aqueous solvent, peak intensity formation based on their powder diffractions using a diffractometer and many more were determined. Their surface areas were also found to be comparable with those in other studies even though a new method of synthesis such as the rapid solvothermal analysis and mechano-chemical assisted synthesis were carried out for all of the MOFs.

CHAPTER FOUR

HYDROGEN GAS ADSORPTIONS

4.0 Sticking Efficiency (θ) the Concept

The way in which hydrogen interacts with the surfaces (binding energy) may also affect adsorption.¹⁵⁷⁻¹⁵⁹ Therefore a new parameter denoted the sticking factor (θ) was developed with the hope that it would correlate better with the wt% hydrogen adsorbed than surface area. The sticking factor (defined as the percent gas adsorbed per m² of surface area per gram of material) was calculated for each gas based on the following eq. 4.0.

$$\theta = \frac{Q_{ads}}{S_{SA}} \times \frac{N_A}{M_{mm}} \quad (4.0)$$

Where Q_{ads} is the weight percentage of gas adsorbed, S_{SA} is the surface area of the MOF in m²/g, N_A is Avogadro's number and M_{mm} is the molar mass of the adsorbed gas.¹⁶⁶ Since the sticking factor is the percentage of hydrogen gas adsorbed per unit area of surface, it actually represents the efficiency with which the molecules are able to bind stick onto the surface. If a material has a large surface area but, due to the nature of the binding sites, has low sticking efficiency, then it is possible that it will absorb a relatively small amount of hydrogen. The sticking factors calculated from Eq.(4.0) are given in Table 4.1 for all of the MOFs included in this work. The weight percents and surface areas used to compute sticking efficiencies (θ) are also included in the tables.

Table 4.1 Low Pressure (LP) and High Pressure (HP) values for hydrogen gas adsorptions on selected MOFs along with their BET surface area and corresponding sticking efficiencies

MOFs	BET ² (m ² /g)	Wt. % (@ 77 K)	Stic. Eff. (@ 77 K) ²⁰ x10	Wt. % (@ 196K)	Stic. Eff. (@ 196K) ²⁰ x10	Wt. % (@ 273K)	Stic. Eff. (@ 273K) ²⁰ x10	Wt. % (@ 298K)	Stic. Eff. (@ 298K) ²⁰ x10
Zn-BDC	2163	1.40(LP)	1.93(LP)	0.027(LP)	0.038(LP)	0.009(LP)	0.012(LP)	0.005(LP)	0.006(LP)
		3.72(HP)	5.13(HP)	1.78(HP)	2.45(HP)	0.95(HP)	1.30(HP)	0.50(HP)	0.69(HP)
Zn-NDC	1599	1.74(LP)	3.24(LP)	0.031(LP)	0.058(LP)	0.009(LP)	0.017(LP)	0.010(LP)	0.02(LP)
		3.16(HP)	5.89(HP)	1.08(HP)	2.01(HP)	0.66(HP)	1.23(HP)	0.45(HP)	0.84(HP)
Zn-Mim	1581	1.26(LP)	2.37(LP)	0.017(LP)	0.031(LP)	0.006(LP)	0.011(LP)	0.004(LP)	0.008(LP)
		3.39(HP)	6.32(HP)	1.26(HP)	2.34(HP)	0.66(HP)	1.23(HP)	0.39(HP)	0.73(HP)
Fe-BTC	1031	0.89(LP)	2.57(LP)	0.022(LP)	0.064(LP)	0.006(LP)	0.017(LP)	0.003(LP)	0.008(LP)
		3.15(HP)	9.10(HP)	1.57(HP)	4.54(HP)	0.61(HP)	1.76(HP)	0.72(HP)	2.08(HP)
Cu-BTC	1398	2.00(LP)	4.26(LP)	0.042(LP)	0.089(LP)	0.011(LP)	0.023(LP)	0.008(LP)	0.017(LP)
		3.56(HP)	7.59(HP)	1.68(HP)	3.58(HP)	0.81(HP)	1.72(HP)	0.60(HP)	1.28(HP)

4.1 Relationship Between Surface Area (S_{SA}) and Sticking Efficiency ($S(\theta)$)

The relationship of the sticking efficiency (Θ) to BET surface area is inversely proportional as shown in Fig. 4.1. From the fig, it can be clearly seen that, as BET surface area of a material decreases, its sticking efficiency increases.

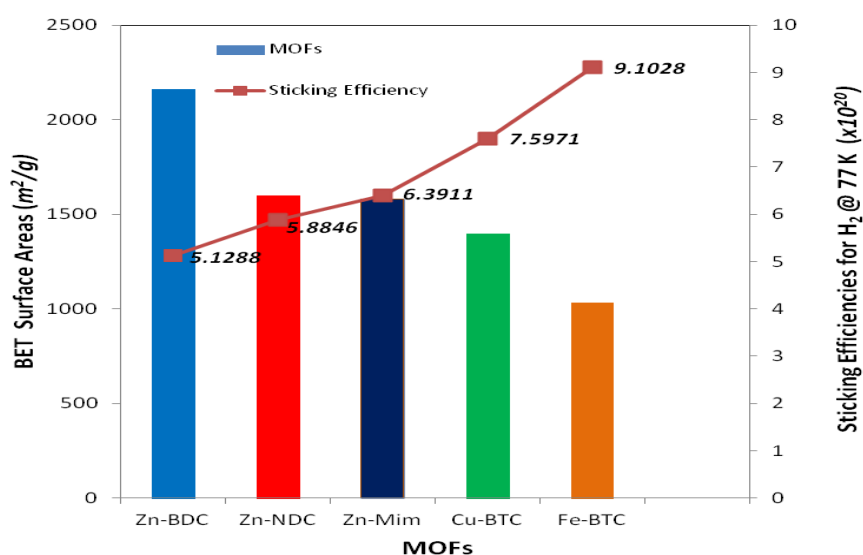


Fig 4.1. Chart showing relationship between BET surface area and sticking efficiencies for hydrogen (H_2) at liquid nitrogen temperature (77 K) under high pressure

4.2 Hydrogen Adsorptions and Isotherms

In addition to the five (5) MOFs that were prepared or purchased for this work, data for twelve (12) others were obtained from the literature. These MOFs contain a variety of linkers and metal clusters. With the additional data from the literature, it should be possible to make meaningful comparisons among the MOFs to determine what correlations exist in their properties. It is of particular interest to determine what effect factors such as the nature of the linkers and metal clusters may have on the hydrogen adsorption capacities of these MOFs.

During adsorption of gas(es), a graphical representation showing the various amounts (weight percent, wt%) of gas(es) adsorbed at each pressure gradient either low or high pressure during different temperature ranges. These are represented by lines drawn from point to point called isotherms. These isotherms are expected to be saturated under high pressures and no-saturations are expected during low pressures especially at room temperatures. Figs 4.2 - 4.5 show isotherms of the studied MOFs from this work at low pressures under different temperatures. For each isotherm, the weight percentage of hydrogen adsorbed up to a pressure of 1 atmosphere was determined. The results are given in Table 4.2 along with data for the 12 MOFs that were selected from the literature. It is apparent that the MOFs have a wide range of adsorption capacities ranging from a high of 3.05 wt% for PCN-12 to a low of 0.88 wt% for IRMOF-18 at 77 K and 1 bar (see Table. 4.2). A plot of wt% versus surface area was made in order to determine if any correlation exists between these two parameters. The plot shows that a correlation exists but that there is a fairly large amount of scatter in the data points. A correlation

coefficient (R^2) was used to represent the degree of scatter in the data points. A value of $R^2 = 1$ would represent perfect correlation whereas $R^2 = 0$ would represent no correlation. In this case (3-synthesized and 2-purchased MOFs), R^2 was 0.0686 for BET surface area at LN_2 versus $R^2 = 0.5738$ of the sticking efficiency. A possible reason for the relatively low correlation coefficient may be the fact that the surfaces in these MOFs are not uniform. They contain a variety of different linkers, metal sites and structures. The different affinities of hydrogen for each of these surfaces may be responsible for the scattered pattern. The amount of hydrogen gas adsorbed on the materials was determined from their various isotherms under low and high pressure (see Fig. 4.2 and Fig. 4.6). Under low pressure and at liquid nitrogen temperature (77 K), the MOF containing copper (Cu) has the highest adsorbing percent weight of two (2 wt.%) compared to the other synthesized or purchased MOFs. While the MOF containing Fe-metal was having the lowest weight percent of 0.89 which is approximately 0.9 wt. %, see Table 4.1 for all data on the BET surface areas and weight percent.

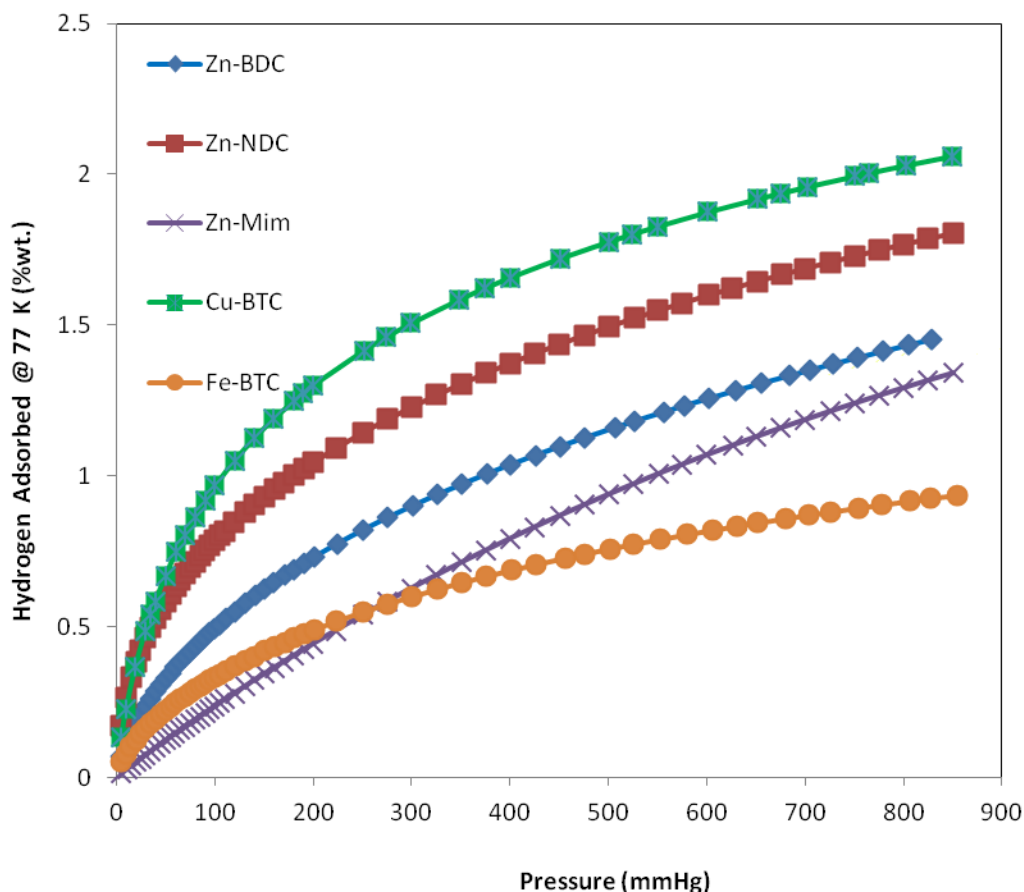


Fig. 4.2 Hydrogen adsorptions Isotherms at low pressure (77 K) for MOFs used in this work

Under low pressures except at room temperatures (298 K), Cu-BTC has the highest adsorption weight percentage as compared to the other studied MOFs. A clear characteristic property of Cu-BTC is that, it is known to possess open metal-sites. Because of its low surface area of $1398 \text{ m}^2/\text{g}$ when compared to Zn-BDC having $2163 \text{ m}^2/\text{g}$, the copper based MOF was expected to store less gas adsorption compared to others. But from this research, a pattern was discovered that, the BET surface area of a material does not necessarily correlate with the amount of gas that can be adsorbed. At room temperature, the binding energies between hydrogen and the MOFs were found to be comparable to their thermal vibration energies, which is known to lead to a very poor

hydrogen gas uptake (typically < 1 wt.%). This has made the comparison and discussion of hydrogen uptake capacity ambiguous and somehow difficult.¹

However, at cryogenic conditions, the relatively strong interactions between gas and MOFs gives rise to greatly enhanced adsorption of hydrogen gas.

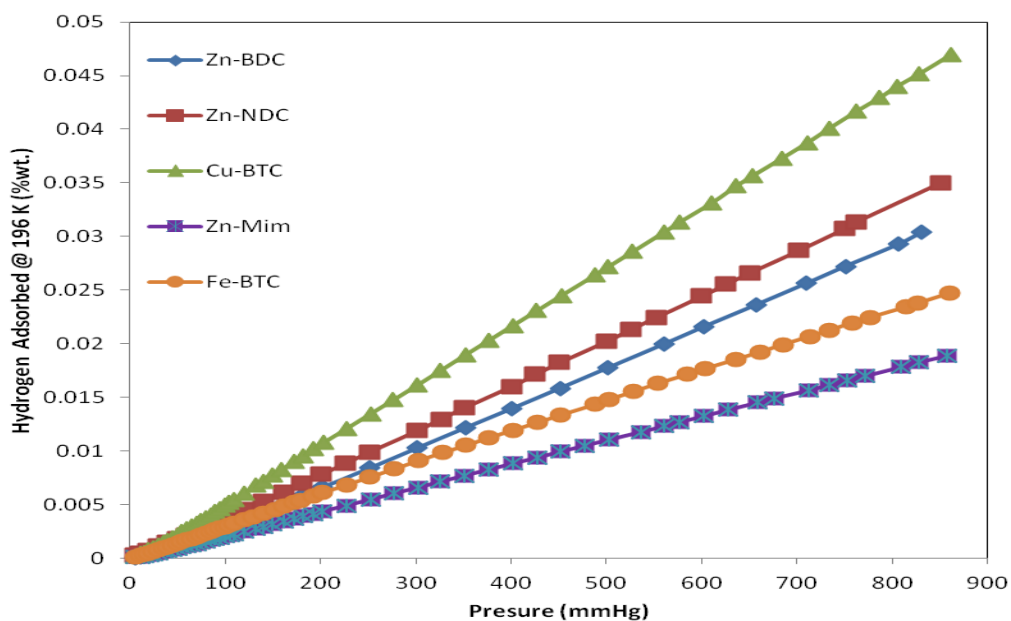


Fig. 4.3. Hydrogen adsorptions Isotherms at low pressure (196 K) for MOFs used in this work

Under high pressure, Zn-BDC has a high adsorbing ability with a weight percent of 3.72 (see table 4.1) and the Fe-containing MOF still remain the low having approximately, 3.15 wt.% under liquid nitrogen temperature (77 K).

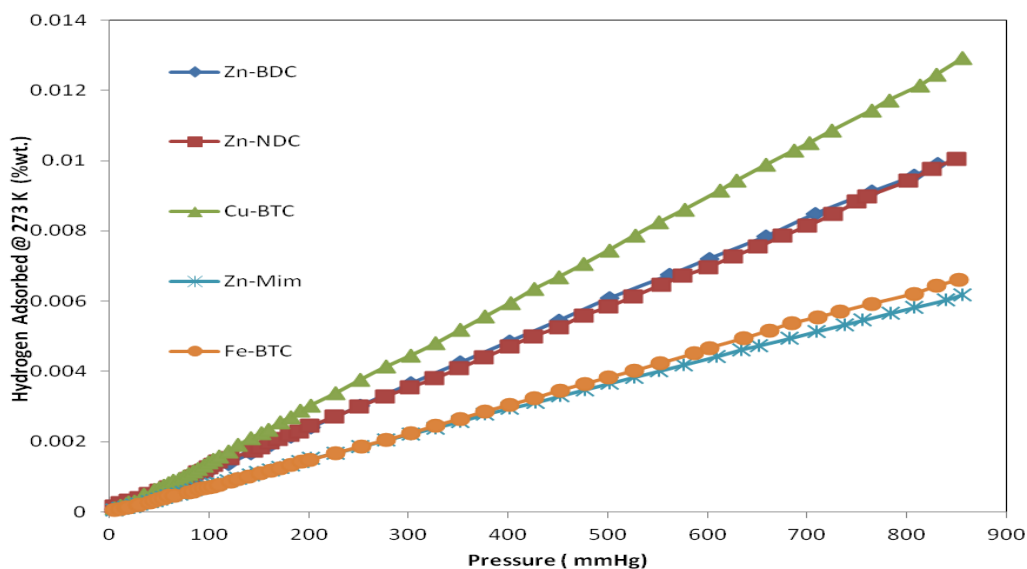


Fig. 4.4. Hydrogen adsorptions Isotherms at low pressure (273 K) for MOFs used in this work

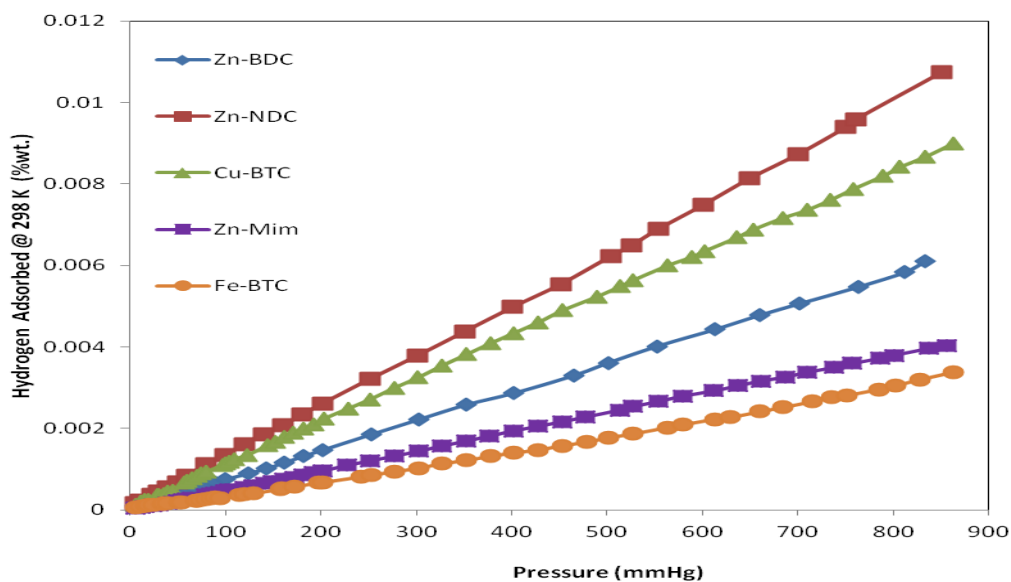


Fig. 4.5. Hydrogen adsorptions Isotherms at low pressure (298 K) for MOFs used in this work

Meanwhile, Cu-BTC was found to have the highest hydrogen gas adsorption at 77 K under low pressure with a value of 2.00 weight percent (wt.%), while Fe-BTC had the lowest with 0.89 wt.%. The studied MOFs weight percentage for the adsorption of

hydrogen under low pressure and at liquid nitrogen temperature are in the descending order of Cu-BTC>Zn-NDC>Zn-BDC>Zn-Mim>Fe-BTC with their corresponding gas adsorption amount of 2.0 wt.%; 1.7 wt.%; 1.4 wt.%; 1.26 wt.%; and 0.89 wt.%. The same trend was found for this descending order at different temperatures of 77 K; 196 K; 273 K; and 298 K.

However, previous and current studies have shown that, saturations doesn't occur under low pressure (< 760 mmHg) as well as ice (273 K) and room temperatures (298 K). The values are listed in Table 4.2 along with data for the 12 additional MOFs that were obtained from the literature. There is a wide range of surface areas from a high of 2300 for UMCM-150 to a low of 420 m²/g for CUK-2. As expected, the MOFs with high surface areas also have high pore volumes. There does not seem to be any relationship between linker size and surface area. For example, Zn-BDC has just one benzene ring in its linker and it has a relatively high surface area of 2163 m²/g whereas CuK-1 and CuK-2 also have one benzene ring with relatively low surface areas. PCN-17 has a relatively large linker with four (4) benzene rings but it has a BET surface area of only 820 m²/g. There also does not seem to be a relationship between the nature of the metal cluster and surface area. For example, the Zn-containing MOFs have surface areas ranging from 2163 to 783 m²/g.¹⁶⁹

Table 4.2 Hydrogen adsorption analysis data at 77 K under low pressure

MOFs	Metal	Organic Linker	Surface Area (m ² g ⁻¹)	H ₂ / 77 K / 1 bar (wt.%)	Sticking Efficiency (x10 ²⁰)	ΔH (kJ/mol)	Ref.
Zn₄-BDC	Zn	<i>H₂bdc</i>	2163	1.40	1.94	5.8	<i>This work</i>
Zn-NDC	Zn	<i>H₂ndc</i>	1599	1.74	3.24	6.0	<i>This work</i>
Zn-Mim	Zn	<i>2-mim</i>	1581	1.26	2.38	5.4	<i>This work</i>
Cu-BTC	Cu	<i>1,3,5-btc</i>	1398	2.00	4.27	7.3	<i>This work</i>
Fe-BTC	Fe	<i>1,3,5-btc</i>	1031	0.89	2.58	5.4	<i>This work</i>
CUK-1	Co	<i>2,4-pdc</i>	630	1.60	1.23	-	179
CUK-2	Co	<i>6-mna</i>	420	0.66	1.21	-	179
TUDMOF-1	Mo	<i>1,3,5-btc</i>	1280	1.75	4.08	-	180
PCN-10	Cu	<i>H₄aobtc</i>	1407	2.34	4.96	-	181
PCN-11	Cu	<i>H₄sbtc</i>	1931	2.55	3.94	19.1	181
PCN-12	Cu	<i>H₄mdip</i>	1943	3.05	4.68	-	181
PCN-12'	Cu	<i>H₄mdip</i>	1577	2.4	4.54	-	181
PCN-17	Yb	<i>H₃tatb</i>	820	0.94	3.42	-	182
IRMOF-18	Zn	<i>tmbdc</i>	1501	0.88	1.75	-	13
UMCM-150	Cu	<i>H₃bptc</i>	2300	2.1	2.72	7.3	183
Cu-BTT	Cu	<i>H₃btt</i>	1710	2.42	4.22	-	184
MOF-74	Zn	<i>dhtp</i>	783	1.75	6.66	8.3	153

The high pressure for this work was also carried out for the synthesized MOFs as well as some computational sited literature studies (see Table 4.3). Fig. 4.6 to Fig. 4.9 contain isotherms that were done using different temperature gradients to determine their gas adsorptions. The isotherms under liquid nitrogen (77 K) show saturation or plateau occurrences, unlike the dry ice (196 K), ice (273 K) and the room (298 K) temperatures which shows no saturations by these MOFs.

Table 4.3 High Pressure Hydrogen adsorption analysis data at 77 K

MOFs	Metal	Organic Linker	Surface Area (m ² g ⁻¹)	H ₂ / 77 K / >1 bar (wt.%)	Sticking Efficiency (x10 ²⁰)	Ref
Zn-BDC	Zn	<i>H₂bdc</i>	2163	3.72	5.13	<i>This work</i>
Zn-NDC	Zn	<i>H₂ndc</i>	1599	3.16	5.89	<i>This work</i>
Zn-Mim	Zn	<i>2-mim</i>	1581	3.39	6.3	<i>This work</i>
Cu-BTC	Cu	<i>1,3,5-btc</i>	1398	3.56	7.59	<i>This work</i>
Fe-BTC	Fe	<i>1,3,5-btc</i>	1031	3.15	9.10	<i>This work</i>
MIL-53(Cr)	Cr	<i>BDC</i>	1100	3.1	8.4	185
Fe-pbpc	Fe	<i>pbpc</i>	1200	3.05	7.5	186
Ni-OH-pbpc	Ni	<i>pbpc</i>	1553	4.15	7.9	186
MOF-505	Cu	<i>bptc</i>	1670	4.02	7.2	187
Cu-tpb	Cu	<i>tpb</i>	1120	2.8	7.5	188
Cu-BDC	Cu	<i>dabco</i>	1300	2.7	6.2	189

The MOF containing the terephthalic acid as its linker (i.e. Zn-BDC) has the highest adsorption capacity compared to the other synthesized MOFs. Their order (decending) in terms of MOF-structures and adsorption weight percent is given as; Zn-BDC>Cu-BTC>Zn-Mim>Zn-NDC>Fe-BTC; with their corresponding weight to be 3.72 (wt.); 3.56 (wt.); 3.39 (wt.); 3.16 (wt.); and 3.15 (wt.) as shown in Table 4.3.

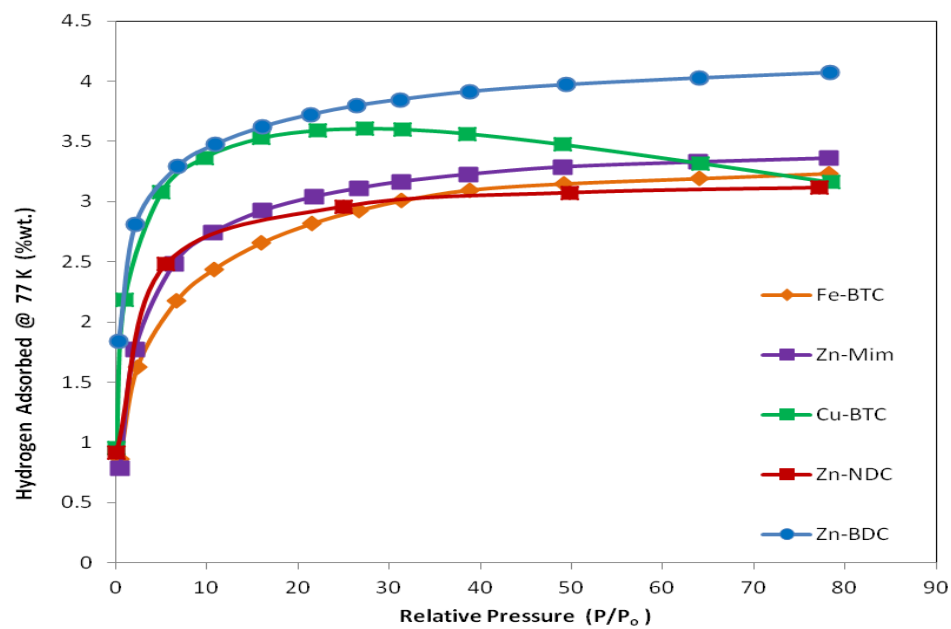


Fig. 4.6. Hydrogen adsorptions Isotherms for high pressure (77 K)MOFs used in this work

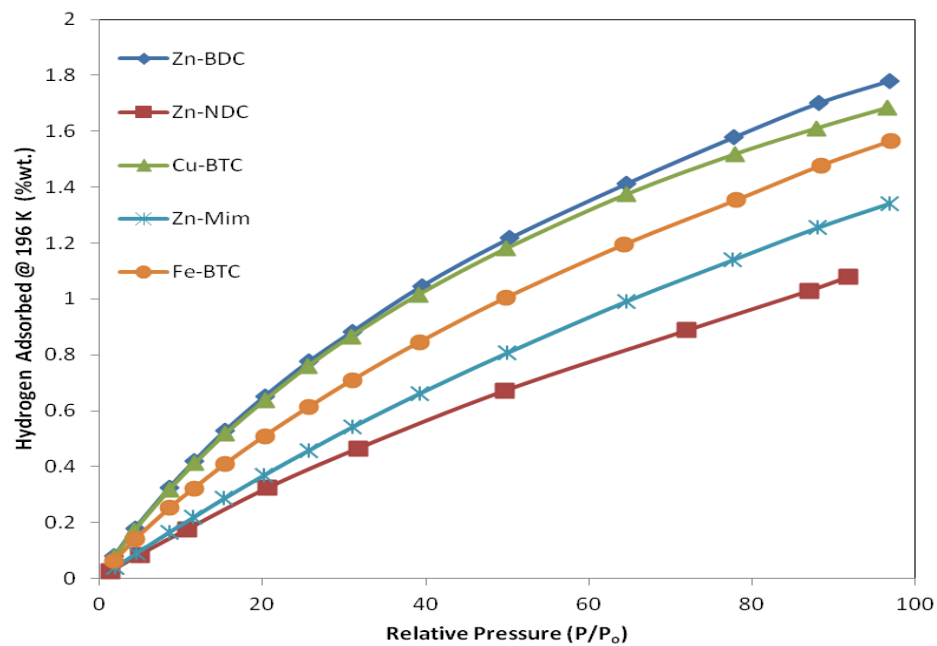


Fig. 4.7. Hydrogen adsorptions Isotherms for high pressure (196 K)MOFs used in this work

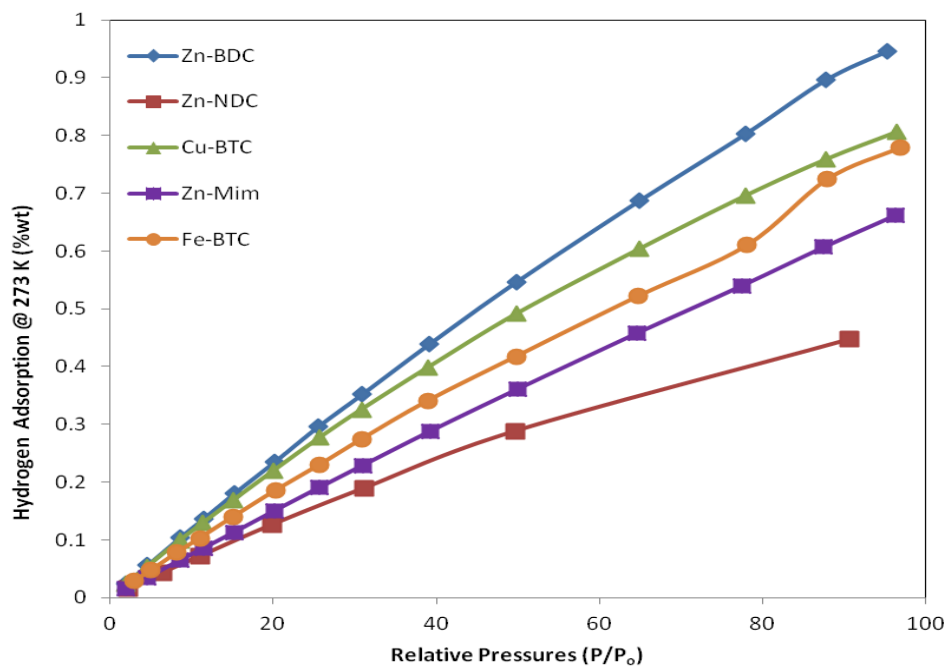


Fig. 4.8. Hydrogen adsorptions Isotherms for high pressure (273 K)MOFs used in this work

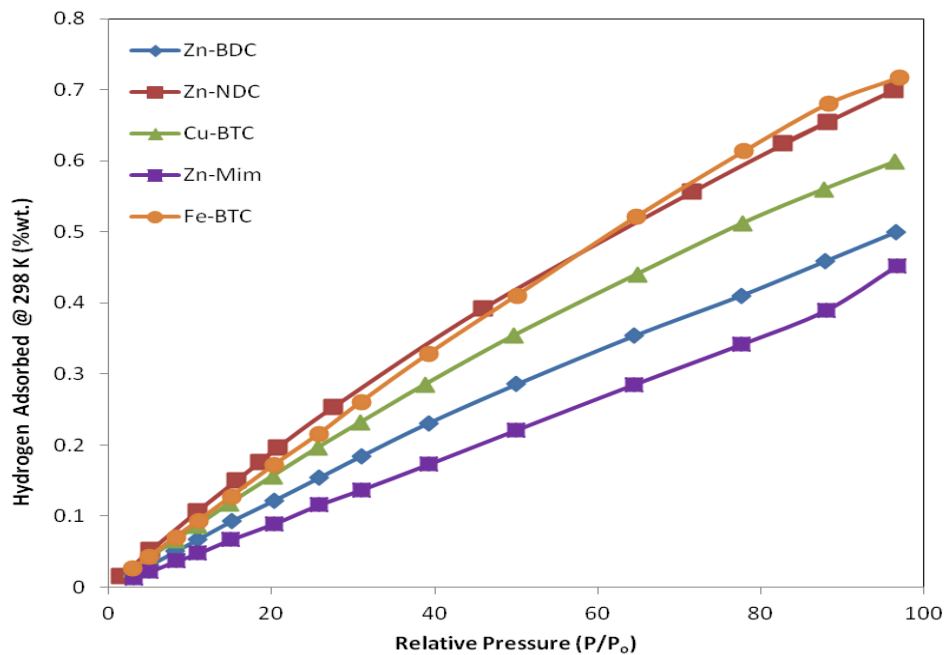


Fig. 4.9. Hydrogen adsorptions Isotherms for high pressure (298 K)MOFs used in this work

Fig. 4.10Ai and Fig. 4.10Bi contain plots of sticking factor versus the weight percentage of hydrogen on the surface. The results show that there is a reasonably good correlation, with $R^2 = 0.5741$ and 0.7345 . This is significantly better than the 0.0681 and 0.5799 in Fig 4.10Aii and Fig.4.10Bii that was obtained when surface area was plotted versus wt% using the same set of MOFs. Also, the results from this work show, in Fig. 4.10 (Ai and Aii) that $R^2 = 0.5741$ for sticking efficiencies and 0.0681 for surface area. However, as noted earlier, these MOFs contain a variety of different metal sites and organic linkers. Since the surfaces of these MOFs would be expected to be different it might be better to examine correlations between surface area and wt% on MOFs containing similar surfaces. However, see Fig.4.13Ai and Fig.4.13Aii for the plot of wt% versus surface area had a significantly less correlation ($R^2 = 0.1016$) than the plot of wt% versus sticking efficiency ($R^2 = 0.5064$). This demonstrated that, in order to make comparisons between surface area and wt% among MOFs, they must have similar surface features. It was also apparent that three of the MOFs (Cu-BTC, Fe-BTC and TUDMOF-1) contained the same BTC linker but different metals (Cu, Fe and Mo, respectively). Therefore plots of wt% versus surface area and sticking factor were constructed to make similar comparisons (see Fig.4.12Ai and Fig. 4.12Aii). Both plots displayed nearly identical correlation coefficients that were both excellent. The plot of wt% versus surface area had a slightly better correlation ($R^2 = 0.9534$) than the plot of wt% versus sticking efficiency ($R^2 = 0.9862$). It is thus evident that both surface area and sticking efficiency correlate well with wt% when the surfaces have similar characteristics (i.e. similar linkers). It was also of interest to determine how well wt% would correlate with surface area and sticking

efficiency in a series of MOFs containing the same metal site but different linkers. Since five of the MOFs contain a Zn metal center but different linkers they were chosen for the comparison. They are Zn-BDC, Zn-NDC, IRMOF-18, MOF-74 and Zn-Mim). It was found that the plot of wt% versus surface area showed almost no correlation with $R^2 = 0.1016$ whereas the plot of wt% versus sticking factor had $R^2 = 0.5064$ (See Fig 4.12Ai and Fig. 4.12Aii). In this series the MOFs contained dissimilar linkers ranging from dicarboxylate and tricarboxylate to methyl imidazole. The poor correlation coefficient demonstrates the importance of having similar linkers when comparing the H_2 gas adsorption capacities of MOFs to surface areas. It is also interesting to note that when sticking factors are used apparently this is not as necessary. Sticking factors are related to the binding energy and therefore comparisons of gas adsorption on different MOFs can be made regardless of the surface make-up. This explains why the graph of wt% versus surface area, containing MOFs with many different linkers, did not give as good a correlation as the one with wt% versus sticking factor. It is also interesting to note that seven of the MOFs contain Cu metal sites. These Cu sites are a bit different than those for many other metals. It has been reported that, in many cases, metal centers are fully coordinated and shielded from their surrounding environment. Thus they have little impact on adsorption. However, the Cu metal clusters are not fully coordinated to the organic-ligands. This leads to coordinative unsaturated sites, which are also termed “open metal sites”.⁵¹ If one compares the sticking factors and hydrogen adsorption capacities of the Cu-containing MOFs with others it is apparent the Cu-containing MOFs are generally clustered at the high end of the graph. This indicates that they have higher

sticking factors and higher adsorption capacities than the other MOFs. The most likely reason for this is that Cu is able to more effectively bind hydrogen due to the open metal sites.

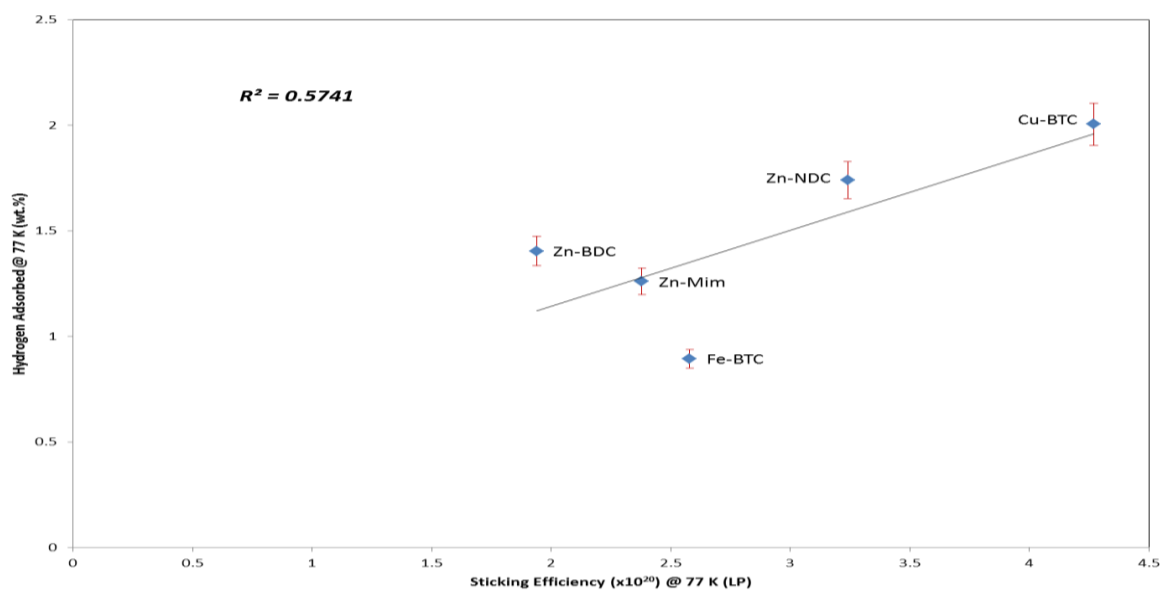


Fig. 4.10 (Ai) Sticking efficiency vs Weight per cent for hydrogen gas adsorbed at 77 K for this work under low pressure (LP)

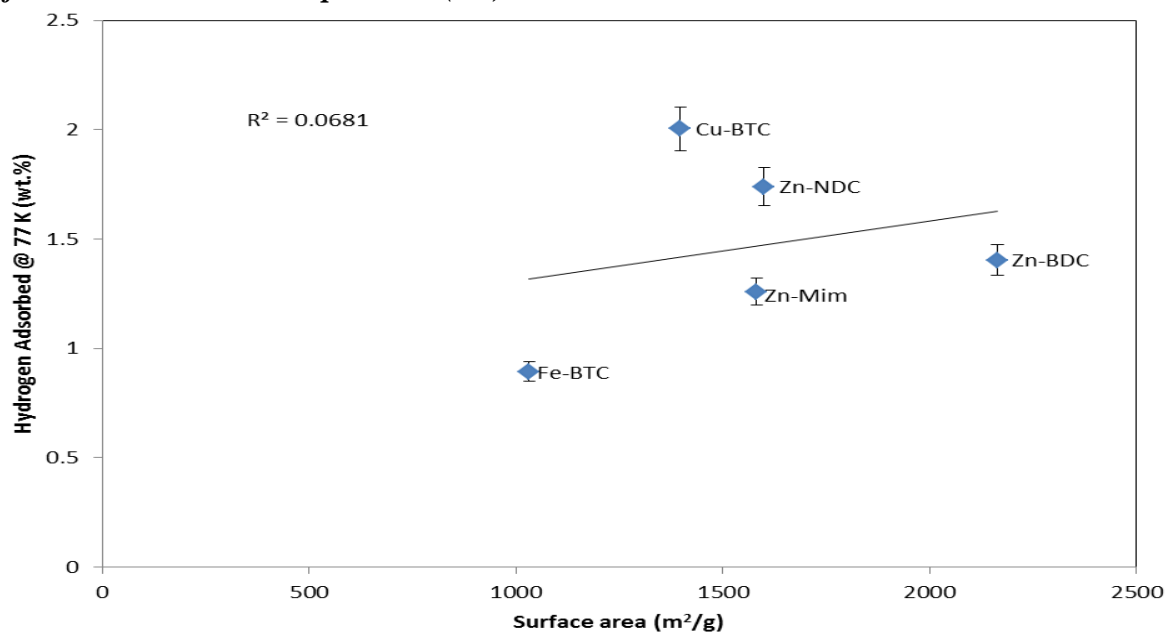


Fig. 4.10 (Aii) Surface area vs Weight per cent for hydrogen gas adsorbed at 77 K for this work under low pressure (LP)

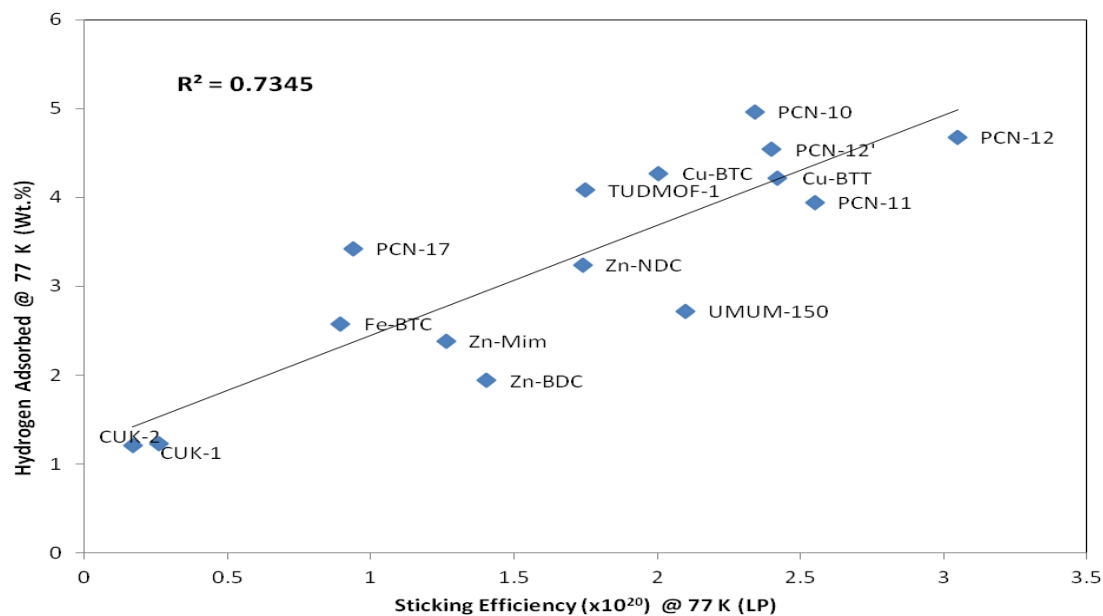


Fig. 4.10 (Bi) Sticking efficiency vs Weight per cent for hydrogen gas adsorbed at 77 K for this work with other studies including this study under low pressure (LP)

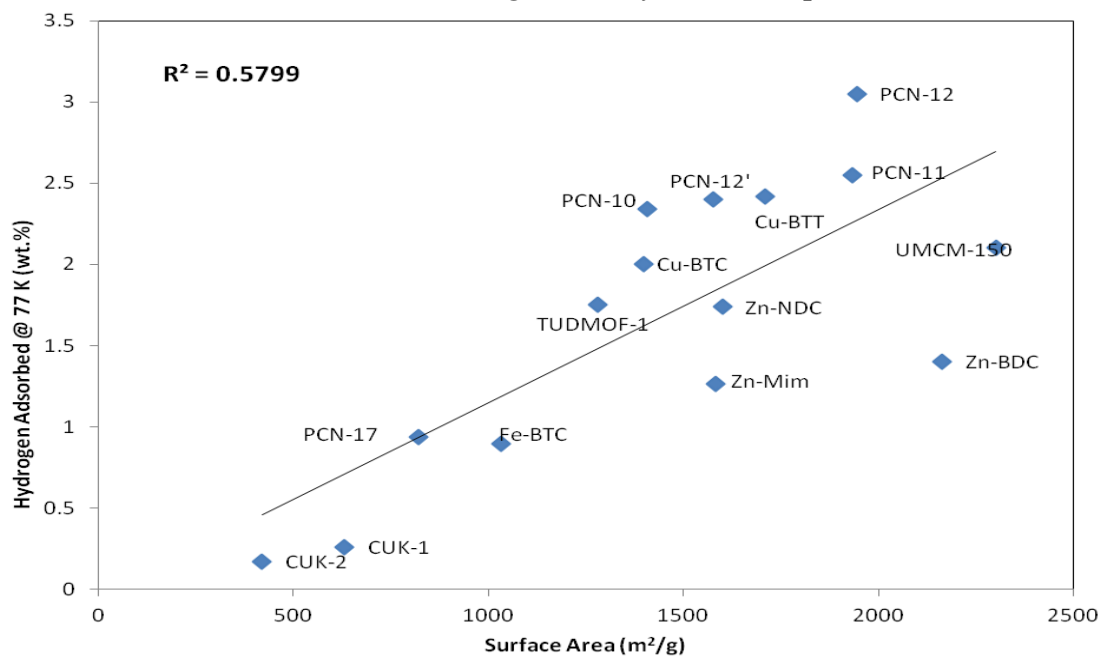


Fig. 4.10 (Bii) Surface area vs Weight per cent for hydrogen gas adsorbed at 77 K for this work other studies including this study under low pressure (LP)

Studies under high pressure show a different trend for H₂-gas adsorption weight percent than with the low pressure analysis. R² values for sticking efficiencies and surface area when measured against the gas (H₂) adsorbed weight percent were 0.2368 and 0.5034 respectively (see Fig 4.11Ai and Aii).

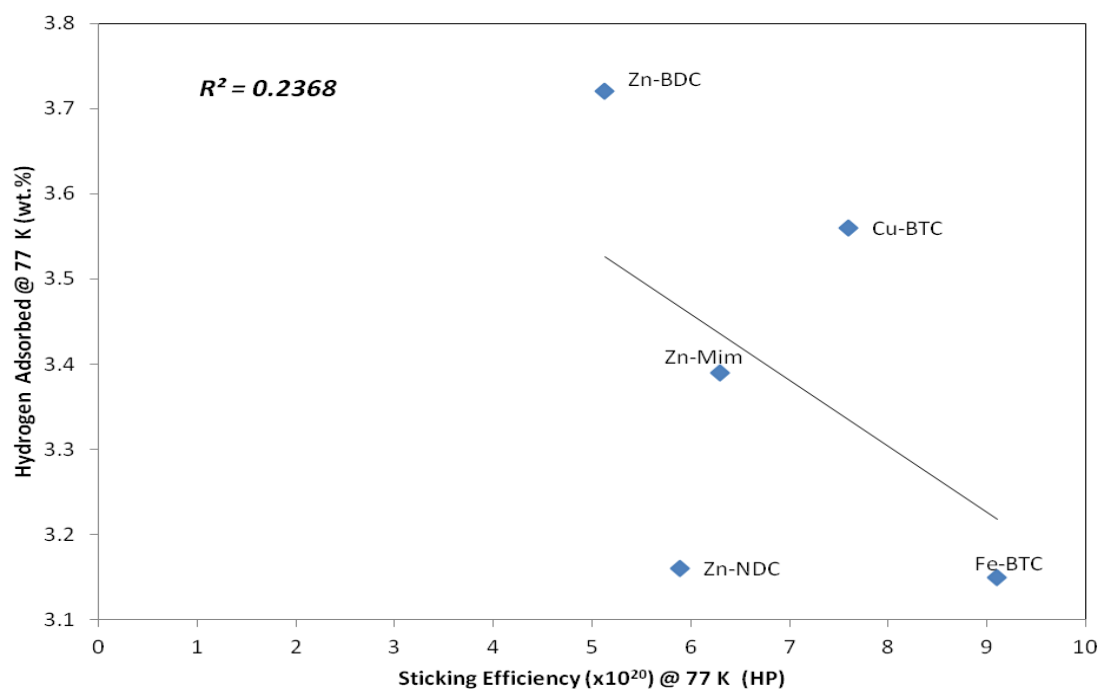


Fig 4.11 (Ai) High Pressure(HP) plots for hydrogen adsorption at 77 K Sticking efficiency vs Weight per cent for hydrogen gas adsorbed at 77 K for this work

However, looking at Fig 4.20 (Ai and Aii), the R-square value for the surface area and weight percent when the MOFs from this work were computed with some MOFs results from other studies, the surface area R² value obtained was 0.1998. While the the R² value for sticking efficiency for same computed work was 0.0004.

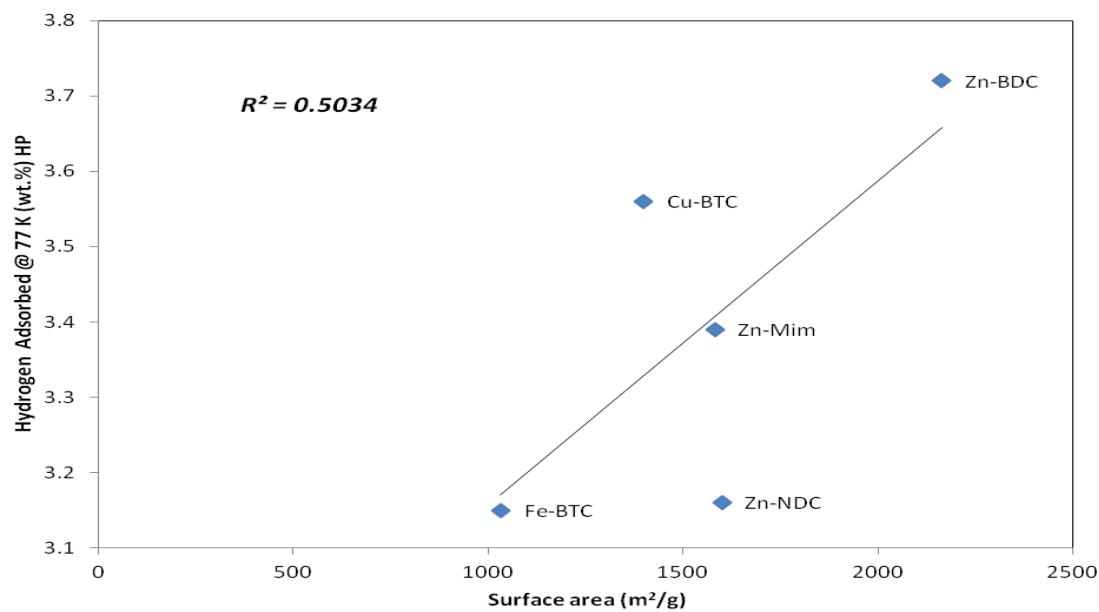


Fig 4.11 (Aii) High Pressure(HP) plots for hydrogen adsorption at 77 K Surface area vs Weight per cent for hydrogen gas adsorbed at 77 K for this work

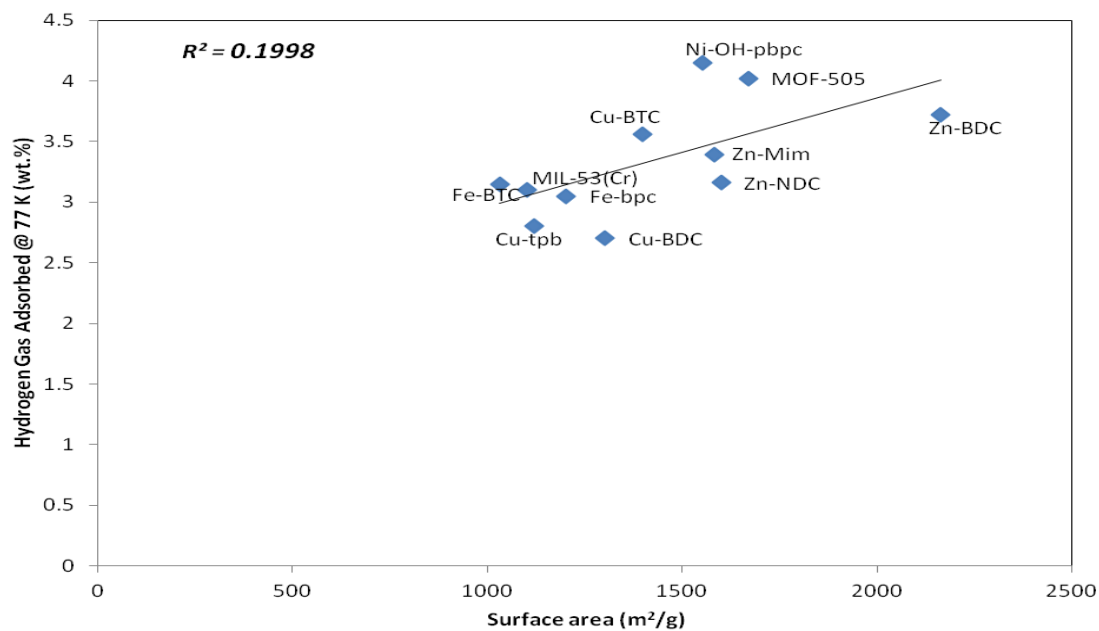


Fig 4.11 (Bi) Surface area vs Weight per cent for hydrogen gas adsorbed at 77 K for this work Other studies including this study under high pressure (HP)

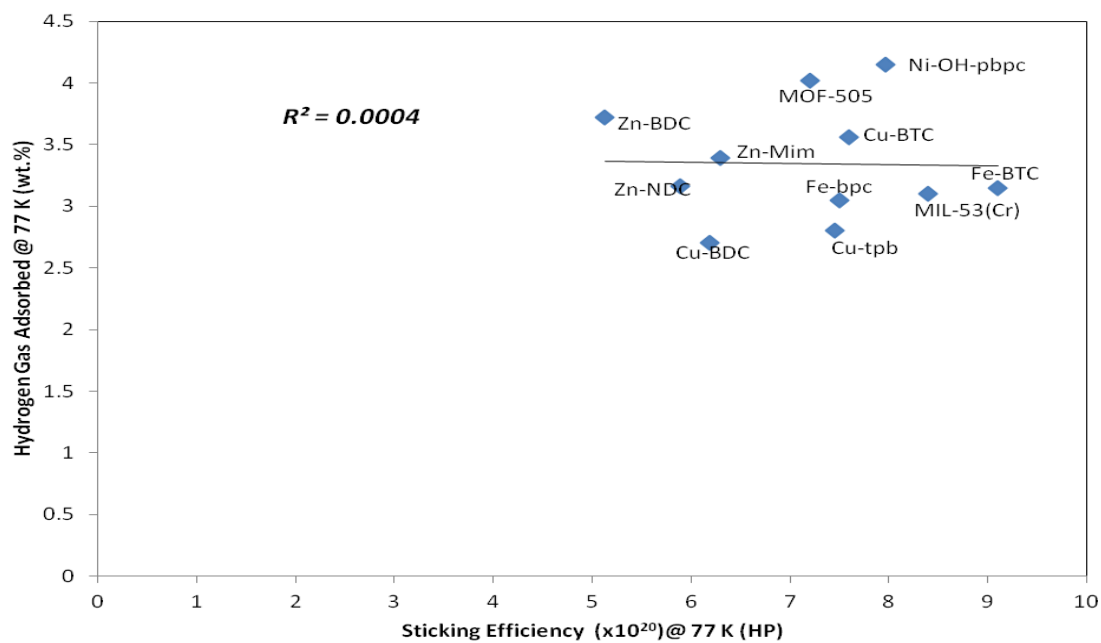


Fig 4.11 (Bii) Other studies including this study sticking efficiency vs hydrogen gas adsorbed at 77 K under high pressure (HP)

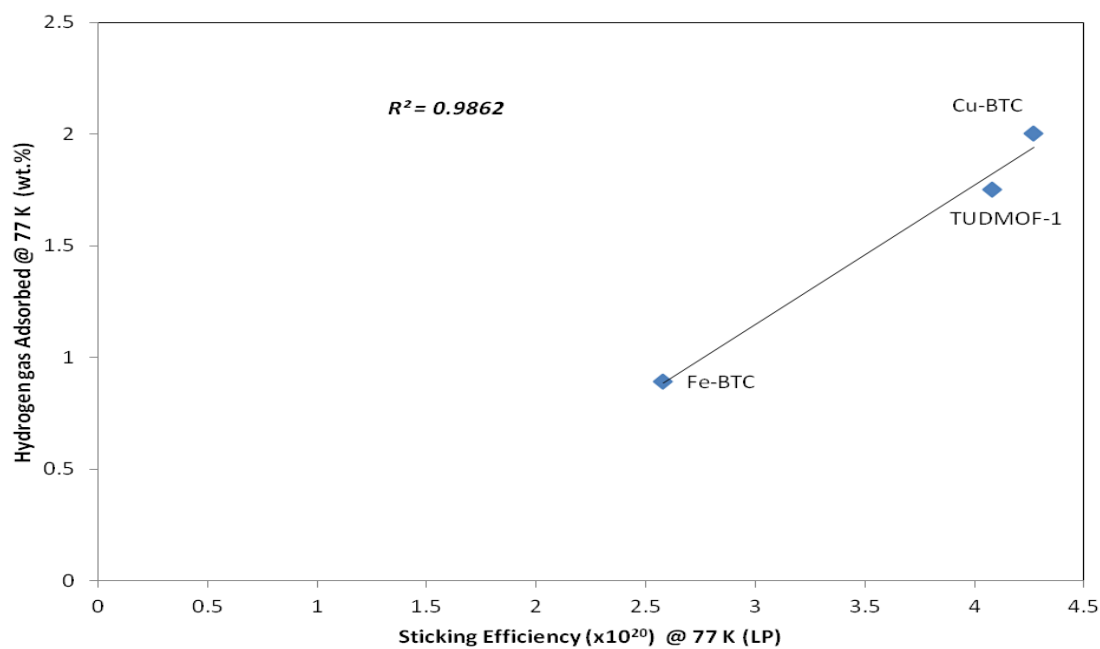


Fig 4.12 (Ai) Low Pressure (LP) plots for hydrogen adsorption at 77 K of MOF with same organic linker for sticking efficiency vs hydrogen adsorbed

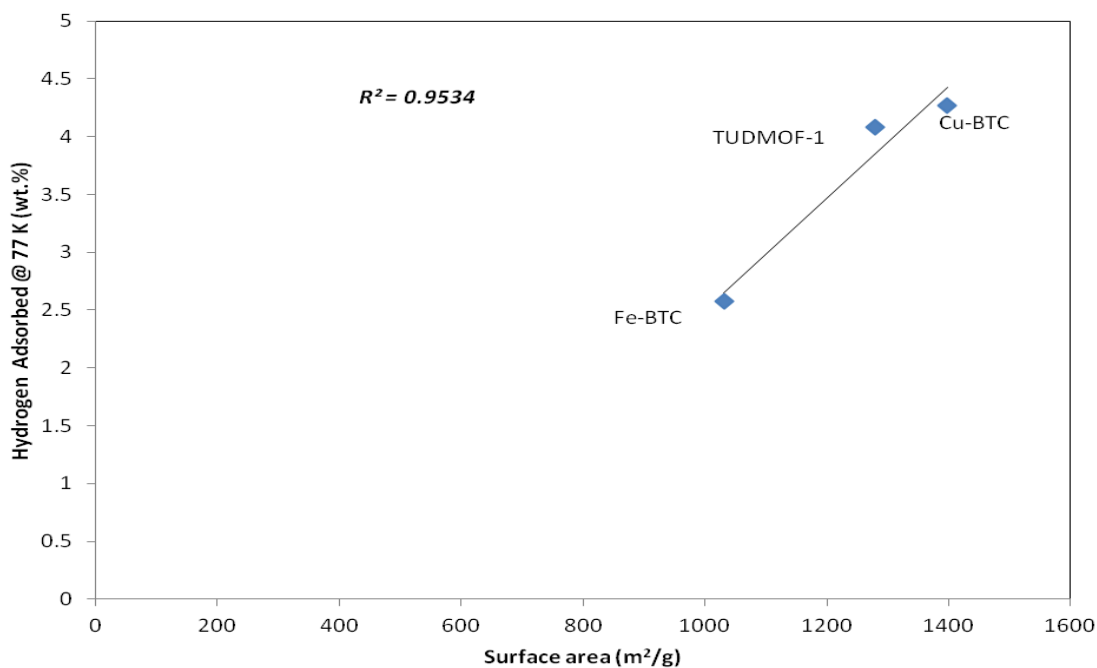


Fig 4.12 (Aii) Low Pressure(LP) plots for hydrogen adsorption at 77 K of MOF with same organic linker for surface area vs hydrogen adsorbed

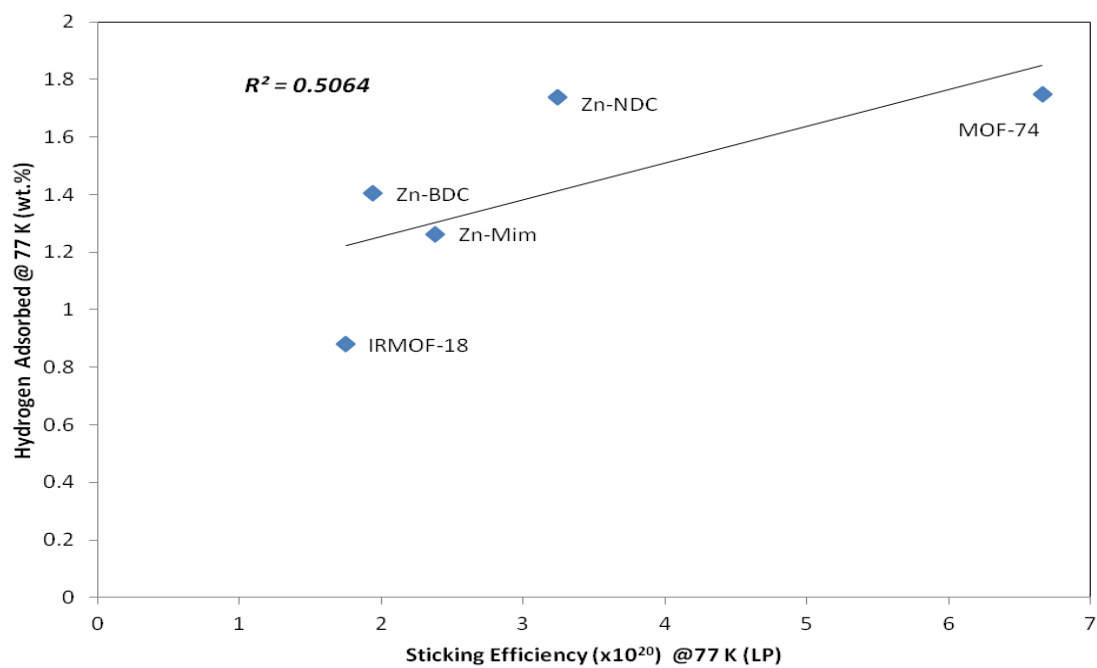


Fig 4.13 (Ai) Low Pressure(LP) plots for hydrogen adsorption at 77 K of MOF with same metal for sticking efficiency vs hydrogen adsorbed

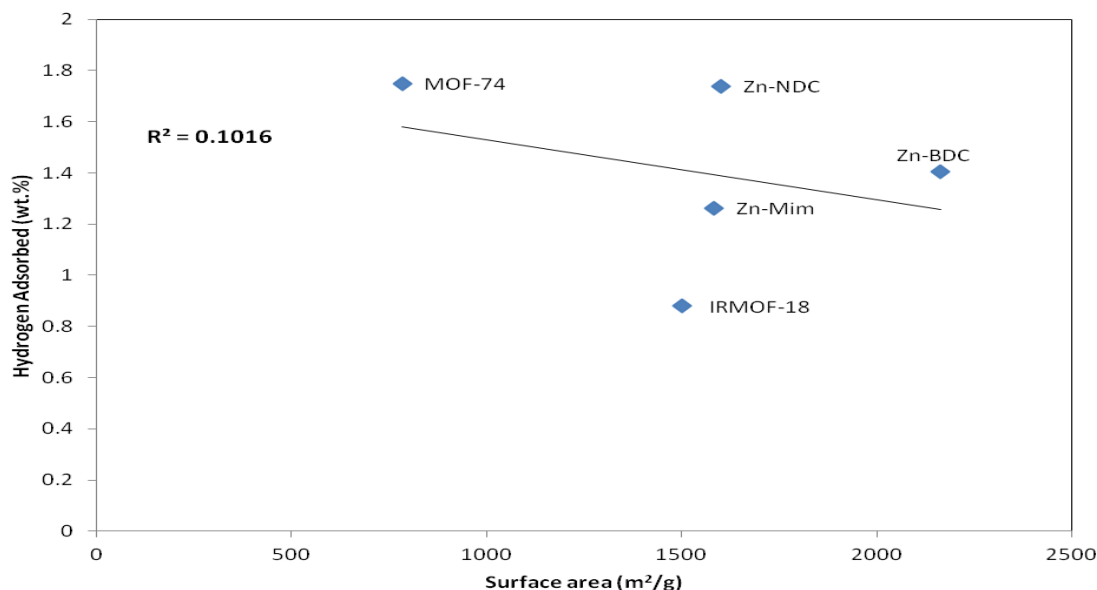


Fig 4.13 (Aii) Low Pressure(LP) plots for hydrogen adsorption at 77 K of MOF with same metal for surface area vs hydrogen adsorbed

4.3 Enthalpy of Adsorptions

Sticking efficiency has been found to correlate well with adsorption capacity. Since sticking efficiency is related to the ability of hydrogen to stick onto the surface of MOFs, it seemed likely that the strength of physisorption (binding energy) on some gas surfaces may be greater than others. If this is the case, enthalpies of hydrogen adsorption for each MOF should reflect these differences. Therefore adsorption enthalpies were obtained by applying the van't Hoff equation using Eq. 4.1 shown below;

$$\ln P_1 - \ln P_2 = - \frac{\Delta H}{R} \left(\frac{1}{T_1} - \frac{1}{T_2} \right) \quad (4.1)$$

Where ΔH is the isosteric heat of adsorption (kJmol^{-1}), T_1 and T_2 are Kelvin temperatures, P_1 and P_2 are adsorbate pressures in (bar) and R is the universal gas constant. For each of the MOFs that were prepared or purchased for this work, the

adsorption pressure was obtained at two temperatures and the adsorption enthalpy was obtained from Eq.(4.1). The adsorption enthalpies are given in Table 4.2 and Table 4.3 along with those reported in the literature for some of the other MOFs. An attempt was made to determine if a correlation exists between sticking factor and heat of adsorption. From the plot of the isosteric heats of adsorption versus sticking factors in Fig. 4.14(Ai & Aii) it can be seen that a good correlation does exist for θ vs ΔH with $R^2 = 0.7844$, compared to BET surface area vs ΔH which has $R^2 = 0.0061$. This demonstrates that the sticking factor is directly related to the strength of adsorption of the sorbate molecule on the surface. Since a correlation was also found between sticking factor and the quantity of hydrogen adsorbed, this confirms that the amount of hydrogen adsorbed on a MOF is related to both the strength of adsorption of the sorbate molecule on the surface as well as the surface area of the MOF.

The studies of the isosteric heat of adsorption at zero coverage shown in Fig. 4.14Ai, and Fig. 4.14Bi, reveals sticking efficiency(Θ) results with correlation of $R^2 = 0.7844$ and 0.7068 for both synthesized MOFs for this work as well as literature data compared to corresponding BET surface area R-square obtained results of 0.0061 and 0.036 (see Fig. 4.14Aii and Fig.4.14Bii)

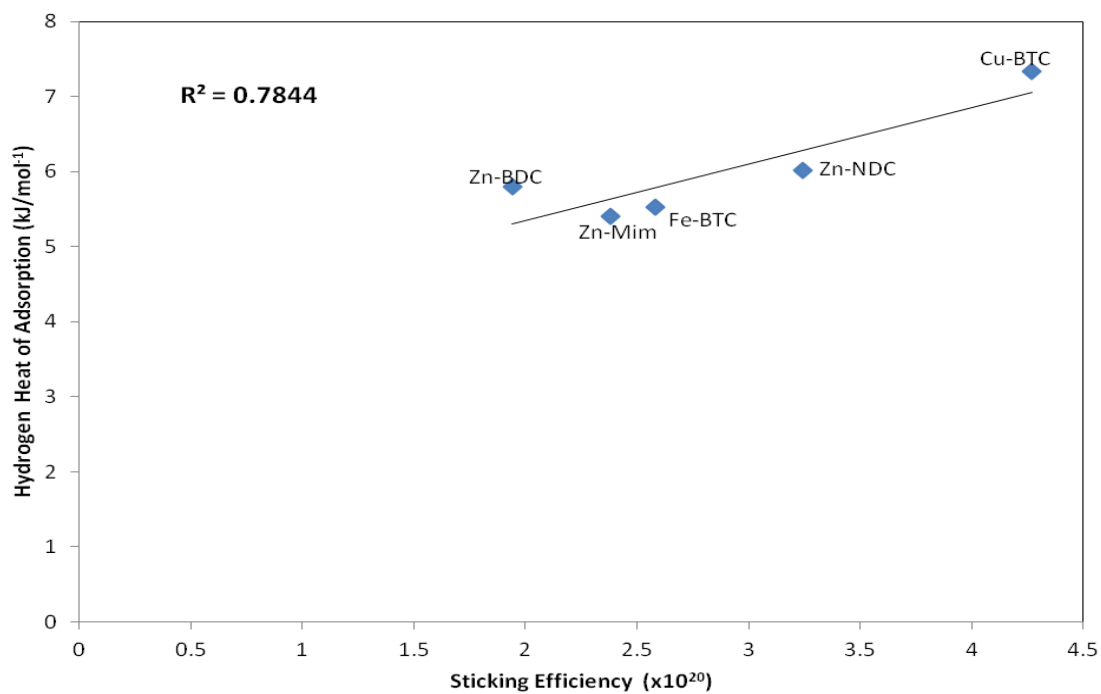


Fig 4.14 (Ai) Sticking efficiency vs enthalpy heat of adsorption for this work

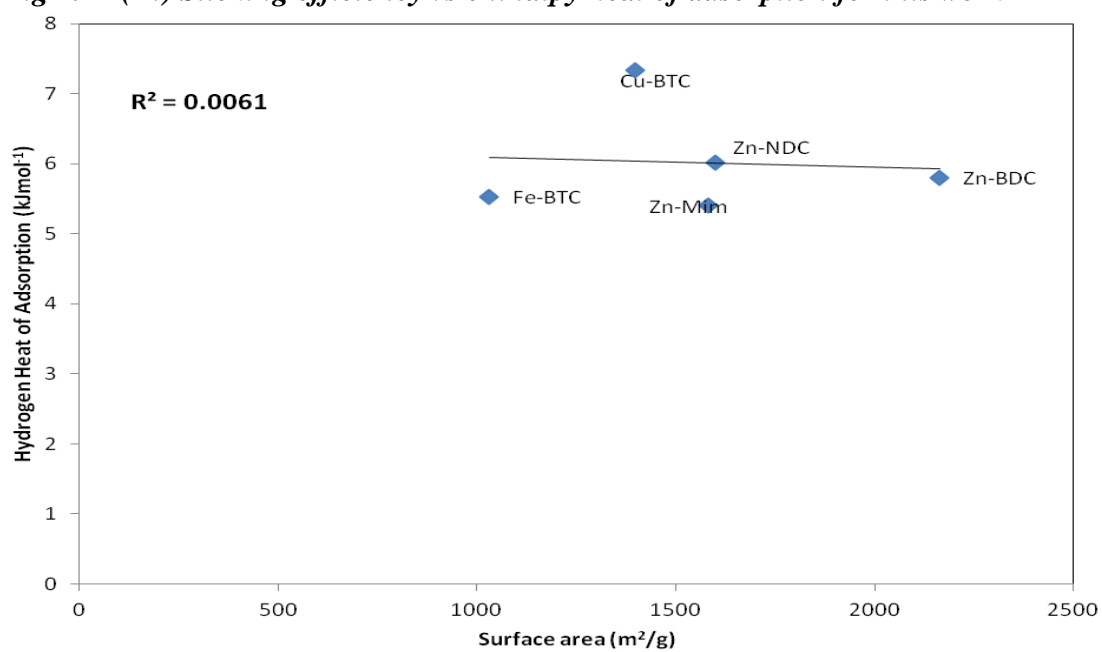


Fig 4.14 (Aii) Surface area vs enthalpy heat of adsorption for this work

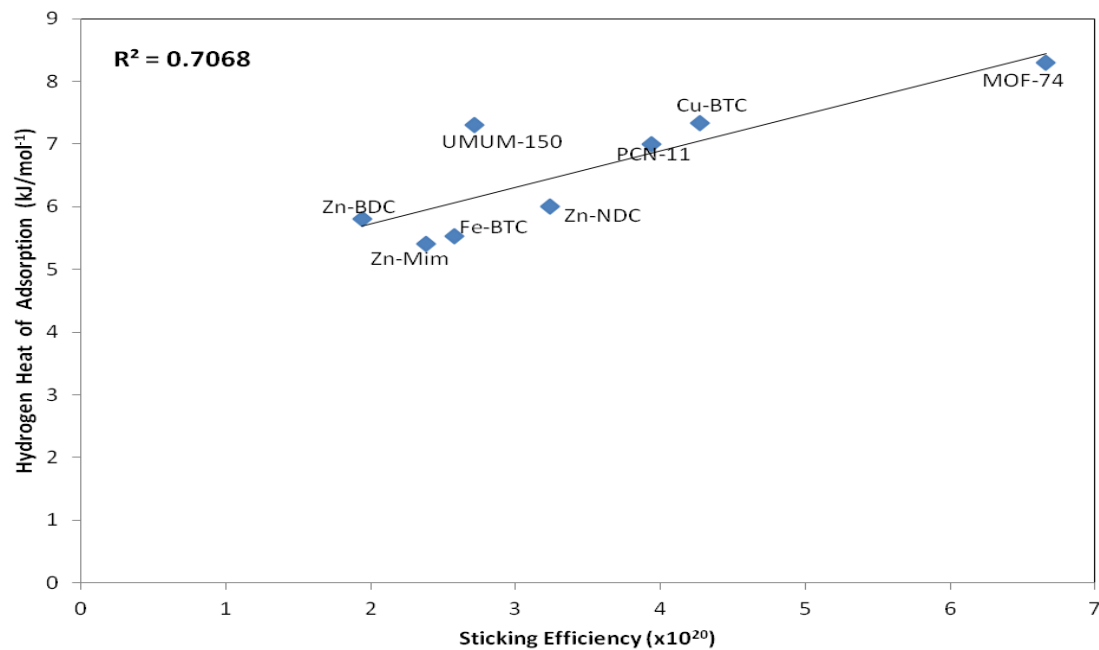


Fig. 4.14 (Bi) Other studies including this study sticking efficiency vs enthalpy heat of adsorption

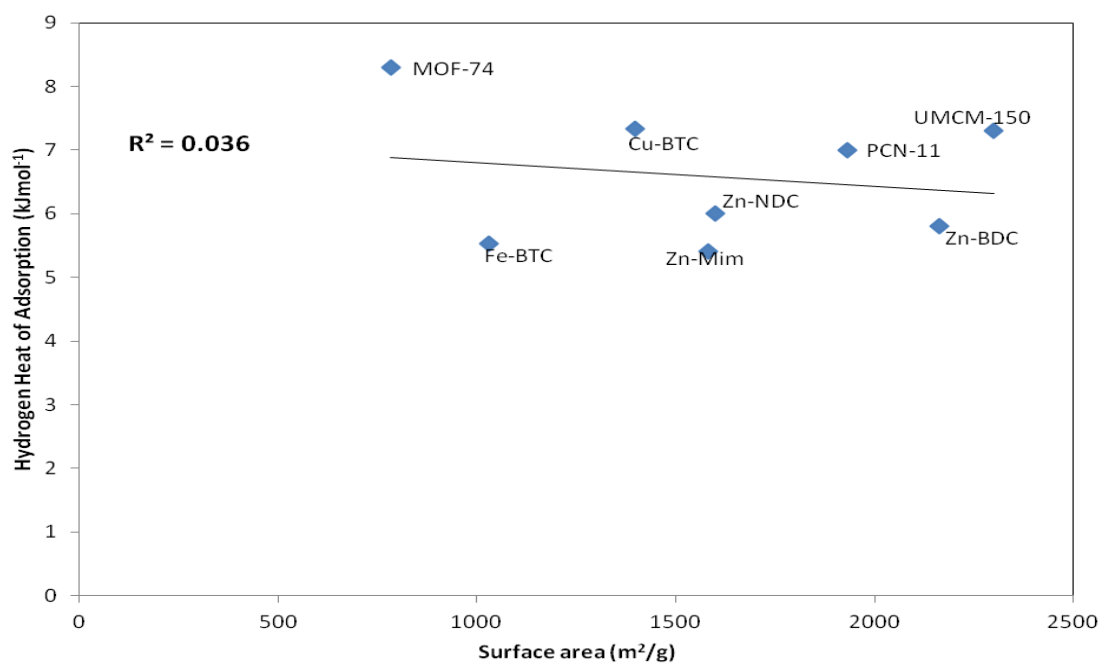


Fig. 4.14 (Bii) Other studies including this study surface area vs enthalpy heat of adsorption

4.4 Summary

Based on the findings from this research work, the new concepts (sticking efficiency), correlate better under low pressure compared to the surface area and vice versa.

In this work, a comparison of the hydrogen adsorption capacities of 17 MOFs was made. Results showed that a better correlation exists between sticking efficiency and hydrogen adsorption capacity than between surface area and adsorption capacity. At low pressure however, when only MOFs containing similar types of linkers were included in the comparison, the surface area correlated somewhat better with adsorption capacity than did sticking efficiency. This demonstrates that sticking efficiency correlates with adsorption capacity for a broader range of dissimilar MOFs than surface area. It was also found that MOFs with open metal sites generally have larger sticking efficiencies and greater H₂ holding capacities than those that do not. Since sticking efficiencies were shown to be proportional to adsorption enthalpy, this demonstrates that sticking efficiency is a direct measure of the strength of hydrogen interaction with the surface.¹⁶⁹

The reason for this observed difference is that at low pressure, saturation of the BET surface area is unachievable as compared to high pressure where it is achievable.

Hence, the fact that sticking efficiency is better than surface area under certain conditions was successfully proven in this work while using hydrogen gas adsorbed under low and high pressure.

CHAPTER FIVE

METHANE GAS ADSORPTIONS

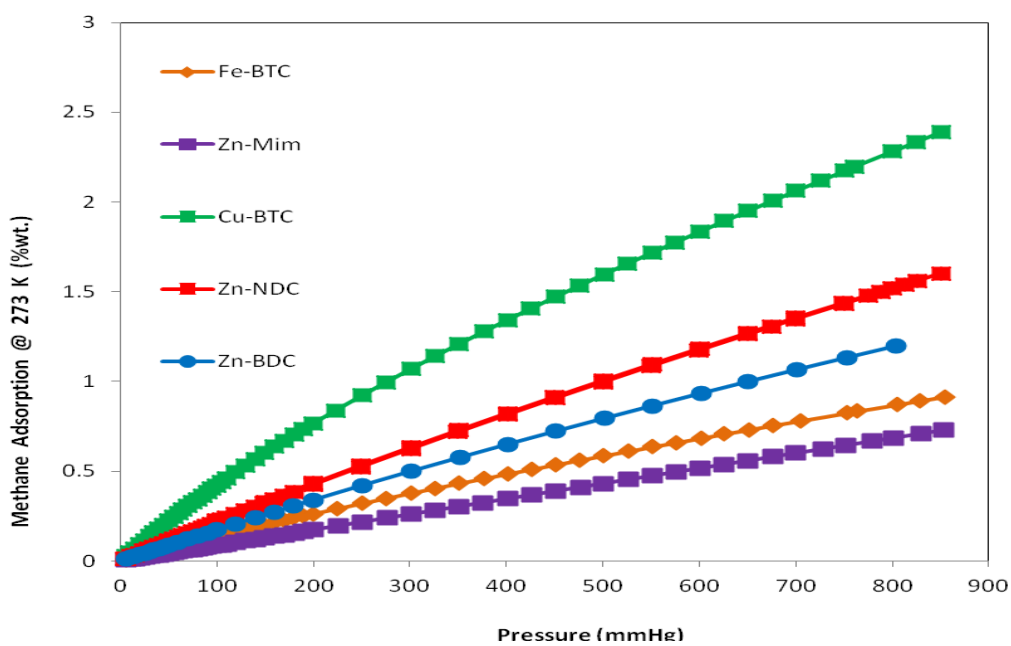
5.0 Methane Gas Adsorption Isotherms

Methane sorption for storage has been less studied in MOFs and other porous materials such as Porous Coordination Network (PCNs), Hyper-Crosslinked Polymer network (HCPs) and others.¹²⁸ Natural gas is primarily composed of > 95% methane with a gravimetric heat of combustion of about 55.7 MJ/kg as compared to gasoline which is about 46.4 J/kg.^{58, 61, 64} Table 5.1 show the results obtained from methane gas adsorption for this work as well as their corresponding isotherms for both low and high pressures (see Fig. 5.1, Fig. 5.2, Fig 5.3 and Fig. 5.4) respectively.

At low pressures for MOFs used in this work, Cu-BTC adsorbs the highest amount of methane at 273 K and 298 K (2.19 wt.% and 1.31 wt.%) respectively. When these MOFs are arranged in descending order; Cu-BTC>Zn-NDC>Zn-BDC>Fe-BTC>Zn-Mim at 273 K. A similar trend can also be noticed for low pressure at room temperature, except for the Zn-BDC and Zn-NDC which has a difference of 0.03 wt.% between them. This is insignificant as there are never saturations from isotherms plots at low pressures, (Fig. 5.1 and Fig. 5.2.). And also instrumentation analysis error exists. Under high pressure, (Fig. 5.3and Fig. 5.4) the isotherms obtained were noticed to have some unsaturation just like the case of low pressure.

Table 5.1 Methane low and high pressure weight percent data

MOFs	Other Name(s)	Wt.% CH ₄	Wt.% CH ₄
		273K	298K
Zn-BDC	MOF-5	1.15 (LP)	0.84(LP)
	[IRMOF-1]	12.82 (HP)	10.56 (HP)
Zn-NDC	MOF-8	1.47 (LP)	0.81(LP)
	[IRMOF-8]	15.79 (HP)	12.44 (HP)
Cu-BTC	MOF-199	2.19(LP)	1.31(LP)
	[HKUST-1]	16.61 (HP)	13.70 (HP)
Zn-Mim	ZIF-8	0.65(LP)	0.42(LP)
	[Z1200]	9.26 (HP)	6.71 (HP)
Fe-BTC	Basolite F300	0.84(LP)	0.55(LP)
		11.29 (HP)	10.29 (HP)

**Fig. 5.1 Methane adsorption Isotherms for low pressure (273 K)MOFs used in this work**

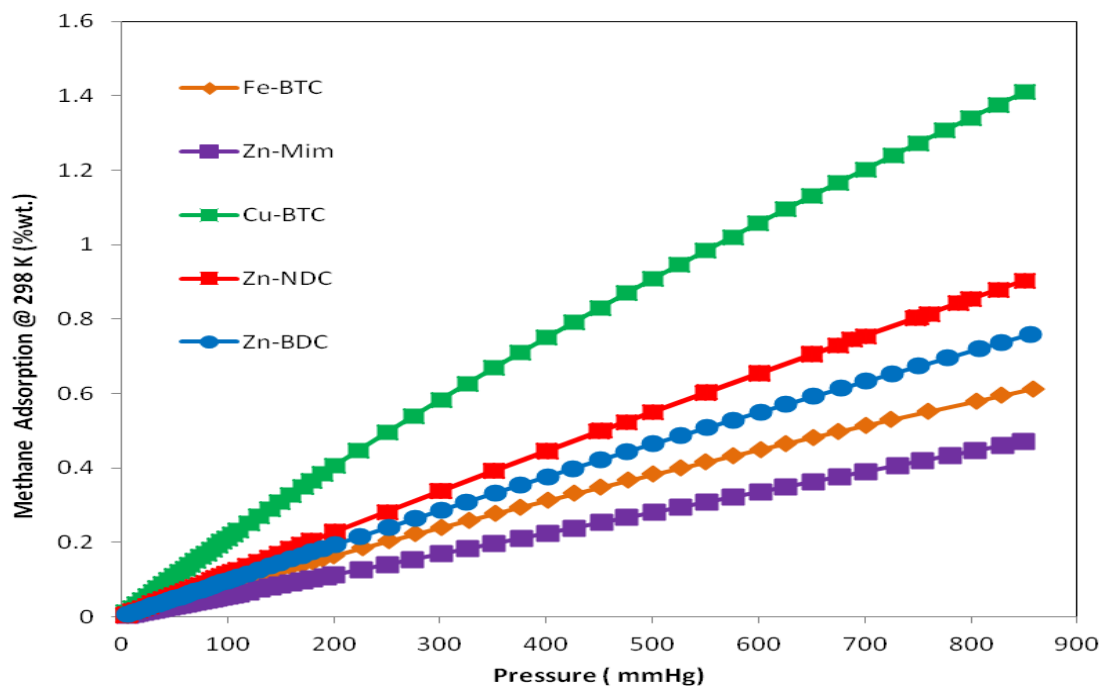


Fig. 5.2. Methane adsorptions Isotherms for low pressure (298 K)MOFs used in this work

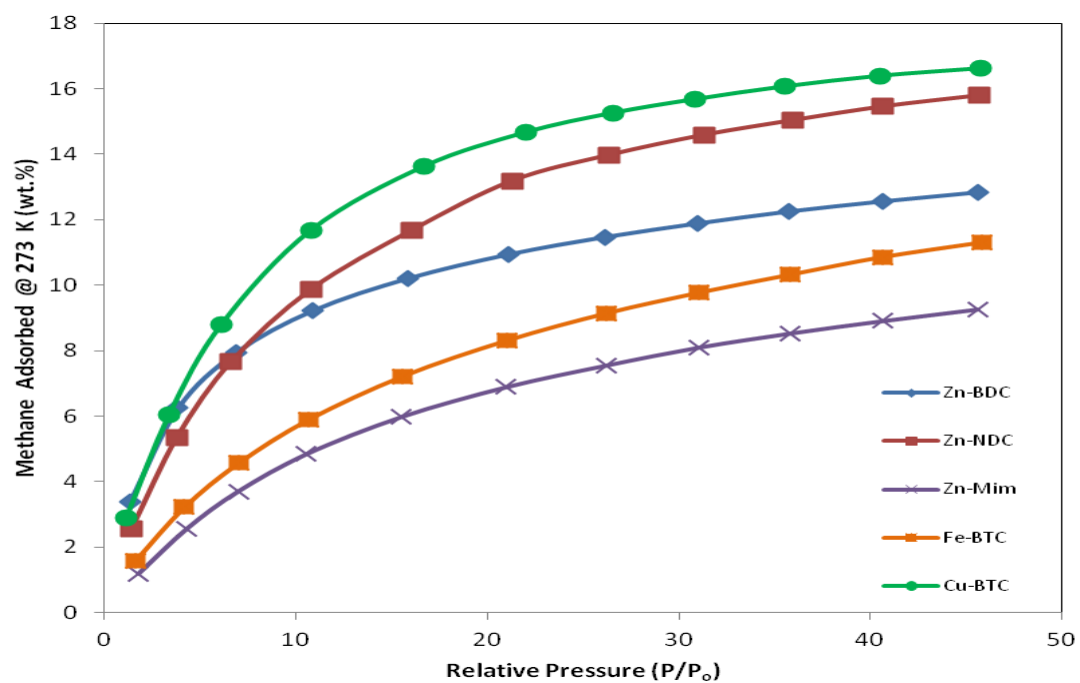


Fig.5.3. Methane adsorption Isotherms for high pressure (273 K)MOFs used in this work

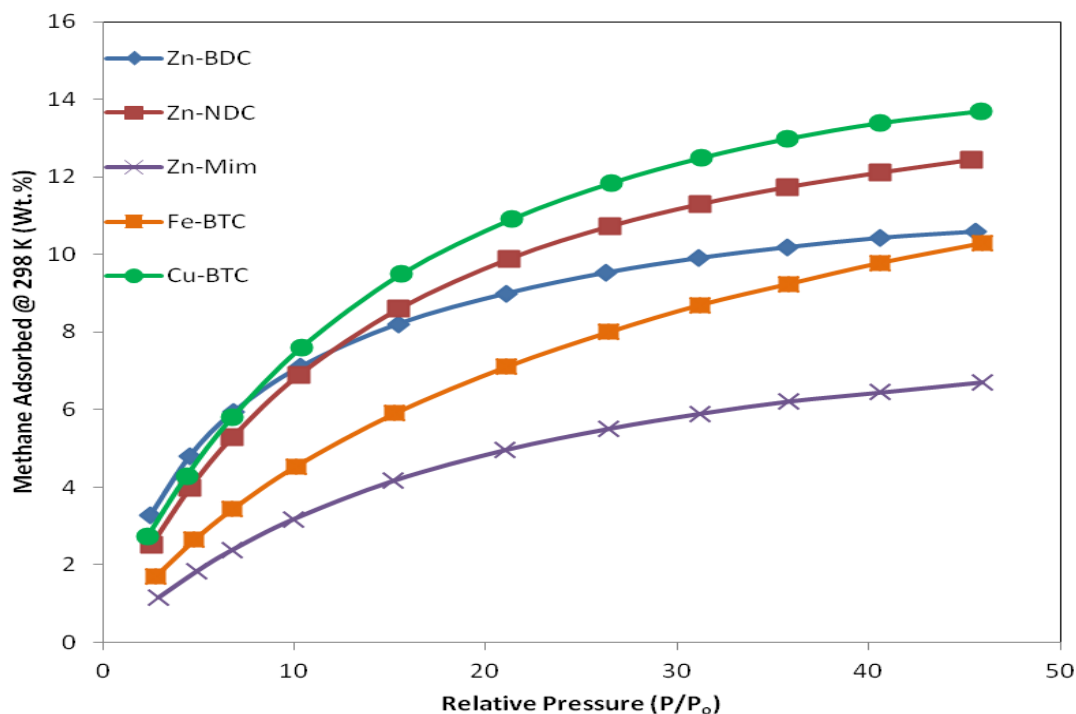


Fig.5.4. Methane adsorption Isotherms for high pressure (298 K)MOFs used in this work

5.1 Methane Adsorption and Sticking Efficiency (Θ)

The relationship between surface area of these MOFs and their sticking efficiencies were determined for data obtained in this research and data from other studies (Table 5.2).

Table 5.2 High pressure data for CH₄ adsorption @ 298 K

Metal + Linker	MOF	CH₄ wt.% @ 298 K	S.E (x10²⁰)	BET m²/g	ΔH (kJ/mol)	Ref
Cr / BTC	MIL-100	12.1	2.39	1900	19	54
Co / BDC	Co ₂ (BDC) ₂ (dabco)	12.2	2.87	1600	-	54
Cu / sBTC	PCN-11	16.3	3.17	1931	14.6	181
Cu / aDIP	PCN-14'	18.9	4.05	1753	30	190
Cu / BTC	Cu-BTC	13.7	3.69	1398	17.6	<i>This Work</i>
Zn / BDC	Zn-BDC	10.6	1.84	2163	15	<i>This Work</i>
Zn / NDC	Zn-NDC	12.4	2.93	1599	16.9	<i>This Work</i>
Fe / BTC	Fe-BTC	10.3	3.76	1031	11	<i>This Work</i>
Zn / Mim	Zn-Mim	6.7	1.6	1581	15.8	<i>This Work</i>
B/BTPA	COF-8	8	2.23	1350	12	128
	HCP-1	6.6	1.3	1904	-	128
	HCP-4	6.5	1.79	1366	-	128
	PPN-1	7.6	2.29	1249	18.1	128
	PPN-2	9.8	2.09	1764	16.4	128

The results at 298 K and high pressures show that, weight percent correlates better with the sticking efficiency. It produces a best fit line where the value of R² was 0.4791 when compared against the surface area whose R² value resulted in 0.0066. See Fig 5.5(Ai and Aii)

Similarly, the R² values of 0.6532 and 0.1445 (see Fig. 5.5Bi and Bii) for sticking efficiency and surface area respectively were recorded at low pressures and room temperature (298 K) for same MOFs and others obtained literature values.

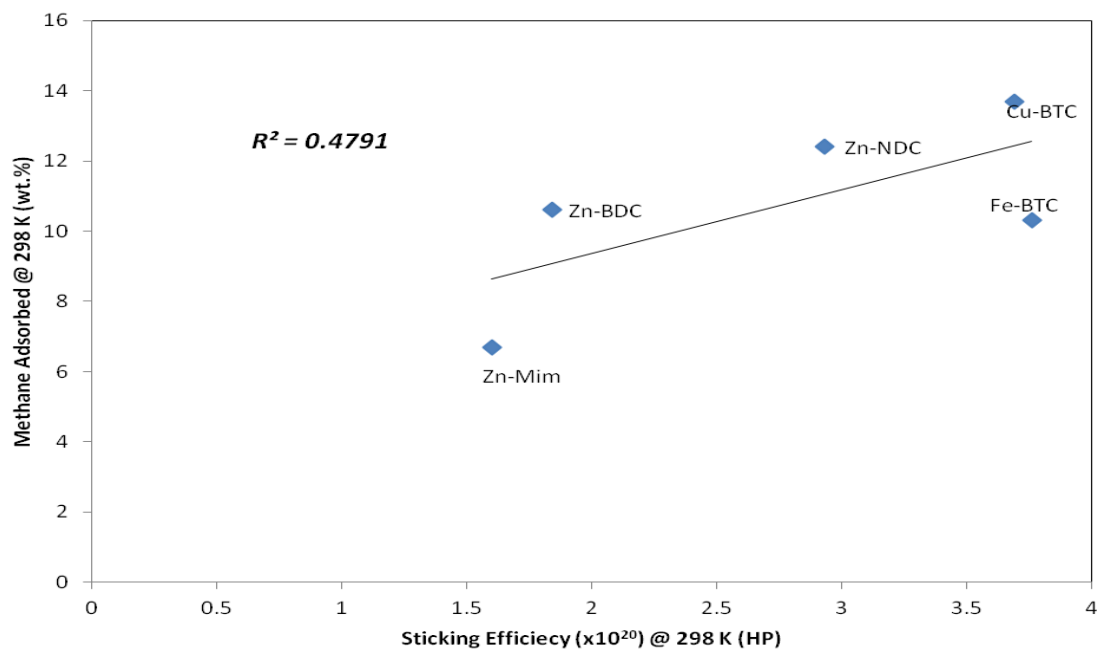


Fig.5.5 (Ai) Sticking efficiency vs Weight per cent for methane gas adsorbed at 298 K under high pressure (HP) for this work

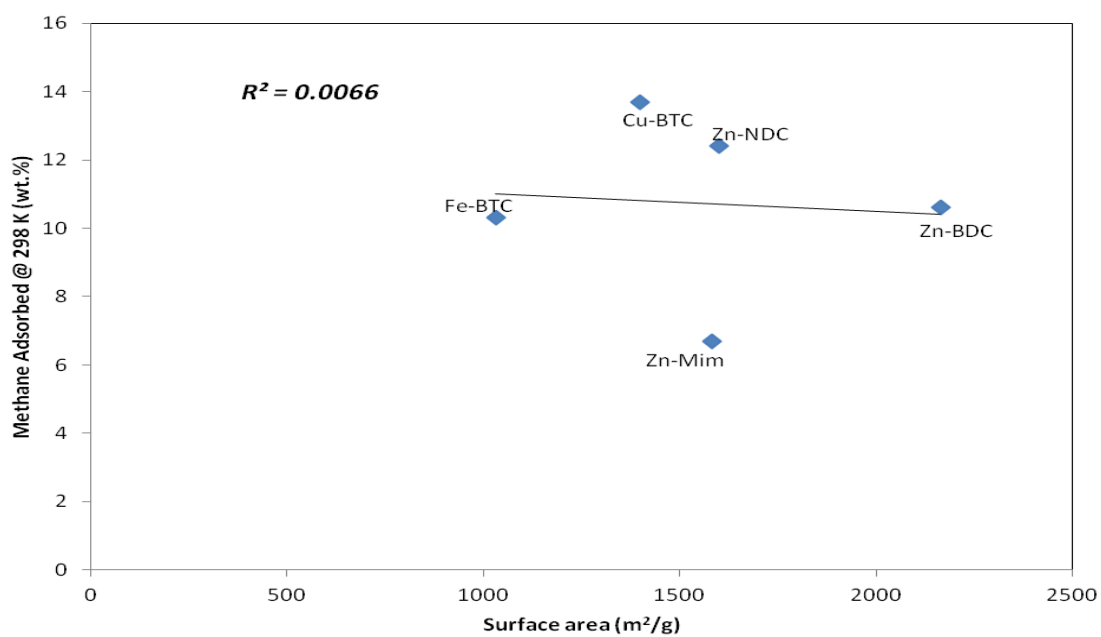


Fig.5.5 (Aii) Surface area vs Weight per cent for methane gas adsorbed at 298 K under high pressure (HP) for this work

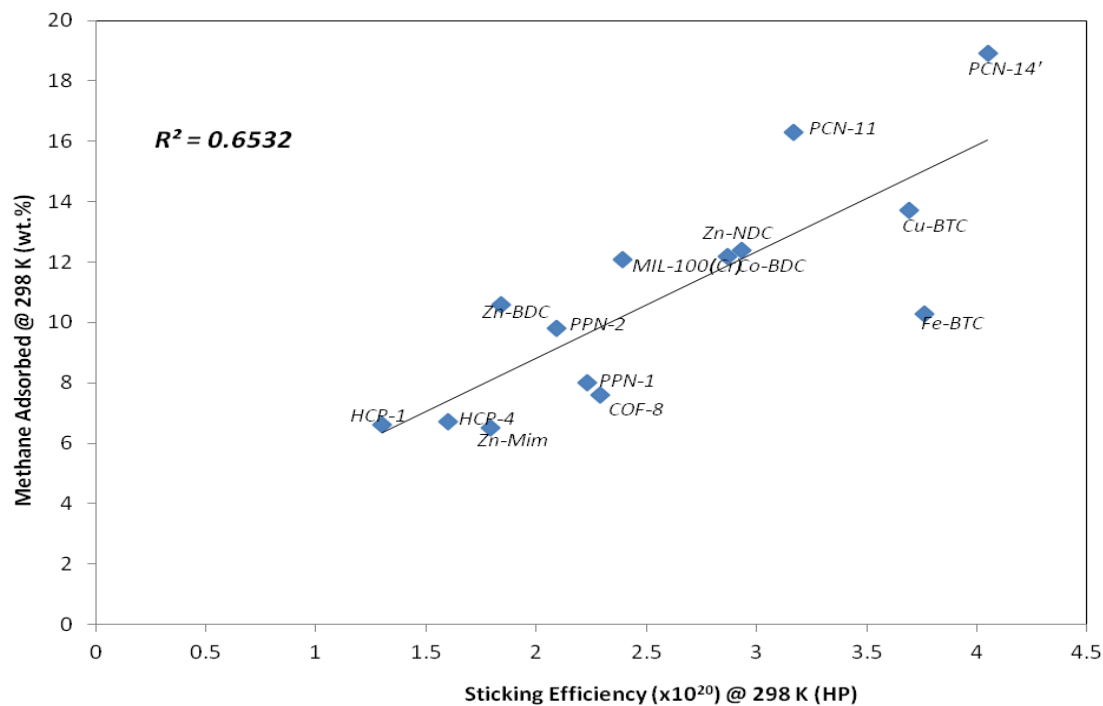


Fig. 5.5(Bi) Other studies including this study for sticking efficiency vs methane adsorbed at 298 K under high pressure (HP)

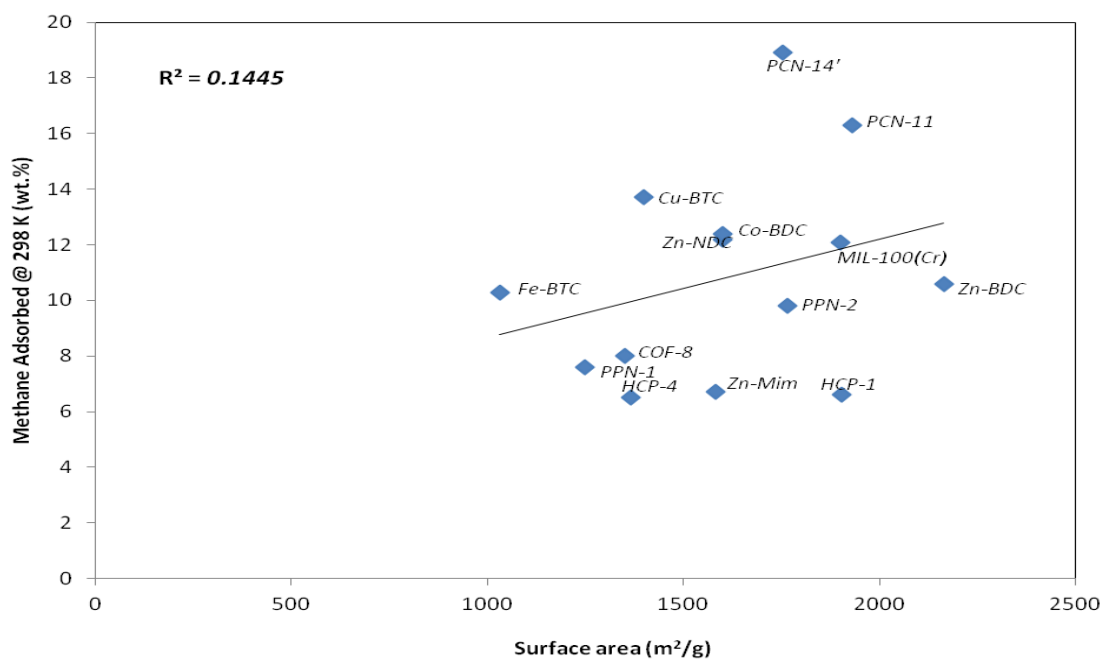


Fig. 5.5(Bii) Other studies including this study for methane adsorbed at 298 K under high pressure (HP)

The interpretations from the graphs for both low pressure and high pressure at room temperatures (298 K) show that MOFs with open-metal sites (Cu-BTC and Fe-BTC) occupied the higher section of the graph. And also, these MOFs have the same linker; 1,3,5-benzenetricarboxylic acid. When this was compared with other MOFs from other studies, the same trends were noticeable.

At ice temperature (273 K), (see Fig. 5.6Ai and Fig. 5.6Aii) the R^2 values were 1×10^{-6} and 0.8369 for the BET surface area and sticking efficiency respectively under low pressures. Cu-BTC occupies the upper end of the line for sticking efficiency. But the surface area plot shows the regression line heading downwards.

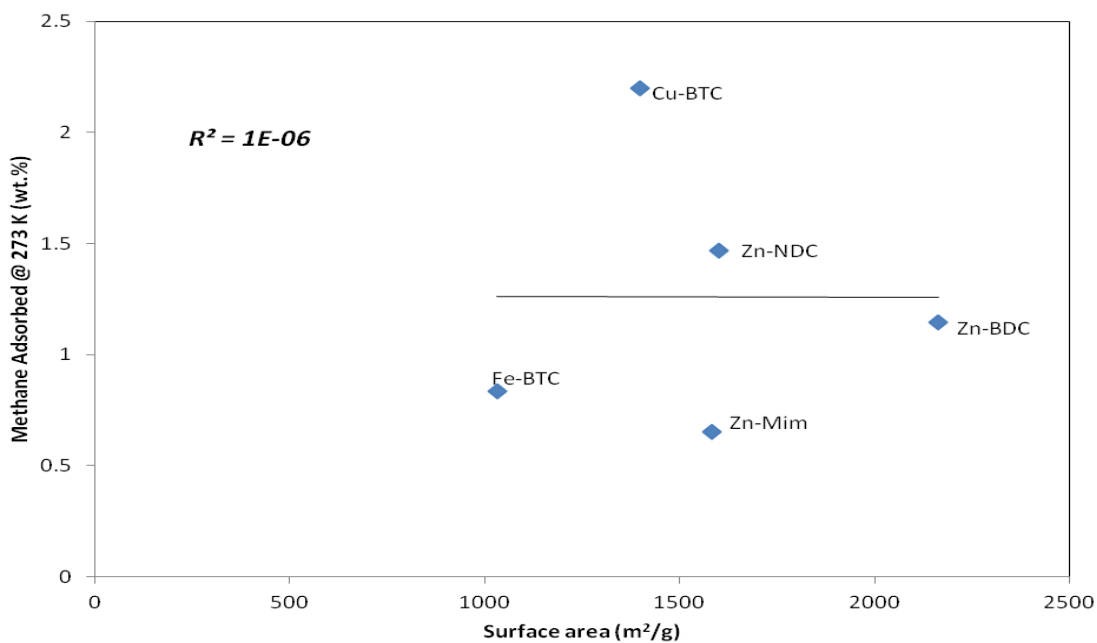


Fig 5.6 (Ai) Low Pressure(LP) plots of surface area vs methane adsorbed for methane adsorption at 273 K

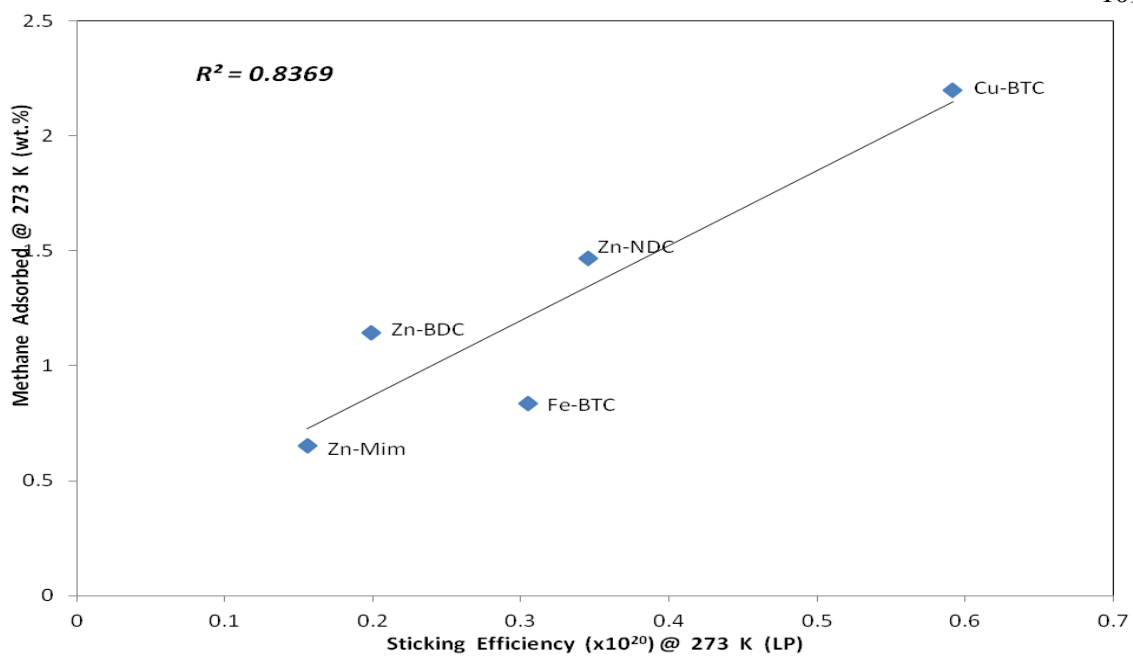


Fig 5.6. (Aii) Low Pressure(LP) plots for sticking efficiency vs methane adsorption at 273 K for this work

Figs. 5.7 (Ai and Aii) show that at room temperature (298 K) under low pressure, the BET surface area R-squared value was 0.0145 versus its sticking efficiency R-squared value which was 0.7528.

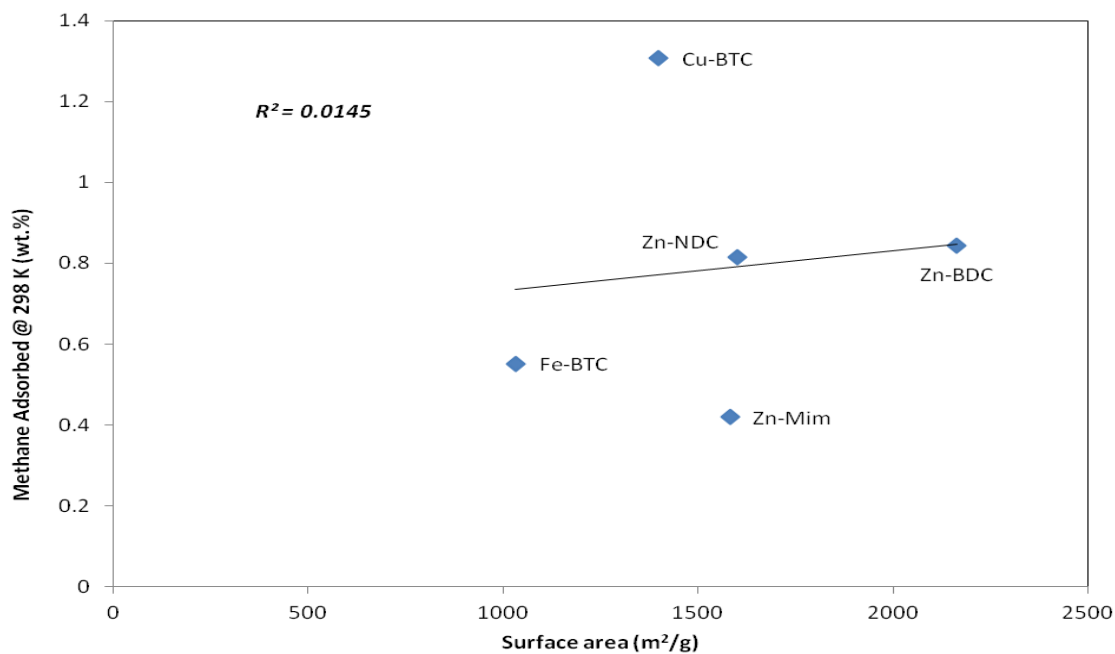


Fig 5.7. (Ai) Low Pressure(LP) plots for surface area vs methane adsorption at 298 K for this work

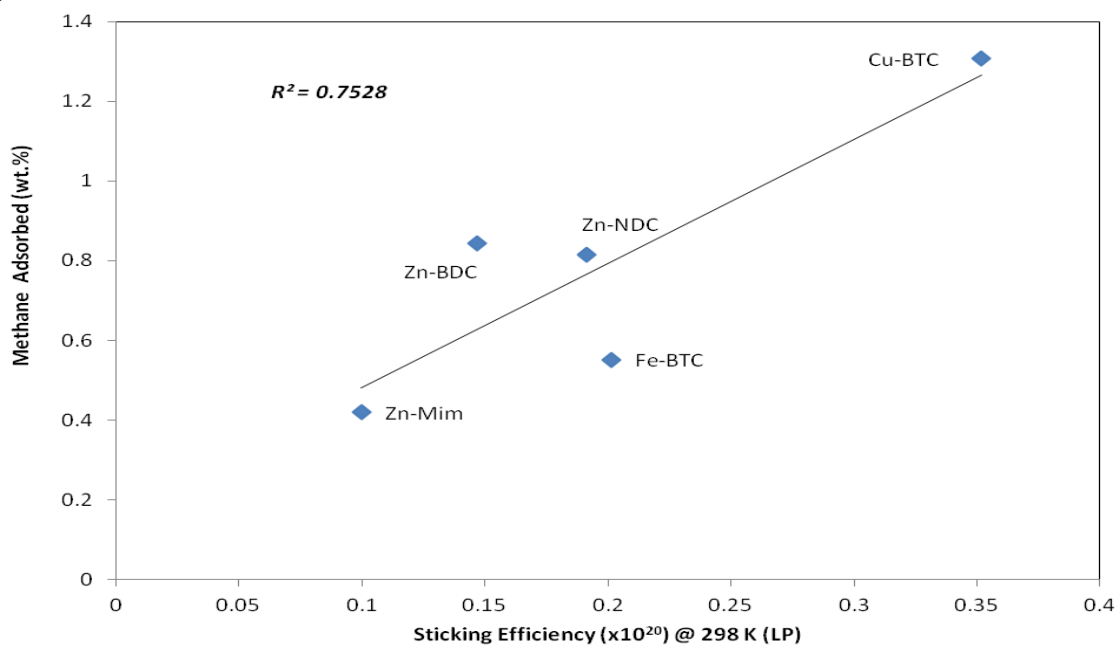


Fig 5.7. (Aii) Low Pressure(LP) plots for sticking efficiency vs methane adsorption at 298 K for this work

At 273 K under high pressure, the BET surface area R-squared value was 0.0024 versus its sticking efficiency R-squared value which was 0.3982 (see Fig. 5.8Ai and Fig. 5.8Aii). This demonstrates that, even at high pressure at temperatures 298 K and 273 K, the R^2 values for their sticking efficiencies were still better than those for their BET surface areas. This is possibly due to the occurrence of unsaturation.

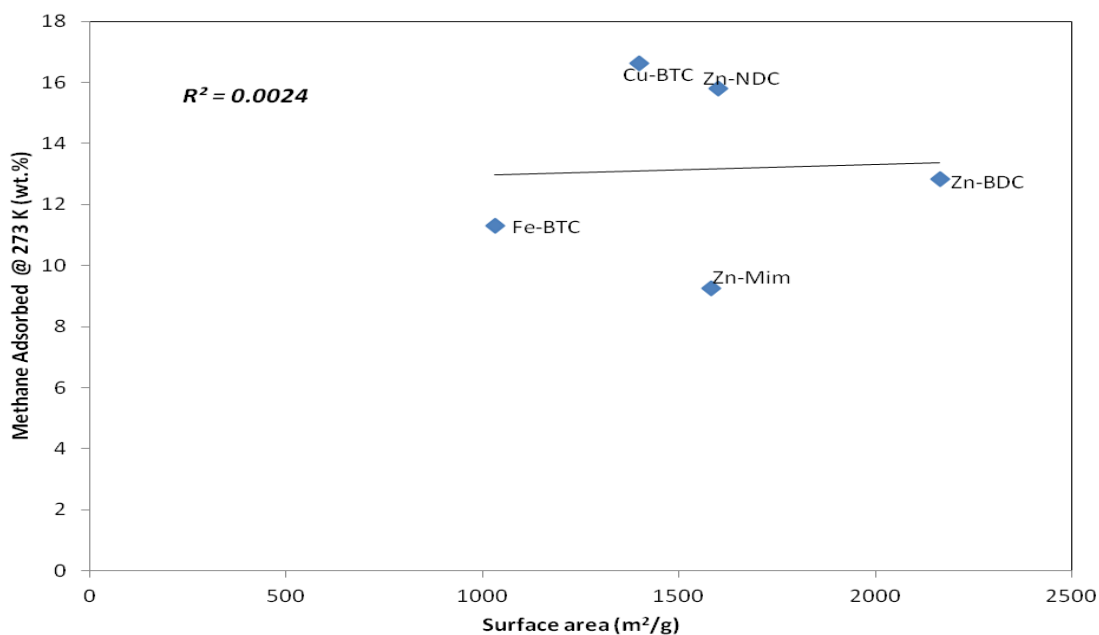


Fig 5.8. (Ai) High Pressure(HP) plots for surface area vs methane adsorption at 273 K for this study

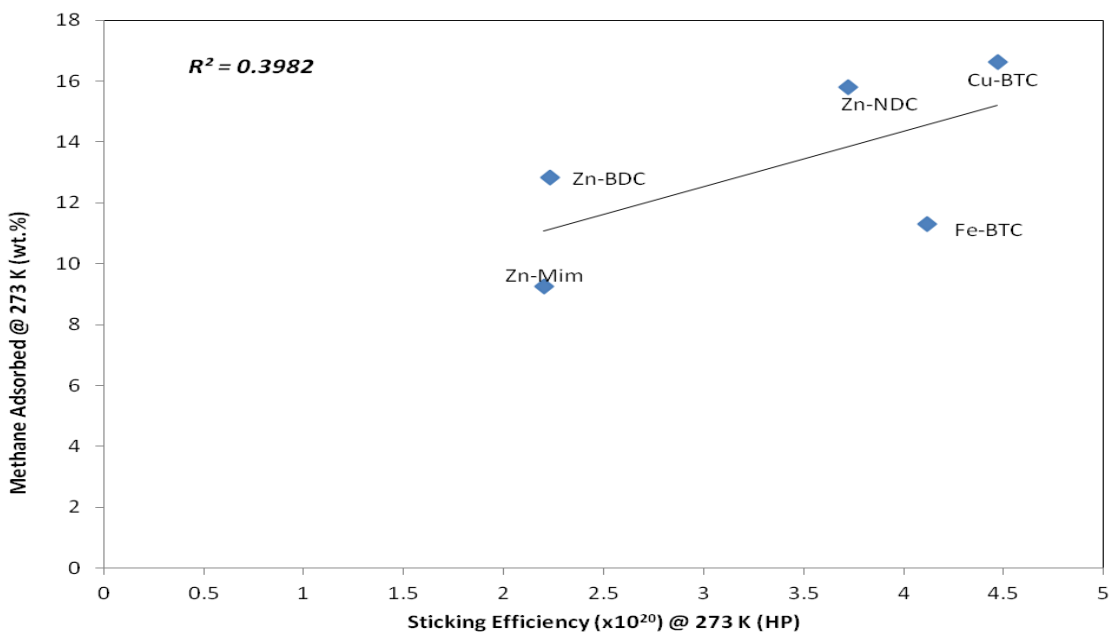


Fig 5.8. (Aii) High Pressure (HP) plots for sticking efficiency vs methane adsorption at 273 K for this study

5.2 Enthalpy of Adsorptions

The isosteric heat of adsorption (at zero coverage) was also determined for these MOFs, and it was correlated with sticking efficiency and surface area. The correlation lines of best fit had R^2 values to be 0.1511 and 0.1795. The graphs are shown in Fig. 5.9Ai and Fig. 5.9Aii, for sticking efficiency and surface area respectively at 273 K. The heat of adsorption is a measure of the binding energies of gas molecules onto the surface of materials. Hence, sticking efficiencies (Θ) correlate well with heat of adsorption (ΔH).

Both results have low R^2 values; however, their BET surface area correlation is still somewhat better than sticking efficiencies. The metal-organic frameworks containing the organic linker terephthalic acid 98 % also appeared in the right hand top section of the graph, except for the iron based MOF (Fe-BTC). This case represents a metal salt having a better sticking efficiency than the other.

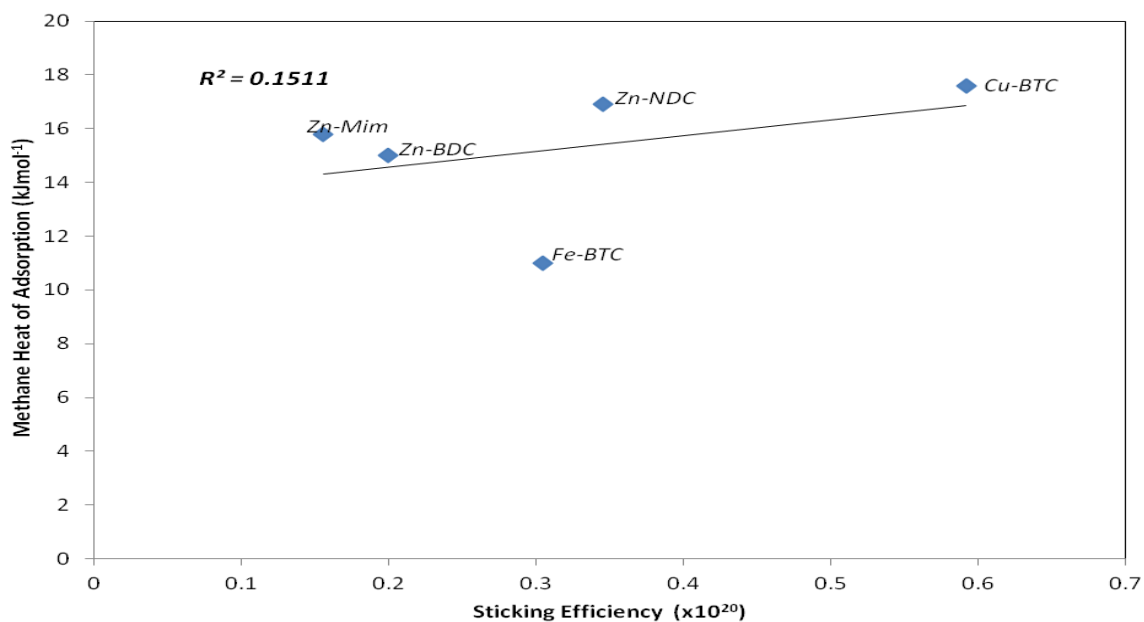


Fig 5.9. (Ai) Sticking efficiency vs enthalpy heat of adsorption for this study

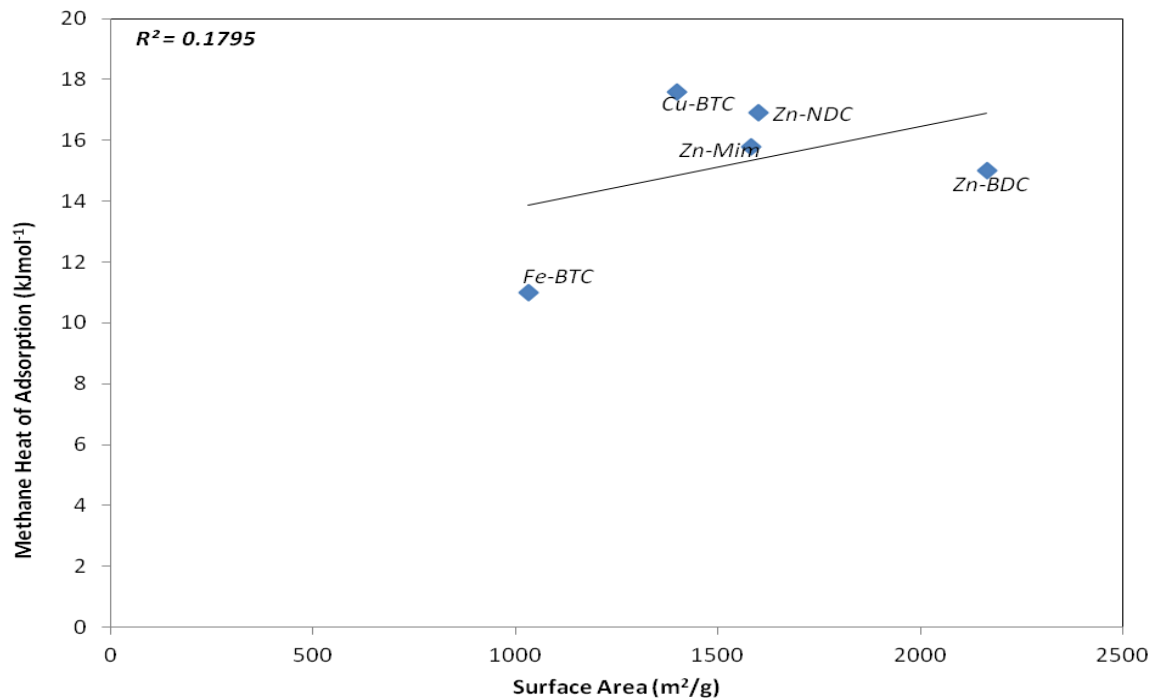


Fig. 5.9. (Aii) Surface area vs enthalpy heat of Adsorption for this study

Table 5.3 show the heat of adsorption at zero coverage for methane gas adsorption at low pressure for this work at 298 K. The data in this table was used to construct plots of heat adsorption versus BET surface area (Fig. 5.9Bi) and heat of adsorption versus sticking efficiency (Fig. 5.9Bii). The graphs showed that, the BET surface area plot had $R^2 = 0.082$; while the sticking efficiency was $R^2 = 0.1361$.

Table 5.3 Low pressure data for CH_4 adsorption @ 298 K

Metal + Linker	MOF	CH_4 wt.% @ 298 K	S.E ($\times 10^{20}$)	BET	ΔH (kJ/mol)	Ref
Cu / BTC	Cu-BTC	1.31	0.35	1398	16.8	<i>This Work</i>
Zn / BDC	Zn-BDC	0.84	0.15	2163	13.2	<i>This Work</i>
Zn / NDC	Zn-NDC	0.81	0.19	1599	15.2	<i>This Work</i>
Fe / BTC	Fe-BTC	0.55	0.2	1031	9.87	<i>This Work</i>
Zn / Mim	Zn-Mim	0.42	0.09	1581	14.7	<i>This Work</i>

The graphs in Fig. 5.9Ci and 5.5Cii show a correlation between ΔH with its θ at 298 K under low pressure. This gives a better results, $R^2 = 0.1344$ when compared to the correlation with its BET surface area under same conditions (<1 Atm., 298 K) which was $R^2 = 0.0929$.

This further demonstrates that, under certain conditions such as low pressures, sticking efficiency (θ) works better than BET surface areas and it (θ) is proportional to the binding energy.

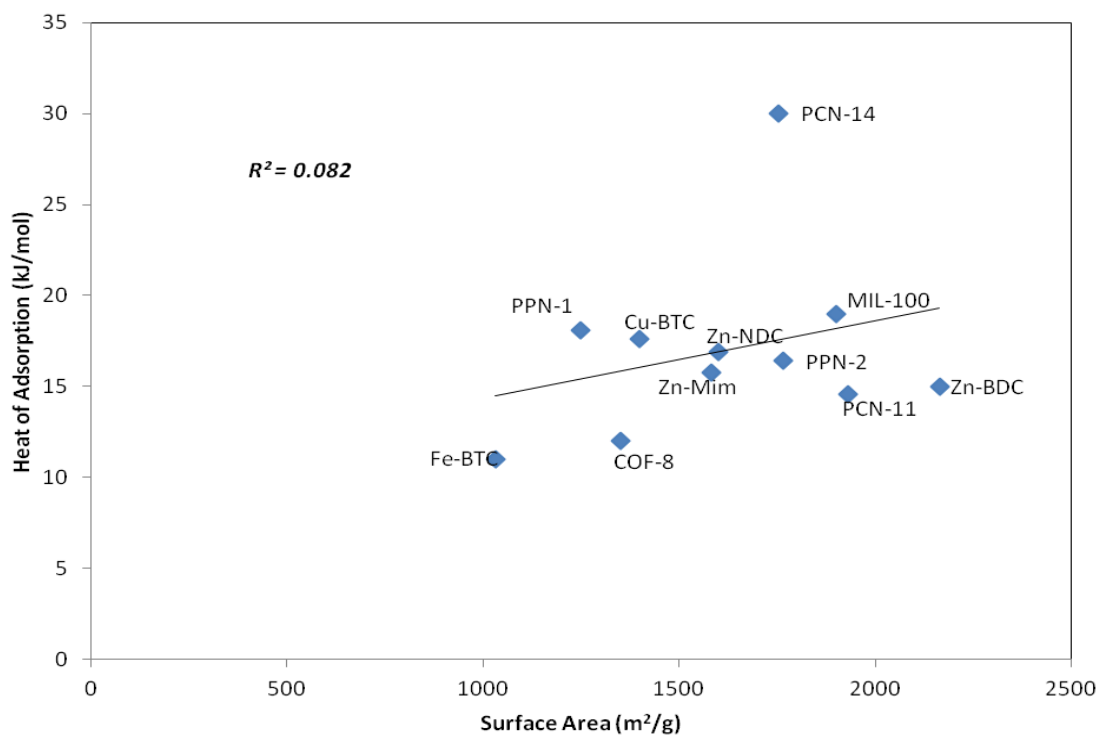


Fig. 5.9 (Bi) Surface area vs enthalpy heat of adsorption at 298 K with other studies

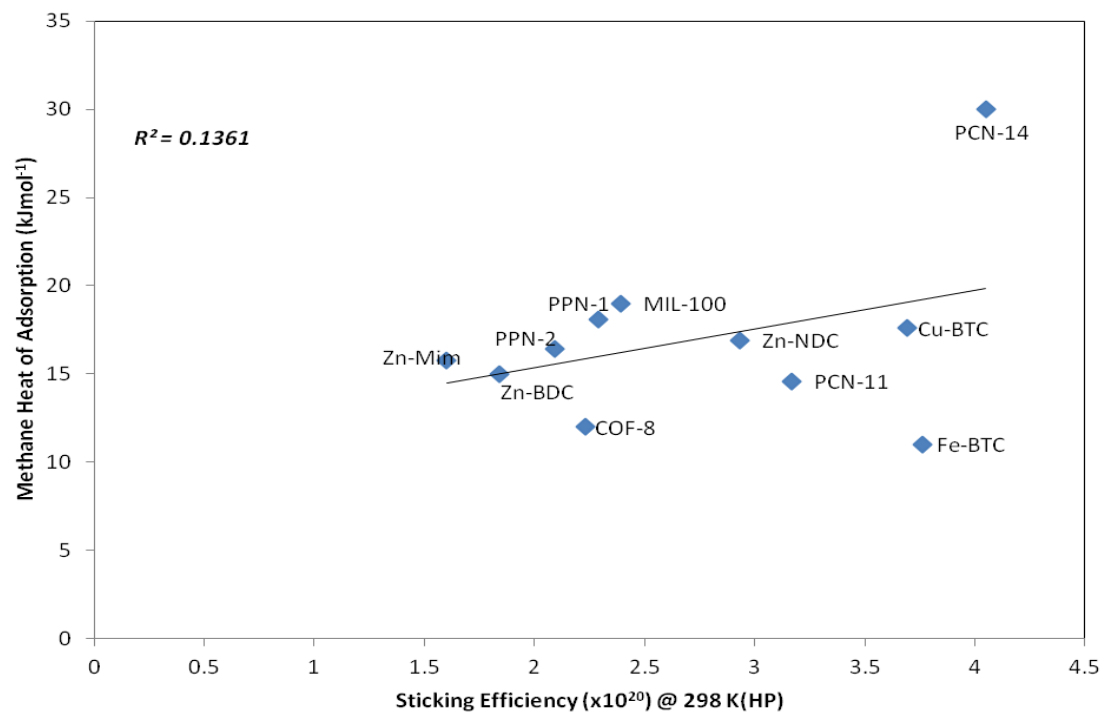


Fig. 5.9. (Bii) Sticking efficiency vs enthalpy heat of adsorption including other studies

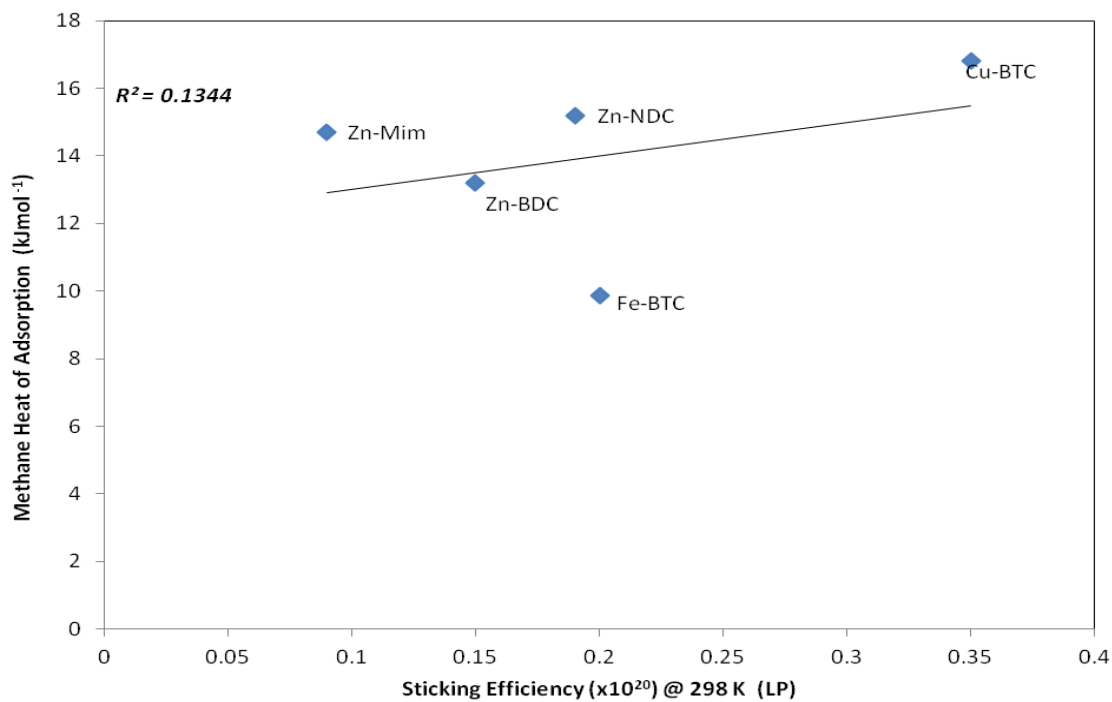


Fig. 5.9. (Ci) Sticking efficiency vs enthalpy heat of adsorption for this study

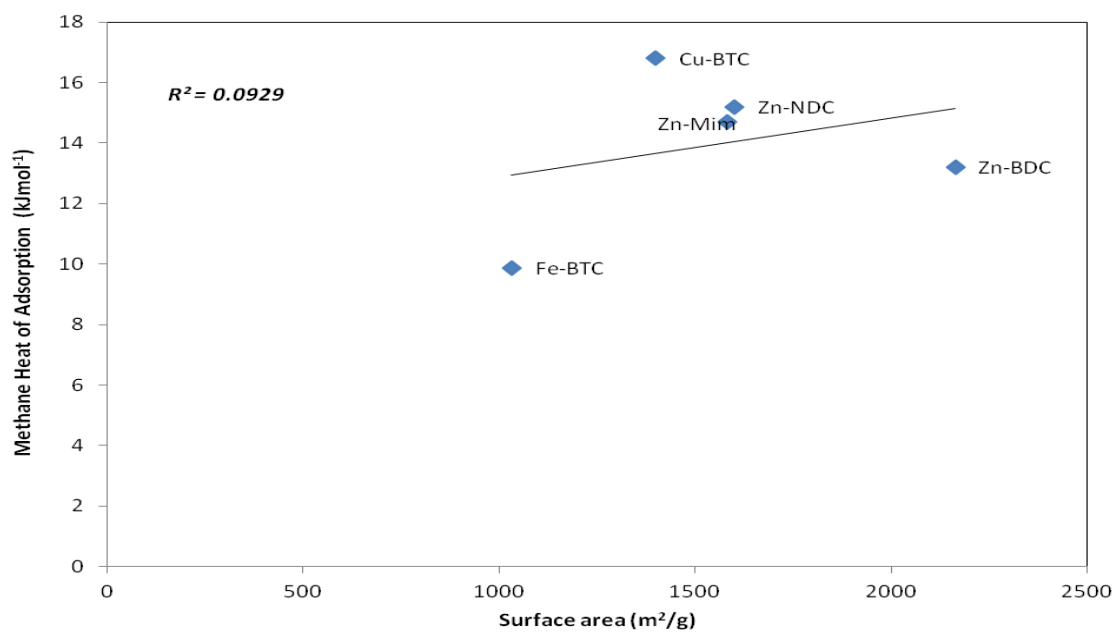


Fig. 5.9. (Cii) Surface area vs anthalpy heat of adsorption at 298 K low pressure for this study

5.3 Summary

In summary, Table 5.4, shows the BET surface area (m^2/g), methane gas adsorptions at different temperatures and pressures along with their corresponding sticking efficiencies.

In the case of methane- CH_4 , the MOFs surfaces still have available sites for gas adsorptions to take place as a result of the unsaturation at both pressures.

Table 5.4 Low Pressure (LP) and High Pressure (HP) calculated values for methane gas adsorptions on selected MOFs

MOFs	BET m^2/g	Wt. % (@ 273K)	Stic. Eff. (@ 273K) $\times 10^{20}$	Wt. % (@ 298K)	Stic. Eff. (@ 298K) $\times 10^{20}$
Zn-BDC	2163	1.15(LP) 12.82(HP)	0.19(LP) 2.23(HP)	0.84(LP) 10.56(HP)	0.15(LP) 1.84(HP)
Zn-NDC	1599	1.47(LP) 15.79(HP)	0.35(LP) 3.72(HP)	0.81(LP) 12.44(HP)	0.19(LP) 2.93(HP)
Zn-Mim	1581	0.65(LP) 9.26(HP)	0.15(LP) 2.20(HP)	0.42(LP) 6.71(HP)	0.09(LP) 1.60(HP)
Fe-BTC	1031	0.84(LP) 11.29(HP)	0.30(LP) 4.12(HP)	0.55(LP) 10.29(HP)	0.20(LP) 3.75(HP)
Cu-BTC	1398	2.19(LP) 16.61(HP)	0.59(LP) 4.47(HP)	1.31(LP) 13.70(HP)	0.35(LP) 3.69(HP)

And also the interactions of their van der Waals forces were also not as strong as that of hydrogen- H_2 at 77 K. Hence, BET surface areas will correlate better with wt.% whenever saturation occurs. In general, it can be stated that, sticking efficiency correlates well for unsaturated surfaces capacities, while BET surface area correlates well when saturation has been achieved.

CHAPTER SIX

CARBON DIOXIDE GAS ADSORPTIONS

6.0 Carbon Dioxide Gas Adsorption Isotherms

Since metal-organic frameworks have been found to be of importance when evaluating or looking for new materials for CO₂ capture, their adsorption capacities and their enthalpies of adsorption are very important. Also understanding the knowledge of their binding environment taking place within the pores of the frameworks can give vital information. The gravimetric uptake of CO₂ which refers to the quantity of CO₂ adsorbed within a unit mass of the materials, forms the basis of mass of the MOFs required to form the absorbent bed. While the volumetric capacities define how the CO₂ can be stored within the material as it also influences the volume of the adsorbent bed.^{37, 191}

Although studies have shown that, high internal surface areas of metal-organic frameworks provide an opportunity for large carbon dioxide adsorption to be achieved due to the efficient packing and close approach of the guest molecules on the pore surface for example, at 35 bar, the volumetric CO₂ adsorption capacity for MOF-177 reaches a storage density of 320 cm³ (STP) / cm³ which is approximately 9 times higher than its quantity stored.³⁷

However this is not always true in all cases. Similar studies have also demonstrated that, MOF-200 with MOF; NU-100 both has surface area of 4530 m²/g and 6143 m²/g

respectively. But their carbon dioxide adsorptions at room temperature (273 K), were 73.9 wt.% and 69.8 wt.% under high pressure respectively.^{111, 192}

The isotherms from this work for low pressure as well as high pressure under different temperature conditions are shown in Fig 6.1 – Fig. 6.4. The data for the weight adsorptions under these conditions are give in Table 6 along with their corresponding calculated sticking efficiencies.

Table 6.1 Low Pressure (LP) and High Pressure (HP) calculated values for carbon dioxide gas adsorptions on selected MOFs

MOFs	BET ² (m ² /g)	Wt. % (@ 273K)	Stic. Eff. (@ 273K) ²⁰ x10	Wt. % (@ 298K)	Stic. Eff. (@ 298K) ²⁰ x10
Zn-BDC	2163	10.5(LP) 48.3(HP)	0.66(LP) 3.06(HP)	7.47(LP) 39.5(HP)	0.47(LP) 2.49(HP)
Zn-NDC	1599	13.2(LP) 61.1(HP)	1.13(LP) 5.20(HP)	7.80(LP) 49.8(HP)	0.67(LP) 4.26(HP)
Zn-Mim	1581	6.1(LP) 40.0(HP)	0.52(LP) 3.46(HP)	2.89(LP) 32.6(HP)	0.25(LP) 2.82(HP)
Fe-BTC	1031	9.2(LP) 55.5(HP)	1.22(LP) 7.37(HP)	5.81(LP) 45.4(HP)	0.77(LP) 6.03(HP)
Cu-BTC	1398	32.4(LP) 63.9(HP)	3.17(LP) 6.26(HP)	18.3(LP) 55.3(HP)	1.79(LP) 5.41(HP)

6.1 Carbon Dioxide Gas Adsorption

The lower-pressure (< 1 atm.) weight percents for the selected metal-organic frameworks collected at temperatures, 298 K and 273 K are presented in Table 6.1, while weight percents for MOFs from this research and cited literatures are presented in Table 6.2. At lower pressure studies, Snurr et. al., reported that Cu-BTC had a Langmuir surface area of 1492 m²/g and adsorbed 18.4 wt.% CO₂ at 298 K.¹⁹³ Pepe et. al. in 2010, reported that

the same MOFs under the same conditions had a surface area of $1400 \text{ m}^2/\text{g}$ and adsorbed 19.8 wt.% CO_2 at 293 K to be ¹⁹⁴. These are comparable to the Cu-BTC carbon dioxide adsorption results from this work which were synthesized using the mechano-chemical assist method. The result of Cu-BTC for this work was 18.3 wt.% CO_2 . The BET Langmuir surface area were $1398 \text{ m}^2/\text{g}$ and $1622 \text{ m}^2/\text{g}$ respectively under same conditions as earlier reported.

The low pressure isotherms representations from this study at 273 K and 298 K are represented in Fig. 6.1 and Fig. 6.2

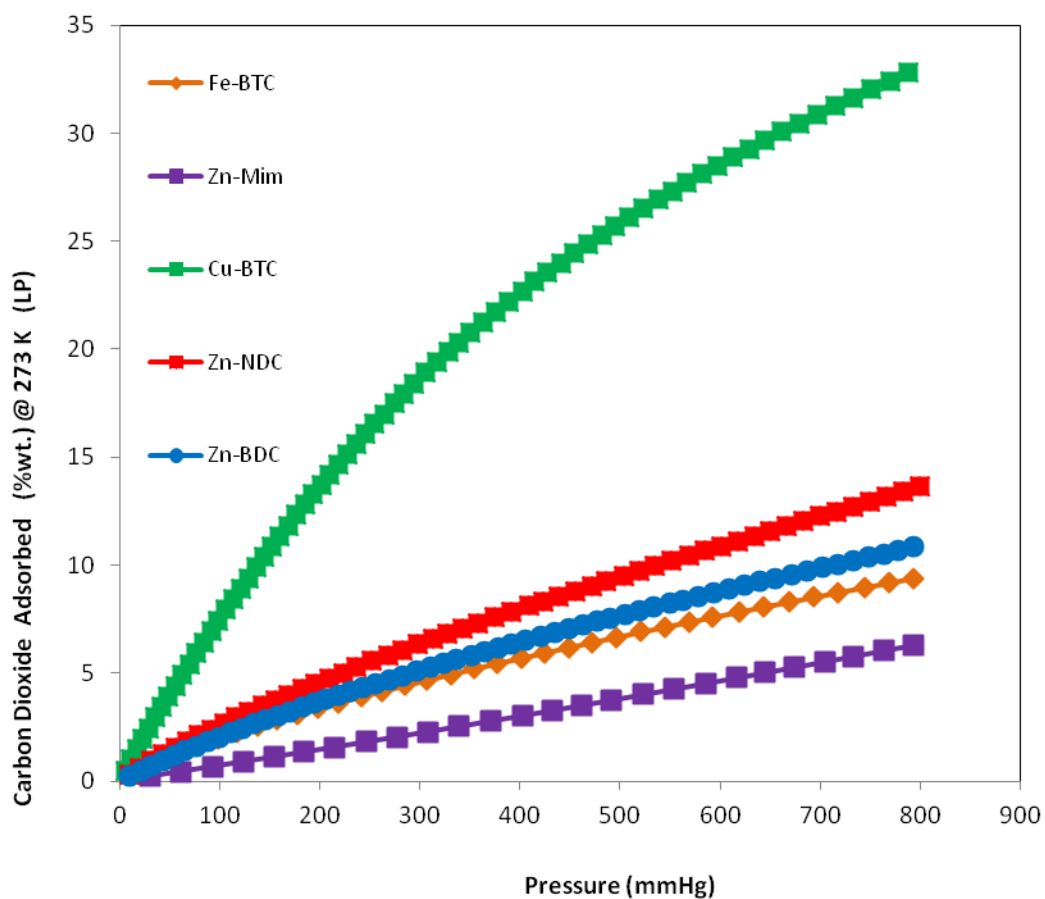


Fig.6.1. Carbon dioxide adsorption Isotherms for low pressure (273 K)MOFs used in this work

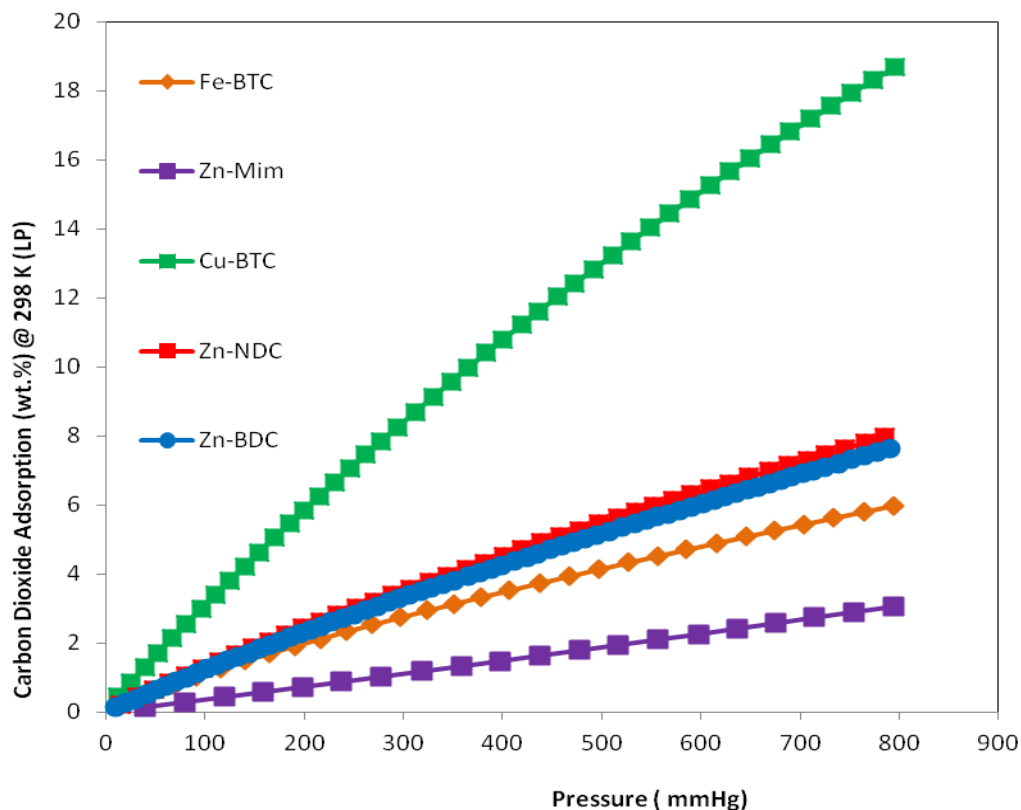


Fig.6.2. Carbon dioxide adsorption Isotherms for low pressure (298 K)MOFs used in this work

Interestingly, the results obtained from rapid solvothermal synthesis of Zn-BDC for this work shows that Zn-BDC has a BET surface area of $2163 \text{ m}^2/\text{g}$. This is approximately two times as much CO_2 (7.47 wt.%) at 298 K under low pressure as was obtained by Yaghi et. al.¹⁹⁵ They found that, Zn-BDC has surface area of $2833 \text{ m}^2/\text{g}$ and a CO_2 wt.% of 4.5 at 298 K under low pressure. Also, Lin et. al.¹⁹⁶ reported a Zn-BDC surface area of $2304 \text{ m}^2/\text{g}$ with CO_2 adsorption of 8.5 wt.% under low pressure and temperature of 296 K. Another study by Yaghi's group,¹⁰¹ reported a surface area for Zn-BDC, as $3320 \text{ m}^2/\text{g}$ at room temperature (298 K) under low pressure and a CO_2 adsorption of 3.2 wt.%.

These results show that, adsorptions of gases do not generally depend on high surface areas of materials.

The isotherms shown on Fig. 6.3 and Fig. 6.4 are the result of CO₂ gas adsorptions under high pressure and at different temperatures. All MOFs used in this work show saturated isotherms. Under high pressure and at ice temperature of 273 K and room temperature of 298 K the metal salt copper (Cu), having the organic linker BTC, had the highest weight percent of the gas adsorptions. Porous materials like MOFs have pores inside which enable them to store gas inside.¹⁹⁷ CO₂ storage at high pressure is not only based on the materials BET surface area, it also based on pore volume. We have earlier shown the relationship between BET surface area and pore volume in a previous chapter in this work. Saturation of CO₂ gas was noticeable from its isotherms at 298 K under high pressure compared to low pressure at 298 K. Hence, the sticking efficiency were not correlating better than BET surface areas.

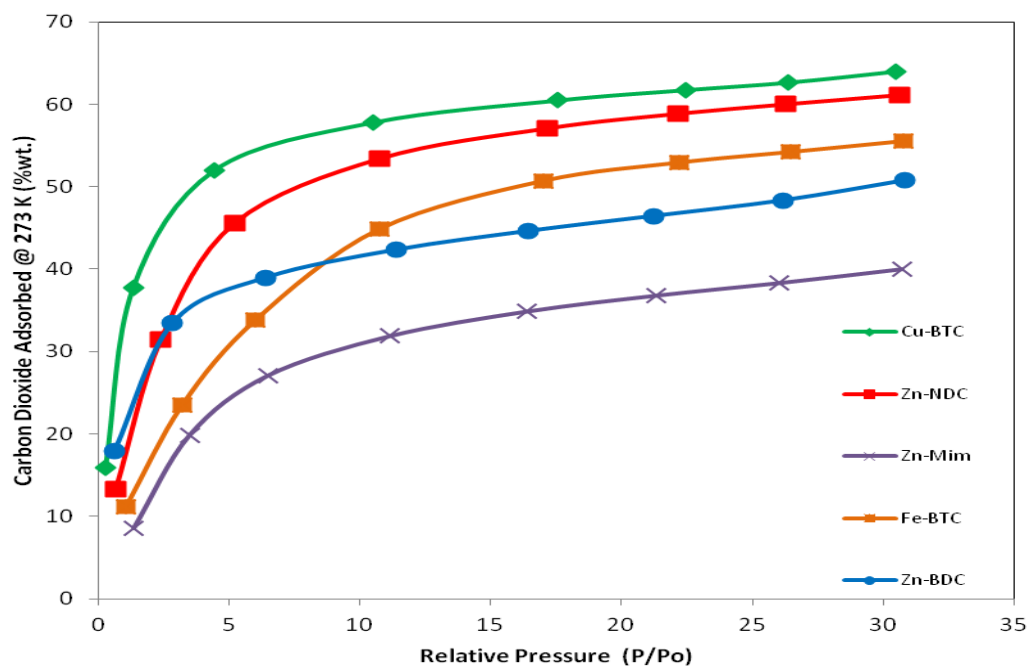


Fig.6.3. Carbon dioxide adsorption Isotherms for high pressure (273 K)MOFs used in this work

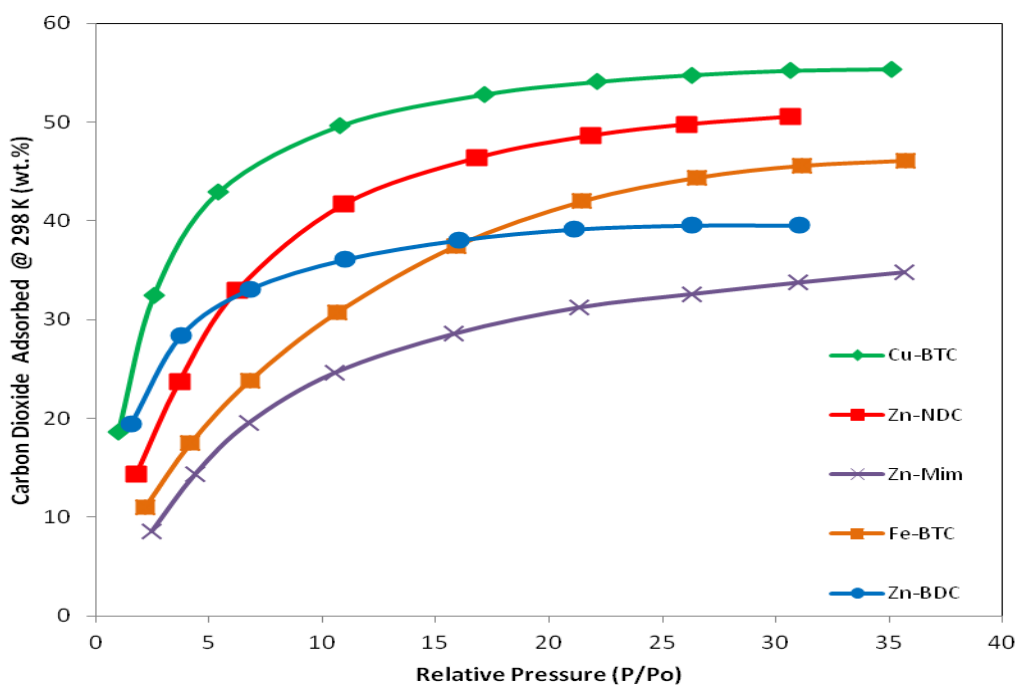


Fig.6.4. Carbon dioxide adsorption Isotherms for high pressure (298 K)MOFs used in this work

Table 6.2 Carbon Dioxide Adsorption Sticking Efficiency (Θ) at Low and High Pressures Studies

MOFs	Metal	Org. Linker	Surface area ($m^2 g^{-1}$)	CO ₂ (Wt.%) 273 K	CO ₂ (Wt.%) 298 K	Sticking Eff. 273 K ($\times 10^{20}$)	Sticking Eff. 298 K ($\times 10^{20}$)	ΔH (kJ mol ⁻¹)	Ref.
Zn-BDC	Zn	BDC	2163	10.5(LP) 48.3(HP)	7.47(LP) 39.5(HP)	0.66(LP) 3.06(HP)	0.47(LP) 2.50	17.6	This Work
Zn-NDC	Zn	NDC	1599	13.2(LP) 61.1(HP)	7.80(LP) 49.8(HP)	1.13(LP) 5.2(HP)	0.67(LP) 4.26(HP)	20.4	This Work
Zn-Mim	Zn	Mim	1581	6.1(LP) 40.0(HP)	2.89(LP) 32.6(HP)	0.52(LP) 3.46(HP)	0.25(LP) 2.82(HP)	19.4	This Work
Cu-BTC	Cu	BTC	1398	32.4(LP) 63.9(HP)	18.3(LP) 55.3(HP)	3.17(LP) 6.26(HP)	1.80(LP) 5.41(HP)	25.1	This Work
Fe.BTC	Fe	BTC	1031	9.2(LP) 55.5(HP)	5.81(LP) 45.4(HP)	1.22(LP) 7.37(HP)	0.77(LP) 6.03(HP)	20	This Work
Cu-EBTC	Cu	BTC	1852	25.9(LP)	-	1.91(LP)	-	-	198
CAU-1	Al	BDC	1268	24.1(LP)	-	2.60(LP)	-	-	199
MOF-23	Cu	NDC	760	8.9(LP)	-	1.60(LP)	-	-	200
SNU-15	Co	MTB	356	7.0(LP)	-	2.69(LP)	-	-	201
BIF-9-Li	Li	BTet β	1523	6.6(LP)	-	0.59(LP)	-	-	202
BIF-9-Cu	Cu	Mim	1287	6.3(LP)	-	0.67(LP)	-	-	202
PCN-6	Cu	TATB	3811	-	15.9(LP)	-	0.57(LP)	-	203
MOF-177	Zn	BTB	5400 4500	- -	3.6(LP) 60.8(HP)	- -	0.15(LP) 1.85(HP)	-	191 37, 41
IRMOF-3	Zn	BDC-NH ₂	2160	-	5.1(LP)	-	0.32(LP)	19	37
MOF-253	Al	bpydc	2160	-	6.2(LP)	-	0.39(LP)	23	204
CPL-2	Cu	pzdc-bpy	633	-	6.6(LP)	-	1.43(LP)	26	37

MOFs	Metal	Org. Linker	Surface area ($m^2 g^{-1}$)	CO ₂ (Wt.%) 273 K	CO ₂ (Wt.%) 298 K	Sticking Eff. 273 K ($\times 10^{20}$)	Sticking Eff. 298 K ($\times 10^{20}$)	ΔH ($kJ mol^{-1}$)	Ref.
Fe-BTT	Fe	BTT	2010	-	13.5(LP)	-	0.92(LP)		205
SNU-50	Cu	bdcppi	2300	-	13.7(LP)	-	0.82(LP)		206
ZIF-78	Zn	nblm	620	-	9.1(LP)	-	2.01(LP)		37, 207
Mg-MOF-74	Mg	dobdc	1174	-	27.5(LP)	-	3.21(LP)	47	208
				68.9(HP)	-	6.12(HP)	-	30	
Co-MOF-74	Co	dobdc	957	-	24.5(LP)	-	3.5(LP)	37	209
Ni-MOF-74	Ni	dobdc	1218	-		-			30
				54.2(HP)		6.09(HP)		209	
MOF-210	Zn	Btb/bpd c	6240		-	-			192
					74.2(HP)	-	1.63(HP)		
MOF-200	Zn	Bbc	4530	-	-	-	-		192
				-	73.9(HP)	-	2.23(HP)		
NU-100	Cu	TCEPE B	6143	-	-	-	-		210
				-	69.8(HP)	-	1.56(HP)		
MOF-205	Zn	BTB- NDC	4460	-	-	-	-		192
				-	62.6(HP)	-	1.92(HP)		
PCN-68	Cu	ptei	5109	-	-	-	-		211
				-	57.2(HP)	-	1.53(HP)		
IMOF-3	Zn	IDC	802	-	8.6(LP)	-	1.47(LP)		212
IRMOF-11	Zn	pdc	2096	-	7.3(LP)	-	0.48(LP)		195
				-		-			
Co21-MOF-5	Co	BDC	2700	-	-	-	-		213
				54.2	-	3.29			

The R-squared value obtained from the sticking efficiency versus wt.% for carbon dioxide gas adsorption in Fig. 6.5(Ai) was 0.9359 and it correlates better than the BET

surface area versus wt.% which was 0.0262 as shown in Fig.6.5(Aii) The regression line had a negative (-) slope under low pressure and at ice temperature (273 K). Also when other cited studies were included the results were $R^2 = 0.5168$ and $R^2 = 0.0637$ for sticking efficiencies and BET surface area versus wt.% respectively, at 273 K(see Fig.6.5 (Bi and Bii)).

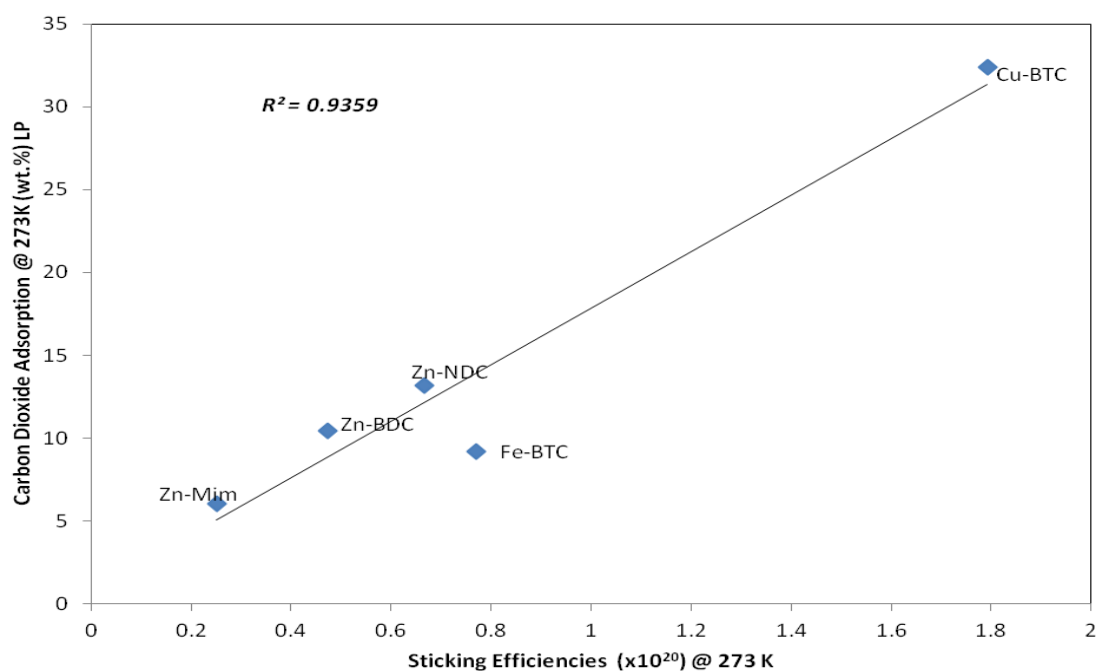


Fig.6.5. (Ai) Sticking efficiency vs carbon dioxide gas adsorbed at 273 K under low pressure (LP) for this work

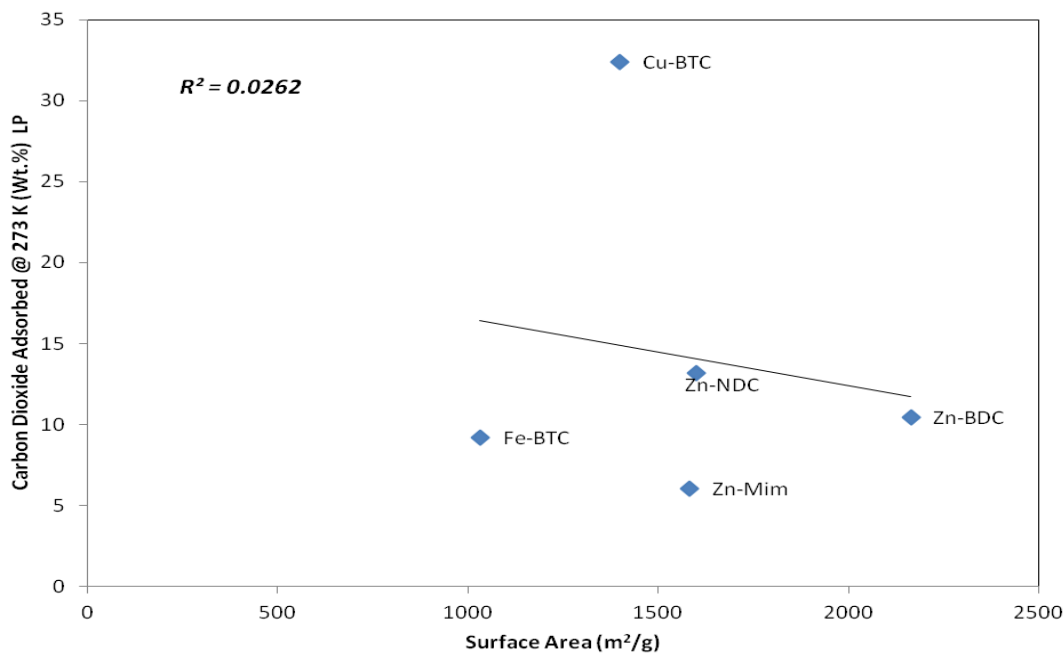


Fig.6.5. (Aii) Surface area vs carbon dioxide gas adsorbed @ 273 K under low pressure (LP) for this work

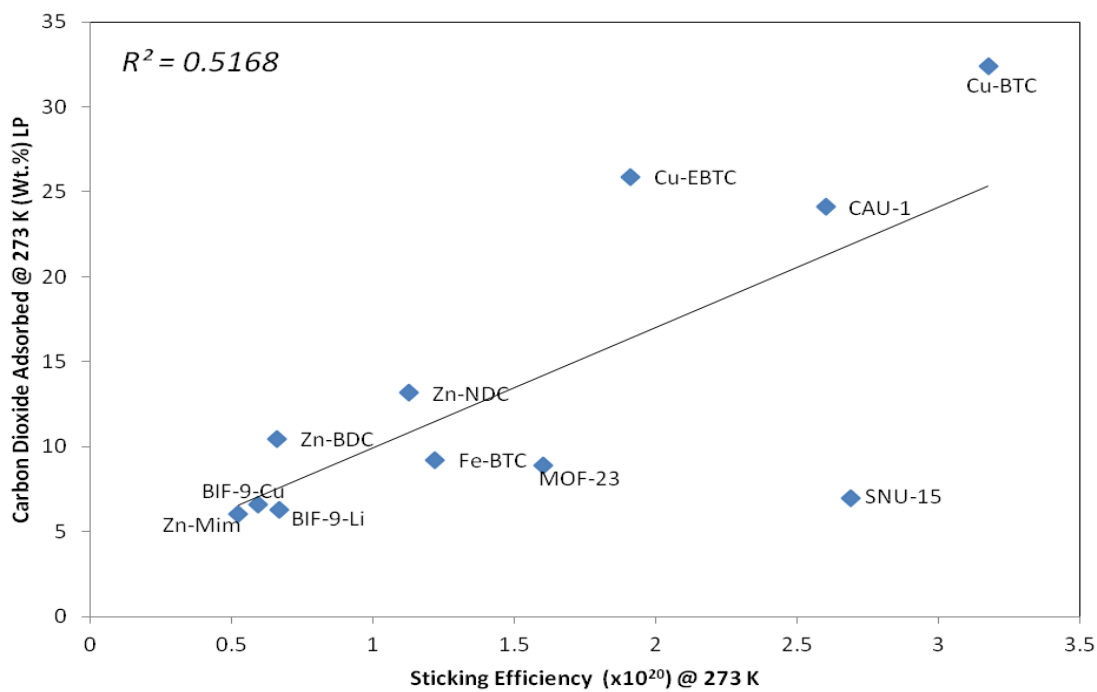


Fig.6.5. (Bi) Sticking efficiency vs carbon dioxide gas adsorbed including other studies

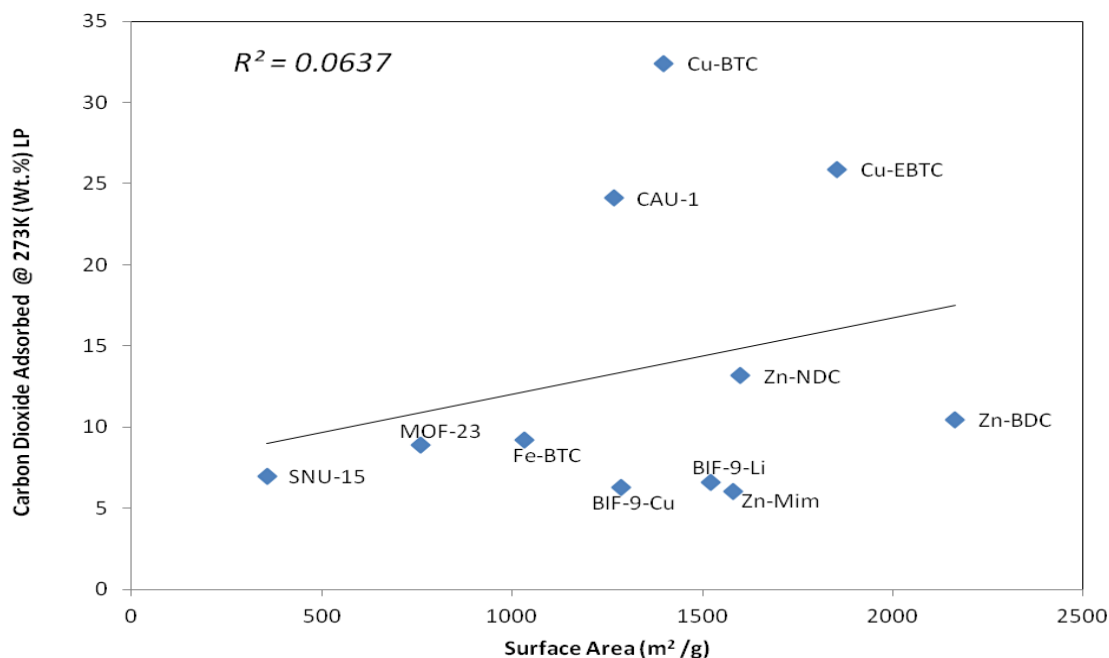


Fig.6.5. (Bii) Surface area vs carbon dioxide gas adsorbed including this stuiesy

The same trend was also observed for CO₂ gas adsorption at 298 K; with $R^2 = 0.9212$ for wt.% versus sticking efficiency as shown in Fig.6.6(Ai), while $R^2 = 0.0095$ for BET surface area at the same room temperature (see Fig. 6.6(Aii)). When their correlations were determined with other MOFs, the obtained R-squared was 0.6798 for sticking efficiency (see Fig.6.6(Bi)) and 0.021 for BET surface area versus their wt.% (see Fig.6.6(Bii)).

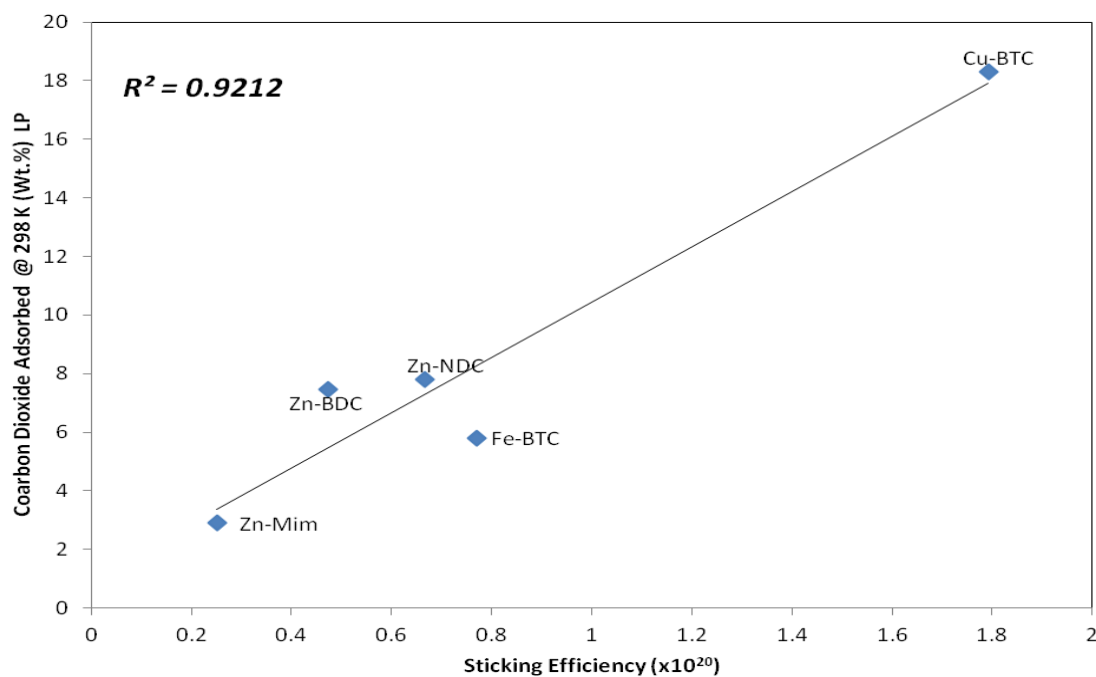


Fig.6.6(Ai). Low pressure (LP) plots for carbon dioxide adsorption at 298 K for sticking efficiency for this work

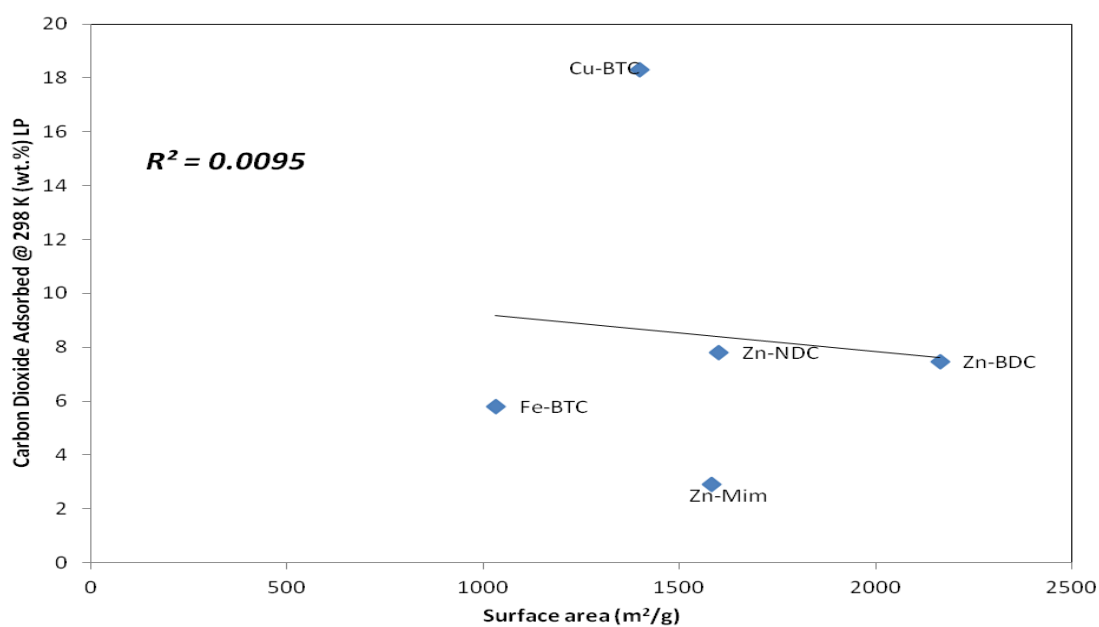


Fig 6.6 (Aii) Low Pressure plots for carbon dioxide adsorption at 298 K with surface area for this work

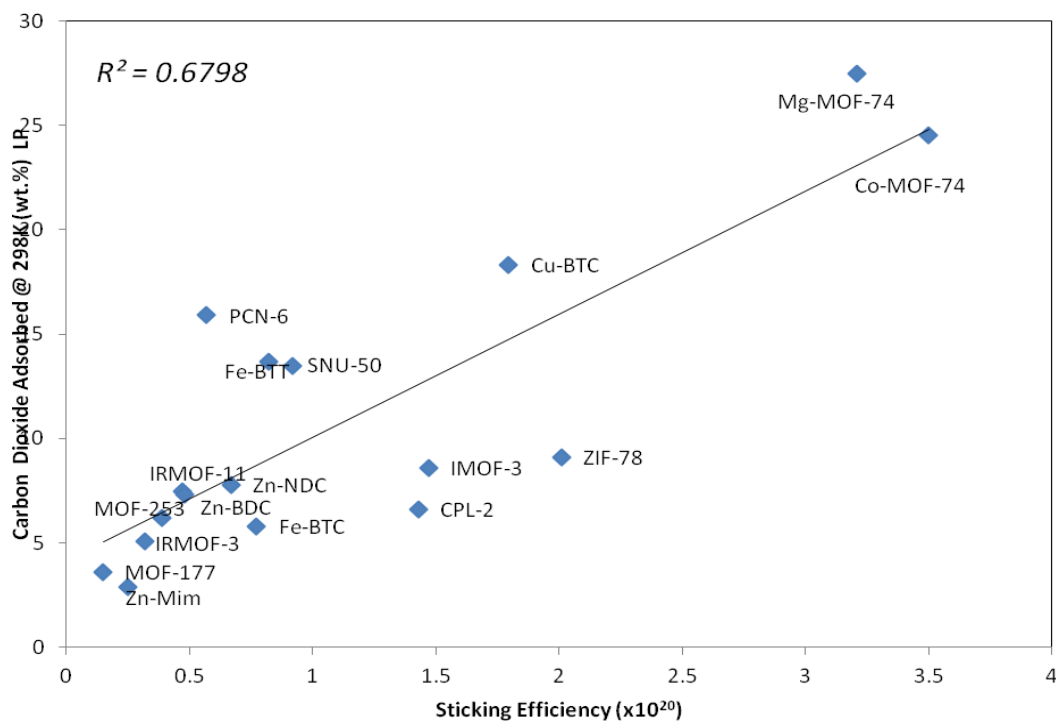


Fig.6.6 (Bi). Other studies (Sticking Efficiency) including this study

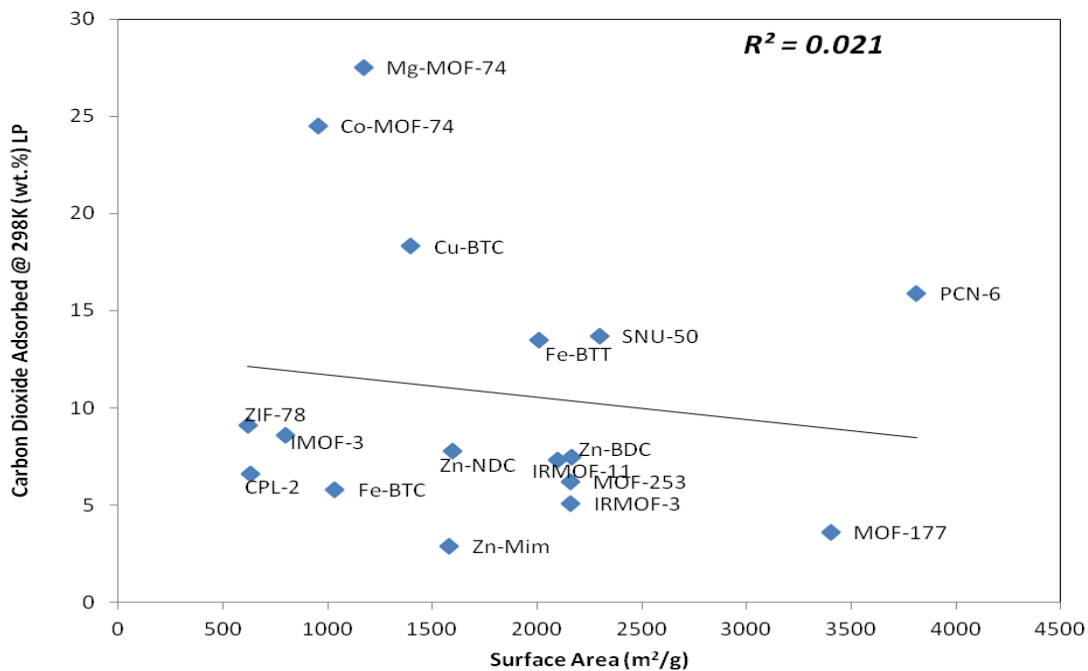


Fig.6.6 (Bii). Other studies (Surface Area) including this study

CO₂ gas adsorption for high pressure was also determined. It was found that similar trends were existed. Fig. 6.7(Ai) and Fig. 6.7(Aii) were obtained for sticking efficiency and had $R^2 = 0.5007$ and BET surface area plot was $R^2 = 0.1346$. When the compared with other literatures, R-squared results obtained were $R^2 = 0.4507$ for sticking efficiency versus wt.% and $R^2 = 0.0665$ for surface area versus wt.% (see Fig' 6.7(Bi) and Fig. 6.7(Bii) at 273 K. It was also observed that at low pressure there was no saturation.

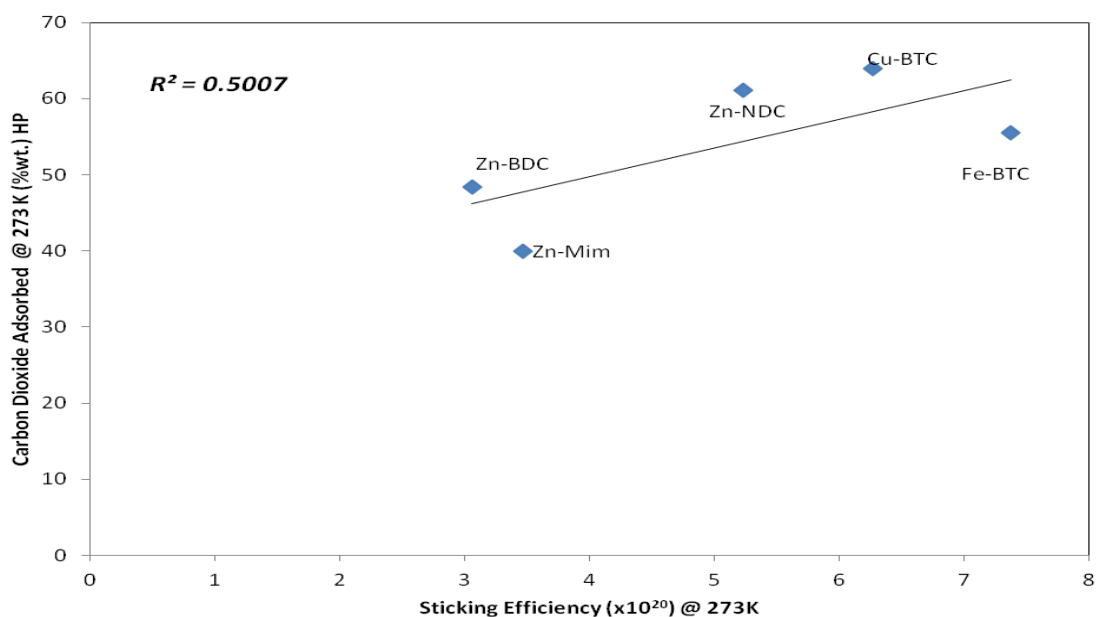


Fig.6.7.(Ai). Sticking efficiency vs weight per cent for carbondioxide at 273 K under high pressure (HP) for this work

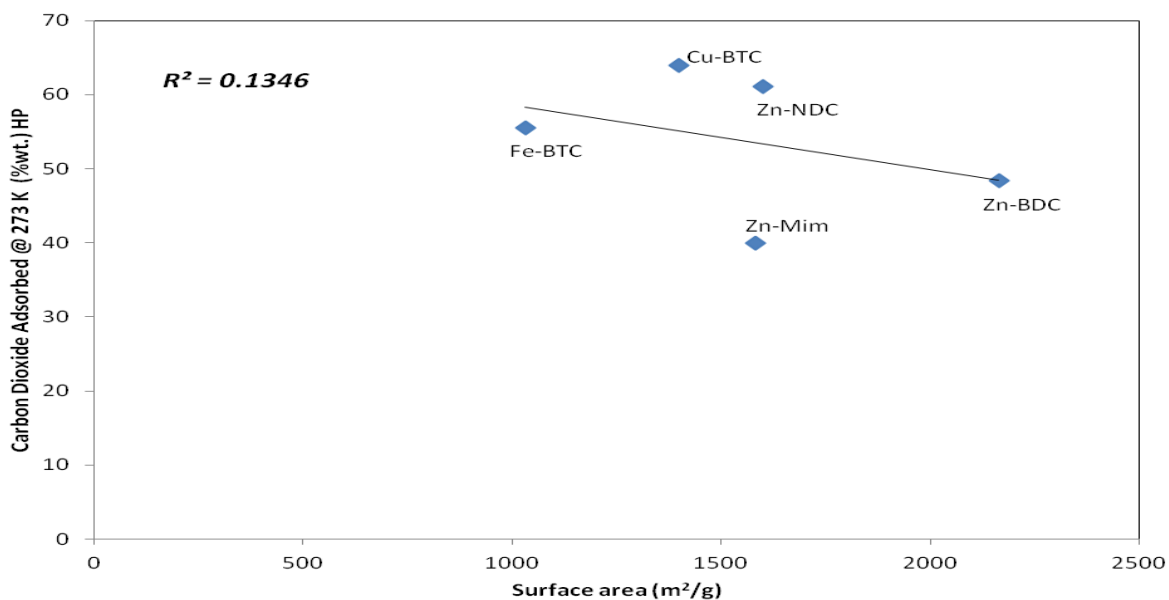


Fig.6.7 (Aii). Surface area vs weight per cent for this work

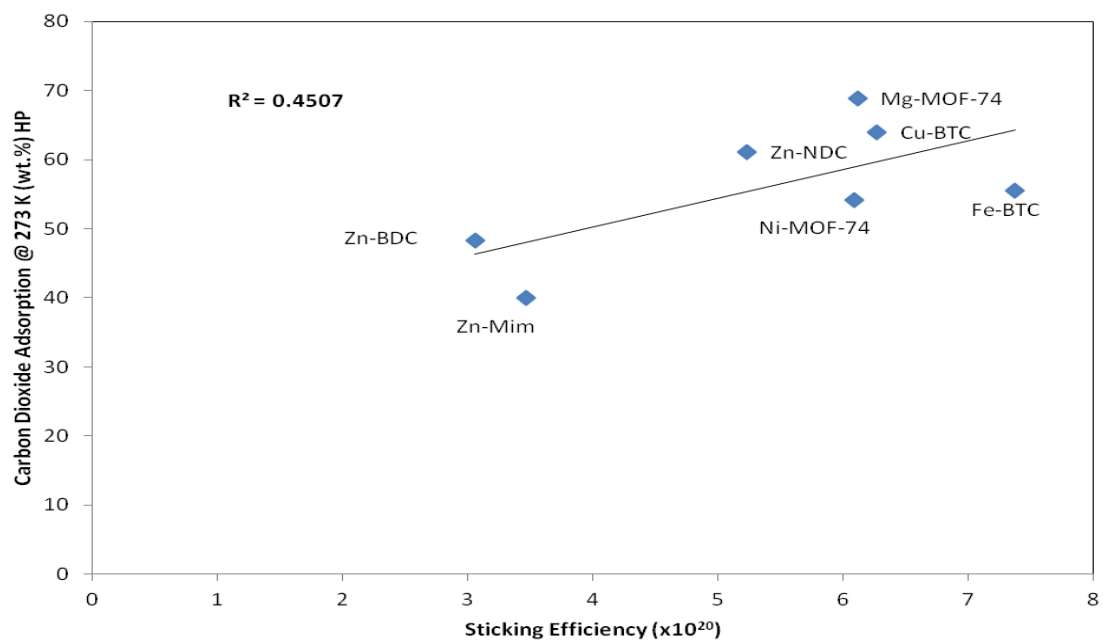


Fig.6.7 (Bi). Other studies for sticking efficiency vs carbon dioxide at 273 K under high pressure(HP)

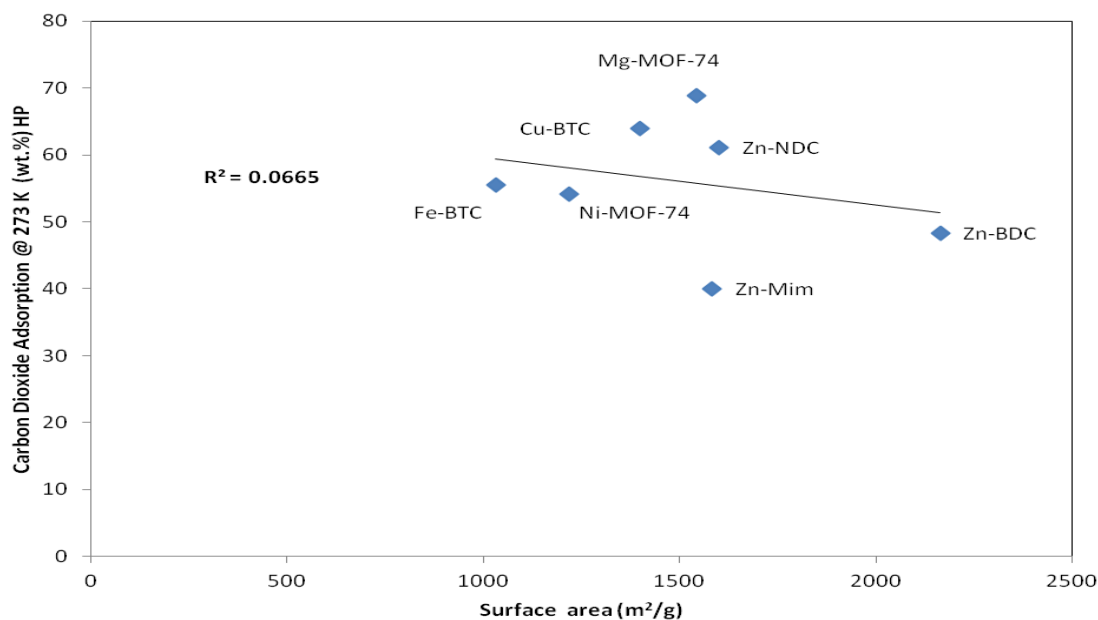


Fig. 6.7 (Bii). Other studies with surface area included this study

However, the story was different at 298 K under high pressure for the sticking efficiency and BET surface area. It was found that there were opposite behavioral properties. At 298 K, the R-square results were 0.5329 and 0.1327 for sticking efficiencies and BET surface areas respectively (see Fig. 6.8(Ai) and Fig. 6.8(Aii)). For other literature studies, their obtained results are shown Fig 6.16 and Fig. 6.17. The $R^2 = 0.2121$ for sticking efficiency with the line having a negative slope. This makes it worse better than surface area which was found to be 0.6742 for BET surface area with a positive slope (see Fig 6.8(Bi) and Fig.6.8(Bii)).

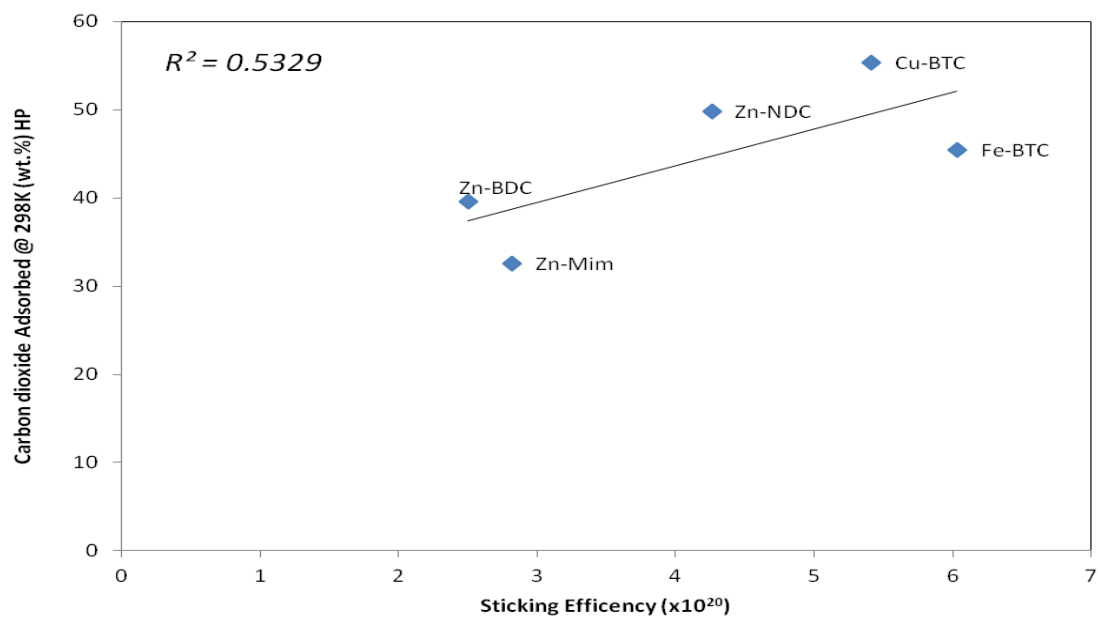


Fig.6.8 (Ai). High Pressure plots for sticking efficiency vs carbon dioxide adsorption at 298K

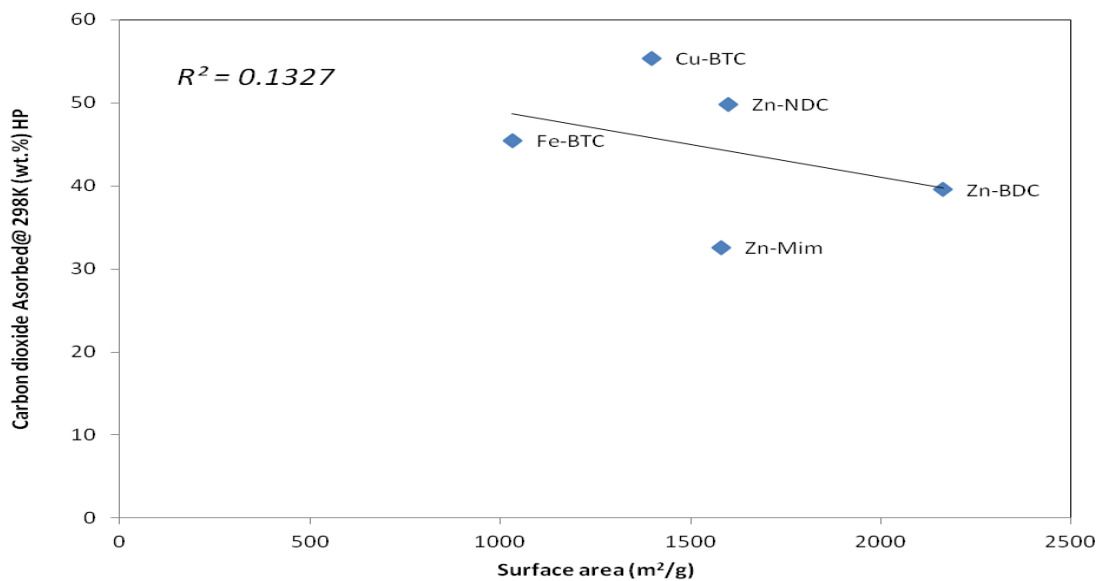


Fig.6.8 (Aii). High Pressure plots for surface area vs carbon dioxide adsorption at 298K

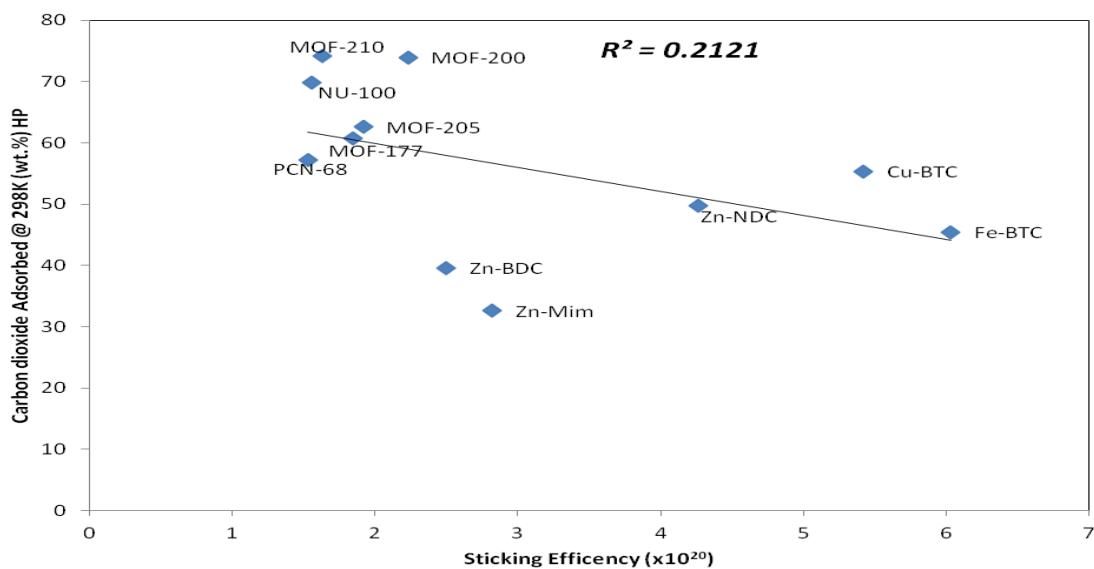


Fig.6.8 (Bi). Other studies for sticking efficiency included in this study

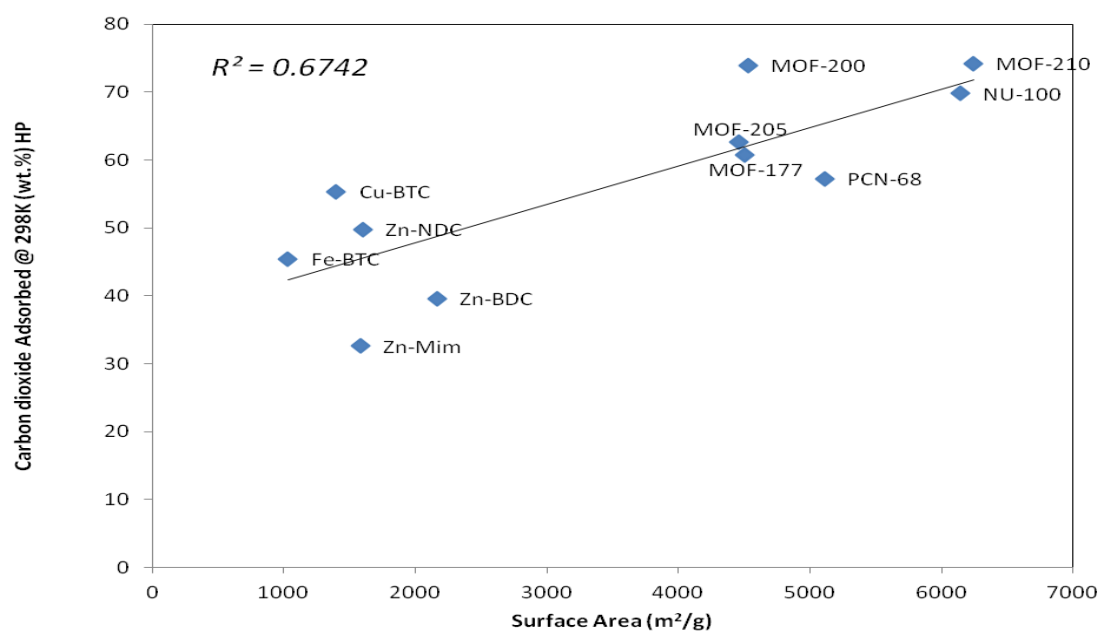


Fig.6.8 (Bii). Other studies for surface area included in this study

6.2 Enthalpy of Adsorptions

The ΔH , which is the isosteric heat of adsorption at zero coverage has been known to be proportional to wt.%. The ΔH versus sticking efficiency and ΔH versus surface area

results had R^2 values of 0.9176 and 0.2443 respectively for synthesized MOFs studied in this work (see Fig.6.9(Ai) and Fig. 6.9(Aii)) below. With other MOFs the R-squared values were 0.8495 for sticking efficiency and 0.2497 for BET surface area. The good correlation with sticking efficiency indicates that the binding energy is directly related to their wt.% at low pressure (see Fig.6.9(Bi) and Fig.6.9(Bii)).

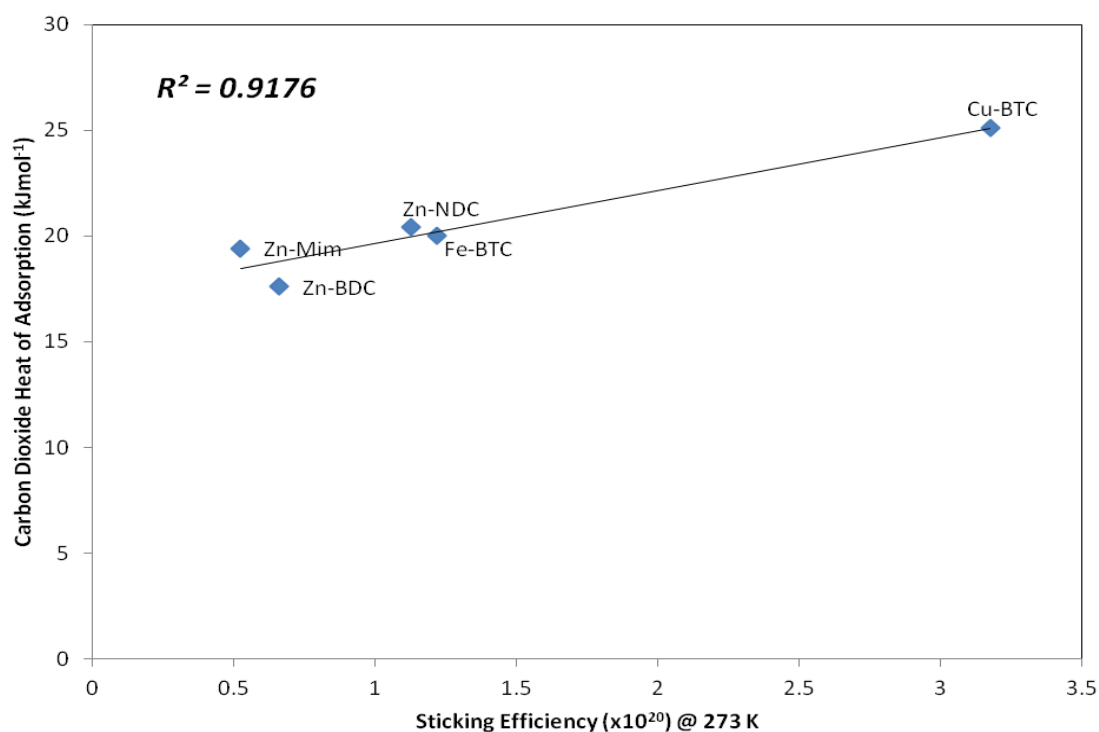


Fig.6.9 (Ai). This study sticking efficiency vs enthalpy heat of adsorption

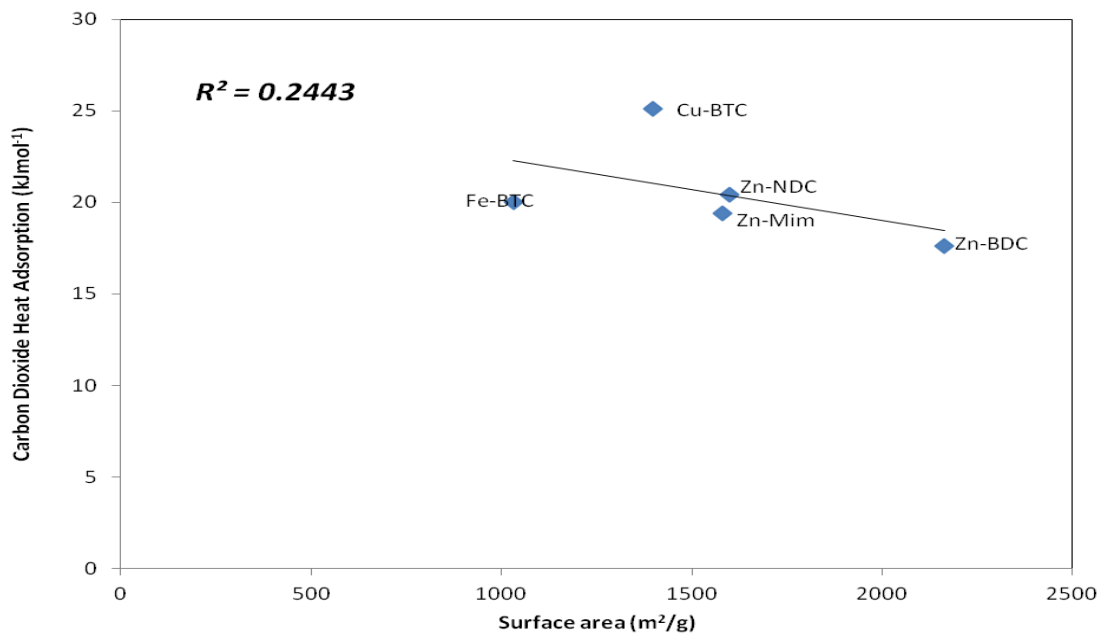


Fig.6.9 (Aii). This study surface area vs enthalpy heat of adsorption

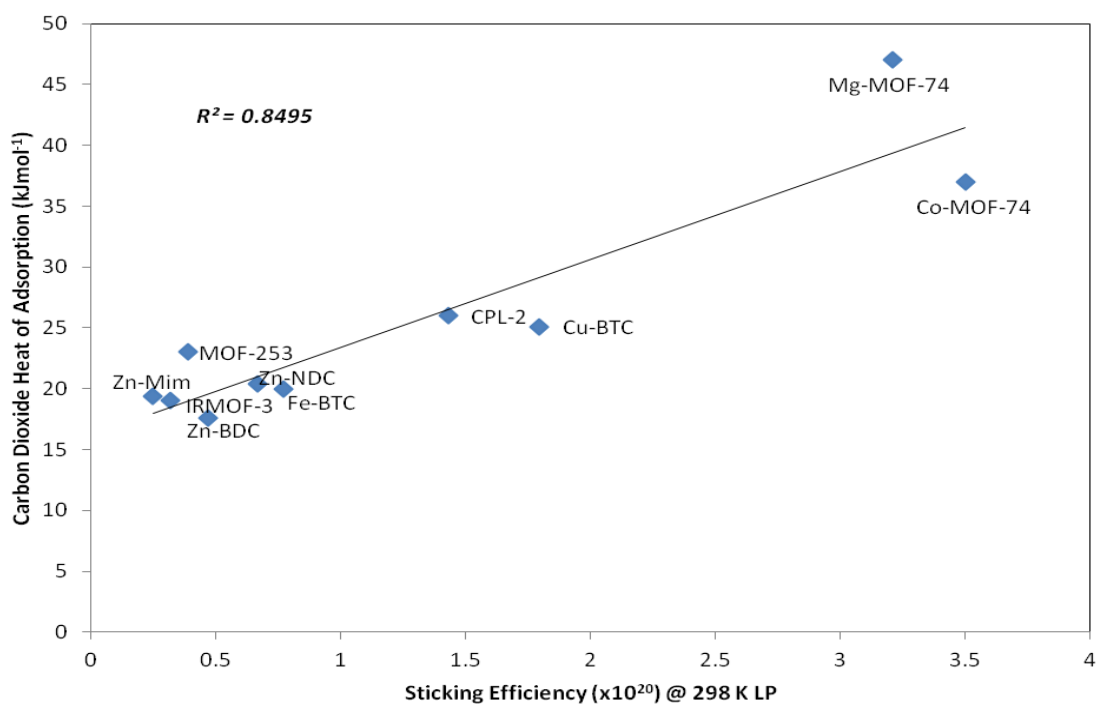


Fig.6.9 (Bi). Other studies for sticking efficiency included in this study

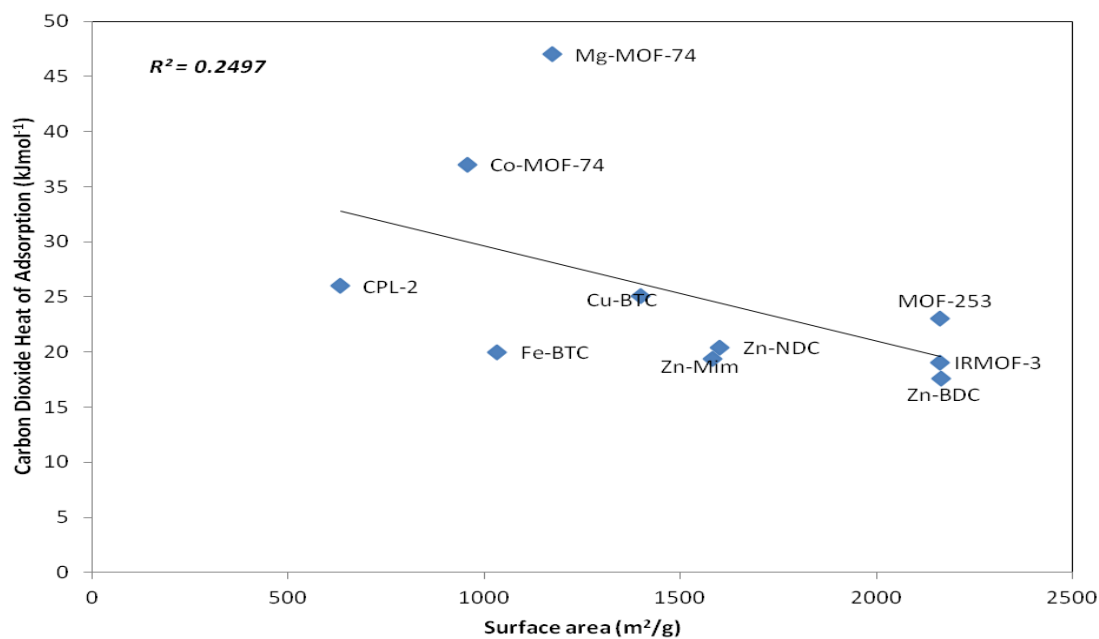


Fig.6.9 (Bii). Other studies surface area included in this study

6.3 Summary

In general, the overall conclusion is that “saturation” and “unsaturation” play a very important role on whether. BET surface area or sticking efficiency correlates with wt.%. When there is unsaturation, the sticking efficiency correlates better than BET surface area. But at 298 K under high pressure the BET surface area correlates better than sticking efficiency.

CHAPTER SEVEN

CONCLUSION

7.0 Research Conclusion

This work demonstrates a novel concept supported by new findings. The metal-organic frameworks selected for this work were carefully chosen, also with some others that were randomly chosen from other studies to illustrate universal behavior of the new trends which were discovered. For example, the copper metal containing MOF have open metal sites. It was of interest to know how these open active sites act during different gas adsorptions used in the course of this research. MOFs having a longer organic linker structures such as the PCN series and others having porous structures were chosen. Results show that better correlations consistently exist between sticking efficiencies and weight percent at low pressures because of unsaturations of material surfaces. It also further deepens the truth that at high pressure studies, saturation was not occurring in the case of methane and the sticking efficiency was still better. But as saturations are achieved, the BET surface area will be having better correlations over the sticking efficiency.

Finally, achieving saturation and un-saturation is the bedrock for the basis of weather sticking efficiency (θ) or BET surface area (m^2/g) is better over one another.

7.1 Future Works Recommendation

This work still requires further development;

- In the area of synthesis, more MOFs with different organic linker(s) structures and inorganic salt(s) should be synthesized in the laboratory; this will help reduce cost and time of productions.
- In area of characterization; MOFs should further be characterized using other adsorbate (gas (es)) for instance, Nitrogen gas (N_2) . And also comparison studies in area of wet chemistry where solvents are mainly of higher use to determine how much liquids – to- gas(es) the materials can handle under different conditions
- Sticking efficiency concept (θ) should be further applied to areas such as using the surface of materials to understand separations techniques and processes, as this (“ θ ”) currently works for gas adsorptions on materials.
- Selectivity studies of the gases (H_2 , CO_2 , CH_4 and N_2) should be further carried out to know which MOFs are best to predict selectivity.
- Finally, attempts should be made to further develop the sticking efficiency equation to accommodate or replace reported BET results with Langmuir results in case the BET results aren’t reported.

REFERENCES

1. D. Zhao, D. Yuan and H.-C. Zhou, *Energy & Environmental Science*, 2008, **1**, 222-235.
2. L. Schlapbach, *MRS bulletin*, 2002, **27**, 675-679.
3. L. Schlapbach and A. Züttel, *Nature*, 2001, **414**, 353-358.
4. L. J. Murray, M. Dinca and J. R. Long, *Chemical Society Reviews*, 2009, **38**, 1294-1314.
5. P. Jena, *The Journal of Physical Chemistry Letters*, 2011, **2**, 206-211.
6. S. S. Han, J. L. Mendoza-Cortes and W. A. Goddard Iii, *Chemical Society Reviews*, 2009, **38**, 1460-1476.
7. L. H. Rude, T. K. Nielsen, D. B. Ravnsbæk, U. Bösenberg, M. B. Ley, B. Richter, L. M. Arnbjerg, M. Dornheim, Y. Filinchuk, F. Besenbacher and T. R. Jensen, *physica status solidi (a)*, 2011, **208**, 1754-1773.
8. B. Schmitz, U. Müller, N. Trukhan, M. Schubert, G. Férey and M. Hirscher, *ChemPhysChem*, 2008, **9**, 2181-2184.
9. M. Hirscher, B. Panella and B. Schmitz, *Microporous and mesoporous materials*, 2010, **129**, 335-339.
10. A. U. Czaja, N. Trukhan and U. Muller, *Chemical Society Reviews*, 2009, **38**, 1284-1293.
11. J. R. Long and O. M. Yaghi, *Chemical Society Reviews*, 2009, **38**, 1213-1214.
12. L. Zhou, *Renewable and Sustainable Energy Reviews*, 2005, **9**, 395-408.
13. J. L. C. Rowsell, A. R. Millward, K. S. Park and O. M. Yaghi, *Journal of the American Chemical Society*, 2004, **126**, 5666-5667.
14. S. K. Bhatia and A. L. Myers, *Langmuir*, 2006, **22**, 1688-1700.
15. Q. Wang and J. K. Johnson, *The Journal of Physical Chemistry B*, 1999, **103**, 4809-4813.
16. Q. Wang and J. K. Johnson, *The Journal of chemical physics*, 1999, **110**, 577-586.
17. M. P. Suh, H. J. Park, T. K. Prasad and D.-W. Lim, *Chemical reviews*, 2011, **112**, 782-835.
18. J. H. Park, W. R. Lee, Y. Kim, H. J. Lee, D. W. Ryu, W. J. Phang and C. S. Hong, *Crystal Growth & Design*, 2014, **14**, 699-704.
19. S. McWhorter, C. Read, G. Ordaz and N. Stetson, *Current Opinion in Solid State and Materials Science*, 2011, **15**, 29-38.
20. A. Züttel, *Naturwissenschaften*, 2004, **91**, 157-172.
21. U. Sahaym and M. G. Norton, *Journal of Materials Science*, 2008, **43**, 5395-5429.
22. J. L. Rowsell and O. M. Yaghi, *Angewandte Chemie International Edition*, 2005, **44**, 4670-4679.
23. S. Satyapal, J. Petrovic, C. Read, G. Thomas and G. Ordaz, *Catalysis Today*, 2007, **120**, 246-256.

24. D. Saha, Z. Wei and S. Deng, *Separation and Purification Technology*, 2009, **64**, 280-287.
25. R. B. Getman, Y.-S. Bae, C. E. Wilmer and R. Q. Snurr, *Chemical Reviews*, 2011, **112**, 703-723.
26. J. Sculley, D. Yuan and H.-C. Zhou, *Energy & Environmental Science*, 2011, **4**, 2721-2735.
27. J. Moellmer, E. Celer, R. Luebke, A. J. Cairns, R. Staudt, M. Eddaoudi and M. Thommes, *Microporous and Mesoporous Materials*, 2010, **129**, 345-353.
28. J.-S. Choi, W.-J. Son, J. Kim and W.-S. Ahn, *Microporous and Mesoporous Materials*, 2008, **116**, 727-731.
29. J. Purewal, D. Liu, J. Yang, A. Sudik, D. Siegel, S. Maurer and U. Müller, *international journal of hydrogen energy*, 2012, **37**, 2723-2727.
30. P. D. Dietzel, V. Besikiotis and R. Blom, *Journal of Materials Chemistry*, 2009, **19**, 7362-7370.
31. X. Lin, J. Jia, P. Hubberstey, M. Schröder and N. R. Champness, *CrystEngComm*, 2007, **9**, 438-448.
32. S. M. Cohen, *Chemical reviews*, 2011, **112**, 970-1000.
33. N. Stock and S. Biswas, *Chemical Reviews*, 2011, **112**, 933-969.
34. S. Orefuwa, E. Iriowen, H. Yang, B. Wakefield and A. Goudy, *Microporous and Mesoporous Materials*, 2013, **177**, 82-90.
35. V. Isaeva and L. Kustov, *Russian Journal of General Chemistry*, 2007, **77**, 721-739.
36. H. Yang, S. Orefuwa and A. Goudy, *Microporous and Mesoporous Materials*, 2011, **143**, 37-45.
37. K. Sumida, D. L. Rogow, J. A. Mason, T. M. McDonald, E. D. Bloch, Z. R. Herm, T.-H. Bae and J. R. Long, *Chemical Reviews*, 2011, **112**, 724-781.
38. S. A. Orefuwa, H. Yang and A. J. Goudy, *Microporous and Mesoporous Materials*, 2012, **153**, 88-93.
39. J. L. Rowsell and O. M. Yaghi, *Microporous and Mesoporous Materials*, 2004, **73**, 3-14.
40. J.-R. Li, Y. Ma, M. C. McCarthy, J. Sculley, J. Yu, H.-K. Jeong, P. B. Balbuena and H.-C. Zhou, *Coordination Chemistry Reviews*, 2011, **255**, 1791-1823.
41. C.-H. Lee, 2013.
42. P. Chen, Z. Xiong, J. Luo, J. Lin and K. L. Tan, *Nature*, 2002, **420**, 302-304.
43. T. M. Wigley and D. S. Schimel, *The carbon cycle*, Cambridge University Press, 2005.
44. N. Stern, *The economics of climate change: the Stern review*, Cambridge University Press, 2007.
45. S. Solomon, *Climate change 2007-the physical science basis: Working group I contribution to the fourth assessment report of the IPCC*, Cambridge University Press, 2007.
46. R. Pachauri and A. Reisinger, *IPCC, Geneva*, 2007.

47. N. Nakicenovic and R. Swart, *Special Report on Emissions Scenarios*, Edited by Nebojsa Nakicenovic and Robert Swart, pp. 612. ISBN 0521804930. Cambridge, UK: Cambridge University Press, July 2000., 2000, **1**.
48. S. Lowell, *Characterization of porous solids and powders: surface area, pore size and density*, Springer, 2004.
49. D. Do and H. Do, *Carbon*, 2003, **41**, 1777-1791.
50. D. Do and H. Do, *Adsorption Science & Technology*, 2003, **21**, 389-423.
51. J. Rouquerol, F. Rouquerol, P. Llewellyn, G. Maurin and K. S. Sing, *Adsorption by powders and porous solids: principles, methodology and applications*, Academic press, 2013.
52. J. D. Figueroa, T. Fout, S. Plasynski, H. McIlvried and R. D. Srivastava, *International Journal of Greenhouse Gas Control*, 2008, **2**, 9-20.
53. Q.-R. Fang, T. A. Makal, M. D. Young and H.-C. Zhou, *Comments on Inorganic Chemistry*, 2010, **31**, 165-195.
54. P. L. Llewellyn, S. Bourrelly, C. Serre, A. Vimont, M. Daturi, L. Hamon, G. De Weireld, J.-S. Chang, D.-Y. Hong and Y. Kyu Hwang, *Langmuir*, 2008, **24**, 7245-7250.
55. R. J. Kuppler, D. J. Timmons, Q.-R. Fang, J.-R. Li, T. A. Makal, M. D. Young, D. Yuan, D. Zhao, W. Zhuang and H.-C. Zhou, *Coordination Chemistry Reviews*, 2009, **253**, 3042-3066.
56. S. Ma and H.-C. Zhou, *Chemical Communications*, 2010, **46**, 44-53.
57. K. R. Matranga, A. L. Myers and E. D. Glandt, *Chemical engineering science*, 1992, **47**, 1569-1579.
58. T. Düren, L. Sarkisov, O. M. Yaghi and R. Q. Snurr, *Langmuir*, 2004, **20**, 2683-2689.
59. X. Duan, J. Yu, J. Cai, Y. He, C. Wu, W. Zhou, T. Yildirim, Z. Zhang, S. Xiang and M. O'Keeffe, *Chemical Communications*, 2013, **49**, 2043-2045.
60. H. Wu, J. M. Simmons, Y. Liu, C. M. Brown, X. S. Wang, S. Ma, V. K. Peterson, P. D. Southon, C. J. Kepert and H. C. Zhou, *Chemistry-A European Journal*, 2010, **16**, 5205-5214.
61. W. Zhou, *The Chemical Record*, 2010, **10**, 200-204.
62. K. Konostas, T. Osl, Y. Yang, M. Batten, N. Burke, A. J. Hill and M. R. Hill, *Journal of Materials Chemistry*, 2012, **22**, 16698-16708.
63. M. Kondo, T. Yoshitomi, H. Matsuzaka, S. Kitagawa and K. Seki, *Angewandte Chemie International Edition in English*, 1997, **36**, 1725-1727.
64. D. Collins, S. Ma and H. Zhou, Wiley-VCH, Hoboken, New Jersey, USA, 2009.
65. B. Yilmaz, N. Trukhan and U. MüLLER, *Chinese Journal of Catalysis*, 2012, **33**, 3-10.
66. Y. Chen, V. Lykourinou, T. Hoang, L.-J. Ming and S. Ma, *Inorganic chemistry*, 2012, **51**, 9156-9158.
67. G. Walker, *Solid-state hydrogen storage: materials and chemistry*, Elsevier, 2008.
68. S. J. Gregg, K. S. W. Sing and H. Salzberg, *Journal of The Electrochemical Society*, 1967, **114**, 279C-279C.

69. S. Brunauer, P. H. Emmett and E. Teller, *Journal of the American Chemical Society*, 1938, **60**, 309-319.
70. V. R. Deitz, *Annals of the New York Academy of Sciences*, 1948, **49**, 315-323.
71. V. Deitz, F. Carpenter and R. Arnold, *Carbon*, 1964, **1**, 245-254.
72. C. H. Giles, D. Smith and A. Huitson, *Journal of Colloid and Interface Science*, 1974, **47**, 755-765.
73. C. H. Giles, A. P. D'Silva and I. A. Easton, *Journal of Colloid and Interface Science*, 1974, **47**, 766-778.
74. M. Ray, *Studies in Surface Science and Catalysis*, 1999, **120**, 977-1049.
75. A. Dąbrowski, *Advances in colloid and interface science*, 2001, **93**, 135-224.
76. K. S. Sing, *Colloids and Surfaces A: Physicochemical and Engineering Aspects*, 2004, **241**, 3-7.
77. I. Langmuir, *Journal of the American Chemical Society*, 1916, **38**, 2221-2295.
78. I. Langmuir, *Journal of the American Chemical Society*, 1917, **39**, 1848-1906.
79. I. Langmuir, *Journal of the American Chemical Society*, 1918, **40**, 1361-1403.
80. M. Dubinin, *Chemical Reviews*, 1960, **60**, 235-241.
81. K. S. Sing and R. T. Williams, *Adsorption Science & Technology*, 2004, **22**, 773-782.
82. V. Finsy, S. Calero, E. García-Pérez, P. J. Merklings, G. Vedts, D. E. De Vos, G. V. Baron and J. F. Denayer, *Physical Chemistry Chemical Physics*, 2009, **11**, 3515-3521.
83. R. Bueno-Pérez, E. García-Pérez, J. J. Gutiérrez-Sevillano, P. J. Merklings and S. Calero, *Adsorption Science & Technology*, 2010, **28**, 823-835.
84. K. Sing, *Pure and Applied Chemistry*, 1982, **54**, 2201-2218.
85. J. Rouquerol, G. V. Baron, R. Denoyel, H. Giesche, J. Groen, P. Klobes, P. Levitz, A. V. Neimark, S. Rigby and R. Skudas, *Microporous and Mesoporous Materials*, 2012, **154**, 2-6.
86. K. S. Sing and R. T. Williams, *Adsorption Science & Technology*, 2005, **23**, 839-853.
87. T. Ohba, T. Matsumura, K. Hata, M. Yumura, S. Iijima, H. Kanoh and K. Kaneko, *The Journal of Physical Chemistry C*, 2007, **111**, 15660-15663.
88. Y.-S. Bae, A. O. z. r. Yazaydin and R. Q. Snurr, *Langmuir*, 2010, **26**, 5475-5483.
89. D. Everett, *Pure and Applied Chemistry*, 1972, **31**, 577-638.
90. P. Schneider, *Applied Catalysis A: General*, 1995, **129**, 157-165.
91. K. S. Sing, *Pure and applied chemistry*, 1985, **57**, 603-619.
92. Y. Jiang, F. T. Willmore, D. Sanders, Z. P. Smith, C. P. Ribeiro, C. M. Doherty, A. Thornton, A. J. Hill, B. D. Freeman and I. C. Sanchez, *Polymer*, 2011, **52**, 2244-2254.
93. H. Jovic and D. N. Theodorou, *Microporous and mesoporous materials*, 2007, **102**, 21-50.
94. Y. Yampolskii and B. Freeman, *Membrane gas separation*, Wiley Online Library, 2010.
95. P. A. Webb and C. Orr, *Analytical methods in fine particle technology*, Micromeritics Instrument Corp, 1997.

96. S. R. Batten, N. R. Champness, X.-M. Chen, J. Garcia-Martinez, S. Kitagawa, L. Öhrström, M. O'Keeffe, M. Paik Suh and J. Reedijk, *Pure and Applied Chemistry*, 2013, **85**, 1715-1724.
97. S. R. Batten, N. R. Champness, X.-M. Chen, J. Garcia-Martinez, S. Kitagawa, L. Öhrström, M. O'Keeffe, M. P. Suh and J. Reedijk, *CrystEngComm*, 2012, **14**, 3001-3004.
98. S. S.-Y. Chui, S. M.-F. Lo, J. P. Charmant, A. G. Orpen and I. D. Williams, *Science*, 1999, **283**, 1148-1150.
99. G. Férey, C. Mellot-Draznieks, C. Serre, F. Millange, J. Dutour, S. Surblé and I. Margiolaki, *Science*, 2005, **309**, 2040-2042.
100. P. D. Dietzel, R. E. Johnsen, H. Fjellvåg, S. Bordiga, E. Groppo, S. Chavan and R. Blom, *Chemical communications*, 2008, 5125-5127.
101. H. Deng, C. J. Doonan, H. Furukawa, R. B. Ferreira, J. Towne, C. B. Knobler, B. Wang and O. M. Yaghi, *Science*, 2010, **327**, 846-850.
102. M. Dinca, A. Dailly, Y. Liu, C. M. Brown, D. A. Neumann and J. R. Long, *Journal of the American Chemical Society*, 2006, **128**, 16876-16883.
103. D. Sun, S. Ma, Y. Ke, D. J. Collins and H.-C. Zhou, *Journal of the American Chemical Society*, 2006, **128**, 3896-3897.
104. K. K. Tanabe and S. M. Cohen, *Chemical Society Reviews*, 2011, **40**, 498-519.
105. L.-B. Sun, J.-R. Li, J. Park and H.-C. Zhou, *Journal of the American Chemical Society*, 2011, **134**, 126-129.
106. W. Cao, Y. Li, L. Wang and S. Liao, *The Journal of Physical Chemistry C*, 2011, **115**, 13829-13836.
107. M. Eddaoudi, J. Kim, N. Rosi, D. Vodak, J. Wachter, M. O'Keeffe and O. M. Yaghi, *Science*, 2002, **295**, 469-472.
108. K. S. Walton and R. Q. Snurr, *Journal of the American Chemical Society*, 2007, **129**, 8552-8556.
109. K. Sing, *Colloids and Surfaces A: Physicochemical and Engineering Aspects*, 2001, **187**, 3-9.
110. D.-C. Zhong, J.-B. Lin, W.-G. Lu, L. Jiang and T.-B. Lu, *Inorganic chemistry*, 2009, **48**, 8656-8658.
111. O. K. Farha, I. Eryazici, N. C. Jeong, B. G. Hauser, C. E. Wilmer, A. A. Sarjeant, R. Q. Snurr, S. T. Nguyen, A. O. z. r. Yazaydin and J. T. Hupp, *Journal of the American Chemical Society*, 2012, **134**, 15016-15021.
112. W. Xuan, C. Zhu, Y. Liu and Y. Cui, *Chemical Society Reviews*, 2012, **41**, 1677-1695.
113. O. M. Yaghi, M. O'Keeffe, N. W. Ockwig, H. K. Chae, M. Eddaoudi and J. Kim, *Nature*, 2003, **423**, 705-714.
114. Y. Liu, J.-H. Her, A. Dailly, A. J. Ramirez-Cuesta, D. A. Neumann and C. M. Brown, *Journal of the American Chemical Society*, 2008, **130**, 11813-11818.
115. I. Beurroies, M. Boulhout, P. L. Llewellyn, B. Kuchta, G. Férey, C. Serre and R. Denoyel, *Angewandte Chemie International Edition*, 2010, **49**, 7526-7529.
116. A. Ghoufi and G. Maurin, *The Journal of Physical Chemistry C*, 2010, **114**, 6496-6502.

117. K. Seki, *Physical Chemistry Chemical Physics*, 2002, **4**, 1968-1971.
118. S. Bourrelly, B. Moulin, A. Rivera, G. Maurin, S. Devautour-Vinot, C. Serre, T. Devic, P. Horcajada, A. Vimont and G. Clet, *Journal of the American Chemical Society*, 2010, **132**, 9488-9498.
119. D. Fairen-Jimenez, S. Moggach, M. Wharmby, P. Wright, S. Parsons and T. Duren, *Journal of the American Chemical Society*, 2011, **133**, 8900-8902.
120. D. Dybtsev, C. Serre, B. Schmitz, B. Panella, M. Hirscher, M. Latroche, P. L. Llewellyn, S. Cordier, Y. Molard and M. Haouas, *Langmuir*, 2010, **26**, 11283-11290.
121. C. Zlotea, D. Phanon, M. Mazaj, D. Heurtaux, V. Guillerm, C. Serre, P. Horcajada, T. Devic, E. Magnier and F. Cuevas, *Dalton Transactions*, 2011, **40**, 4879-4881.
122. S. Kitagawa, R. Kitaura and S. i. Noro, *Angewandte Chemie International Edition*, 2004, **43**, 2334-2375.
123. O. K. Farha and J. T. Hupp, *Accounts of chemical research*, 2010, **43**, 1166-1175.
124. D. J. Tranchemontagne, J. L. Mendoza-Cortés, M. O'Keeffe and O. M. Yaghi, *Chemical Society Reviews*, 2009, **38**, 1257-1283.
125. A. Phan, C. J. Doonan, F. J. Uribe-Romo, C. B. Knobler, M. O'keeffe and O. M. Yaghi, *Acc. Chem. Res.*, 2010, **43**, 58-67.
126. S.-Y. Ding and W. Wang, *Chemical Society Reviews*, 2013, **42**, 548-568.
127. J.-X. Jiang and A. I. Cooper, in *Functional Metal-Organic Frameworks: Gas Storage, Separation and Catalysis*, Springer, 2010, pp. 1-33.
128. T. A. Makal, J.-R. Li, W. Lu and H.-C. Zhou, *Chemical Society Reviews*, 2012, **41**, 7761-7779.
129. H.-C. Zhou, J. R. Long and O. M. Yaghi, *Chemical reviews*, 2012, **112**, 673-674.
130. J.-R. Li, J. Sculley and H.-C. Zhou, *Chemical reviews*, 2011, **112**, 869-932.
131. D. Zhao, D. J. Timmons, D. Yuan and H.-C. Zhou, *Accounts of chemical research*, 2010, **44**, 123-133.
132. A. D. Wiersum, J.-S. Chang, C. Serre and P. L. Llewellyn, *Langmuir*, 2013, **29**, 3301-3309.
133. Q. Yang, S. Vaesen, F. Ragon, A. D. Wiersum, D. Wu, A. Lago, T. Devic, C. Martineau, F. Taulelle and P. L. Llewellyn, *Angewandte Chemie*, 2013, **125**, 10506-10510.
134. L. T. Nguyen, C. V. Nguyen, G. H. Dang, K. K. Le and N. T. Phan, *Journal of Molecular Catalysis A: Chemical*, 2011, **349**, 28-35.
135. R. C. Huxford, J. Della Rocca and W. Lin, *Current opinion in chemical biology*, 2010, **14**, 262-268.
136. P. Horcajada, C. Serre, G. Maurin, N. A. Ramsahye, F. Balas, M. Vallet-Regí, M. Sebban, F. Taulelle and G. Férey, *Journal of the American Chemical Society*, 2008, **130**, 6774-6780.
137. T. Loiseau, C. Serre, C. Huguenard, G. Fink, F. Taulelle, M. Henry, T. Bataille and G. Férey, *Chemistry-A European Journal*, 2004, **10**, 1373-1382.
138. G. Lu and J. T. Hupp, *Journal of the American Chemical Society*, 2010, **132**, 7832-7833.

139. W.-G. Lu, L. Jiang, X.-L. Feng and T.-B. Lu, *Inorganic chemistry*, 2009, **48**, 6997-6999.
140. R. T. Yang, *Adsorbents: fundamentals and applications*, John Wiley & Sons, 2003.
141. T. Ben, H. Ren, S. Ma, D. Cao, J. Lan, X. Jing, W. Wang, J. Xu, F. Deng and J. M. Simmons, *Angewandte Chemie*, 2009, **121**, 9621-9624.
142. A. V. Neimark, F.-X. Coudert, A. Boutin and A. H. Fuchs, *The journal of physical chemistry letters*, 2009, **1**, 445-449.
143. A. Boutin, M. A. Springuel-Huet, A. Nossov, A. Gédéon, T. Loiseau, C. Volkringer, G. Férey, F. X. Coudert and A. H. Fuchs, *Angewandte Chemie International Edition*, 2009, **48**, 8314-8317.
144. B. Panella, M. Hirscher, H. Pütter and U. Müller, *Advanced Functional Materials*, 2006, **16**, 520-524.
145. L. Pan, M. B. Sander, X. Huang, J. Li, M. Smith, E. Bittner, B. Bockrath and J. K. Johnson, *Journal of the American Chemical Society*, 2004, **126**, 1308-1309.
146. S. S. Kaye, A. Dailly, O. M. Yaghi and J. R. Long, *Journal of the American Chemical Society*, 2007, **129**, 14176-14177.
147. J. M. Hicks, C. Desgranges and J. Delhommelle, *The Journal of Physical Chemistry C*, 2012, **116**, 22938-22946.
148. N. L. Rosi, J. Eckert, M. Eddaoudi, D. T. Vodak, J. Kim, M. O'Keeffe and O. M. Yaghi, *Science*, 2003, **300**, 1127-1129.
149. L. Wang, N. R. Stuckert, H. Chen and R. T. Yang, *The Journal of Physical Chemistry C*, 2011, **115**, 4793-4799.
150. Q. Yao, J. Su, O. Cheung, Q. Liu, N. Hedin and X. Zou, *Journal of Materials Chemistry*, 2012, **22**, 10345-10351.
151. P. Krawiec, M. Kramer, M. Sabo, R. Kunschke, H. Fröde and S. Kaskel, *Advanced Engineering Materials*, 2006, **8**, 293-296.
152. Z. Guo, H. Wu, G. Srinivas, Y. Zhou, S. Xiang, Z. Chen, Y. Yang, W. Zhou, M. O'Keeffe and B. Chen, *Angewandte Chemie International Edition*, 2011, **50**, 3178-3181.
153. J. L. Rowsell and O. M. Yaghi, *Journal of the American Chemical Society*, 2006, **128**, 1304-1315.
154. K. S. Park, Z. Ni, A. P. Côté, J. Y. Choi, R. Huang, F. J. Uribe-Romo, H. K. Chae, M. O'Keeffe and O. M. Yaghi, *Proceedings of the National Academy of Sciences*, 2006, **103**, 10186-10191.
155. H. Wu, W. Zhou and T. Yildirim, *Journal of the American Chemical Society*, 2007, **129**, 5314-5315.
156. W. Zhou, H. Wu, M. R. Hartman and T. Yildirim, *The Journal of Physical Chemistry C*, 2007, **111**, 16131-16137.
157. P. Srepusharawoot, C. M. Araújo, A. Blomqvist, R. H. Scheicher and R. Ahuja, *The Journal of chemical physics*, 2008, **129**, 164104.
158. T. A. Maark and S. Pal, *International Journal of Hydrogen Energy*, 2010, **35**, 12846-12857.

159. N. Nijem, L. Kong, Y. Zhao, H. Wu, J. Li, D. C. Langreth and Y. J. Chabal, *Journal of the American Chemical Society*, 2011, **133**, 4782-4784.
160. Y.-S. Bae, D. Dubbeldam, A. Nelson, K. S. Walton, J. T. Hupp and R. Q. Snurr, *Chemistry of Materials*, 2009, **21**, 4768-4777.
161. N. A. Khan and S. H. Jhung, *Bull. Korean Chem. Soc.*, 2009, **30**, 2921-2926.
162. W.-J. Son, J. Kim, J. Kim and W.-S. Ahn, *Chemical Communications*, 2008, 6336-6338.
163. Z. Ni and R. I. Masel, *Journal of the American Chemical Society*, 2006, **128**, 12394-12395.
164. C. G. Carson, K. Hardcastle, J. Schwartz, X. Liu, C. Hoffmann, R. A. Gerhardt and R. Tannenbaum, *European Journal of Inorganic Chemistry*, 2009, **2009**, 2338-2343.
165. D.-W. Jung, D.-A. Yang, J. Kim, J. Kim and W.-S. Ahn, *Dalton Trans.*, 2010, **39**, 2883-2887.
166. E. Iriowen, S. Orefuwa and A. Goudy, *Journal of Alloys and Compounds*, 2015, **645**, **Supplement 1**, S242-S246.
167. Z.-Q. Li, L.-G. Qiu, T. Xu, Y. Wu, W. Wang, Z.-Y. Wu and X. Jiang, *Materials Letters*, 2009, **63**, 78-80.
168. M. Mamatha, B. Bogdanović, M. Felderhoff, A. Pommerin, W. Schmidt, F. Schüth and C. Weidenthaler, *Journal of alloys and compounds*, 2006, **407**, 78-86.
169. E. Iriowen, S. Orefuwa and A. Goudy, *Journal of Alloys and Compounds*, 2015.
170. B. Panella and M. Hirscher, *Advanced Materials*, 2005, **17**, 538-541.
171. K.-S. Lin, A. K. Adhikari, M.-T. Tu, C.-H. Wang and C.-L. Chiang, *Journal of nanoscience and nanotechnology*, 2013, **13**, 2549-2556.
172. C.-M. Wu, M. Rathi, S. P. Ahrenkiel, R. T. Koodali and Z. Wang, *Chemical Communications*, 2013, **49**, 1223-1225.
173. J. Hafizovic, M. Bjørgen, U. Olsbye, P. D. Dietzel, S. Bordiga, C. Prestipino, C. Lamberti and K. P. Lillerud, *Journal of the American Chemical Society*, 2007, **129**, 3612-3620.
174. D. J. Tranchemontagne, J. R. Hunt and O. M. Yaghi, *Tetrahedron*, 2008, **64**, 8553-8557.
175. Y. Zhang, Q. Gao, Z. Lin, T. Zhang, J. Xu, Y. Tan, W. Tian and L. Jiang, *Scientific reports*, 2014, **4**.
176. A. G. Wong-Foy, A. J. Matzger and O. M. Yaghi, *Journal of the American Chemical Society*, 2006, **128**, 3494-3495.
177. D. N. Dybtsev, H. Chun and K. Kim, *Angewandte Chemie*, 2004, **116**, 5143-5146.
178. J. Y. Lee, D. H. Olson, L. Pan, T. J. Emge and J. Li, *Advanced Functional Materials*, 2007, **17**, 1255-1262.
179. S. M. Humphrey, J. S. Chang, S. H. Jhung, J. W. Yoon and P. T. Wood, *Angewandte Chemie International Edition*, 2007, **46**, 272-275.
180. M. Kramer, U. Schwarz and S. Kaskel, *Journal of Materials Chemistry*, 2006, **16**, 2245-2248.

181. X.-S. Wang, S. Ma, K. Rauch, J. M. Simmons, D. Yuan, X. Wang, T. Yildirim, W. C. Cole, J. J. López and A. d. Meijere, *Chemistry of Materials*, 2008, **20**, 3145-3152.
182. S. Ma, X. S. Wang, D. Yuan and H. C. Zhou, *Angewandte Chemie International Edition*, 2008, **47**, 4130-4133.
183. A. G. Wong-Foy, O. Lebel and A. J. Matzger, *Journal of the American Chemical Society*, 2007, **129**, 15740-15741.
184. M. Dincă, W. S. Han, Y. Liu, A. Dailly, C. M. Brown and J. R. Long, *Angewandte Chemie International Edition*, 2007, **46**, 1419-1422.
185. G. Férey, M. Latroche, C. Serre, F. Millange, T. Loiseau and A. Percheron-Guégan, *Chemical communications*, 2003, 2976-2977.
186. J. Jia, X. Lin, C. Wilson, A. J. Blake, N. R. Champness, P. Hubberstey, G. Walker, E. J. Cussen and M. Schröder, *Chemical Communications*, 2007, 840-842.
187. X. Lin, J. Jia, X. Zhao, K. M. Thomas, A. J. Blake, G. S. Walker, N. R. Champness, P. Hubberstey and M. Schröder, *Angewandte Chemie International Edition*, 2006, **45**, 7358-7364.
188. M. Dinca, A. Dailly, C. Tsay and J. R. Long, *Inorganic chemistry*, 2008, **47**, 11-13.
189. T. Takei, J. Kawashima, T. Ii, A. Maeda, M. Hasegawa, T. Kitagawa, T. Ohmura, M. Ichikawa, M. Hosoe and I. Kanoya, *Bulletin of the Chemical Society of Japan*, 2008, **81**, 847-856.
190. S. Ma, D. Sun, J. M. Simmons, C. D. Collier, D. Yuan and H.-C. Zhou, *Journal of the American Chemical Society*, 2008, **130**, 1012-1016.
191. J. A. Mason, K. Sumida, Z. R. Herm, R. Krishna and J. R. Long, *Energy & Environmental Science*, 2011, **4**, 3030-3040.
192. H. Furukawa, N. Ko, Y. B. Go, N. Aratani, S. B. Choi, E. Choi, A. Ö. Yazaydin, R. Q. Snurr, M. O'Keeffe and J. Kim, *Science*, 2010, **329**, 424-428.
193. A. O. Yazaydin, A. I. Benin, S. A. Faheem, P. Jakubczak, J. J. Low, R. R. Willis and R. Q. Snurr, *Chemistry of Materials*, 2009, **21**, 1425-1430.
194. P. Aprea, D. Caputo, N. Gargiulo, F. Iucolano and F. Pepe, *Journal of Chemical & Engineering Data*, 2010, **55**, 3655-3661.
195. A. R. Millward and O. M. Yaghi, *Journal of the American Chemical Society*, 2005, **127**, 17998-17999.
196. Z. Zhao, Z. Li and Y. Lin, *Industrial & Engineering Chemistry Research*, 2009, **48**, 10015-10020.
197. M. Nandi and H. Uyama, *The Chemical Record*, 2014, **14**, 1134-1148.
198. Y. Hu, S. Xiang, W. Zhang, Z. Zhang, L. Wang, J. Bai and B. Chen, *Chemical Communications*, 2009, 7551-7553.
199. X. Si, C. Jiao, F. Li, J. Zhang, S. Wang, S. Liu, Z. Li, L. Sun, F. Xu and Z. Gabelica, *Energy & Environmental Science*, 2011, **4**, 4522-4527.
200. H. Furukawa, J. Kim, N. W. Ockwig, M. O'Keeffe and O. M. Yaghi, *Journal of the American Chemical Society*, 2008, **130**, 11650-11661.
201. Y. E. Cheon and M. P. Suh, *Chemical Communications*, 2009, 2296-2298.

202. T. Wu, J. Zhang, C. Zhou, L. Wang, X. Bu and P. Feng, *Journal of the American Chemical Society*, 2009, **131**, 6111-6113.
203. J. Kim, S.-T. Yang, S. B. Choi, J. Sim, J. Kim and W.-S. Ahn, *Journal of Materials Chemistry*, 2011, **21**, 3070-3076.
204. E. D. Bloch, D. Britt, C. Lee, C. J. Doonan, F. J. Uribe-Romo, H. Furukawa, J. R. Long and O. M. Yaghi, *Journal of the American Chemical Society*, 2010, **132**, 14382-14384.
205. K. Sumida, S. Horike, S. S. Kaye, Z. R. Herm, W. L. Queen, C. M. Brown, F. Grandjean, G. J. Long, A. Dailly and J. R. Long, *Chemical Science*, 2010, **1**, 184-191.
206. T. K. Prasad, D. H. Hong and M. P. Suh, *Chemistry-A European Journal*, 2010, **16**, 14043-14050.
207. D. Banerjee, J. Liu and P. K. Thallapally, *Comments on Inorganic Chemistry*, 2014, 1-21.
208. Z. Bao, L. Yu, Q. Ren, X. Lu and S. Deng, *Journal of colloid and interface science*, 2011, **353**, 549-556.
209. A. O. z. r. Yazaydin, R. Q. Snurr, T.-H. Park, K. Koh, J. Liu, M. D. LeVan, A. I. Benin, P. Jakubczak, M. Lanuza and D. B. Galloway, *Journal of the American Chemical Society*, 2009, **131**, 18198-18199.
210. O. K. Farha, A. Ö. Yazaydin, I. Eryazici, C. D. Malliakas, B. G. Hauser, M. G. Kanatzidis, S. T. Nguyen, R. Q. Snurr and J. T. Hupp, *Nature chemistry*, 2010, **2**, 944-948.
211. D. Yuan, D. Zhao, D. Sun and H. C. Zhou, *Angewandte Chemie International Edition*, 2010, **49**, 5357-5361.
212. F. Debatin, A. Thomas, A. Kelling, N. Hedin, Z. Bacsik, I. Senkowska, S. Kaskel, M. Junginger, H. Müller and U. Schilde, *Angewandte Chemie International Edition*, 2010, **49**, 1258-1262.
213. J. A. Botas, G. Calleja, M. Sánchez-Sánchez and M. G. Orcajo, *Langmuir*, 2010, **26**, 5300-5303.

CURRICULUM VITAE

Esosa Iriowen (Ph.D)

Center for Hydrogen Storage & Research (CHSR)

Department of Chemistry

Delaware State University

Dover, DE19901.

Tel: 302-857-7659 (Office) 302-252-5626(Mobile)

xse.iriowen@yahoo.com

Education

2015 Ph.D in Applied Chemistry

Department of Chemistry

Delaware State University – **Dover, U.S.A**

Advisor – Dr. Andrew Goudy

Dissertation: Adsorption of Hydrogen, Methane, and Carbon Dioxide Gases in Metal-Organic Frameworks, using the Sticking Efficiency Concept. (***A New Approach***)

2010 M.Sc. in Chemistry (*Environmental & Analytical*)

Department of Chemistry

Delaware State University - **Dover, U.S.A.**

Advisor – Dr. Qiquan Wang

Thesis: Effect of Saint Jones River Sediment Amendment on Soil Microbial and Enzymatic Activities in Two Different Soils

2008 C. Cert. in Sustainable Development

Centre for Environment & Developmental Studies (CEMUS)

Uppsala University – **Uppsala, Sweden**

Course Coordinator(s) – Dr. Malin Östman & Dr. Johan Älvgren

Course Study: *Interdisciplinary Field Studies, Seminars & Discourses*

2007 M.Sc. (*Tech.*)- Exploration and Environmental Geochemistry

Department of Chemical Engineering & Geosciences

Lulea University of Technology – **Lulea, Sweden**

Advisor(s): Dr. Anders Winderlund & Dr. Johan Ingri

Thesis: Tailings Groundwater Composition at the Kristineberg Mine-Site, Northern Sweden. [2007:027-ISSN:1653-0187-ISRN: LTU-PB-EX--07/027—SE](#)

1998 B.Sc. in Industrial Chemistry
 Department of Chemistry
 Ambrose Alli University – **Ekpoma, Nigeria**
Advisor: Dr. Mark Cyril Azih
Thesis: Analysis of Brewery Effluents

Research

2010 - Present **Delaware State University.** (*Department of Chemistry*)
(Research Associate) Center for Hydrogen Storage & Research (CHSR)

Some Job Responsibilities;

- Developed a **Novel concept procedure** (*Sticking Efficiency*) for calculating quantity of gas adsorbed on certain materials
- Synthesized samples materials for characterization and analysis
- Write technical reports or prepare graphs or charts to document experimental results

2010 **Delaware State University** (*Department of Agriculture & Natural Resources*) **collaboration** with Delaware National Estuary.
(Volunteer Service) Research

Reserve as a partner organization (USDA / REEIS)

Project Number: **DELX0029-08**

2008 – 2010 **Delaware State University** (*Department of Chemistry*)
(Research Assistant Center for Integrated Biologic & Environmental Research (CIBER)
(& Teaching Assistant)

Some Job Responsibilities:

- Collect water sediment and poultry manures samples and prepare them for analysis
- Set up and measure physical and chemical properties using techniques such as spectroscopy, and many others
- Write technical reports or prepare graphs or charts to document experimental results

2006 **Geological Survey of Sweden**
(Student Intern) Field Exploration Unit **Field Study:** Sampling & Mapping of geological outcrops and boulders

Some Job Responsibilities:

- Utilize imaging software capabilities such as SHM, AUOCAD/GIS and others
- Quantitative Powder metallurgy including: PSD, average particle size, saturation, etc.
- Prepare samples for analysis and maintain a communication and information relationship between field and Main office

2005 – 2007 **Lulea University of Technology** (Department of Chemical Engineering
(*M.Sc. Candidate*) & Geosciences)

Some Job Responsibilities:

- Obtaining samples from remediation mine-site and measuring physical and chemical properties. Investigating the effects of mine-waste on environmental
- Studying the effects of aluminum (Al) and Iron (Fe) in the Black Sea in Sweden (Environmental Geochemistry Studies)
- Trained in the use of Inductive Coupling Plasma Techniques-Mass Spectroscopy (*ICP-MS*)

1990 – 2005 **Tradotech LTD**
(*Quality Assurance & Quality Control (QA/QC)*)

Some Job Responsibilities:

- Set up and measure physical and chemical properties to meet quality control standards
- Investigate quality of environmental materials needed for operations to ensure they are conformed to ISON / SHELL standard.
- Visit environmental sites for on-going projects
- Attended Management meetings weekly and also represent the company on high-profile company meetings, policy making and decision.

Scholarships, Grants, and Awards

2011 - 2015 Center for Hydrogen Storage & Research (*CHSR*); US- Department of Energy and Transport (*US-DOE/DOT*)

2013 ***Session Chair & Discussion Leader***
Gordon Research and Seminars (*GRS*) Lucca, *Italy*.
Full Travel and Accommodation sponsorship

2008 – 2011 Center for Integrated Biologic & Environmental Research (*CIBER*) and National Science Foundation - Experimental Program to Stimulate Competitive Research (*NSF - EPSCoR*)

- 2006** **Geological Survey of Sweden**
Student Intern Field Exploration Grant
- 2006** **Course Participant:**
Modeling of Environmental Pollutants: Partitioning, Transport & Exposure
(Stockholm University, Department of Applied Environmental Science)
Swedish Government Grant Program for Developing Countries
- 2006** **Workshop Participant**
3 rd European Workshop in Clay Geosciences
Characterization of Solid-Water interface reactions of metals and Actinides on clays and clay minerals University of Jena (Germany), Geosciences
Department (Student Research Travel and Accommodation Grant Award)
- 2005 – 2007** Swedish Government Grant Program for Developing Countries
Master's Degree Studies at Lulea University of Technology (**Sweden**)

Instrumentations, Personal and Interpersonal Skills:

- Used special instrumentation such as Gas Chromatograph-Mass Spectrophotometry Analyzer (**GC/MS**), High Performance Liquid Chromatography (**HPLC**), Spectrophotometer, Porosity Analyzer (**BET**), High Volumetric Pressure Analyzer (**HPVA**), Scanning Electron Microscope (**SEM**), Fourier Transform Infrared Spectroscopy (**FTIR**), Thermogravimetric Analyzer (**TGA/DTA**), X-Ray Diffractometer (**XRD**), Laser Dispersion Particle Size Analyzer (**LDPSA**), Ultraviolet-Visible Spectroscopy (**UV-VIS**), knowledge of *Chemometrics* application Water Probes, pH-Instant determination instrument, Sediment Core sample grabber, Field Geo-Compass instruments, and many others
- Knowledgeable in the use of other instruments such as *Lab Planetary Micro-mill*, *Atomic Absorption spectrophotometer (AA)*, *Pressure-Composition-Isotherm (PCI)*, *Gas Sorption Analyzer (GSA)* and *Residual Gas Analyzer (RGA)*
- Skilled with computer systems and proficient in the use of various software packages including **GIS/AUTOCAD**, **PHREECQ** (Level 1-4), Stockholm Model (**SHM**), **MICROSOFTS/Office Suites (Word, Excel, PowerPoint)**, **ChemDraw**, **ChemCAD** and others
- Trained and managed four(4) undergraduate students and one(1) Graduate student to achieve significant improvements in their academic productivity towards their research work

- Strong aptitude towards creative idea generation and problem solving, with potentials to understand big pictures as well as technical detail
- Self-starter that can carry out tasks with minimal oversight I posses a team oriented spirit; and willing to share with, listen to and help others
- Excellent written and verbal skills; ability to explain data and results clearly and communicate effectively through Oral, Poster and Scientific article publications

Scientific Presentations and Seminars

Gordon Research Conference (Hydrogen-Metal Systems): Fundamental Aspects of Hydrogen Interaction with Materials and Novel Energy Applications
Sticking Efficiencies Determinations on some Metal-Organic Frameworks for Gas Adsorptions. Iriowen, E., and Goudy, A., July 12-19th , 2015 Easton, U.S.A.
(Poster Presentation)

5th Annual School of Graduate Studies and Research Symposium: *Using sticking efficiency and surface area to determine gas adsorption on selected metal organic-frameworks.*
 Iriowen. E and Goudy. A. Delaware State University. April, 17th 2015. Dover, DE., U.S.A.
(Oral Presentation)

14th International Symposium on Metal-Hydrogen Systems: *Fundamentals and applications Comparative Studies of Sticking Efficiencies in Gas Adsorptions Analysis on Selected Metal Organic Frameworks.* Iriowen, E., Orefuwa, S., and Goudy, A. 20-25 July 2014 Salford, Manchester, United Kingdom **(Poster Presentation)**

4th Annual School of Graduate Studies and Research Symposium, *Understanding the Concepts of Sticking Efficiencies on Selected Gas Adsorption on Metal Organic - Frameworks.* Iriowen, E., Orefuwa, S., and Goudy, A. Delaware State University. April, 25th 2014. Dover, DE., U.S.A. **(Poster Presentation)**

Gordon Research Conference (Hydrogen-Metal Systems): *Hydrogen Interactions in Energy Storage.* *Sticking Efficiencies of Different Gases on Metal Organic Frameworks.* Iriowen, E., Orefuwa, S., Yang, H-W., and Goudy, A., July 14-19th , 2013 Lucca, Italy **(Poster Presentation)**

Gordon Research Seminar (Hydrogen-Metal Systems) *Hydrogen in Metals and Compounds* *Sticking Efficiencies of Different Gases on Metal Organic Frameworks.* Iriowen, E., Orefuwa, S., Yang, H-W., and Goudy, A., July 13-14th, 2013 Lucca, Italy **(Poster Presentation)**

3rd Annual School of Graduate Studies and Research Symposium, "BEYOND BEYOND"
 Delaware State University. *Sticking Efficiencies of Metal Organic Frameworks on Different Gases* **Iriowen, E., Orefuwa, S., Yang, H-W., and Goudy, A., April, 26th 2013. Dover, DE., U.S.A. (Poster Presentation)**

The Promise and Perils of Emerging Technologies:
 College of Mathematics, Natural Sciences and Technology, Delaware State University.
 April 12th 2013 **Dover. DE., U.S.A. (Seminar)**

Ethics Seminar Series College of Mathematics, Natural Sciences and Technology,
 Delaware State University. February 3rd - April 12th 2013 **Dover. DE U.S.A. (Seminars)**

World Hydrogen Energy Conference:"Enhancing Hydrogen Storage Capacity in Isoreticular Metal-Organic Framework (IRMOF-8): Synthesis and Functionalization"
 Orefuwa, S.A, Yang, H., **Iriowen, E.**, Alexander, D., Wakefield, B., and Goudy, A. **Toronto, Canada. June 3-7, 2012. (Poster Presentation)**

Environmental Concerns on Animal Manure
 Q. Wang*, R. Xuan, A. A. Blassengale, L. Arisi, **E. Iriowen. Delaware State University, Dover, U.S.A. (Poster Presentation)**

3rd European Workshop in Clay Geosciences
 Characterization of Solid-Water interface reactions of metals and actinides on clays and clay minerals March 14–15, 2006 University of Jena **Jena, Germany. (Workshop & Seminar Attendee)**

Professional Affiliations

Gamma Sigma Epsilon-(<i>Chemistry Honors</i>)	(GSE)
American Chemical Society	(ACS)
Chemical Institute of Canada	(CIC)
International Association of Applied Geochemists	(IAG)

List of Journal Publications

Iriowen, E., Orefuwa, S., & Goudy, A. (2015). The Role of Sticking Efficiencies in Hydrogen Gas Adsorption on Metal Organic Frameworks. *Journal of Alloys and Compounds*. J. Alloys Comp 645 (2015) S242–S246

Orefuwa, S., **Iriowen, E.**, Yang, H., Wakefield, B., & Goudy, A. **(2013).** Effects of nitro-

functionalization on the gas adsorption properties of isoreticular metal-organic framework-eight (IRMOF-8). *Journal of Microporous and Mesoporous Materials*, 177, 82-90

Qiquan, W., **Iriowen, E.**, Yuan, S., and Sparks, D.L. (2011). Impact of Sediment from St. Jones River, Delaware, USA on Microbial Functional Stability in Two Local Soils. *Journal of Bioremediation & Biodegradation*. ISSN: 2155-6199 JBRBD, <http://dx.doi.org/10.4172/2155-6199.S1-005>

Professional Reference(s)

Andrew Goudy (Ph.D)

(Director & Advisor)

Center for Hydrogen Storage & Research (CHSR)

Department of Chemistry

Delaware State University,

Dover, DE.19904

Tel: +1302-857-6534

Email: agoudy@dsu.edu

Cherese Winstead (Ph.D)

(Chair Person)

Department of Chemistry

Delaware State University,

Dover, DE.19904

Tel: +1302-857-6251

Email: cwinstead@dsu.edu

Bizuneh Workie (Ph.D)

(Faculty & Course Professor)

Department of Chemistry

Delaware State University

Dover, Delaware. 19904

Tel: +1302-857-6545

Email: bworkie@desu.edu

PUBLICATIONS FROM THIS RESEARCH

- 1. The Role of Sticking Efficiencies in Hydrogen, Carbon Dioxide and Methane Gas Adsorption on Metal-Organic Frameworks**
E. Iriowen and A. Goudy (*Submitted to (Elsevier) Journal of Alloys and Compounds October, 2015*).
- 2. The role of sticking efficiencies in hydrogen gas adsorption on metal-organic frameworks**
E. Iriowen, S. Orefuwa and A. Goudy, *Journal of Alloys and Compounds*, **2015**, 645, Supplement 1, S242-S246.
- 3 Effects of nitro-functionalization on the gas adsorption properties of isostructural metal-organic framework- eight (IRMOF-8)**
S. Orefuwa, *E. Iriowen*, H. Yang, B. Wakefield and A. Goudy, *Microporous and Mesoporous Materials*, **2013**, 177, 82-90.